Politecnico di Torino

ScuDo
Scuola di Dottorato ~ Doctoral School
WHAT YOU ARE, TAKES YOU FAR

Doctoral Dissertation
Doctoral Program in Mechanical Engineering (35^{th}cycle)

Nonlinear and Linearized Analysis of Vibrations of Loaded Anisotropic Beam/Plate/Shell Structures

By

Rodolfo Azzara

******

Supervisor(s):
Prof. Erasmo Carrera
Prof. Alfonso Pagani
Prof. Matteo Filippi

Doctoral Examination Committee:
Prof. ..., Referee, University of...
Prof. ..., Referee, University of...
Prof. ..., University of...
Prof. ..., University of...
Prof. ..., University of...

Politecnico di Torino
2023

Declaration

I hereby declare that, the contents and organization of this dissertation constitute my own original work and does not compromise in any way the rights of third parties, including those relating to the security of personal data.

Rodolfo Azzara
2023

* This dissertation is presented in partial fulfillment of the requirements for **Ph.D. degree** in the Graduate School of Politecnico di Torino (ScuDo).

Alla mia famiglia.

"*Ho fatto quello che ho potuto,*
non credo di essere andato così male."
Diego Armando Maradona

Acknowledgements

First of all, I would like to sincerely thank my supervisor Prof. Erasmo Carrera for the opportunity, the trust placed in me, and the time dedicated to me over these years. His expert guidance was a fundamental contribution to my professional and personal growth. For this and much more, I may only continue to thank him.
I am also deeply grateful to my supervisors, Prof. Alfonso Pagani and Prof. Matteo Filippi, who continuously supported and encouraged me with their example and dedication to research.
Thank to Prof. Marco Petrolo and Prof. Enrico Zappino for their constant and kind support.
I deeply thank Dr. Riccardo Augello for always being available over all these years.
The content of this thesis would be empty without the contribution and support of my colleagues from the Mul2 Group of the Politecnico di Torino. In particular, the guys from "*Ufficio 30*": Alberto, Marco, Mattia, Rebecca and Michele, thank you for making every working day fun.
Thanks also to all the other guys who have been there during this period. All have played a crucial role in my research activity.
Finally, in these last words, I would like to thank my family and my love Alba for their patience and generous support.

GRAZIE A TUTTI.

Rodolfo Azzara

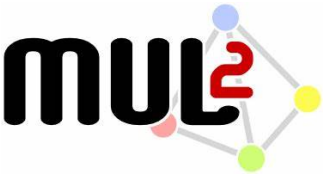

Abstract

The dynamic behaviour of a structure plays a crucial role in its function in many technical areas and its knowledge is important from the preliminary design phase with a significant impact on safety, performance and comfort. It is a matter of fact that stability considerations are a fundamental and inevitable topic in the design of many engineering structures employed in various fields. The concept of stability is intrinsically a dynamical one, and the formal analogy between buckling and vibration has stimulated the use of the vibration (dynamic) approach as a standard procedure in the design of structures to get important information to characterize buckling behaviours. One of the most important and employed non-destructive methods to compute large-scale aerospace structures' critical buckling load is the Vibration Correlation Technique (VCT). This method computes the buckling load and the equivalent boundary conditions by interpolating the natural frequencies of the structures for progressively increasing applied loadings without reaching instabilities.

In this context, the present work intends to propose an advance toward the efficient implementation of a novel numerical approach for carrying out nonlinear vibration-buckling investigations of isotropic, classical composite and variable-angle-tow (VAT) composite beam, plate and shell structures subjected to different mechanical and thermal loadings in order to predict buckling loads, to characterize the natural frequencies variation for progressively increasing loadings and to provide an efficient means for the verification of the experimental VCT results.

The dynamic characteristics of any structure are inherently a property of the equilibrium conditions. For this reason, the availability of accurate mathematical models able to deal with higher-order phenomena, which may occur within the structure, is of pivotal relevance. The presented nonlinear approach is formulated in the well-established Carrera Unified Formulation (CUF) framework. Basically, the CUF, by using an index notation, allows to unify all the theories of structures in a single formula and to formulate very refined beam, plate and shell models in a simple way. According to CUF, the 3D displacement field can be expressed as an arbitrary expansion of the generalized displacements. Depending on the choice of the polynomials employed in the expansion, various classes of beam, plate and shell models can be implemented. In detail, both Taylor-like (TE) and

Lagrange (LE) polynomials are considered for developing the kinematic expansion. With this procedure, the nonlinear governing equations and the relative finite element arrays of the one-dimensional (1D) and two-dimensional (2D) theories are formulated in terms of Fundamental Nuclei (FNs). FNs represent the basic building blocks of the proposed formulation. All Green-Lagrange strain components are employed because far nonlinear regimes are investigated. Furthermore, the geometrical nonlinear equations are written in a total Lagrangian framework and solved with an opportune Newton-Raphson method along with a path-following approach based on the arc-length constraint.
The importance of correctly choosing the structural theory, kinematic model and nonlinear strain measure model to perform accurate analyses is remarked through various numerical results. In detail, the need to adopt higher-order and full nonlinear strain models is emphasized in the analyses in order to accurately evaluate the 3D stress fields and undamped nonlinear dynamic responses of isotropic and composite structures. Several examples for different equilibrium conditions in the moderate and large displacement fields are proposed. The validity of the presented formulation is demonstrated and important modal aberrations as a consequence of the loading, the nonlinear equilibrium state, and the material anisotropy are discussed. The results document the excellent accuracy and reliability of the presented methodology and show the potentialities of this numerical tool able to analyze cases that are difficult to study experimentally.

Keywords: Finite Element Method; Carrera Unified Formulation; Higher-order beam/plate/shell models; Isotropic material; Composite material; Variable stiffness composites; Geometrical nonlinearity; Buckling; Large-deflection; Post-buckling; Vibration analysis; Vibration Correlation Technique; Nonlinear dynamic response.

Table of contents

List of figures

List of tables

Nomenclature

Symbols

A	Area
$\mathbf{b}_l$	Linear differential operators
$\mathbf{b}_{nl}$	Nonlinear differential operators
$\mathbf{B}$	Coupling matrix
$\mathbf{B}_l$	Linear algebraic matrices
$\mathbf{B}_{nl}$	Nonlinear algebraic matrices
$\mathbf{C}$	Material linear elastic matrix
$\mathbf{d}_t$	Time step
$\mathbf{E}$	Young's module
$\mathbf{E}_L$	Young's module of the loading part
$\mathbf{E}_R$	Young's module of the research object
f	Natural frequency
F_τ	Expansion functions
$\mathbf{E}$	Shear module
I	Moment of inertia
$\mathbf{K}_s$	Secant stiffness matrix
$\mathbf{K}_\sigma$	Geometric stiffness
$\mathbf{K}_T$	Tangent stiffness matrix
$\mathbf{L}_{ext}$	Work of the external loads
$\mathbf{L}_{ine}$	Work of the inertia loads
$\mathbf{L}_{int}$	Work of the strain energy
$\mathbf{M}$	Mass matrix
N	Order of the expansion
N_i	Shape function
P, p	Applied external load
$\mathrm{P}_{\mathrm{inner}}$	Inner pressure

R, θ	Radius and curvature
$\mathbf{u}_\tau, \mathbf{u}_{\tau i}$	Generalized displacement vector and finite element nodal parameters
V	Volume
x, y, z	Cartesian system
α,β,z	Orthogonal curvilinear system
δ	Variation
$\boldsymbol{\epsilon}$	Strain vector
Φ	Eigenvector
ω	Angular frequency
ρ	Density
$\boldsymbol{\sigma}$	Stress vector
ν	Poisson's ratio

Superscripts and subscripts

i	Collocation index of the variable
j	Collocation index of the variation
s	Expansion index of the variable
τ	Expansion index of the variable

Acronyms/Abbreviations

1D	One-dimensional
2D	Two-dimensional
3D	Three-dimensional
ABQ	Abaqus software
CW	Component-wise
CUF	Carrera Unified Formulation
DOFs	Degrees Of Freedom
E-B	Euler-Bernoulli
ESL	Equivalent Single Layer
FE	Finite Element
FEM	Finite Element Method
FNs	Fundamental nuclei
FSDT	First order Shear Deformation Theory
HHT-α	Hilber-Hughes-Taylor-α
LE	Lagrange Expansion

LEN	Lagrange Expansion of order N
LW	Layerwise
MAC	Modal assurance criterion
MITC	Mixed Interpolation of Tensorial Components
NR	Newton-Raphson
PVD	Principle of Virtual Displacements
TE	Taylor Expansion
TEN	Taylor Expansion of order N
VAT	Variable-angle-tow
VCT	Vibration Correlation Technique
VK	von Kármán

Chapter 1

Introduction

1.1 Structural dynamics and stability

Aerospace structures are usually required to operate in particular conditions that take into account mechanical and thermal loadings. This characteristic, associated with the need to save weight and material and have high performance in new structures and machines, has led to the consideration of stability problems more and more important. Typically, structures show failures primarily due to material failure or structural instability. Generally speaking, stability considerations are a crucial and inevitable topic in the design of many engineering structures, employed in various fields, for example, aeronautical, space, civil, mechanical or naval engineering. In this context, the designer faces numerous structural problems related to the stability of the various components. Consequently, several studies have investigated the instability behaviours of the beam, plate and shell structures, both theoretically and experimentally [1–3].

The main goal of the structural problems is to derive configurations of loaded systems that satisfies the equilibrium conditions, compatibility, and load-displacement relationships of materials. For this purpose, it is required to examine whether the resulting equilibrium configurations are stable and, then, consider the structure satisfactory from a structural point of view. The stability loss due to compressive loadings is typically called structural or geometrical instability, generally called as *buckling*. The latter phenomenon consists of sudden changes of equilibrium configurations at certain critical loads. The evaluation of the buckling load is equivalent to finding that load under which the structure exhibits a stable equilibrium state, but if perturbed, it moves away from this position, becoming unstable. Buckling failures are potentially very dangerous and can facilitate the collapse of several types of engineering structures [4]. It should be emphasized that in any type of stability loss, changes in geometries or configurations involve the introduction

of new additional forces or changes in the nature of forces that existed in undeformed structures. In terms of new forces that arise during the structural stability loss, a classification of instability can be given as follows: 1. Flexural buckling; 2. Torsional buckling; 3. Torsional-flexural buckling; 4. Snap-through buckling. Furthermore, instability, which refers to the buckling of structures under static loads, is called static buckling, while it is defined as dynamic buckling if dynamic loads are considered. An extensive discussion on the fundamentals of stability theory can be found in Ref. [5].

In linear mechanics of deformable bodies, the displacement is proportional to the load. However, the essence of buckling is a disproportionate increase in displacements resulting from a small increase in loads. As a consequence, buckling analyses are a subtopic of nonlinear rather than linear mechanics. Therefore, buckling is a nonlinear phenomenon and that linearized analyses are used only for reasons of analytical convenience. Nevertheless, a linearized analysis gives suitable results for design use for many applications. Nevertheless, there are three typical situations where nonlinear analyses are needed:

1. A linearized analysis indicates the loading level in which a new deformation pattern begins to develop. It also determines the initial mode of this pattern, but it gives no information about the shape of the secondary path;

2. In some cases, pre-buckling nonlinearity must be considered to accurately determine the critical load. In such cases, the stability equation for determining the bifurcation point are linear, but the variable coefficients in stability equations are governed by the nonlinear equations of equilibrium;

3. Lastly, in more general cases, stability losses occur at a limit point instead of at a bifurcation point. In such cases, the buckling load has to be determined by solving the nonlinear equilibrium equations.

In this research, stress and strain are assumed to obey the law of Hooke. Consequently, the nonlinearity is purely geometrical. The collapse load of structures is usually defined by a maximum in the load-displacement curves. To find such a maximum, the governing nonlinear differential equations are solved for a stepwise increasing load or displacement, typically the Newton-Raphson (NR) approach. A detailed discussion of the NR method and other similar approaches is presented in Ref. [6]. Analytical solutions of these equations generally cannot be obtained [7].

Structural instability analyses have been studied for many centuries. Euler [8] introduced the critical load concept of elastic structures in which the equilibrium bifurcates, also providing the solutions of buckling loads of column structures with various constraints. However, the critical loads calculated by the latter could not be experimentally

demonstrated. The reason of this lack was discussed by Young [9], who explained that imperfections such as initial curvature, initial bending moments or load eccentricity play a crucial role in the stability problem. Consequently, he obtained a formula that is now known as the magnification factor for deflections and bending moments in column structures due to axial loading. Then, Kirchhoff [10] explained the theory of geometrically nonlinear large-deflections and developed an elegant solution for deflection curves, called the *elastica*, in terms of elliptic integrals. The effect of shear, that occurs in column structures with a low effective shear stiffness, was demonstrated by Engesser [11]. Over the years, many efforts have been focused on studying the stability of beam, plate and shell structures by trying to formulate new methods to accurately predict buckling and still today it is a challenge among researchers and scientists [12–16].

It is common knowledge that buckling does not always mean failures. Thus, it is also needed to investigate post-buckling behaviours and vibration features of buckled thin-walled structures under various loadings. In addition, there is also analogies between post-buckling and nonlinear vibration. For example, the typically unstable post-buckling equilibrium curve of shell structures, represented by a negative slope of nonlinear paths, compared to the linear characteristic, corresponds to the softening vibration behaviour. This often observed behaviour shows how the vibration frequency decreases as the amplitude vibration increases. Vibrational analyses of structures is not only a relevant topic in itself, but known the connections between the vibrational behaviour and that of deformation, it is widely used as an approach to study the stability of a structure. Although the vibration behaviours of these structures has significant applications in structural engineering, the available literature on this topic is generally limited to the pre-buckling regime [17, 18], whereas researches on the thin-walled structures vibrations in post-buckling regimes have not received detailed investigation.

The concept of stability is intrinsically a dynamical one. The formal analogies between buckling and vibrations have stimulated the use of the vibration (dynamic) approach as a standard procedure in the design of structures to get informations which are important to characterize the buckling behaviours [19, 20]. The analytical or qualitative methods are almost always approximate and, therefore, even a physical analysis of the vibration systems is more difficult if nonlinear; these solution methods must be integrated by digital or analogue calculation techniques. On the other hand, numerical methods have led to the understanding of new phenomena in the field of strongly nonlinear systems. Similarly, solution stability investigations are also more difficult because the existence of multiple stable solutions is common in nonlinear systems. If natural frequencies of a structure coincides with the frequency of external excitations, a phenomenon known as resonance

occurs, which leads to excessive deformation and failures. Due to the devastating effects that vibrations can have on structures, vibration analysis has become a crucial step in the design of many engineering systems in order to study and characterize the natural frequency variation under different loading conditions. In detail, the resonance frequencies of nonlinear systems change with the vibration amplitudes. For very small amplitudes, they coincide with the natural frequencies of the linear approximations. For larger amplitudes, the resonance frequencies decrease with amplitudes for softening systems and increase with amplitudes for hardening systems.

A number of different approaches, analytical, numerical and experimental, have been used for determining critical conditions through vibration data for elastic structures which are subjected to instability. Especially, the experimental campaign continues to be indispensable for the design and validation of methodologies of the modern structures. Nevertheless, one of the objectives of researchers over the years was to reduce both the time and cost of operations of these complex tests to derive the buckling loads. One of the effective methods is to adopt non-destructive experimental tests to assess critical loads of structures. Southwell developed one of the first non-destructive approaches to compute buckling loads of a simple structure, such as thin beam [21], which was improved by Galletly and Reynolds [22] to be also applicable for stiffened cylindrical shell structures. One of the most studied non-destructive methodologies that offer a valid alternative to the conventional classic stress tests adopted by the aerospace industries for the assessment of buckling is the Vibration Correlation Technique (VCT). The latter appears to be a promising approach for non-destructive buckling estimation in experiments. The main characteristic of these methods is that of not having the need to load the structure up to instability.

The concept of vibration-buckling correlation was considered at the beginning of the 20^{th} century by Sommerfeld [23], but only in the 1950s, some experimental investigations were carried out by Chu [24], Lurie [25], and Meier [26], among others. Readers are referred to [3] for a meticulous review of the theories, applications, experimental setup, and results of VCT approaches on different structures. For a clearer evaluation of VCT applications on beam, plate and shell structures, it is significant to divide the method according to its purpose: 1. identification of actual boundary conditions and 2. direct prediction of buckling load.

By comparing theoretical and experimental results, significant discrepancies were noticed. The cause of this is linked to the presence of imperfections in the real structure, observed for the first time as early as the early 1900s by Southwell [21]. For example, buckling loads of thin-walled composite structures are very imperfection sensitive, and

their reliable identification requires knowledge of the worst realistic imperfections. Numerous studies have shown that the force-carrying capacity may be significantly improved by using composite structures. Nevertheless, the imperfection sensitivity is still not fully understood and improved design guidelines for such materials still do not exist. As a consequence, several projects were conducted to investigate the buckling behaviour of such imperfection-sensitive structures. Flügge [27] and Donnell [28] were the first authors to explain formulations by taking into account the effects of initial geometric imperfections, but the nonlinear analyses failed to calculate the experimental buckling loads. Flügge's and Donnell's theories prove a gradual appearance of buckles with an increase in the compressive loadings, while in the experiments, buckling is typically characterized by a sudden dynamic buckling event and a corresponding reduction in the force. Since buckling is a phenomenon that occurs dynamically, many researchers have been involved in the evaluation of the nonlinear transient response to characterize and understand the dynamic behaviour of structures under time-dependent loadings. For example, Budiansky [29] examined the concept of the buckling of elastic strictures under time-dependent loads. Chamis [30] provided several analyses on dynamic buckling and post-buckling of composite shell models. Numerical dynamic analyses on thin-walled laminated composite cylindrical shells under longitudinal impact loadings were performed by Chitra and Priyadarsini [31] through the commercial software Abaqus. Buckling analyses of fiber-reinforced composite shell structures with four plies subjected to impulsive axial compressive loadings were conducted by Bisagni [32]. An interesting monograph on the study of buckling and post-buckling behaviours of thin-walled structures under static or dynamic loadings is the book of Kubiak [33].

Since the limitations of analytical approaches, many efforts were concentrated on the development of numerical methods able to provide accurate solutions in order to verify the experimental results and provide important preliminary results. In most practical problems, the solution demands the application of approximated computational methodologies. The advent of the Finite Element Method (FEM) [34] has overcome many of these difficulties. Several problems in stability and vibration analyses of structures may be very complex due to initial geometric imperfections, geometry, anisotropy, nonlinearity, and the number of degrees of freedom, and their solution can require powerful formulations. The earliest nonlinear finite element (FE) analyses were carried out by Oden [35] and Zienkiewicz [36]. Over the years, many research efforts have focused on improving effective formulations that can accurately perform nonlinear static and dynamic analyses [37–39] in order to give reliable and valid tools for developing new designs and providing a means of verification of the experimental tests.

1.2 Scope and outline

In view of the aforementioned issues in stability investigations, a rigorous and efficient modelling technique is indispensable for engineers to exploit the potential of engineering structures better. In this context, the present thesis represents an advance toward the efficient implementation of numerical methods to accurately carry out nonlinear vibration-buckling investigations of isotropic and composite beam, plate and shell structures, including geometrical nonlinearity. A broad range of problems is considered during this research period, including stress analyses, buckling analyses, free-vibration analyses, vibration analyses of mechanically- and thermally-loaded structures, transient analyses and multibody analyses.

The focus of this work is on the implementation of a novel modelling framework, based on a unified formulation of structural theories and the FEM, able to describe buckling behaviours, examined in terms of static, load-displacement curves, and dynamic, vibration-buckling correlation or time response, for different structures. Emphasis is on understanding the behaviour of the structure, considering different geometries, material properties, boundary conditions and loadings, and the evaluation of the buckling loads, natural frequencies variation and stresses distribution.

The founding basis of this research is based on the principle that the vibration is a property of the state of equilibrium. Consequently, in order to be able to carry out accurate analyses on the vibrations of loaded structures and to characterize in detail how these modes vary, it is mandatory to correctly calculate the state of equilibrium. To achieve this last aspect, it is essential to have an efficient method capable of capturing all the complex nonlinear phenomena that may occur within a structure. Therefore, an approach which takes into account higher-order phenomena is needed.

In this context, the presented linear and nonlinear studies are conducted by using the Carrera Unified Formulation (CUF) [40]. CUF was implemented first for plate and shell models [41, 42] and, subsequently, also for beams [43]. The main novelty of CUF models turns out to be that the order of the theory is a free parameter or may be an input of analyses and it may be chosen performing convergence studies. CUF may also be assumed as a tool to assess the accuracy of any structural model in a unified manner. For the sake of completeness, the reader is referred to [44–52] for the application of the CUF in different engineering problems.

The main novelties of this thesis are: (i) Several kinematic assumptions for beams, plates and shells are implemented and compared regarding the numerical accuracy and efficiency for the computation of the three-dimensional (3D) stress fields in generic isotropic and laminated structures subjected to large displacements and rotations; (ii) the

effect of various geometrically nonlinear strain measures on the response of isotropic and composite structures is investigated; (iii) some advances in the nonlinear vibration analysis of beam, plate and shell models are discussed, studying the effect of pre-stress states on the natural frequencies; (iv) analytical and numerical vibration-buckling correlation of mechanically- and thermally-loaded structures are presented; (v) new static and dynamic benchmark cases for isotropic, laminated composite and variable-angle-tow beam, plate and shell structures are proposed through refined FE modelling.

The thesis is composed of six chapters that describe the development of a platform, using higher-order structural numerical models, for geometrically nonlinear static and dynamic analyses of isotropic and composite beams, plates and shell subjected to mechanical or thermal loading. The general layout of the present research is as follows:

- **Chapter 2** starts with a brief discussion of the Vibration Correlation Technique (VCT). After that, a brief bibliographic survey on classical and refined structural theories for beam, plate and shell structures and the related analytical solution formulations for computing the critical load through vibration data is provided.

- **Chapter 3** introduces the higher-order one-dimensional (1D) and two-dimensional (2D) models adopted in this research. The presented methodology is formulated in the CUF domain. Within the CUF, the beam, plate and shell kinematics are expressed as the generic expansion of the generalized displacements employing arbitrary cross-sectional and thickness functions. Depending on the choice of functions type and order, various beam, plate and shell theories may be derived. In the present work, both the Lagrange-like (LE) and Taylor-like (TE) polynomials are considered. To study the reinforced structures, the component-wise (CW) method is adopted. When laminated composite structures are analyzed, the Layerwise (LW) and Equivalent-Single-Layer (ESL) kinematics are adopted. According to CUF and introducing the FEM, the nonlinear governing equations are expressed in a general but unified and compact manner in terms of *Fundamental Nuclei* (*FNs*), which stand for the basic building blocks of the proposed theory, by exploiting the Principle of Virtual Displacements (PVD).

- **Chapter 4** presents geometrically nonlinear static and nonlinear dynamic formulations employed in this research to study different problems. Furthermore, some numerical examples are presented to highlight the importance of correctly choosing the structural theory, kinematic model and nonlinear strain measures model in order to perform accurate analyses, in terms of large-deflections, post-buckling and dynamic response in the time domain. The need to adopt higher-order and

full nonlinear models is emphasized in the analysis to accurately evaluate the 3D stress fields and nonlinear transient responses in isotropic and composite structures. Once the best model has been chosen, this methodology will be used to perform the vibration problem of the loaded structures, the main theme of this thesis.

- **Chapter 5** discusses some of the results obtained. The interest is primarily focused on the efficiency and reliability of the presented numerical approach when applied to vibration analysis of pre-stressed thin-walled structures in the highly nonlinear regime. In particular, the virtual VCT results compared to the experimental one showed excellent accuracy and reliability of the presented approach. Results showed the potential of refined 1D and 2D theories to reduce the computational costs of real problems simulation without drastically compromising the accuracy.

- **Chapter 6** gives a summary of the present work and some concluding remarks to highlight the major outcomes of this thesis. Some research ideas are proposed as topics for future investigations based on the developments achieved during the scope of the current PhD program.

- **Appendix A** provides other results of important nonlinear problems studied during this research work. In detail, first, large-deflection and post-buckling analyses are investigated in a total Lagrangian domain by using the NR method with a path-following method based on the arc-length constraints. Then, several beam and plate structures with different initial configurations, loadings and boundary conditions are investigated to prove the accuracy and capability of the presented nonlinear dynamic methodology. Results are compared to commercial FEM software solutions and with results found in the available literature. Dynamic analyses are performed over different time intervals using the HHT-α methods. Furthermore, the latter method is also employed in the proposed multibody tool, where Lagrange multipliers are adopted to model mechanical systems with constraints. Some preliminary simple multibody problems are presented to show the capability of the proposed CUF-based multibody tool, where the main advantage is to consider flexible components simply and with high accuracy. As is well known, the computational analysis cost is related directly to the size of the time step, which has to be adopted for accuracy and stability. For this reason, convergence analyses of the mesh approximation and time step size are performed for each case study. Note that for all the considered examples, damping is neglected and higher-order beam/plate models are adopted. Particular emphasis is related to the importance of choosing

the appropriate kinematic theory to accurately describe the dynamic behaviours of the considered structure.

- **Appendix B** lists journal articles and conference proceedings which resulted during the course of the present work.

Chapter 2

Buckling prediction from vibration data

This chapter intends first to provide an overview of the relevant literature devoted to estimating the critical buckling load through vibration measurements and then a review on the development of 1D and 2D theories and the analytical resolution based on the dynamic approach to derive buckling loads through vibration data for the Euler-Bernoulli beam (E-B), Kirchhoff plate and cylindrical shell structure, assuming simply-supported boundary conditions.

It is well-known that the differential equations governing 3D elasticity problems may be resolved analytically only for a limited number of cases. In fact, the solution to 3D problems in closed-form is impossible in the general case relating to any geometries, boundaries and load conditions. Therefore, it is necessary to introduce simplifying hypotheses to move from 3D to 2D and 1D and solve the problem in an approximate form. Different analytical approaches are employed to solve stability problems of certain systems, such as the imperfection criterion, the Euler criterion, the Lagrange criterion and the dynamic (vibration) criterion [53]. Unlike the previous criteria, the latter also takes into account the inertia forces and allows to compute critical loads by analyzing the variation of structure's vibrations. In addition, the dynamic criterion must be employed if non-conservative forces are applied.

Analytical evaluations of critical loads can be obtained only for some simple structures under certain load and constraint conditions. For this reason, several experimental and numerical methods were developed over the years to derive an accurate procedure for predicting critical load and structural behaviour.

2.1 State of art: Vibration Correlation Technique

Over the years, several researchers have simultaneously focused on the problems of vibration and elastic stability [54]. Several studies investigated both phenomena to understand the effects on the vibration responses triggered by the local or global instabilities, see [3, 55–57]. A detailed evaluation of the dynamic behaviour (i.e., modal shapes and natural frequencies) is required for a reliable design and verification of the working structure. In addition, it can be pointed out that the equilibrium state and the pre-stress condition of a structure highly affect its modal characteristic. For example, when large displacement and rotations occur within a working service of a component, its equilibrium conditions change, so it is expected that its dynamic properties change as well. For this reason, it is crucial to investigate the changing of modal shapes and natural frequencies in the case of geometrical nonlinear situations, i.e., when the equilibrium condition is far from the trivial states ($\boldsymbol{u} = 0$).

The idea of using the natural frequencies variation of an axially-loaded structure to identify critical buckling loads (P_{cr}) appeared at the beginning of the 20^{th} century from the work of Sommerfeld [23], in which he observed that the first natural frequency of a cantilever beam with a variable mass at the free end decreases approaching zero as the mass was increased up to the amount required to buckle the structure. Various analytical formulations that relate the applied loads and natural frequencies for the different structures have been established. Among others, the foundation of the VCT is considered the work developed by Massonnet [58], in which the linear relation between the applied loadings and the squared loaded natural frequencies for simply-supported beam, plate and cylindrical shell structures was demonstrated. It reads:

$$\mathrm{f}^2 + \mathrm{P} = 1 \tag{2.1}$$

in which f indicates the loaded natural frequency and P the axially applied force. This study represents the basis of experimental non-destructive procedures that have been proposed in the last decades to predict the buckling load from the pre-buckling regime. Among the different techniques that were developed, the Southwell plot affirmed on static responses and the VCT based on vibrational responses are the most used.

The Southwell plot [59] represents the first non-destructive method, which appeared in the early 1930s, for computing the critical load based on measurements of a simple beam structure. Next, the practicality of this methodology was promptly verified by Donnell [60], in which the approach was demonstrated valid for any n^{th} theoretical buckling loads, and Fisher [61], where the technique was validated for rectangular spars subjected to

combined loadings, typically found in aeronautical applications. Subsequently, several authors improved the method and extensively studied its applicability. For instance, Horton *et al.* [62] thoroughly examined the application for column and plate structures, demonstrating that the methodology is valid for structures with deformations of less than half the thickness. A modified form of the Southwell plot to investigate the lateral-torsional buckling of columns was explained by Stratford *et al.* [63, 64]. The Southwell plot is employed to investigate the buckling of plate structures with some inherent limitations, due to the nonlinear extensional strains, which influence the exact value of the load. Readers are referred to [2, 60, 65] for some applications on plate structures.

On the other hand, in the early 1950s the classic VCT was established at the Caltech University for the direct estimation of critical loads and equivalent boundary conditions by interpolating the natural frequencies of the structures for increasing applied loadings without reaching instability conditions [24, 25, 66]. VCT is a powerful approach, specially for structures with unknown or imperfect boundary conditions in which analytical or numerical solutions to the problem are not available. This technique consists in plotting the experimental data in the classical characteristic graph, f^2 vs P, and then applying a linear relationship of best fit, see Fig. 2.1, to extrapolate the buckling load value when the natural frequency reaches zero.

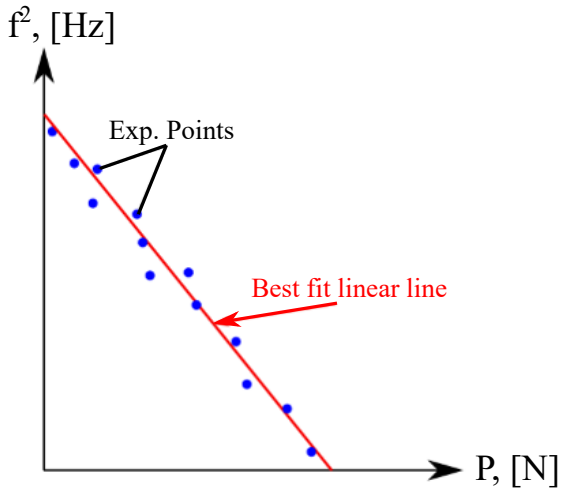

Fig. 2.1 Calculation of predicted buckling load using the VCT.

VCTs were applied to columns-beams [67–69] for decades by reaching maturity in industrial applicability, while further improvements are still being developed for plate and shell structures. In fact, this methodology is simple for studying beams with different constraints, in which the first vibration mode shapes are still similar to the corresponding buckling mode shapes. The curve $f^2 - P$, linear for simply-supported constraints, deviates

slightly from linearity for different boundary conditions, allowing VCT based on the best linear fit to be successfully used [70]. In contrast, the applicability of this approach to derive the buckling of plate and shell models is not straightforward. Studies have shown that even for simply-supported plates the curves deviate from linearity resulting in poor estimates of instability [25]. Particularly, this technique is not yet mature and suitable for curved panels or cylindrical shells with imperfections or unstable buckling behaviours. In this context, different VCT tests were carried out over the years. Mandal [71] analyzed different 2D structures with simply-supported boundary conditions by analyzing the mode changes with increasing progressive loadings. Experimental and numerical investigations for flat stiffened carbon fiber-reinforced polymer panels were conducted by Chaves-Vargas *et al.* [72] to predict the critical load using the classic VCT with a deviation of 5% compared to the experimental value. Kennedy and Lo [73] evaluated the reliability of the VCT to evaluate shear buckling loads of simply-supported plate structures. Several identical spherical shell structures subjected to static external pressure were tested by Okubo and Whittier [74]. The analysis proved that extrapolating the nonlinear relation between f^2 and P to the abscissa would lead to appropriate estimations of critical loads. At the Technion, researchers noted that the method is essentially a curve fit of the experimental data, and thus a new formula for linking the frequency and applied load was convenient for those cases that present a sharp bend close to the buckling load [3]:

$$\mathrm{f}^q = A - BP \tag{2.2}$$

in which A and B denote fitting constants and the exponent q leads the extrapolated load level to match exactly the experimental buckling load. The parameter q is an empirical value calculated from experimental data. By adopting this new formula, Segal [75] carried out different studies on stiffened cylinders calculating the optimal value q_{OPT} in terms of geometric characteristics. A new relation between the natural frequencies and the applied compression loadings was presented by Souza *et al.* [76, 77]. In this work, a modified graph in terms of the parametric forms $(1-\mathrm{P})^2$ and $1-\mathrm{f}^4$ was adopted. Therefore, the new relationship is:

$$(1-\mathrm{P})^2 + (1+\zeta^2)(1-\mathrm{f}^4) = 1 \tag{2.3}$$

in which ζ^2 stands for the square of the drop of buckling loads due to the initial imperfections. Recently, a second-order equation to represent the classic characteristic chart was formulated by Abramovich *et al.* [78]. Different metallic and composite curved panels were tested to confirm the validity of these approaches. A semi-analytical VCT

formulation to calculate critical loads of shell structures was suggested by Jansen *et al.* [79]. Arbelo *et al.* [80, 81] implemented an empirical-VCT based on the considerations done by Souza by using the applied force in the parametric form $(1-\mathrm{P})^2$ as a quadratic function of the loaded natural frequency represented as $1-\mathrm{f}^2$. This second-order equation occurs through a best-fit procedure, from which ζ^2 is extrapolated as a minimum, see Fig. 2.2 and Ref. [81]. Singhtanadgid and Sukajit [82] obtained from the differential

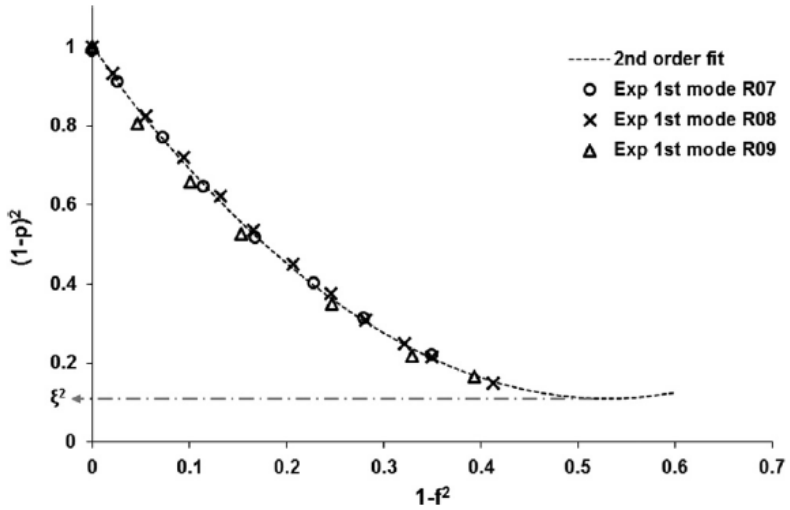

Fig. 2.2 Trend of $(1-\mathrm{P})^2$ as a function of $1-\mathrm{f}^2$ as established in Ref. [81].

governing equations the link between applied loading and natural frequency of plates. Next, Skukis *et al.* [83] assessed the suitability of the VCT for estimating instability in metal shells subjected to compression. The experimental prediction of the buckling loads was compared with the numerical solutions. The experimental verification of the VCT robustness to investigate the buckling of laminated shells was carried out by Franzoni *et al.* [84]. The same author [85] provided analytical and numerical verifications of the VCT to calculate the critical loads of imperfection-sensitive isotropic shells. Other interesting studies were presented in [57, 86, 87].

A brief review of the works carried out on the vibration-buckling correlation of beam, plate and shell models is reported in the following sections, including simple analytical resolutions.

2.2 Beam

Beam models were developed extensively over the last several decades for structural design and analyses of thin structures. One of the advantages of these models is to reduce

the 3D problem to a set of 1D variables, which depend only on the beam axis coordinate. Clearly, 1D (beam) structural theories are simpler and more computationally efficient than 2D (plate/shell) ones or 3D (solid) elastic solutions.

The first beam model was presented by Euler and Bernoulli (EBBT) [88]. This method together with those of de Saint-Venant [89] and Timoshenko (TBT) [90] represent the classical theories of the beam. The first two theories do not account for transverse shear deformations, whereas the latter assumes a uniform shear distribution along the cross-section of the beam model. An interesting comparison between EBBT and TBT was presented in [91]. These models give reasonably good results when thin, solid section and homogeneous structures are subject to flexure. Nevertheless, analyses of deep, thin-walled, open section beam structures can require more sophisticated theories to obtain sufficiently accurate results [92]. In order to overcome their limits, many theories were proposed in the literature including the introduction of the shear correction factors [93, 94], rotary inertia [95], warping effects [96, 97], the Saint-Venant based 3D solutions and the implementation of the Proper Generalized Decompositions (PGD) method [98, 99], Variational Asymptotic Beam Sectional Analysis (VABS) based on the Variational Asymptotic Method (VAM) [100], the Generalized Beam Theory [101] and the CUF [102]. Detailed considerations on higher-order beam theories were provided by Washizu [103]. Other important works on higher-order beams are those published by Kapania and Raciti [104, 105] and Carrera *et al.* [106].

Stability and dynamic analyses of beams are one of the most important parts of the structural design process. In particular, several engineering structures are subjected to axial loadings in their applications. Therefore, accurate predictions of dynamic responses and buckling loads are of crucial importance. For this reason, several researchers have studied the linear and nonlinear vibration behaviour of beams subjected to mechanical or thermal loads, both experimentally and theoretically. For instance, one of the earlier works in this context was presented by Srinivasan [107], in which the Ritz-Galerkin technique is used to compute the governing nonlinear differential equation of dynamic equilibrium for forced vibration of simply-supported structures. A semi-analytical theory for studying the nonlinear dynamic analyses of simply-supported and clamped beams was presented by Azrar *et al.* [108, 109], in which Hamilton's principle, spectral analysis, Lagrange's equation, and harmonic balance methods are employed. Natural frequencies of Timoshenko beam structures were studied by Abramovich [110]. Piana *et al.* [111] provided a comparison between numerical and experimental results for thin-walled non-symmetric cruciform beams subjected to compressive loads. A 1D FE model to perform the forced nonlinear vibration analysis of laminated beam structures was developed by

Elkaimbillah *et al.* [112]. The effect of axial loadings on forced vibrations of beam structures was provided by Virgin and Plaut [113]. Experimental and numerical vibration correlation of pre-stress reinforced composite aeronautical structures was explained by Cabral *et al.* [114]. Free-vibration analyses of composite Timoshenko beams subjected to axial loadings was performed by Banerjee [115] adopting the dynamic stiffness method. By considering the coupling of flexural and torsional vibration modes, several analytical approaches were formulated to derive the buckling and vibrations of thin-walled composite structures [116–118]. Results of experimental tests were compared by advanced FE models employing the CUF. For example, a virtual VCT approach was presented by Pagani *et al.* [119] to evaluate the nonlinear vibrations of metallic and laminated beam structures. An efficient CUF-based method for the evaluation of vibrations and buckling loads of thin-walled structures subjected to axial loadings was provided by Augello *et al.* [120]. Accurate refined FE approaches to carry out numerical VCT analyses for laminated 1D structures under compressive loadings were shown in [121]. The amount of work available in the literature on experiments on thermal instability is not, however, large. As an example, various experiments in heated composite plate structures were performed by Gutiérrez Alvarez and Bisagni [122]. Murphy [123] carried out thermal buckling analyses for clamped, rectangular plates by considering energy considerations and experimental investigations. Bhagat and Yeyaraj [124] carried out various experiment tests to evaluate the effect of non-uniform temperature distributions on the thermal buckling of shell structures. Jeyaraj [125] provided free-vibration and buckling analyses of metallic plates with thermal pre-stress. Finally, the topic of mode jumping or mode change through mechanically or thermally induced instability has been addressed on limited occasions [126].

2.2.1 Analytical formulation

A beam is a 1D structure in which the axial extension, L, is predominant when compared to other dimensions (a,h) orthogonal to it. Typically, this geometry is represented by means of a Cartesian reference system (x,y,z), where the y-axis indicates the beam axis and the plane $x - z$ is the cross-section, as illustrated in Fig. 2.3. In the following mathematical considerations, the EBBT beam model with simply-supported conditions is assumed. Starting from the a priori hypotheses for the Euler-Bernoulli beam, the displacement, strain and stress field is derived. Thus, the nonlinear equilibrium equations are obtained in the dynamic case. Then, by considering the dynamic criterion, buckling loads are computed in relation to natural frequencies.

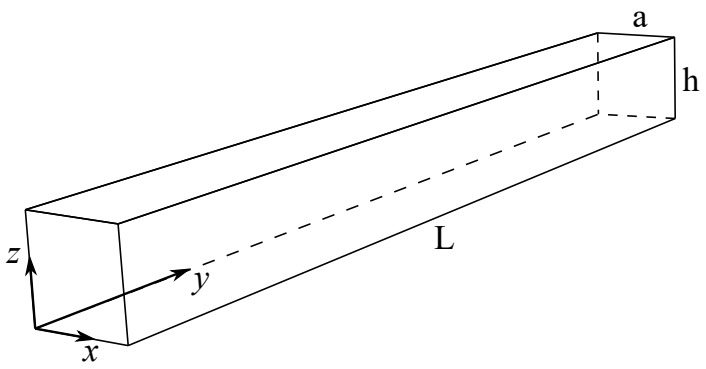

Fig. 2.3 Geometry and reference system of a beam.

Displacement, strain and stress field

The EBBT is described from the following a priori assumptions:

- the cross-section is rigid on its plane $x - z$;
- the cross-section rotates around a neutral surface remaining plane;
- the cross-section remains orthogonal to the neutral surface during deformation.

Therefore, Euler and Bernoulli consider negligible the deformation of the cross-section compared to the undergone deformation. Namely:

$$\begin{cases} \epsilon_{xx} = \frac{\partial u}{\partial x} = 0 \\ \\ \epsilon_{zz} = \frac{\partial w}{\partial z} = 0 \\ \\ \gamma_{xz} = \epsilon_{xz} = \frac{\partial u}{\partial z} + \frac{\partial w}{\partial x} = 0 \end{cases} \tag{2.4}$$

Upon these assumptions, the in-plane displacements u_x and u_z depend only on the coordinate y. The displacement field of the EBBT is then:

$$\begin{cases} u(x,y,z) = u_s(y) \\ \\ v(x,y,z) = v_s(y) + \phi_z(y)x + \phi_x(y)z \\ \\ w(x,y,z) = w_s(y) \end{cases} \tag{2.5}$$

in which ϕ_z and ϕ_x indicate the rotation angles along the $z-$ and x-axis. By considering the third assumption, one has:

$$\gamma_{xy} = \gamma_{yz} = 0 \tag{2.6}$$

Equations 2.5 and 2.6 allow to obtained the rotation angles in relation to the in-plane displacements:

$$\begin{cases} \gamma_{xy} = \epsilon_{xy} = \frac{\partial v}{\partial x} + \frac{\partial u}{\partial y} = \phi_z + \frac{\partial u_s}{\partial y} \quad \Rightarrow \quad \phi_z = \frac{\partial u_s}{\partial y} \\ \gamma_{yz} = \gamma_{yz} = \frac{\partial_v}{\partial z} + \frac{\partial w}{\partial y} = \phi_x + \frac{\partial w_s}{\partial y} \quad \Rightarrow \quad \phi_x = \frac{\partial w_s}{\partial y} \end{cases} \tag{2.7}$$

By substituting Eq. 2.7 in Eq. 2.5, the displacement field may be rewritten as follows:

$$\begin{cases} u(x,y,z) = u_s(y) \\ v(x,y,z) = v_s(y) - \frac{\partial u_s}{\partial y}x - \frac{\partial w_s}{\partial y}z \\ w(x,y,z) = w_s(y) \end{cases} \tag{2.8}$$

Regarding the strain field, the EBBT accounts for the axial strain only. Hence:

$$\epsilon_{yy} = \frac{\partial v}{\partial y} = v_{,y} = \frac{\partial v_s}{\partial y} - \frac{\partial^2 u_s}{\partial y^2}x - \frac{\partial^2 w_s}{\partial y^2}z \tag{2.9}$$

in which the first term represents the membrane deformation and the other, being the second-order derivatives of the transverse displacements, are the curvatures.

Since the aim of this section is computing the buckling load through analytical procedure, geometrical nonlinearities are included. Particularly, the classical von Kármán 1D nonlinear approximation is adopted.

$$\epsilon_{yy} = \epsilon^l_{yy} + \epsilon^{nl}_{yy} = v_{,y} + \frac{1}{2}w_{,y}^2 \tag{2.10}$$

The deformation is related to stress via the Hooke's law:

$$\sigma_{yy} = E\epsilon_{yy} \tag{2.11}$$

where E stands for the Young's modulus.

Nonlinear governing equilibrium equation

Upon the E-B hypotheses, the stress resultants that affect the normal stress σ_{yy} are only N, M_x and M_z.

$$\begin{aligned} N &= \int_A \sigma_{yy}\, dA \\ M_x &= \int_A \sigma_{yy} z\, dA \\ M_z &= \int_A \sigma_{yy} x\, dA \end{aligned} \tag{2.12}$$

where A represents the beam cross-section area.

The PVD is exploited to express the nonlinear governing equilibrium equations. It states that the sum of all the virtual work made by the internal, external and inertial forces existing in the system in any arbitrary infinitesimal virtual displacements satisfying the prescribed geometrical constraints is zero. Thus,

$$\delta L_{int} = \delta L_{ext} + \delta L_{dyn} \tag{2.13}$$

where δL_{int}, δL_{ext} and δL_{dyn} are the virtual variation of the strain energy, external loadings and dynamic work.. Their expressions are given below:

$$\begin{aligned} \delta L_{int} &= \int_V \left(\sigma_{yy} \delta \epsilon^l_{yy} + \sigma_{yy} \delta \epsilon^{nl}_{yy} \right)\, dV \\ \delta L_{ext} &= \int_l p_z \delta w\, dl \\ \delta L_{dyn} &= \int_V \rho(\ddot{u}\delta u + \ddot{v}\delta v + \ddot{w}\delta w)\, dV \end{aligned} \tag{2.14}$$

in which V denotes the volume ($dV = dA\, dz$), p_z indicates the applied external load along the z-axis, ρ represents the density and the superposed dots stand for time differentiation.

Buckling and vibrations of the beam under compressive loading

Consider the problem displayed in Fig. 2.4 and the E-B displacement field in the in-plane case.

To derive the nonlinear equilibrium equations of the considered problem in an explicit form, each contribution has to be evaluated. In the subsequent mathematical operations, the integration by parts was carried out, shifting the derivatives from the virtual variations of the displacements to the stress characteristics.

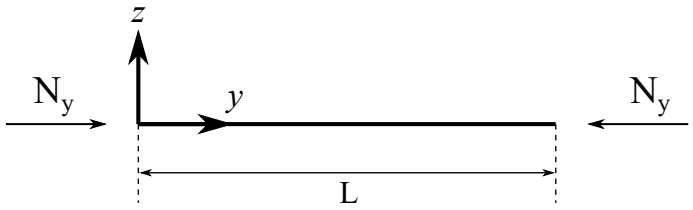

Fig. 2.4 Beam subjected to compressive loadings.

The contributions for the virtual strain energy are expressed as follows:

$$\begin{aligned}
&\int_V \boldsymbol{\sigma_{yy}\delta\epsilon^{l}_{yy}}\, \boldsymbol{dA\, dy} = \int_l \int_A \sigma_{yy}(\delta v_s, y - z\delta w_{s,yy})\, dA\, dl = \\
&= \int_l (N_y \delta v_{s,y} - M_x \delta w_{s,yy})\, dl = -\int_l (N_{y,y}\, \delta v_s + M_{x,yy}\, \delta w_s)\, dl + \\
&+ \int_\eta (N_y \delta v_s - M_x \delta w_{s,y} + M_{x,y}\, \delta w_s)\, d\eta
\end{aligned} \tag{2.15}$$

$$\begin{aligned}
&\int_V \boldsymbol{\sigma_{yy}\delta\epsilon^{nl}_{yy}}\, \boldsymbol{dA\, dy} = \int_V \sigma_{yy}\delta(\tfrac{1}{2} w_{,y}^{2})\, dV = \int_V \sigma_{yy} w_{s,y}\, \delta w_{s,y}\, dV = \\
&= \int_l N_y w_{s,y}\, \delta w_{s,y} = -\int_l (N_y w_{s,y})_{,y}\, \delta w_s\, dl + \int_\eta N_y w_{s,y}\, \delta w_s\, d\eta
\end{aligned}$$

Regarding the virtual dynamic work, one has:

$$\begin{aligned}
&\int_V \boldsymbol{\rho(\ddot{u}\delta u + \ddot{v}\delta v + \ddot{w}\delta w)\, dV} = \int_V [\rho \ddot{u}_s \delta u_s + \rho(\ddot{v}_s - z\ddot{w}_{s,y})(\delta v_s - z w_{s,y}) + \rho \ddot{w}_s \delta w_s]\, dV = \\
&= \int_V [\rho \ddot{u}_s \delta u_s + \rho \ddot{v}_s \delta v_s - \rho z \ddot{v}_s \delta w_{s,y} - \rho z \ddot{w}_{s,y}\, \delta v_s + \rho z^2 \ddot{w}_{s,y}\, \delta w_{s,y} + \rho \ddot{w}_s \delta w_s]\, dV = \\
&= \int_l [I_0 \ddot{u}_s \delta u_s + (I_0 \ddot{v}_s - I_1 \ddot{w}_{s,y})\delta v_s + I_0 \ddot{w}_s \delta w_s + (-I_1 \ddot{v}_s + I_2 \ddot{w}_{s,y})\delta w_{s,y}]\, dl = \\
&= -\int_l [I_0 \ddot{u}_s \delta u_s + (I_0 \ddot{v}_s - I_1 \ddot{w}_{s,y})\delta v_s + I_0 \ddot{w}_s \delta w_s + (-I_1 \ddot{v}_{s,\,y} + I_2 \ddot{w}_{s,yy})\delta w_s]\, dl + \\
&+ \int_\eta (-I_1 \ddot{v}_s + I_2 \ddot{w}_{s,y})\delta w_s\, d\eta
\end{aligned} \tag{2.16}$$

where $(I_0, I_1, I_2) = \int_A \rho(1, z, z^2)\, dA$ are the mass, static moment and moment of inertia per unit length.

Upon evaluating each contribution, the nonlinear equilibrium equations in the dynamic case for the considered problem are written as follows:

$$\begin{cases} N_{y,y}\,\delta v_s = (I_0\ddot{v}_s - I_1\ddot{w}_{s,y}) \\ \\ M_{x,yy} + (\bar{N}_y w_{s,yy}) = I_0\ddot{w}_s + (-I_1\ddot{v}_{s,y} + I_2\ddot{w}_{s,yy}) \end{cases} \tag{2.17}$$

where the $N_y = \bar{N}_y$ is considered constant on the beam only for the nonlinear contribution.

Initial hypotheses are formulated to derive critical buckling load using the dynamic criterion. These assumptions are:

- $p_z = 0$;
- $[B] = 0$, no coupling between the membrane and flexural-torsional effects. $[B]$ represents the coupling matrix;
- $I_1 = I_2 = 0$.

and the Navier method is used to compute the closed-form solution of the proposed governing equations under the specific conditions of geometry, boundary and material in which this resolution is valid. Therefore, according to the Navier approach, the following harmonic assumptions are done for displacements:

$$\begin{aligned} u(x;t) &= U sin(\alpha x) e^{i\omega t} \\ \\ w(x;t) &= W cos(\alpha x) e^{i\omega t} \end{aligned} \tag{2.18}$$

where the terms $\alpha = \frac{m\pi}{L}$, in which m denotes the half-wave number along the beam-axis.

Equation 2.18 indicates the displacement field of a simply-supported beam and it satisfies the following boundary condition:

$$\begin{cases} u(0) = u(L) = 0 \\ \\ v(0) = v(L) = 0 \\ \\ w(0) = w(L) = 0 \end{cases} \tag{2.19}$$

Upon the assumptions made, one has:

$$\begin{aligned} N_y &= EAv_{s,y} \\ \\ M_x &= -EI_x w_{s,yy} \end{aligned} \tag{2.20}$$

By substituting Eq. 2.20 in Eq. 2.17 and omitting the mathematical passages, the final form of the equation used to compute buckling loads is:

$$\begin{aligned}(-EI_x\alpha^4 - \bar{N}_y + I_0\omega^2)Wcos(\alpha x)e^{i\omega t} = 0 \\ \Rightarrow \qquad \omega^2 = \tfrac{\alpha^4 EI_x + \alpha^2 \bar{N}_y}{I_0}\end{aligned} \tag{2.21}$$

The latter equation provides a relation between applied loadings and natural frequencies. The critical load value is shown in Fig. 2.5.

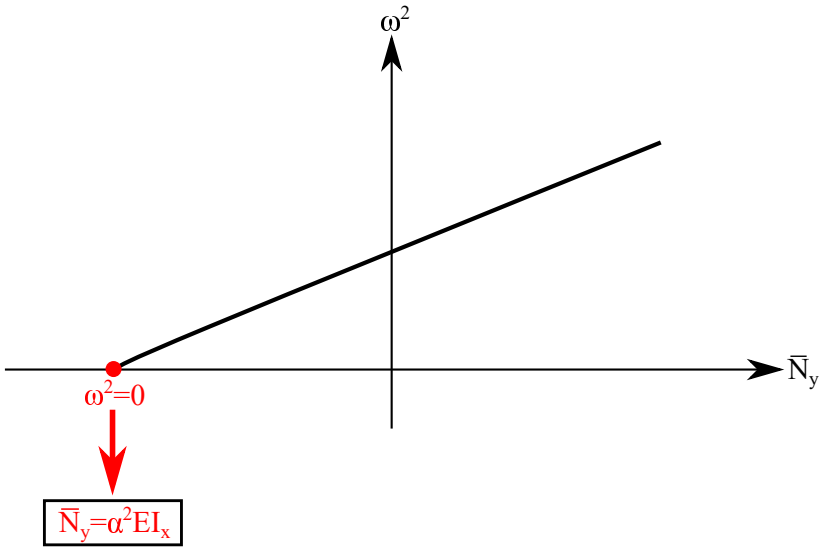

Fig. 2.5 The evaluation of the buckling load value through dynamic criterion. Euler-Bernoulli beam.

2.3 Plate

The modelling of a structure employing 2D elements turns out to be a classic problem in structure theory. Generally speaking, the plate is a special limiting case of the shell without curvature. The plate thickness is small compared with the surface dimensions and may be either constant or variable. Plate structures, in particular those in composite, are being increasingly employed in aerospace industries as well as in other fields. For example, the plates are adopted on surfaces in aircraft wings, plate girder webs, bridges, buildings or ship hulls. Different shapes and sizes are considered, e.g., circular or rectangular plates, thin or thick plates. In particular, thin plate structures, usually adopted in aerospace engineering, are very stiff for in-plane loadings, but they are quite flexible in bending. A

good understanding of their static and dynamic structural responses, deformation and stress distribution, natural frequencies variation and buckling behaviours under different loads and boundary conditions is needed to use them efficiently.

Several approaches have been used for eliminating the thickness coordinate (z). One of the most used is to adopt axiomatic assumptions on the unknowns in the z-direction by imposing a polynomial expansion. The classical mathematical formulations of plate structures were provided by Love-Kirchhoff [127] and Reissner-Mindlin [128, 129]. The first model, called Kirchhoff–Love plate Theory [130], does not consider the shear stress, whereas it is included in the second one, called First Shear Deformation Theory (FSDT) [131], but are assumed constant along the structure thickness. Both models may lead to very inaccurate results as far as the local response of thick laminated structures is concerned.

In the works of Carrera [132, 133], the importance of adopting higher-order models for performing reliable analysis of multi-layered structures was highlighted. Furthermore, the importance of describing the inter-laminar stresses accurately was studied by many researchers [134, 135, 133]. As a consequence, it was observed that both transversal displacements and stresses must be continuous to obtain reliable results. These requirements are referred to as C_z^0 requirement.

Several high-order shear deformation theories (HSDTs) that involve higher-order terms in Taylor's expansions of the displacement in thickness coordinates were formulated to overcome the FSDT limitations. For instance, the first to present improved theories for plates was Hildebrand *et al.* [136]. Librescu [137] formulated higher-order displacement-based shear deformation theories for studying composite plates. Lo *et al.* [138, 139] provided a closed-form solution for composite plates with a higher-order model that include the effect of transverse deformations. Putcha and Reddy [140] formulated a mixed shear flexible FE based on a higher-order theory. Recently, Carrera [141–145] provided refined 2D models able to evaluate laminated composite plates with high accuracy.

As previously mentioned, when structures are subject to axial loads, they may experience a loss of stability that is manifested in the local growth of motion in the vicinity of equilibrium leading to buckling. Especially, the plates often have significant post-buckled strength [146]. This suggests that dynamic behaviour in the post-buckled regime may also be of interest. Furthermore, plates may exhibit large deflections that result in a coupling between the in-plane and bending deformations like for beams. Contrary to the beams, plates have additional capacity to resist loads beyond their buckling state and their failure load is much higher. Failure loads for plates may be found

by analyzing their post-buckling behaviour. For this reason, it is crucial to accurately introduce nonlinearities for carrying out reliable analyses of plate structures.

The topic of nonlinear static and transient analysis of plates has a vivid interest in the literature. A short overview of some studies on plates will now be given. Von Kármán [147] extended the Kirchhoff method to study the finite deformation of 2D structures, taking into account geometrical nonlinearities. Chu and Herrmann [148] were the pioneers in nonlinear vibration analyses of plate structures. Reddy [149] provided nonlinear plate theories that include cubic terms in the surface kinematics. One of the most interesting aspects of plates is that they can show jumps in their post-buckled equilibrium behaviour if high compressive loads are applied [150, 151]. This secondary bifurcation is associated with an interaction between buckling modes and is often referred to as mode jumping [152, 153] and has received a particular interest in the literature [154, 155]. Tracking the movement of natural frequencies before and during this phenomenon can shed light on this interesting aspect of the dynamics of axially loaded structures. Interest in mode jumping was initiated by the classic study of Stein [150]. Stein noticed that the plate would suddenly jump to a different buckled equilibrium configuration in the post-buckled regime. This typically corresponds to an often sudden change of the wave-number of the buckled form. It may also happen that on subsequent unloading, the system may not follow the original path: Hysteresis occurs [156]. By using trigonometric formulas provided by Fourier, Navier [157] obtained the exact vibration solutions for rectangular plates with simply-supported edges. Then, Poisson [158] extended Navier's study to circular plates. The extended plate theory which considered the combined bending and stretching actions of plates was attributed to Kirchhoff [127]. An extensive collection of theoretical and experimental solutions for the buckling of plates is available in the six-part Handbook for Structural Stability, published by the National Advisory Committee for Aeronautics [159]. In addition, a large amount of similar material has been made available in the recent book by Baker *et al.* [160]. Vibration analyses of different plates considering various sets of constraints are examined in the Leissa's book [161]. The literature review on nonlinear plate vibrations is provided by Chia [162, 163]. In addition, nonlinear vibrations of rectangular composite flat panels were thoroughly studied by Noor *et al.* [164] and Harras *et al.* [165]. Many theoretical studies on the large amplitude vibrations of plate structures are available in the literature, however, the experimental results are not numerous. Some experimental results are provided by Amabili [166, 167]. Buckling prediction of plates using the VCT was provided by Abramovich *et al.* [78]. VCT results for the buckling load prediction of sandwich plates structures with iso-grid cores can be found in [168]. In this context, the following sections will provide both an analytical

formulation and numerical methodology to evaluate the critical buckling load using the vibration data.

2.3.1 Analytical formulation

In the following mathematical considerations, a plate model, illustrated in Fig. 2.6, with simply-supported conditions is assumed.

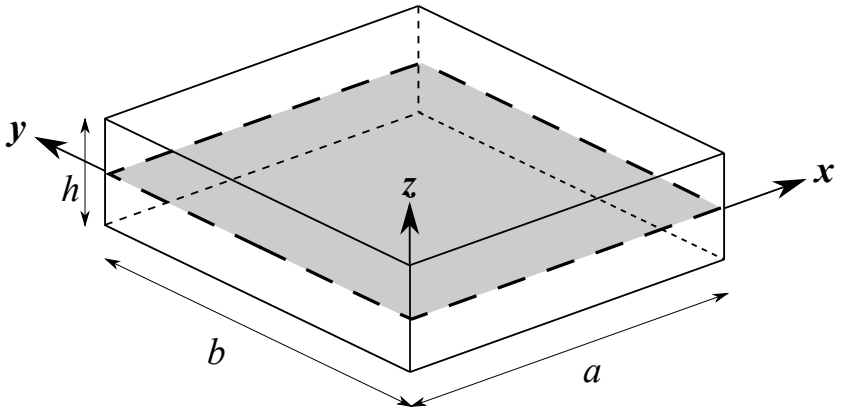

Fig. 2.6 Geometry and reference system of a plate.

Starting from the a priori hypotheses for the Kirchhoff theory, the displacement, strain and stress field is derived. Thus, the nonlinear equilibrium equations are obtained in the dynamic case. Then, by considering the dynamic criterion, the buckling load values are computed in relation to natural frequencies.

Displacement, strain and stress field

The Kirchhoff plate theory derives from the following assumptions:

1. transverse normal segments remain straight after deformation. Namely, the displacement in the plane u and v are linear with respect to z;
2. such segments do not lengthen and shorten: $\epsilon_{zz} = 0$;
3. they remain orthogonal to the average surface when they rotate: $\gamma_{xz} = \epsilon_{xz} = 0$, $\gamma_{yz} = \epsilon_{yz} = 0$.

According to these hypotheses, holds:

$$\begin{aligned} u(x,y,z) &= u^0(x,y) + \phi_x(x,y)z \\ v(x,y,z) &= v^0(x,y) + \phi_y(x,y)z \\ w(x,y,z) &= w^0(x,y) \end{aligned} \tag{2.22}$$

in which ϕ_x and ϕ_y denote the rotations of the transverse normals around the x and y axis. The strain-displacement relation are:

$$\begin{cases} \epsilon_{xx} = \frac{\partial u}{\partial x} = u_{,x} \\ \epsilon_{yy} = \frac{\partial v}{\partial y} = v_{,y} \\ \epsilon_{zz} = \frac{\partial w}{\partial z} = w_{,z} \\ \epsilon_{xz} = \frac{\partial u}{\partial z} + \frac{\partial w}{\partial x} = u_{,z} + w_{,x} \\ \epsilon_{yz} = \frac{\partial v}{\partial z} + \frac{\partial w}{\partial y} = v_{,z} + w_{,y} \\ \epsilon_{xy} = \frac{\partial u}{\partial y} + \frac{\partial v}{\partial x} = u_{,y} + v_{,x} \end{cases} \tag{2.23}$$

in which a compact notation to indicate derivatives is employed (e.g., $u_{,x}$ stands for the derivative of u as a function of x).

On the basis of the hypotheses, the angles of rotation can be obtained as derivatives of the transverse displacements. Namely:

$$\begin{cases} \epsilon_{xz} = u_{,z} + w_{,x} = \phi_x + w^0{}_{,x} = 0 \quad \Rightarrow \quad \phi_x = -w^0{}_{,x} \\ \epsilon_{yz} = v_{,z} + w_{,y} = \phi_y + w^0{}_{,y} = 0 \quad \Rightarrow \quad \phi_y = -w^0{}_{,y} \end{cases} \tag{2.24}$$

Therefore, the displacement field of the Kirchhoff plate model is:

$$\begin{aligned} u(x,y,z) &= u^0(x,y) - w^0{}_{,x}\,(x,y) \\ v(x,y,z) &= v^0(x,y) - w^0{}_{,y}\,(x,y) \\ w(x,y,z) &= w^0(x,y) \end{aligned} \tag{2.25}$$

By substituting Eq. 2.25 in Eq. 2.23 and considering Eq. 2.24, one obtains the only deformations in the plane included by the Kirchhoff model. Thus:

$$\begin{cases} \epsilon_{xx} = u^0{}_{,x} - z w^0{}_{,xx} = \epsilon^0_{xx} + z k_{xx} \\ \epsilon_{yy} = v^0{}_{,y} - z w^0{}_{,yy} = \epsilon^0_{yy} + z k_{yy} \\ \epsilon_{xy} = u^0{}_{,y} - z w^0{}_{,xy} + v^0{}_{,x} - z w^0{}_{,xy} = \epsilon^0_{xy} + z k_{xy} \end{cases} \tag{2.26}$$

The deformation vector can be seen as composed of one part that has the physical meaning of membrane deformations (ϵ^0) and the other of flexural ones (k).

The nonlinearity is included because one is interested in post-buckling problems. In particular, the classical von Kármán 2D nonlinear approximation is considered. The strain-displacement may be rewritten as:

$$\begin{cases} \epsilon_{xx} = u_{,x} + \frac{1}{2} w^2{}_{,x} = \epsilon^l_{xx} + \epsilon^{nl}_{xx} \\ \epsilon_{yy} = v_{,y} + \frac{1}{2} w^2{}_{,y} = \epsilon^l_{yy} + \epsilon^{nl}_{yy} \\ \epsilon_{xy} = u_{,y} + v_{,x} + w_{,x}\, w_{,y} = \epsilon^l_{xy} + \epsilon^{nl}_{xy} \end{cases} \tag{2.27}$$

in which ϵ^l indicates the linear components of the strain, while ϵ^{nl} the nonlinear ones, respectively.

Since a plane tension state ($\sigma_{zz} = \sigma_{xz} = \sigma_{yz} = 0$) is considered for the Kirchhoff plate model, the stress-strain relation is:

$$\{\boldsymbol{\sigma}\} = [\boldsymbol{C}]\,\{\boldsymbol{\epsilon}\} \tag{2.28}$$

in which $\boldsymbol{C}$ represents material elastic matrix.

Nonlinear governing equilibrium equation

By considering the assumptions done, the internal forces acting on a plate are illustrated in Fig. 2.7. These represent forces and moments per unit of length, Hence:

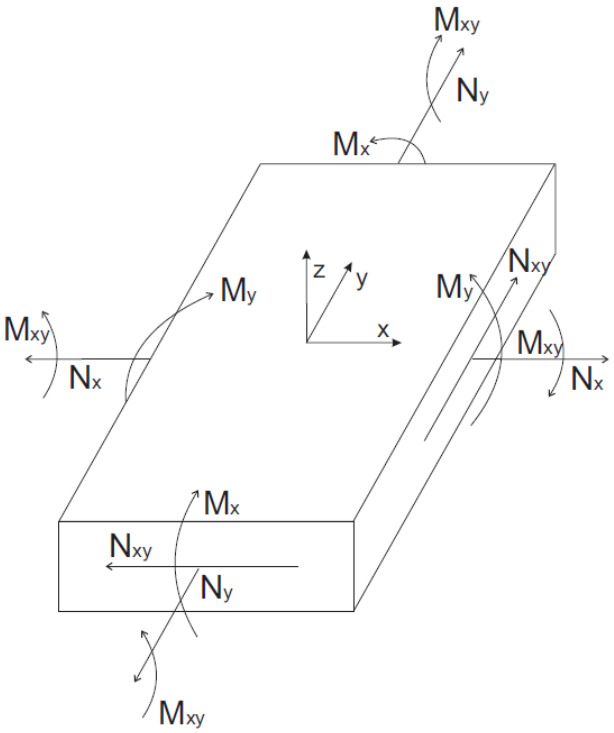

Fig. 2.7 Internal forces in the Kirchhoff plate.

$$
\begin{aligned}
N_x &= \int_{-h/2}^{h/2} \sigma_{xx}\, dz, \qquad & M_x &= \int_{-h/2}^{h/2} \sigma_{xx} z\, dz \\
N_y &= \int_{-h/2}^{h/2} \sigma_{yy}\, dz, \qquad & M_y &= \int_{-h/2}^{h/2} \sigma_{yy} z\, dz \\
N_{xy} &= \int_{-h/2}^{h/2} \sigma_{xy}\, dz, \qquad & M_{xy} &= \int_{-h/2}^{h/2} \sigma_{xy} z\, dz
\end{aligned}
\tag{2.29}
$$

Consider pure mechanical problems, the PVD is exploited to derive the nonlinear equations. Thus:

$$
\delta L_{int} = \delta L_{ext} + \delta L_{dyn} \tag{2.30}
$$

where δL_{int}, δL_{ext} and δL_{dyn} are the virtual variation of the strain energy, external loadings and dynamic work. Their expressions are given below:

$$\begin{aligned}
\delta L_{int} &= \int_V [(\sigma_{xx}\delta\epsilon^l_{xx} + \sigma_{yy}\delta\epsilon^l_{yy} + \sigma_{xy}\delta\epsilon^l_{xy}) + (\sigma_{xx}\delta\epsilon^{nl}_{xx} + \sigma_{yy}\delta\epsilon^{nl}_{yy} + \sigma_{xy}\delta\epsilon^{nl}_{xy})]\, dV \\
\delta L_{ext} &= \int_\Omega p_z \delta w \; d\Omega \\
\delta L_{dyn} &= \int_V \rho(\ddot{u}\delta u + \ddot{v}\delta v + \ddot{w}\delta w)\, dV
\end{aligned} \tag{2.31}$$

in which V denotes the volume ($dV = d\Omega\, dz$), Ω indicates the surface, p_z is the applied external load along the z-axis, ρ represents the density and the superposed dots stands for time differentiation.

In order to solve these equations, each single contribution has to be computed. Regarding the contributions of the strain energy virtual variation, one obtains:

$$\begin{aligned}
\int_V \boldsymbol{\sigma_{xx}\delta\epsilon^l_{xx}}\, \boldsymbol{d\Omega\, dz} &= \int_\Omega (N_x \delta u^0_{,x} - M_x \delta w_{,xx})\, d\Omega = \\
&= -\int_\Omega (N_{x,x}\, \delta u^0 + M_{x,xx}\, \delta w^0)\, \delta\Omega + \int_\Gamma (N_x \delta u^0 - M_x \delta w^0_{,x} + M_{x,x}\, \delta w^0)\, d\Gamma \\
\\
\int_V \boldsymbol{\sigma_{yy}\delta\epsilon^l_{yy}}\, \boldsymbol{d\Omega\, dz} &= \int_\Omega (N_y \delta v^0_{,y} - M_y \delta w_{,yy})\, d\Omega = \\
&= -\int_\Omega (N_{y,y}\, \delta v^0 + M_{y,yy}\, \delta w^0)\, \delta\Omega + \int_\Gamma (N_y \delta v^0 - M_y \delta w^0_{,y} + M_{y,y}\, \delta w^0)\, d\Gamma \\
\\
\int_V \boldsymbol{\sigma_{xy}\delta\epsilon^l_{xy}}\, \boldsymbol{d\Omega\, dz} &= \int_\Omega (N_{xy} \delta u^0_{,y} + N_{xy} \delta v^0_{,x} - 2M_{xy} \delta w_{,xy}{}^0)\, d\Omega = \\
&= -\int_\Omega (N_{xy,y}\, \delta u^0 + N_{xy,x}\, \delta v^0 + 2M_{xy,xy}\, \delta w^0)\, d\Omega + \\
&\quad \int_\Gamma (N_{xy} \delta u^0 + N_{xy} \delta v^0 - 2M_{xy} \delta w^0_{,x} + 2M_{xy,y}\, \delta w^0)\, d\Gamma
\end{aligned} \tag{2.32}$$

$$\int_V \boldsymbol{\sigma_{xx}\delta\epsilon^{nl}_{xx}}\, \boldsymbol{d\Omega\, dz} = \int_V \sigma_{xx}\delta(\tfrac{1}{2}w_{,x}^{2})\, d\Omega\, dz = \int_V \sigma_{xx} w_{,x}^{0}\, \delta w_{,x}^{0} d\Omega dz =$$

$$= \int_\Omega N_x w_{,x}^{0}\, \delta w_{,x}^{0}\, d\Omega = -\int_\Omega (N_x w_{,x}^{0})_{,x}\, \delta w^0\, d\Omega + \int_\Gamma (N_x w_{,x}^{0})\delta w^0\, d\Gamma$$

$$\int_V \boldsymbol{\sigma_{yy}\delta\epsilon^{nl}_{yy}}\, \boldsymbol{d\Omega\, dz} = \int_V \sigma_{yy}\delta(\tfrac{1}{2}w_{,y}^{2})\, d\Omega\, dz = \int_V \sigma_{yy} w_{,y}^{0}\, \delta w_{,y}^{0} d\Omega dz =$$

$$= \int_\Omega N_y w_{,y}^{0}\, \delta w_{,y}^{0}\, d\Omega = -\int_\Omega (N_y w_{,y}^{0})_{,y}\, \delta w^0\, d\Omega + \int_\Gamma (N_y w_{,y}^{0})\delta w^0\, d\Gamma$$

$$\int_V \boldsymbol{\sigma_{xy}\delta\epsilon^{nl}_{xy}}\, \boldsymbol{d\Omega\, dz} = \int_V \sigma_{xy}\delta(w_{,x}^{0}\, w_{,y}^{0})\, dV = \int_\Omega N_{xy}(w_{,x}^{0}\, \delta w_{,y}^{0} + w_{,y}^{0}\, \delta w_{,x}^{0})\, d\Omega =$$

$$= -\int_\Omega [(N_{xy} w_{,x}^{0})_{,y})\delta w^0 + (N_{xy} w_{,y}^{0})_{,x}\, \delta w^0]\, d\Omega +$$

$$+ \int_\Gamma [(N_{xy} w_{,x}^{0})\delta w^0 + (N_{xy} w_{,y}^{0})\delta w^0]\, d\Gamma \tag{2.33}$$

Since the dynamic procedure is considered, the virtual variation of the dynamic work is evaluated.

$$\delta L_{dyn} = \int_V [\rho(\ddot{u}^0 - z\ddot{w}_{,x}^{0})(\delta u^0 - z\delta w_{,x}^{0}) + \rho(\ddot{v}^0 - z\ddot{w}_{,y}^{0})(\delta v^0 - z\delta w_{,y}^{0}) + \rho\ddot{w}^0\delta w^0]\, dV =$$

$$= \int_V [\rho\ddot{u}^0\delta u^0 - \rho z\ddot{w}^0\delta u^0 - z\rho\ddot{w}_{,x}^{0}\, \delta u^0 + \rho z^2\ddot{w}_{,x}^{0}\, \delta w_{,x} + \rho\ddot{v}^0\delta v^0 - \rho z\ddot{w}\delta v^0 -$$

$$- z\rho\ddot{w}\delta v^0 - z\rho\ddot{w}_{,y}\, \delta v^0 + \rho z^2\ddot{w}_{,y}\, \delta w_{,y} + \rho\ddot{w}^0\delta w^0]\, dv = \int_\Omega [(I_0\ddot{u}^0 - I_1\ddot{w}_{,x})\delta u^0 +$$

$$+ (I_0\ddot{v}^0 - I_1\ddot{w}_{,y})\delta v^0 + I_0\ddot{w}^0\delta w^0 + (-I_1\ddot{u}^0 + I_2\ddot{w}_{,x})\delta w_{,x}^{0} +$$

$$+ (-I_1\ddot{v}^0 + I_2\ddot{w}_{,y}^{0})\delta w_{,y}^{0}\, d\Omega = -\int_\Omega [(I_0\ddot{u}^0 - I_1\ddot{w}_{,x}^{0})\delta u^0 + (I_0\ddot{v}^0 - I_1\ddot{w}_{,y})\delta v^0 +$$

$$+ I_0\ddot{w}^0\delta w^0 + (I_1\ddot{u}_{,x}^{0} - I_2\ddot{w}_{,xx} + I_1\ddot{v}_{,y}^{0} - I_2\ddot{w}_{,yy}^{0})\delta w^0]\, d\Omega +$$

$$+ \int_\Gamma [(-I_1\ddot{u}^0 + I_2\ddot{w}_{,x}^{0})\delta w^0 + (-I_1\ddot{v}^0 + I_2\ddot{w}_{,y})\delta w^0]\, d\Gamma \tag{2.34}$$

where $(I_0, I_1, I_2) = \int_z \rho(1, z, z^2)\, dz$ represent the mass, static moment and moment of inertia per unit of area.

Upon evaluating each contribution, the nonlinear equations in the dynamic case are written as follows:

$$\begin{cases} N_{x,x} + N_{xy,y} = I_0 \ddot{u}^0 - I_1 \ddot{w}_{,x} \\ \\ N_{xy,x} + N_{y,y} = I_0 \ddot{v}^0 - I_1 \ddot{w}_{,y} \\ \\ -M_{x,xx} - M_{y,yy} - 2M_{xy,xy} = -I_0 \ddot{w}^0 - I_1(\ddot{u}^0_{,x} + \ddot{v}^0_{,y}) + I_2(\ddot{w}^0_{,xx} - \ddot{w}^0_{,yy}) + \\ \\ \qquad + [(N_x w^0_{,x})_{,x} + (N_y w^0_{,y})_{,y} + (N_{xy} w^0_{,x})_{,y} + (N_{xy} w^0_{,y})_{,x}] - p_z \end{cases} \tag{2.35}$$

Consider the $N_x = \bar{N}_x$, $N_y = \bar{N}_y$, $N_{xy} = \bar{N}_{xy}$ constant on the plate only for the nonlinear contribution. Namely:

$$\begin{cases} N_{x,x} + N_{xy,y} = I_0 \ddot{u}^0 - I_1 \ddot{w}_{,x} \\ \\ N_{xy,x} + N_{y,y} = I_0 \ddot{v}^0 - I_1 \ddot{w}_{,y} \\ \\ -M_{x,xx} - M_{y,yy} - 2M_{xy,xy} = -I_0 \ddot{w}^0 - I_1(\ddot{u}^0_{,x} + \ddot{v}^0_{,y}) + I_2(\ddot{w}^0_{,xx} - \ddot{w}^0_{,yy}) + [(\bar{N}_x w^0_{,x})_{,x} + \\ \\ \qquad + (\bar{N}_y w^0_{,y})_{,y} + (\bar{N}_{xy} w^0_{,x})_{,y} + (\bar{N}_{xy} w^0_{,y})_{,x}] - p_z \end{cases} \tag{2.36}$$

Then, both the nonlinear equilibrium equations and stability equations are examined to calculate the buckling load.

$$\begin{cases} \delta L = 0 \\ \\ \delta^2 L = 0 \end{cases} \tag{2.37}$$

Evaluating the buckling load value is equivalent to finding the values of $\bar{N}_x, \bar{N}_y, \bar{N}_{xy}$ that satisfy the stability equation.

Buckling of the plate under compressive loadings

Consider the problem illustrated in Fig. 2.8. The constitutive equations of the Kirchhoff plate are:

$$\begin{cases} \{N\} = [A]\{\epsilon^0\} + [B]\{k\} \\ \\ \{M\} = [B]\{\epsilon^0\} + [D]\{k\} \end{cases} \tag{2.38}$$

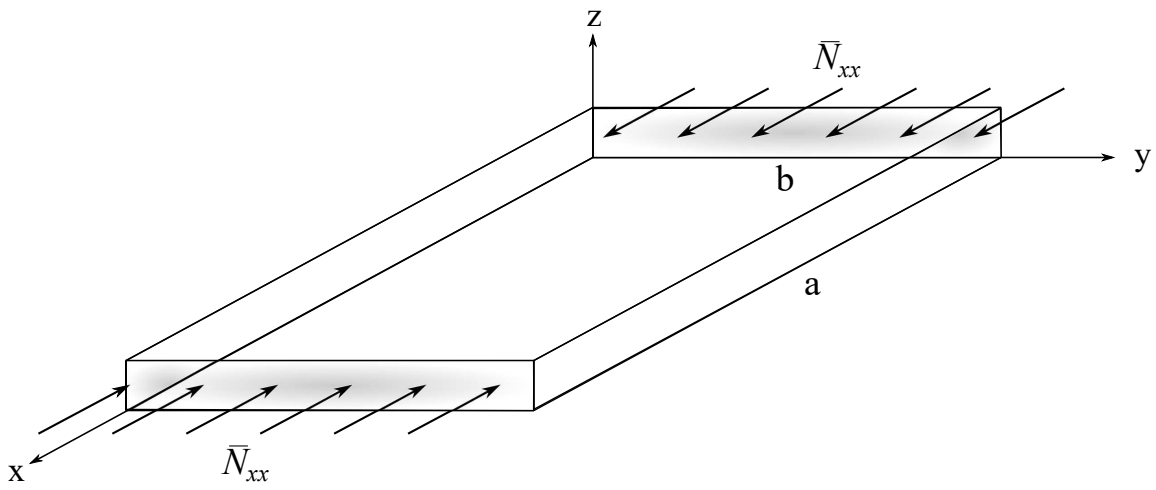

Fig. 2.8 Plate subjected to compressive loadings.

in which $[A]$ represents the membrane stiffness matrix, $[B]$ is coupling matrix and $[D]$ indicates the flexural-torsional stiffness matrix.

To compute the critical buckling load through the dynamic criterion, initial hypotheses are made. These assumptions are:

- $p_z = 0$;
- $[B] = 0$, no coupling between the membrane and flexural-torsional effects;
- $I_1 = I_2 = 0$.

Furthermore, the stability equation of the considered problem is:

$$-M_{x,xx} - M_{y,yy} - 2M_{xy,xy} = -I_0\ddot{w}^0 + \bar{N}_x w^0_{,xx} \tag{2.39}$$

The Navier method is employed to compute the closed-form solution of the proposed governing equations for the particular geometry, boundary and material condition in which this resolution is valid. Therefore, according to the Navier approach, the following harmonic assumptions are done for the displacements:

$$w(x, y; t) = W sin(\alpha x) sin(\beta y) e^{i\omega t} \tag{2.40}$$

where the terms $\alpha = \frac{m\pi}{b}$ and $\beta = \frac{n\pi}{a}$, in which m and n stand for the half-wave number along the x-axis and y-axis.

Equation 2.40 indicates the displacement field of a simply-supported plate and it satisfies the following boundary condition:

$$\begin{cases} x = 0, a & \rightarrow \quad w^0 = 0, M_x = 0 \\ \\ y = 0, b & \rightarrow \quad w^0 = 0, M_y = 0 \end{cases} \tag{2.41}$$

By omitting the mathematical passages and neglecting the terms that are not involved in this problem, the final form of the equation used to compute the critical buckling load is:

$$[-D_{11}\alpha^4 - D_{22}\beta^4 - 2(D_{12} + 2D_{66})\alpha^2\beta^2 + I_0\omega^2 - \alpha^2\bar{N}_x]Wsin(\alpha x)sin(\beta y)e^{i\omega t} = 0$$

$$\Rightarrow \qquad \omega^2 = \frac{D(\alpha^4+\beta^4+2\alpha^2\beta^2)-\alpha^2\bar{N}_x}{I_0} \tag{2.42}$$

where $D = D_{11} = D_{22} = D_{12} + 2D_{66} = \frac{Eh^3}{12(1-\nu^2)}$ The latter equation provides a relation between the applied loads and natural frequencies. Finally, the critical load value is shown in Fig. 2.9.

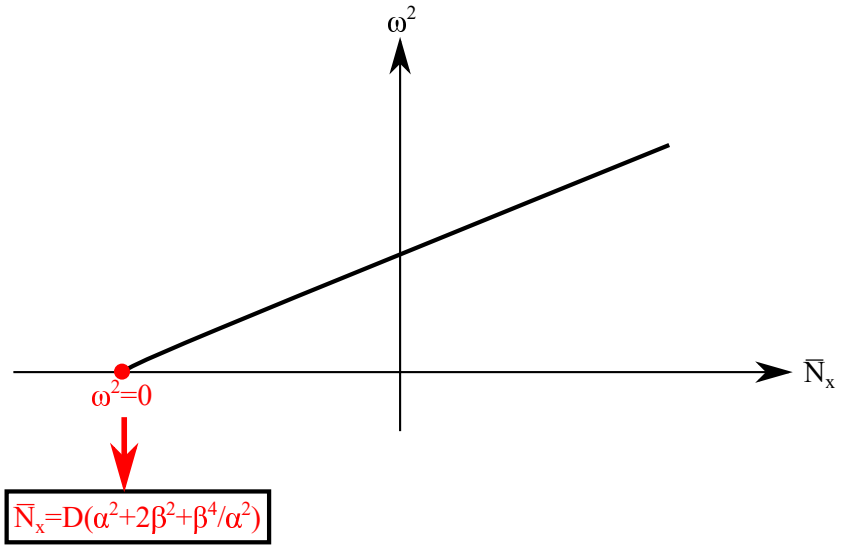

Fig. 2.9 The evaluation of the buckling load value through dynamic criterion. Kirchhoff plate.

2.4 Shell

Nowadays, shell models are used extensively in various engineering fields, for instance, in aerospace and civil engineering, among others. The main feature of these structures is to achieve large displacements and rotations without having plasticity. This ability is an aspect of fundamental importance if linked to the industrial need to produce more advantageous structures in terms of costs and performances. Basically, shells are curved lightweight constructions that can support external forces with high efficiency. Their exceptional mechanical properties are due to the curvature, which generates the coupling between the membrane and the flexural behaviours, both in single and double curve models. In addition, the shell structures, even if they undergo large displacements and rotations when extreme external forces are applied, still preserve the post-buckling stiffness.

The literature about shells theories is large [169–171]. The works of Poisson [158], Love [172], Mindlin [129], Kirchhoff [173], Reissner [174] and Cauchy [175] are the classical formulations available in the literature. Over the years, several higher-order 2D theories were formulated to overcome the drawbacks of the classical studies' hypotheses. For example, Reddy [176] developed a refined through-the-thickness kinematics, accounting for higher-order shear deformations, to study 2D laminated structures. Mashat *et al.* [177] carried out an assessment of the relevance of displacement variables in refined theories for isotropic and multi-layered shell structures, employing axiomatic/asymptotic techniques. The refined theories of shells were unified by Carrera in his early work [42]. The reader is referred to [178, 179] for other significant analyses on shell theories.

The complexity of the shell structure analyses is related to curvature. In fact, a modification of the curvature may produce a totally different force and, therefore, different behaviours of the structure [180]. Moreover, the shells collapse due to buckling long before the material's failure strength is reached due to the optimal distribution of the material. Due to their geometry, these structures may present large displacements, as a function of the shell thickness, associated with small strains before the collapse. Therefore, nowadays, there is a vivid interest in the buckling behaviours of shell structures. Most shell stability problems, as they are posed in practical engineering, cannot be solved analytically. Consequently, numerical methods must be applied.

The shell structures are often subjected to dynamic loadings that cause vibrations; vibration amplitudes of the order of the thickness of the shell may be easily achieved in several applications. If the vibration amplitude is small enough, the dynamics of a shell can be adequately predicted by linear analyses. On the other hand, if the amplitude is of the order of the shell thickness, nonlinear effects should be considered. In this context,

Donnell [28] provided nonlinear theories of circular cylindrical shell structures considering the simplifying shallow-shell hypothesis. Novozhilov [181] established a nonlinear theory for doubly curved shell models with constant curvature. Additional nonlinear shell theories were provided by Naghdi and Nordgren [182], employing the Kirchhoff hypotheses, and by Libai and Simmonds [183]. A linear higher-order shear deformation theory of the shell was formulated by Reddy and Liu [176]. This theory was extended to nonlinear deformations by Dennis and Palazotto [184]. Studies comparing the results for nonlinear vibrations of circular cylindrical shells with various constraints are limited. In fact, most of the literature deals with simply-supported boundary conditions. Not many studies on shells with different constraints are available. Matsuzaki and Kobayashi [185] analyzed large amplitude vibrations of clamped circular cylindrical shell structures theoretically and experimentally. In addition, different analyses of circular cylindrical shells with various boundary conditions were carefully performed by Amabili [186]. Numerically predicted responses of orthogrid-stiffened circular cylinders under compressive loadings were evaluated by Haynie and Hilburger [187] to compare several lower bound buckling load prediction methods. Horton *et al.* [188] presented non-destructive procedure to determine the buckling loads of shells. The buckling loads prediction of cylindrical shell structures under compression based on a non-destructive methodology was provided by Fan [189]. In detail, the 3D representation of probe force, probe displacement and prescribed axial load are determined via the repeatedly probing the shell under different prescribed axial loads. Consequently, the critical buckling load of the shell is predicted by the fitting curve which reflects the relation between the maximum probe force and the prescribed axial load. The same approach was used by Hutchinson and Thompson [190] to evaluate the buckling of entire spherical shell structures subjected to combined pressure. Readers are referred to [191] for details about the probing technique. For completeness, reviews on nonlinear vibrations of shell structures may be found in [192, 193].

2.4.1 Analytical formulation

Preliminaries

Typically, the shell geometry is represented using an orthogonal curvilinear reference system (α, β, z), as shown in Fig. 2.10, where $\alpha - \beta$ denote the surface and z indicates the thickness. Consider shells with constant thickness and constant radii of curvature R_α and R_β throughout the Ω domain.

If P is a generic point on the reference curved surface Ω, it is identified by the position vector $\boldsymbol{r}_\Omega = \boldsymbol{r}_\Omega(\alpha, \beta)$. The coordinates α and β coincide with the curvature lines of the

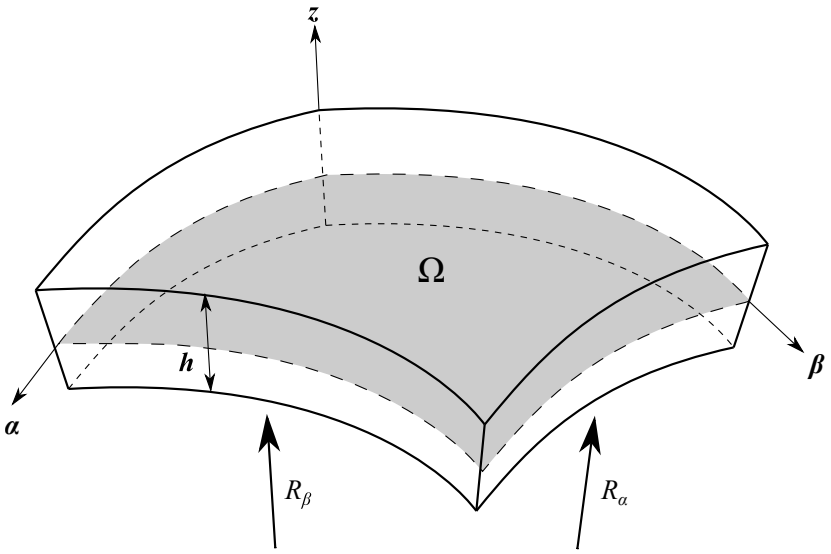

Fig. 2.10 Representative geometry and reference system of the doubly-curved shell model.

mean surface and the unit vectors in the directions α and β are indicated respectively with $\boldsymbol{a}$ and $\boldsymbol{b}$:

$$\boldsymbol{a} = \frac{1}{A}\frac{\partial \boldsymbol{r}}{\partial \alpha} \qquad \boldsymbol{b} = \frac{1}{B}\frac{\partial \boldsymbol{r}}{\partial \beta} \tag{2.43}$$

where:

$$A^2 = \frac{\partial \boldsymbol{r}}{\partial \alpha} \cdot \frac{\partial \boldsymbol{r}}{\partial \alpha} \qquad B^2 = \frac{\partial \boldsymbol{r}}{\partial \beta} \cdot \frac{\partial \boldsymbol{r}}{\partial \beta} \tag{2.44}$$

A and B stand for the coefficients of the first fundamental form of shell reference surface.

If we consider two points of coordinate $(\alpha,\, \beta)$ and $(\alpha + d\alpha,\, \beta + d\beta)$ arbitrarily near to each other and both lying on the surface, the increment of the vector ds in moving from the first point to the second one is defined as follows:

$$ds^2 = d\boldsymbol{r} \cdot d\boldsymbol{r} = A^2(d\alpha)^2 + B^2(d\beta)^2 \tag{2.45}$$

The unit vector perpendicular to the mean surface is denoted by $\boldsymbol{n}$, and is chosen in such a way as to form a right-handed orthogonal system.

$$\boldsymbol{n} = \boldsymbol{a} \times \boldsymbol{b} \tag{2.46}$$

Therefore, the generic position of the point P outside the reference surface of the shell is identified by the following vector:

$$\boldsymbol{r} = \boldsymbol{r}_\Omega(\alpha, \beta) + \zeta \boldsymbol{n}(\alpha, \beta) \tag{2.47}$$

in which ζ represents the distance of the point from the reference surface. From Eq. 2.47, the vectors of the local basis are obtained as follows:

$$\begin{aligned} \boldsymbol{g}_1 &= \frac{\partial \boldsymbol{u}}{\partial \alpha} = A\left(1+\frac{\zeta}{R_\alpha}\right)\boldsymbol{a} \\ \boldsymbol{g}_2 &= \frac{\partial \boldsymbol{u}}{\partial \beta} = B\left(1+\frac{\zeta}{R_\beta}\right)\boldsymbol{b} \\ \boldsymbol{g}_3 &= \frac{\partial \boldsymbol{u}}{\partial \zeta} = \{n\} \end{aligned} \tag{2.48}$$

with:

$$\begin{aligned} &g_{11} = A^2\left(1+\tfrac{\zeta}{R_\alpha}\right)^2, \qquad g_{22} = B^2\left(1+\tfrac{\zeta}{R_\beta}\right)^2, \qquad g_{33} = 1, \\ &g_{23} = g_{31} = g_{12} = 0 \end{aligned} \tag{2.49}$$

The volume of a fundamental element is:

$$dV = AB\left(1+\frac{\zeta}{R_\alpha}\right)\left(1+\frac{\zeta}{R_\beta}\right)d\alpha\, d\beta\, d\eta \tag{2.50}$$

Finally, the relations that link the local Cartesian reference system to the orthogonal curvilinear coordinates are the following:

$$dx = A\left(1+\frac{\zeta}{R_\alpha}\right)d\alpha, \qquad dy = B\left(1+\frac{\zeta}{R_\beta}\right)d\beta, \qquad dz = \zeta \tag{2.51}$$

If the radii of curvature R_α and R_β are supposed to be constant throughout domain Ω, the coefficients A and B are equal to 1. Thus:

$$H_\alpha = \left(1+\frac{\zeta}{R_\alpha}\right), \qquad H_\beta = \left(1+\frac{\zeta}{R_\beta}\right) \tag{2.52}$$

Displacement, strain and stress field

One of the most commonly used models to describe shell structures is the Koiter method which is based on Kirchhoff-Love (KL) hypotheses. In this model,transverse strains are negligible with respect to the other components of the strain. The following are the hypotheses introduced by Kirchhoff-Love:

- Thin shells are considered: the thickness h is negligible compared to the other two dimensions, $\frac{h}{a}, \frac{h}{b} \ll 1$;
- h is constant;

- $\epsilon_{zz} \ll \epsilon_{\alpha\alpha}, \epsilon_{\beta\beta}$;
- $\epsilon_{\alpha z} = \epsilon_{\beta z} = 0$.

According to Koiter's model, the displacement field is the following:

$$\begin{aligned} u(\alpha, \beta, z) &= u^0(\alpha, \beta) + z\phi_\alpha(\alpha, \beta) \\ v(\alpha, \beta, z) &= v^0(\alpha, \beta) + z\phi_\beta(\alpha, \beta) \\ w(\alpha, \beta, z) &= w^0(\alpha, \beta) \end{aligned} \tag{2.53}$$

where ϕ_α and ϕ_β represent the rotations of the transverse normals around the α and β axis. The strain-displacement relation are expressed as follows:

$$\begin{cases} \epsilon_{\alpha\alpha} = \frac{1}{H_\alpha}\left(u_{,\alpha} + \frac{w}{R_\alpha}\right) \\ \epsilon_{\beta\beta} = \frac{1}{H_\beta}\left(v_{,\beta} + \frac{w}{R_\beta}\right) \\ \epsilon_{zz} = w_{,z} \\ \epsilon_{\alpha z} = u_{,z} - \frac{u}{H_\alpha R_\alpha} + \frac{w_{,\alpha}}{H_\alpha} \\ \epsilon_{\beta z} = v_{,z} - \frac{v}{R_\beta H_\beta} + \frac{w_{,\beta}}{H_\beta} \\ \epsilon_{\alpha\beta} = \frac{v_{,\alpha}}{H_\alpha} + \frac{u_{,\beta}}{H_\beta} \end{cases} \tag{2.54}$$

Upon the KL assumptions, one has:

$$\begin{aligned} \epsilon_{zz} = 0 \quad &\rightarrow \quad w = w^0(\alpha, \beta) \\ \epsilon_{\alpha z} = 0 \quad &\rightarrow \quad \phi_\alpha = \frac{u^0}{R_\alpha} - w_{,\alpha} \\ \epsilon_{\beta z} = 0 \quad &\rightarrow \quad \phi_\beta = \frac{v^0}{R_\beta} - w_{,\beta} \end{aligned} \tag{2.55}$$

Therefore, the displacement field of the shell may be rewritten as:

$$\begin{cases} u(\alpha,\beta,z) = u^0(\alpha,\beta) + z\left[\frac{u^0(\alpha,\beta)}{R_\alpha} - w^0_{,\alpha}(\alpha,\beta)\right] \\ v(\alpha,\beta,z) = v^0(\alpha,\beta) + z\left[\frac{v^0(\alpha,\beta)}{R_\beta} - w^0_{,\beta}(\alpha,\beta)\right] \\ w(\alpha,\beta,z) = w^0(\alpha,\beta) \end{cases} \tag{2.56}$$

By introducing the geometrical nonlinearities, the classical von Kármán 2D nonlinear approximation are considered. The strain-displacement relation in general curvilinear coordinates are:

$$\begin{cases} \epsilon_{\alpha\alpha} = \frac{1}{H_\alpha}\left(u^0_{,\alpha} + z\frac{u^0_{,\alpha}}{R_\alpha} - z w^0_{,\alpha\alpha} + \frac{w^0}{R_\alpha}\right) + \frac{1}{2}\frac{(w^0_{,\alpha})^2}{H^2_\alpha} \\ \epsilon_{\beta\beta} = \frac{1}{H_\beta}\left(v^0_{,\beta} + z\frac{v^0_{,\beta}}{R_\beta} - z w^0_{,\beta\beta} + \frac{w^0}{R_\beta}\right) + \frac{1}{2}\frac{(w^0_{,\beta})^2}{H^2_\beta} \\ \epsilon_{\alpha\beta} = \frac{u^0_{,\beta}}{H_\beta} + \frac{v^0_{,\alpha}}{H_\alpha} + z\frac{v^0_{,\alpha}}{H_\alpha R_\beta} + z\frac{u^0_{,\beta}}{H_\beta R_\alpha} - z\frac{w^0_{,\alpha\beta}}{H_\beta} - z\frac{w^0_{,\beta\alpha}}{H_\alpha} + \frac{w^0_{,\alpha} w^0_{,\beta}}{H_\alpha H_\beta} \end{cases} \tag{2.57}$$

The stress vector is obtained from the constitutive equations.

$$\{\boldsymbol{\sigma}\} = [\boldsymbol{C}]\{\boldsymbol{\epsilon}\} \tag{2.58}$$

Nonlinear governing equilibrium equations

The internal forces acting on the shell are the following:

$$\begin{aligned} N_\alpha &= \textstyle\int_{-h/2}^{h/2} \sigma_{\alpha\alpha} H_\beta \, dz, \qquad M_\alpha = \int_{-h/2}^{h/2} z\sigma_{\alpha\alpha} H_\beta \, dz \\ N_\beta &= \textstyle\int_{-h/2}^{h/2} \sigma_{\beta\beta} H_\alpha \, dz, \qquad M_\beta = \int_{-h/2}^{h/2} z\sigma_{\beta\beta} H_\alpha \, dz \\ N_{\alpha\beta} &= \textstyle\int_{-h/2}^{h/2} \sigma_{\alpha\beta} H_\beta \, dz, \qquad M_{\alpha\beta} = \int_{-h/2}^{h/2} z\sigma_{\alpha\beta} H_\beta \, dz \\ N_{\beta\alpha} &= \textstyle\int_{-h/2}^{h/2} \sigma_{\beta\alpha} H_\alpha \, dz, \qquad M_{\beta\alpha} = \int_{-h/2}^{h/2} z\sigma_{\beta\alpha} H_\alpha \, dz \end{aligned} \tag{2.59}$$

The PVD is employed to obtain the nonlinear equations. Namely:

$$\delta L_{int} = \delta L_{ext} + \delta L_{dyn} \tag{2.60}$$

Their expressions for a shell structures are:

$$\begin{aligned}
\delta L_{int} &= \int_V \left(\sigma_{\alpha\alpha}\delta\epsilon_{\alpha\alpha} + \sigma_{\beta\beta}\delta\epsilon_{\beta\beta} + \sigma_{\alpha\beta}\delta\epsilon_{\beta\alpha}\right) H_\alpha H_\beta \, dV \\
\delta L_{ext} &= \int_A p_z \delta w H_\alpha H_\beta \, d\alpha \, d\beta \\
\delta L_{dyn} &= \int_V \rho(\ddot{u}\delta u + \ddot{v}\delta v + \ddot{w}\delta w) H_\alpha H_\beta \, dV
\end{aligned} \tag{2.61}$$

in which $dV = d\alpha \, d\beta \, dz$ ($d\Omega = d\alpha \, d\beta$).

To derive the nonlinear equilibrium equations of the considered shell problem in an explicit form, each contribution has to be evaluated.

$$\boldsymbol{\int_V (\sigma_{\alpha\alpha}\delta\epsilon_{\alpha\alpha}) H_\alpha H_\beta\, d\alpha\, d\beta\, dz} = \int_V \left\{\sigma_{\alpha\alpha}\delta\left[\frac{1}{H_\alpha}\left(u,^0_\alpha + z\frac{u,^0_\alpha}{R_\alpha} - z w,^0_{\alpha\alpha} + \frac{w^0}{R_\alpha}\right) + \frac{1}{2}\frac{(w,^0_\alpha)^2}{H_\alpha^2}\right]\right\}$$

$$H_\alpha H_\beta d\alpha\, d\beta\, dz = \int_V \left(\sigma_{\alpha\alpha}\frac{\delta u,^0_\alpha}{H_\alpha} + \sigma_{\alpha\alpha} z\frac{\delta u,^0_\alpha}{H_\alpha R_\alpha} - \sigma_{\alpha\alpha} z\frac{\delta w,^0_{\alpha\alpha}}{H_\alpha} + \sigma_{\alpha\alpha}\frac{\delta w^0}{R_\alpha H_\alpha} + \sigma_{\alpha\alpha}\frac{\delta(w,^0_\alpha)^2}{2H_\alpha^2}\right)$$

$$H_\alpha H_\beta\, d\alpha\, d\beta\, dz = \int_\Omega \left(N_\alpha \delta u,^0_\alpha + M_\alpha \frac{\delta u,^0_\alpha}{R_\alpha} - M_\alpha \delta w,^0_{\alpha\alpha} + N_\alpha\frac{\delta w^0}{R_\alpha} + \frac{N_\alpha w,^0_\alpha \delta w,^0_\alpha}{H_\alpha}\right)\, d\Omega =$$

$$= -\int_\Omega \left(N_{\alpha,\alpha}\,\delta u^0 - M_{\alpha,\alpha}\,\frac{\delta u^0}{R_\alpha} + M_{\alpha,\alpha\alpha}\,\delta w^0 + N_\alpha\frac{\delta w^0}{R_\alpha} + \frac{(N_\alpha w,^0_\alpha),_\alpha}{H_\alpha}\delta w^0\right)\, d\Omega +$$

$$+\int_\Gamma \left(N_\alpha \delta u^0 + M_\alpha\frac{\delta u^0}{R_\alpha} - M_\alpha \delta w,^0_\alpha + M_{\alpha,\alpha}\,\delta w^0 + \frac{(N_\alpha w,_\alpha)}{H_\alpha}\delta w^0\right)\, d\Gamma$$

$$\boldsymbol{\int_V (\sigma_{\beta\beta}\delta\epsilon_{\beta\beta}) H_\alpha H_\beta\, d\alpha\, d\beta\, dz} = \int_V \left\{\sigma_{\beta\beta}\delta\left[\frac{1}{H_\beta}\left(v,^0_\beta + z\frac{v,^0_\beta}{R_\beta} - z w,^0_{\beta\beta} + \frac{w^0}{R_\beta}\right) + \frac{1}{2}\frac{(w,^0_\beta)^2}{H_\beta^2}\right]\right\} H_\alpha H_\beta$$

$$d\alpha\, d\beta\, dz = \int_V \left(\sigma_{\beta\beta}\frac{\delta v,^0_\beta}{H_\beta} + \sigma_{\beta\beta} z\frac{\delta v,^0_\beta}{H_\beta R_\beta} - \sigma_{\beta\beta} z\frac{\delta w,^0_{\beta\beta}}{H_\beta} + \sigma_{\beta\beta}\frac{\delta w^0}{R_\beta H_\beta} + \sigma_{\beta\beta}\frac{\delta(w,^0_\beta)^2}{2H_\beta^2}\right) H_\alpha H_\beta\, d\alpha$$

$$d\beta\, dz = \int_\Omega \left(N_\beta \delta v,^0_\beta + M_\beta\frac{\delta v,^0_\beta}{R_\beta} - M_\beta \delta w,^0_{\beta\beta} + N_\beta\frac{\delta w^0}{R_\beta} + \frac{N_\beta w,^0_\beta}{H_\beta}\delta w,^0_\beta\right)\, d\Omega =$$

$$= -\int_\Omega \left(N_{\beta,\beta}\,\delta v^0 - M_{\beta,\beta}\,\frac{\delta v^0}{R_\beta} + M_{\beta,\beta\beta}\,\delta w^0 + N_\beta\frac{\delta w^0}{R_\beta} + \frac{(N_\beta w,^0_\beta),_\beta}{H_\beta}\delta w^0\right)\, d\Omega +$$

$$+\int_\Gamma \left(N_\beta \delta u^0 + M_\beta\frac{\delta u^0}{R_\beta} - M_\beta \delta w,^0_\beta + M_{\beta,\beta}\,\delta w^0 + \frac{(N_\beta w,_\beta)}{H_\beta}\delta w^0\right)\, d\Gamma$$

$$\boldsymbol{\int_V (\sigma_{\alpha\beta}\delta\epsilon_{\alpha\beta}) H_\alpha H_\beta\, d\alpha\, d\beta\, dz} = \int_V \left[\sigma_{\alpha\beta}\delta\left(\frac{u,^0_\beta}{H_\beta} + \frac{v,^0_\alpha}{H_\alpha} + z\frac{v,^0_\alpha}{H_\alpha R_\beta} + z\frac{u,^0_\beta}{H_\beta R_\alpha} - z\frac{w,^0_{\alpha\beta}}{H_\beta} - z\frac{w,^0_{\beta\alpha}}{H_\alpha} + \frac{w,^0_\alpha w,^0_\beta}{H_\alpha H_\beta}\right)\right]$$

$$H_\alpha H_\beta\, dV = \int_V [\sigma_{\alpha\beta}\frac{\delta u,^0_\beta}{H_\beta} + \sigma_{\alpha\beta}\frac{\delta v,^0_\alpha}{H_\alpha} + \sigma_{\alpha\beta} z\frac{\delta v,^0_\alpha}{H_\alpha R_\beta} + \sigma_{\alpha\beta} z\frac{\delta u,^0_\beta}{H_\beta R_\alpha} - \sigma_{\alpha\beta} z\frac{\delta w,^0_{\alpha\beta}}{H_\beta} - \sigma_{\alpha\beta} z\frac{\delta w,^0_{\beta\alpha}}{H_\alpha} +$$

$$+\sigma_{\alpha\beta}\frac{\delta(w,^0_\alpha w,^0_\beta)}{H_\alpha H_\beta}] H_\alpha H_\beta\, dV = \int_\Omega (N_{\beta\alpha}\delta u,^0_\beta + N_{\alpha\beta}\delta v,^0_\alpha + M_\alpha\beta\frac{\delta v,^0_\alpha}{R_\beta} + M_\beta\alpha\frac{\delta u,^0_\beta}{R_\alpha} - M_{\beta\alpha}\delta w,^0_{\alpha\beta} +$$

$$-M_{\alpha\beta}\delta w,^0_{\beta\alpha} + N_{\alpha\beta}\frac{\delta w,^0_\beta \delta w,^0_\alpha}{H_\beta}\; N_{\beta\alpha}\frac{\delta w,^0_\alpha \delta w,^0_\beta}{H_\alpha})\, d\Omega = -\int_\Omega [N_{\beta\alpha,\beta}\,\delta u^0 + N_{\alpha\beta,\alpha}\,\delta v^0 - M_{\alpha\beta,\alpha}\,\frac{\delta v^0}{R_\beta} +$$

$$-M_{\beta\alpha,\beta}\,\frac{\delta u^0}{R_\alpha} + M_{\beta\alpha,\alpha\beta}\,\delta w^0 + M_{\alpha\beta,\beta\alpha}\,\delta w^0 \; + \frac{1}{H_\beta}(N_{\alpha\beta} w,^0_\beta)_{,\alpha}\,\delta w^0 + \frac{1}{H_\alpha}(N_{\beta\alpha} w,^0_\alpha)_{,\beta}\,\delta w^0]\, d\Omega +$$

$$+\int_\Gamma (N_{\beta\alpha}\delta u^0 + N_{\alpha\beta}\delta v^0 + M_{\alpha\beta}\frac{\delta v^0}{R_\beta} + M_{\beta\alpha}\frac{\delta u^0}{R_\alpha} \; - M_{\beta\alpha}\delta w,^0_\alpha + M_{\beta\alpha,\beta}\,\delta w^0 - M_{\alpha\beta}\delta w,^0_\beta +$$

$$+M_{\alpha\beta,\alpha}\,\delta w^0 + \frac{1}{H_\beta}(N_{\alpha\beta}\delta w,^0_\beta)\delta w^0 + \frac{1}{H_\alpha}(N_{\beta\alpha}\delta w,^0_\alpha)\delta w^0\, d\Gamma \tag{2.62}$$

Regarding the virtual variation of the dynamic work, one has:

$$\begin{aligned}
&\int_V \boldsymbol{\rho(\ddot{u}\delta u+\ddot{v}\delta v+\ddot{w}\delta w)H_\alpha H_\beta\, dV} = \int_V[\rho(\ddot{u}^0+z(\tfrac{\ddot{u}^0}{R_\alpha}-\ddot{w}_{,\alpha}^{\,0}))(\delta u^0+z(\tfrac{\delta u^0}{R_\alpha}-\delta w_{,\alpha}^{\,0}))+\rho(\ddot{v}^0+\\
&+z(\tfrac{\ddot{v}^0}{R_\beta}-\ddot{w}^0{}_{,\beta}^{\,0}))(\delta v^0+z(\tfrac{\delta v^0}{R_\beta}-\delta w_{,\beta}^{\,0}))+\rho(\ddot{w}^0)(\delta w^0)]H_\alpha H_\beta\, dV = \int_\Omega[(I_0\ddot{u}^0+2I_1\tfrac{\ddot{u}^0}{R_\alpha}+I_2\tfrac{\ddot{u}^0}{R_\alpha^2}+\\
&-I_1\ddot{w}_{,\alpha}^{\,0}-I_2\tfrac{\ddot{w}_{,\alpha}}{R_\alpha})\delta u^0+(I_0\ddot{v}^0+2I_1\tfrac{\ddot{v}^0}{R_\beta}+I_2\tfrac{\ddot{v}^0}{R_\beta^2}-I_1\ddot{w}_{,\beta}^{\,0}-I_2\tfrac{\ddot{w}_{,\beta}}{R_\beta})\delta v^0+I_0\ddot{w}^0\delta w^0\ +(-I_1\ddot{u}^0-I_1\tfrac{\ddot{u}^0}{R_\alpha}+\\
&+I_2\ddot{w}_{,\alpha}^{\,0})\delta w_{,\alpha}^{\,0}+(-I_1\ddot{v}^0-I_1\tfrac{\ddot{v}^0}{R_\beta}+I_2\ddot{w}_{,\beta}^{\,0})\delta w_{,\beta}{}^0]H_\alpha H_\beta\, d\Omega = -\int_\Omega[(I_0\ddot{u}^0+2I_1\tfrac{\ddot{u}^0}{R_\alpha}\ +I_2\tfrac{\ddot{u}^0}{R_\alpha^2}+\\
&-I_1\ddot{w}_{,\alpha}^{\,0}-I_2\tfrac{\ddot{w}_{,\alpha}}{R_\alpha})\delta u^0+(I_0\ddot{v}^0+2I_1\tfrac{\ddot{v}^0}{R_\beta}+I_2\tfrac{\ddot{v}^0}{R_\beta^2}-I_1\ddot{w}_{,\beta}^{\,0}-I_2\tfrac{\ddot{w}_{,\beta}}{R_\beta})\delta v^0+I_0\ddot{w}^0\delta w^0\ +(-I_1\ddot{u}_{,\alpha}^{\,0}-I_1\tfrac{\ddot{u}_{,\alpha}^{\,0}}{R_\alpha}+\\
&+I_2\ddot{w}_{,\alpha\alpha}^{\,0}-I_1\ddot{v}_{,\beta}^{\,0}-I_1\tfrac{\ddot{v}_{,\beta}^{\,0}}{R_\beta}+I_2\ddot{w}_{,\beta\beta}^{\,0})\delta w^0]H_\alpha H_\beta\, d\Omega\ +\int_\Gamma[(-I_1\ddot{u}^0-I_1\tfrac{\ddot{u}^0}{R_\alpha}+I_2\ddot{w}_{,\alpha}^{\,0}-I_1\ddot{v}^0+\\
&-I_1\tfrac{\ddot{v}^0}{R_\beta}+I_2\ddot{w}_{,\beta}^{\,0})\delta w^0]H_\alpha H_\beta\, d\Gamma
\end{aligned} \tag{2.63}$$

where $(I_0, I_1, I_2) = \int_z \rho(1, z, z^2)\, dz$ stand for the mass, static moment and moment of inertia per unit of length.

Upon evaluating each contribution, the nonlinear equilibrium equations in the dynamic case are written as follows:

$$\left\{\begin{aligned}
&-N_{\alpha,\alpha}-N_{\beta\alpha,\beta}+\tfrac{M_{\alpha,\alpha}}{R_\alpha}+\tfrac{M_{\beta\alpha,\beta}}{R_\alpha}=(-I_0\ddot{u}^0-2I_1\tfrac{\ddot{u}^0}{R_\alpha}-I_2\tfrac{\ddot{u}^0}{R_\alpha^2}+I_1\ddot{w}_{,\alpha}^{\,0}+I_2\tfrac{\ddot{w}_{,\alpha}}{R_\alpha})H_\alpha H_\beta\\
&-N_{\beta,\beta}-N_{\alpha\beta,\alpha}+\tfrac{M_{\beta,\beta}}{R_\beta}+\tfrac{M_{\alpha\beta,\alpha}}{R_\beta}=(-I_0\ddot{v}^0-2I_1\tfrac{\ddot{v}^0}{R_\beta}-I_2\tfrac{\ddot{v}^0}{R_\beta^2}+I_1\ddot{w}_{,\beta}^{\,0}+I_2\tfrac{\ddot{w}_{,\beta}}{R_\beta})H_\alpha H_\beta\\
&-M_{\alpha,\alpha\alpha}-\tfrac{N_\alpha}{R_\alpha}-\tfrac{(\bar{N}_\alpha w_{,\alpha\alpha}^{\,0})}{H_\alpha}-M_{\beta,\beta\beta}-\tfrac{N_\beta}{R_\beta}-\tfrac{(\bar{N}_\beta w_{,\beta\beta}^{\,0})}{H_\beta}-M_{\beta\alpha,\alpha\beta}-M_{\alpha\beta,\beta\alpha}+\\
&\qquad-\tfrac{1}{H_\beta}(\bar{N}_{\alpha\beta}w_{,\beta\alpha}^{\,0})-\tfrac{1}{H_\alpha}(\bar{N}_{\beta\alpha}w_{,\alpha\beta}^{\,0})=p_z+(-I_0\ddot{w}^0+I_1\ddot{u}_{,\alpha}^{\,0}+I_1\tfrac{\ddot{u}_{,\alpha}^{\,0}}{R_\alpha}-I_2\ddot{w}_{,\alpha\alpha}^{\,0}+\\
&\qquad+I_1\ddot{v}_{,\beta}^{\,0}+I_1\tfrac{\ddot{v}_{,\beta}^{\,0}}{R_\beta}-I_2\ddot{w}_{,\beta\beta}^{\,0})H_\alpha H_\beta
\end{aligned}\right. \tag{2.64}$$

in which the $N_\alpha = \bar{N}_\alpha,\ N_\beta = \bar{N}_\beta,\ N_{\alpha\beta} = \bar{N}_{\alpha\beta}$ are considered constant on the shell only for the nonlinear contribution.

Buckling of a cylindrical shell

Figure 2.11 depicts the considered problem, in which $H_\alpha = 1$ is assumed, including the boundary conditions (S = simply-supported, F = free) applied and the highlighted part representing the area subjected to compressive loadings. Especially, the classical problem of the cylindrical bending ($\frac{\partial}{\partial \alpha} = 0$) is considered in the following resolution.

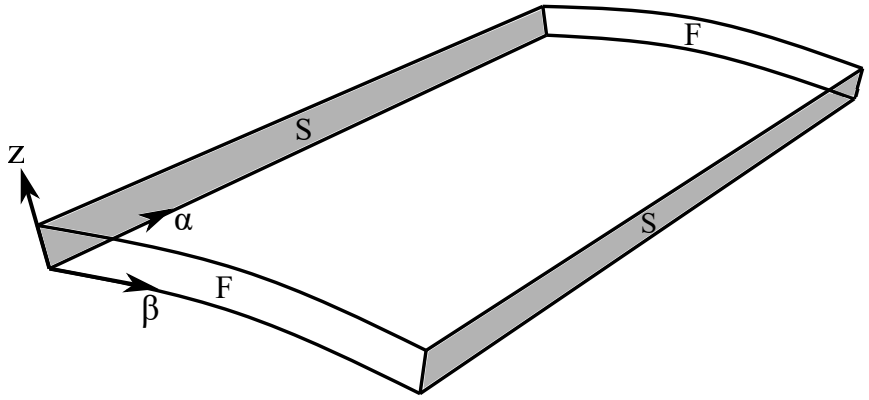

Fig. 2.11 Cylindrical shell.

In order to compute the critical buckling load through the dynamic criterion, initial hypotheses are made. These assumptions are:

- $p_z = 0$;
- $[B] = 0$, no coupling between the membrane and flexural-torsional effects;
- $I_1 = I_2 = 0$.

By introducing the Navier method and considering simply-supported boundary conditions, one has:

$$\begin{aligned} u(\alpha,\beta;t) &= U cos(\zeta\alpha) sin(\eta\beta) e^{i\omega t} \\ v(\alpha,\beta;t) &= V sin(\zeta\alpha) cos(\eta\beta) e^{i\omega t} \\ w(\alpha,\beta;t) &= W sin(\zeta\alpha) sin(\eta\beta) e^{i\omega t} \end{aligned} \tag{2.65}$$

$$\begin{cases} \alpha = 0, a & \rightarrow \quad w^0 = 0, M_\alpha = 0 \\ \beta = 0, b & \rightarrow \quad w^0 = 0, M_\beta = 0 \end{cases} \tag{2.66}$$

where the terms $\zeta = \frac{m\pi}{a}$ and $\eta = \frac{n\pi}{b}$, in which m and n are the half-wave number along the α-axis and β-axis and a and b stand for the lengths along the α- and β-direction,

respectively. Therefore, the relation between natural frequencies and external applied loadings is obtained by solving the following system:

$$\begin{cases} -N_{\beta,\beta} + \frac{M_{\beta,\beta}}{R_\beta} = -I_0 \ddot{v}^0 H_\beta \\ \\ -M_{\beta,\beta\beta} - \frac{N_\beta}{R_\beta} = -I_0 \ddot{w}^0 H_\beta + \frac{\bar{N}_\beta}{H_\beta} w^0_{,\beta\beta} \end{cases} \tag{2.67}$$

Omitting mathematical passages, the final form of the equation to calculate the natural frequency variation as a function of the different applied loads is:

$$\omega^4 \left(-I_0^2 H_\beta^2\right) + \omega^2 \left(A I_0 \eta^2 - \frac{D I_0 H_\beta \eta^2}{H_\beta R_\beta^2} + I_0 D \eta^4 - \frac{I_0 A}{R_\beta^2} + I_0 \bar{N}_\beta \eta^2\right) - \frac{AD\eta^6}{H_\beta^2} + \frac{A^2\eta^2}{R_\beta^2 H_\beta^2} +$$

$$- \frac{A\bar{N}_\beta \eta^4}{H_\beta^2} + + \frac{D^2\eta^6}{H_\beta^2 R_\beta^2} - \frac{AD\eta^2}{R_\beta^4 H_\beta^2} + \frac{D\bar{N}_\beta \eta^4}{R_\beta^2 H_\beta^2} + \frac{DA\eta^4}{R_\beta^2 H_\beta^2} - \frac{A^2\eta^2}{R_\beta^2 H_\beta} - \frac{D^2\eta^6}{R_\beta^2 H_\beta^2} + \frac{AD\eta^4}{R_\beta^2 H_\beta^2} = 0 \tag{2.68}$$

where $A = \frac{Eh}{1-\nu^2}$.

2.5 Validation examples

In this section, the analytical solutions for 1D and 2D example cases compared to numerical results obtained using Abaqus [194] are reported to prove the validity and reliability of previously shown formulations.

Beam A simply-supported square beam structure under compressive load in the y-direction is presented as the first validation example. The structure has the following geometrical data: length, L, equal to 100 m and the side, a = h, of the square cross-section is 1 m. The material properties for this structure are the following: $E = 70$ GPa, $\nu = 0.3$ and $\rho = 2700$ kg/m^3. The structure is modelled via the commercial software Abaqus, modelling the beam structures by employing 10 B32 beam elements.

Figure 2.12 shows the first natural frequency variation with respect to the applied compressive loadings with the comparison between the numerical solution and the analytical one. Table 2.1 shows the linearized buckling load of the beam structure under compressive loadings with the comparison with the analytical solution. In addition, Fig. 2.13 illustrates the first buckling mode shape.

Plate The second validation case deals with a simply-supported square plate under compressive loadings. The geometrical and material data are the following: a = b =

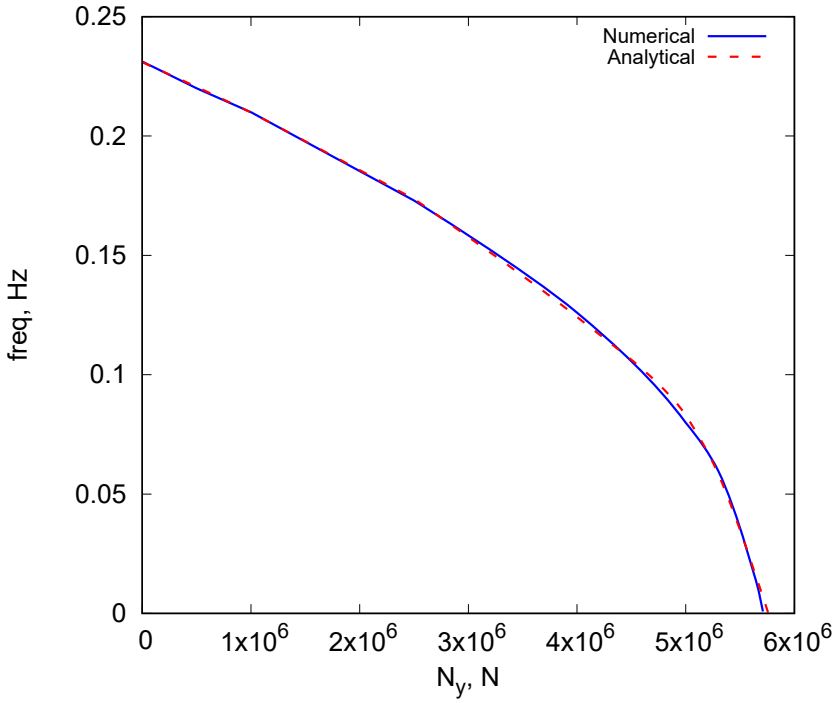

Fig. 2.12 The first natural frequency variation vs the applied compression. Beam structure.

Method	Buckling Load
Numerical	5.67×10^6
Analytical	5.75×10^6

Table 2.1 The linearized bucking load in [N] of the beam structure.

Fig. 2.13 First buckling mode shape of the beam structure under compressive loadings.

10 m, h = 0.1 m, $E = 70$ GPa, $\nu = 0.3$ and $\rho = 2700$ kg/m^3. The numerical solution is obtained employing the commercial software Abaqus, modelling the structure with 10×10 S4R shell elements.

Figure 2.14 provides the first natural frequency variation versus applied compressive loadings with the comparison between the numerical solution and the analytical one. Table 2.2 illustrates the comparison between the linearized critical buckling load obtained

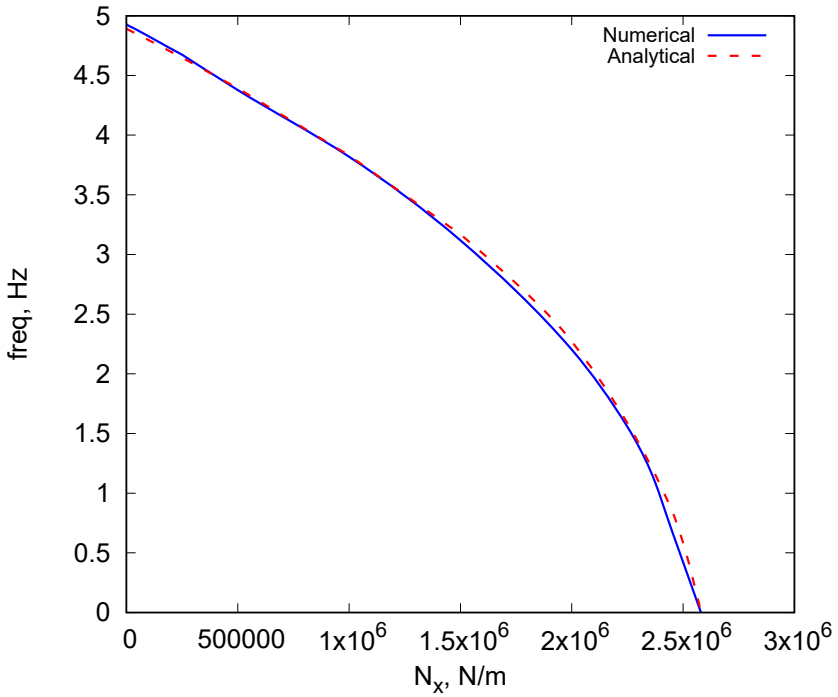

Fig. 2.14 The first natural frequency variation versus the applied compressive loading. Plate structure.

numerically and the analytical solution for the plate structure under compressive loadings, whereas the first buckling mode shape is displayed in Fig. 2.15.

Method	Buckling Load
Numerical	2.51×10^6
Analytical	2.58×10^6

Table 2.2 The linearized bucking load in [N/m] of the plate structure.

Shell Finally, the following case deals with a simply-supported cylindrical shell under compressive loadings. The material and geometrical data of the cylindrical shell are the

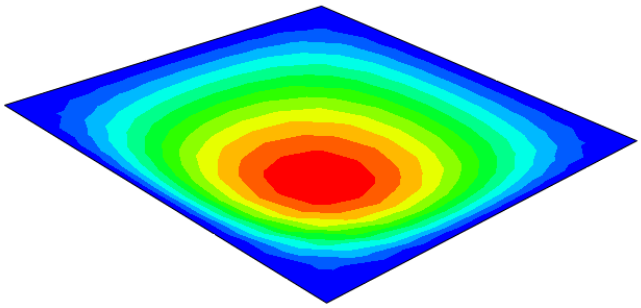

Fig. 2.15 First buckling mode shape of the plate structure under compressive loadings.

following: E= 70 GPa and $\nu = 0.3$, and L = 508 mm, $R_\beta = 2540$ mm, $\theta = 0.1$ rad and thickness equal to 5.08 mm. The numerical solution is obtained using the commercial software Abaqus, modelling the structure with 20×20 S4R shell elements. Table 2.3 shows the comparison between the linearized critical buckling load obtained numerically and the analytical solution for the cylindrical shell structure under compressive loadings. For completeness, Fig. 2.16 depicts the natural frequency variation of the first three

Method	Buckling Load
Numerical	32.1
Analytical	35.0

Table 2.3 The linearized bucking load in [N/mm] of the cylindrical shell structure.

modes for increasing applied loads, including the mode shapes.

2.6 Limitations of the analytical method

Analytical formulations for the buckling evaluation using the dynamic criterion were presented. In particular, simply-supported boundary conditions were considered. Analytical solutions to complex dynamics problems with more sophisticated geometries and boundary conditions are mathematically laborious, so that many simplifying assumptions may be required to achieve a closed-form solution for such problems. Of course, when closed-form solutions can be derived, analytical ones are preferred. Nevertheless, when an exact closed-form solution cannot be obtained, alternative solution techniques, including semi-analytical and numerical methods, are essential. Specifically, numerical solutions based on the FEM are the best alternative.

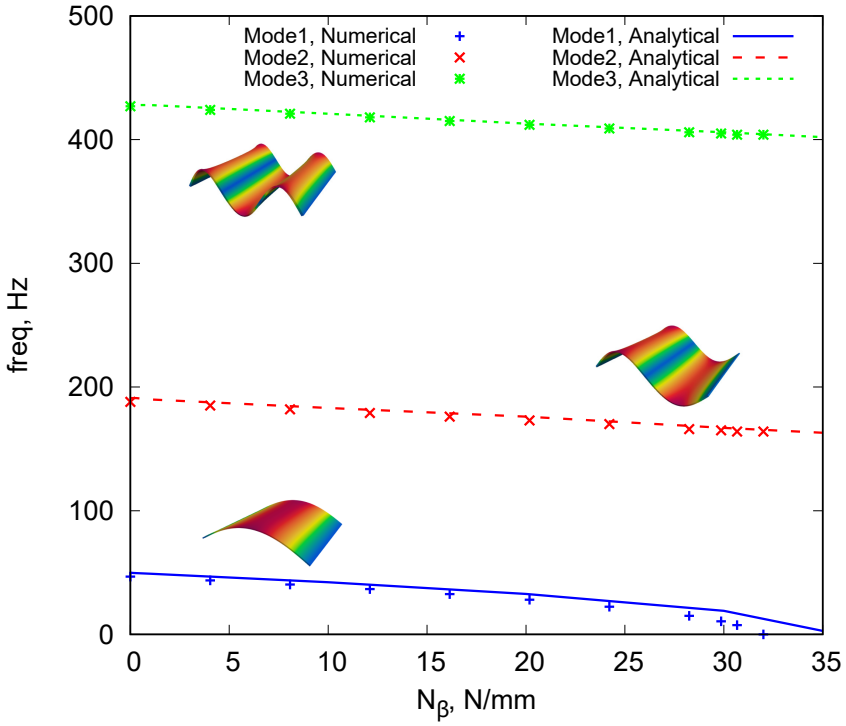

Fig. 2.16 The natural frequency variation of the first three modes as a function of the applied compressive loads. Cylindrical shell structure.

The approach used in the analytical dynamic criterion to evaluate buckling loads by exploiting the trend of natural frequencies is the basis of the VCT. This method is a non-destructive approaches used in aerospace industries to predict the buckling load. This technique computes the critical loads and equivalent boundary conditions by interpolating the natural frequencies of the structures for increasing applied loadings without reaching instability. However, even this experimental method shows limitations, for example, the evaluation of structures under thermal or shear loads.

One of the main limitations of the analytical theory is that it may only be used for structures with specific boundary and loadings conditions. Moreover, transcendental governing equations can be simplified into an algebraic system of equations only if the axial motions are decoupled from the transversal ones. This is possible only if the material coupling is absent, i.e., if the structure is homogeneous or the laminae of the composite structure are isotropic, or the resulting laminate is symmetric and balanced cross-ply. Another limitation is related to the assumptions introduced to compute the solution in closed-form by using the Navier method.

Therefore, in the following chapters, a novel numerical methodology will be proposed, which will overcome all of the above limitations to address the general case without restrictions.

Chapter 3

Derivation of higher-order 1D and 2D models using CUF

This chapter introduces the Carrera Unified Formulation (CUF) and its application in the straightforward development of 1D (beam) and 2D (plate, shell) higher-order models in a hierarchical and automatic manner within a finite element domain. Basically, CUF, using an index notation, allows to unify all the theories of structures in a single formula and to formulate very refined models in a simple way. The fundamental concept of the framework is the introduction of expansion functions, in addition to standard finite element interpolation functions, to enrich the kinematic description of the beam cross-section and plate/shell thickness. This approach leads to 1D and 2D CUF models, which are similar to 3D solid-FEA in terms of solution accuracy, but require considerably less computational effort [40].
First, the notation, geometry and displacement, stress and strain vectors are defined. Then, the geometrical and material relations and the nonlinear governing equations are expressed, including the explicit form of the matrices. For brevity, some details were omitted, but interested readers may find them in [34, 103].

3.1 Preliminaries

Consider beam and plate models described by employing a Cartesian system (x,y,z), whereas an orthogonal curvilinear system (α,β,z) for shells, as depicted in Fig. 3.1. In detail, for a beam the y indicates the beam axis and $x-z$ the cross-section, while for a plate and shell model the $x-y$ and $\alpha-\beta$ denotes the two in-plane directions, respectively, and z stands for the through-the-thickness direction. The choice of the cross-section or thickness is arbitrary since it does not affect the following theoretical formulation.

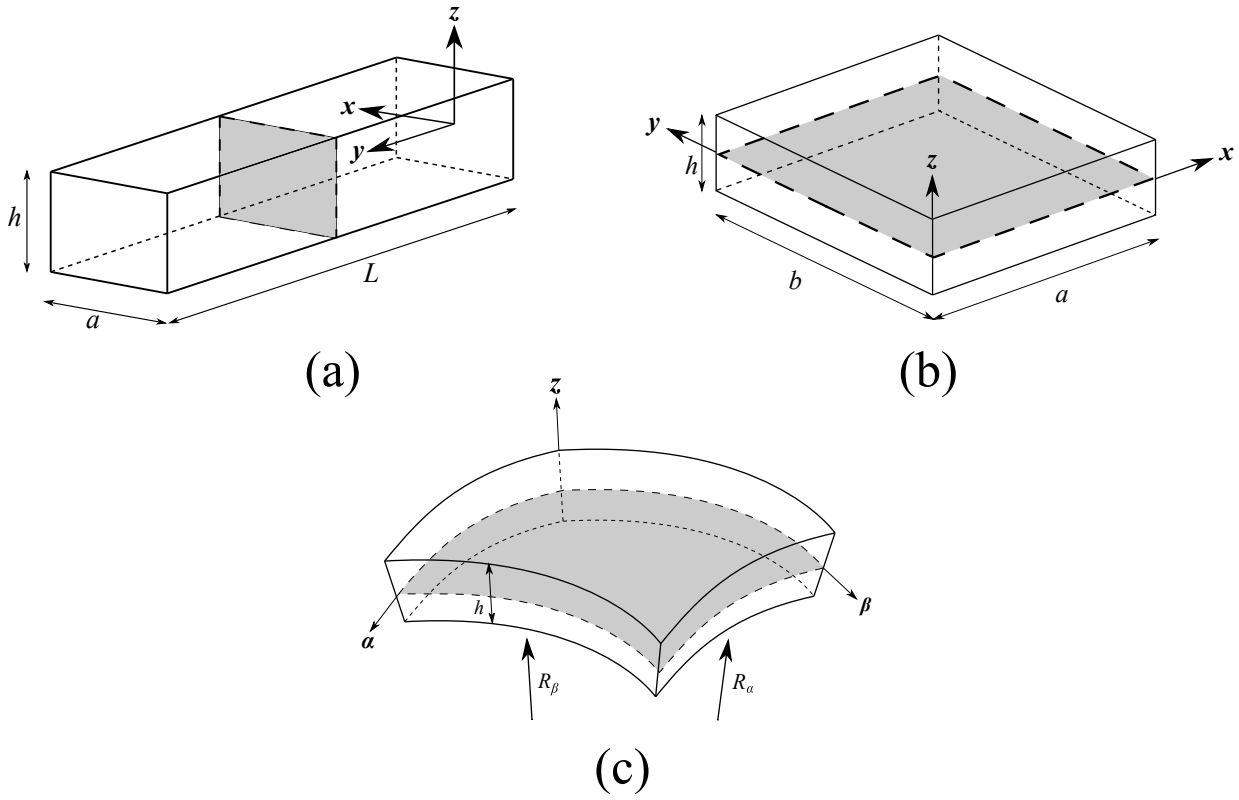

Fig. 3.1 Representative geometry and reference system of the (a) beam, (b) plate and (c) doubly-curved shell.

Consider the 3D displacement vector of a generic point within the structural domain, which may be expressed as follows:

$$\begin{aligned} \textit{Beam, Plate}: \quad & \boldsymbol{u}(x,y,z;t)^k = \{u_x^k \; u_y^k \; u_z^k\}^{\mathrm{T}} \\ \textit{Shell}: \quad & \boldsymbol{u}(\alpha,\beta,z;t)^k = \{u_\alpha^k \; u_\beta^k \; u_z^k\}^{\mathrm{T}} \end{aligned} \tag{3.1}$$

in which the superscript k is the k^{th}-layer if a laminated structure is considered and T is the transpose operator. Stresses, $\boldsymbol{\sigma}$, and strains, $\boldsymbol{\epsilon}$, are expressed in vectorial form with no loss of generality,

$$\begin{aligned} \textit{Beam, Plate}: \quad & \boldsymbol{\epsilon}^k = \{\epsilon_{xx}^k \; \epsilon_{yy}^k \; \epsilon_{zz}^k \; \epsilon_{xz}^k \; \epsilon_{yz}^k \; \epsilon_{xy}^k\}^{\mathrm{T}} \\ & \boldsymbol{\sigma}^k = \{\sigma_{xx}^k \; \sigma_{yy}^k \; \sigma_{zz}^k \; \sigma_{xz}^k \; \sigma_{yz}^k \; \sigma_{xy}^k\}^{\mathrm{T}} \\ \textit{Shell}: \quad & \boldsymbol{\epsilon}^k = \{\epsilon_{\alpha\alpha}^k \; \epsilon_{\beta\beta}^k \; \epsilon_{zz}^k \; \epsilon_{\alpha z}^k \; \epsilon_{\beta z}^k \; \epsilon_{\alpha\beta}^k\}^{\mathrm{T}} \\ & \boldsymbol{\sigma}^k = \{\sigma_{\alpha\alpha}^k \; \sigma_{\beta\beta}^k \; \sigma_{zz}^k \; \sigma_{\alpha z}^k \; \sigma_{\beta z}^k \; \sigma_{\alpha\beta}^k\}^{\mathrm{T}} \end{aligned} \tag{3.2}$$

When dealing with large displacements/rotations of highly flexible structures, accurate definitions of strains and stresses are needed to carry out reliable nonlinear analyses. The Lagrangian formulations are typically used in the pure geometrically nonlinear analyses. There are two incremental Lagrangian formulations that are adopted to compute the deformation and stress states in continuum problems: 1. the total Lagrangian (TL) formulation and 2. the updated Lagrangian (UL) formulation. In detail, in the first approach, strains are written in terms of the undeformed configuration. In the second approach, strains are expressed as a function of deformed configurations in the UL approach. A detailed description of the many advantages of adopting a Lagrangian method is given in Pai's book [195].

Hence, the proposed nonlinear methodology is developed using the TL formulations and employs the Green-Lagrange (GL) strain tensor $\boldsymbol{\epsilon}$, that is work-conjugate to the Second Piola-Kirchhoff (PK2) stress tensor $\boldsymbol{\sigma}$. The displacement-strain relations are written as:

$$\boldsymbol{\epsilon}^k = \boldsymbol{\epsilon}_l^k + \boldsymbol{\epsilon}_{nl}^k = (\boldsymbol{b}_l + \boldsymbol{b}_{nl})\boldsymbol{u}^k \tag{3.3}$$

in which $\boldsymbol{b}_l$ and $\boldsymbol{b}_{nl}$ are the 6×3 linear and nonlinear differential operators and they are defined for beam, plate and shell model as follows:

$$Beam,\ Plate:\ \boldsymbol{b}_l = \begin{bmatrix} \partial_x & 0 & 0 \\ 0 & \partial_y & 0 \\ 0 & 0 & \partial_z \\ \partial_z & 0 & \partial_x \\ 0 & \partial_z & \partial_y \\ \partial_y & \partial_x & 0 \end{bmatrix}, \qquad \boldsymbol{b}_{nl} = \begin{bmatrix} P_{11}\frac{1}{2}(\partial_x)^2 & P_{12}\frac{1}{2}(\partial_x)^2 & P_{13}\frac{1}{2}(\partial_x)^2 \\ P_{21}\frac{1}{2}(\partial_y)^2 & P_{22}\frac{1}{2}(\partial_y)^2 & P_{23}\frac{1}{2}(\partial_y)^2 \\ P_{31}\frac{1}{2}(\partial_z)^2 & P_{32}\frac{1}{2}(\partial_z)^2 & P_{33}\frac{1}{2}(\partial_z)^2 \\ P_{41}\partial_x\,\partial_z & P_{42}\partial_x\,\partial_z & P_{43}\partial_x\,\partial_z \\ P_{51}\partial_y\,\partial_z & P_{52}\partial_y\,\partial_z & P_{53}\partial_y\,\partial_z \\ P_{61}\partial_x\,\partial_y & P_{62}\partial_x\,\partial_y & P_{63}\partial_x\,\partial_y \end{bmatrix}$$

$$\boldsymbol{b}_l = \begin{bmatrix} \frac{\partial_\alpha}{H_\alpha} & 0 & \frac{1}{H_\alpha R_\alpha} \\ 0 & \frac{\partial_\beta}{H_\beta} & \frac{1}{H_\beta R_\beta} \\ 0 & 0 & \partial_z \\ \partial_z - \frac{1}{H_\alpha R_\alpha} & 0 & \frac{\partial_\alpha}{H_\alpha} \\ 0 & \partial_z - \frac{1}{H_\beta R_\beta} & \frac{\partial_\beta}{H_\beta} \\ \frac{\partial_\beta}{H_\beta} & \frac{\partial_\alpha}{H_\alpha} & 0 \end{bmatrix},$$

$Shell:$

$$\boldsymbol{b}_{nl} = \begin{bmatrix} P_{11}\frac{1}{2H_\alpha^2}\left[(\partial_\alpha)^2 + \frac{2u_z\partial_\alpha}{R_\alpha} + \frac{u_\alpha}{R_\alpha^2}\right] & P_{12}\frac{(\partial_\alpha)^2}{2H_\alpha^2} & P_{13}\frac{1}{2H_\alpha^2}\left[(\partial_\alpha)^2 - \frac{2u_\alpha\partial_\alpha}{R_\alpha} + \frac{u_z}{R_\alpha^2}\right] \\ P_{21}\frac{(\partial_\beta)^2}{2H_\beta^2} & P_{22}\frac{1}{2H_\beta^2}\left[(\partial_\beta)^2 + \frac{2u_z\partial_\beta}{R_\beta} + \frac{u_\beta}{R_\beta^2}\right] & P_{23}\frac{1}{2H_\beta^2}\left[(\partial_\beta)^2 - \frac{2u_\beta\partial_\beta}{R_\beta} + \frac{u_z}{R_\beta^2}\right] \\ P_{31}\frac{1}{2}(\partial_z)^2 & P_{32}\frac{1}{2}(\partial_z)^2 & P_{33}\frac{1}{2}(\partial_z)^2 \\ P_{41}\frac{1}{H_\alpha}\left(\partial_\alpha\,\partial_z + \frac{u_z\partial_z}{R_\alpha}\right) & P_{42}\frac{\partial_\alpha\,\partial_z}{H_\alpha} & P_{43}\frac{1}{H_\alpha}\left(\partial_\alpha\,\partial_z - \frac{u_\alpha\partial_z}{R_\alpha}\right) \\ P_{51}\frac{\partial_\beta\,\partial_z}{H_\beta} & P_{52}\frac{1}{H_\beta}\left(\partial_\beta\,\partial_z + \frac{u_z\partial_z}{R_\beta}\right) & P_{53}\frac{1}{H_\beta}\left(\partial_\beta\,\partial_z - \frac{u_\beta\partial_z}{R_\beta}\right) \\ P_{61}\frac{1}{H_\alpha H_\beta}\left(\partial_\alpha\,\partial_\beta + \frac{u_z\partial_\beta}{R_\alpha} + \frac{u_\beta}{R_\alpha R_\beta}\right) & P_{62}\frac{1}{H_\alpha H_\beta}\left(\partial_\alpha\,\partial_\beta + \frac{u_z\partial_\alpha}{R_\beta}\right) & P_{63}\frac{1}{H_\alpha H_\beta}\left(\partial_\alpha\,\partial_\beta - \frac{u_\alpha\partial_\beta}{R_\alpha} - \frac{u_\beta\partial_\alpha}{R_\beta}\right) \end{bmatrix} \tag{3.4}$$

where $P_{ij}(i = 1-6, j = 1-3)$ indicate the parameters assumed to simplify or tune the nonlinear strain measures and ∂_x stands for the derivative along the x direction, so that $\partial_x = \frac{\partial(\cdot)}{\partial x}$. The same symbol is considered for α, β, y and z directions.

Over the years, researchers have developed several approximate geometrically nonlinear models for 1D and 2D structures from simplifications of the full 3D geometrical relations. For example, the von Kármán strain theory for 2D structures represents the classic geometrically nonlinear model, see [196]. Considering small rotations, the hypotheses of 2D von Kármán models state that only the nonlinear terms of Eq. 3.4, which are associated with the in-plane partial derivatives of the transverse displacements, cannot be neglected. Therefore, the only non-zero components of geometrically nonlinear strains are P_{13}, P_{23}, and $P_{63} \neq 0$. By adding the P_{31} and P_{32} components, the nonlinear shear effects are included. According to the von Kármán hypotheses, in the case of 1D models, the only non-zero component is $P_{23} \neq 0$. The P_{32} strain component should also be activated if the nonlinear shear effects are considered. For completeness, various geometrically nonlinear strain measures are displayed in Fig. 3.2, in which the black dots denote the activated nonlinear strain components with reference to the matrix $\boldsymbol{b}_{nl}$ in Eq. 3.4. Therefore, it is possible to derive different geometrically nonlinear models by cancelling

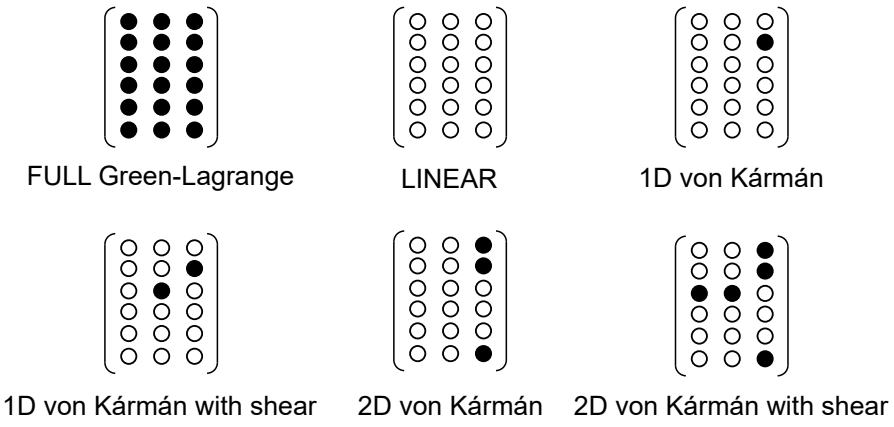

Fig. 3.2 Different geometrically nonlinear strain models.

or adding different nonlinear strain terms from or into the CUF *FNs* in order to evaluate their effect on the static and transient nonlinear response is investigated.

The stress-strain relation may be expressed employing the material properties. In the present research, the material properties are assumed linear and, therefore, Hooke's law is considered. Its compact vectorial form is:

$$\boldsymbol{\sigma}^k = \boldsymbol{\sigma}_l^k + \boldsymbol{\sigma}_{nl}^k = \mathbf{C}^k(\boldsymbol{\epsilon}_l^k + \boldsymbol{\epsilon}_{nl}^k) \tag{3.5}$$

in which $\boldsymbol{C}^k$ stands for the material linear elastic matrix. In orthotropic material case, the matrix $\boldsymbol{C}^k$ is:

$$\boldsymbol{C}^k = \begin{bmatrix} C_{11}^k & C_{12}^k & C_{13}^k & 0 & 0 & C_{16}^k \\ & C_{22}^k & C_{23}^k & 0 & 0 & C_{26}^k \\ & & C_{33}^k & 0 & 0 & C_{36}^k \\ & & & C_{44}^k & C_{45}^k & 0 \\ & & & & C_{55}^k & 0 \\ sym & & & & & C_{66}^k \end{bmatrix} \tag{3.6}$$

where the coefficients depend on the Young moduli E, the Poisson ratios ν, the shear moduli G and the fiber angle orientation θ [197].

By considering variable-angle-tow (VAT) composite structures, the fiber has a general orientation function of the space coordinates, i.e., $\theta(x, y)$ or $\theta(\alpha, \beta)$. As a result, we get:

$$\boldsymbol{\sigma}^k = \widetilde{\mathbf{C}}^k \boldsymbol{\epsilon}^k \tag{3.7}$$

where:

$$\widetilde{\boldsymbol{C}}^k = \boldsymbol{T}^{\mathrm{T}} \boldsymbol{C}^k \boldsymbol{T} \tag{3.8}$$

where $\boldsymbol{T}$ is the rotation matrix [198].

In VAT structures, the orientation angle of the fiber is allowed to change continuously along a curvilinear path on each ply. So, the laminate has a different stiffness value in each position. In the present thesis, VAT composite plate and shell structures with a linear fiber angle variation over the lamina are analyzed, see Fig. 3.3a, in which the expression given by Gürdal [199] is employed. It reads:

$$\theta(x') = \Phi + T_0 + \frac{(T_1 - T_0)}{d} |x'| \tag{3.9}$$

where the fiber path has a rotation of an angle Φ with respect to a certain reference direction placed at an arbitrary point O, see Fig. 3.3b. The fiber orientation angle at this point is T_0 and varies along a direction x' oriented by angle Φ from the original coordinate axis x. The fiber orientation assumes the value T_1 at a characteristic distance d from the reference point. By considering this rotation angle, the fiber orientation path

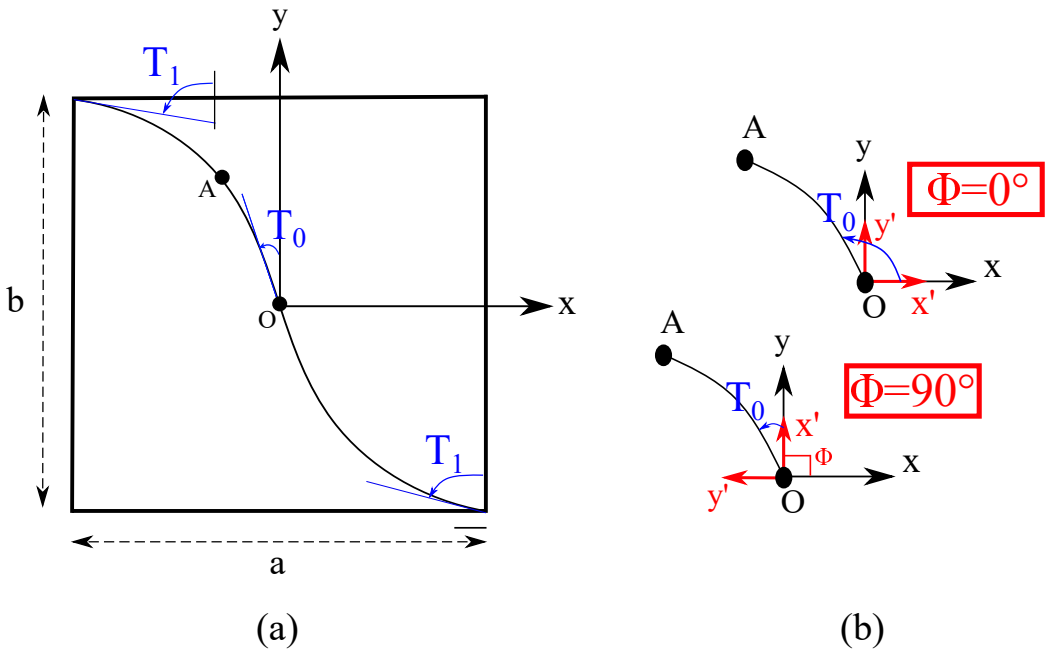

Fig. 3.3 Generic representation of a VAT model.

$\theta(x, y)$ can be formulated as $\theta(x')$, where $x' = x\,cos\Phi + y\,sin\Phi$. The parameter d is commonly equals to $a/2$ or $b/2$ when Φ= 0° or Φ= 90°, while a and b denote the width and length of the 2D structure.

It should be highlighted that, as a finite element approximation is used in this work, fibre angle is allowed to vary at each Gauss point in the plate or shell element. So, the FE arrays can be derived by integrating the material elastic coefficients coherently with the shape function approximation order. On the contrary, the lamination angle is assumed generally constant in the entire element domain in FE models of VAT structures modelled with commercial software. Therefore, the proposed methodology ensures a more accurate and efficient modelling and analysis of VAT structures [200].

3.2 Carrera Unified Formulation

The development of advanced models capable of addressing various structural analyses was a topic of great interest in the structural community for decades. In overcoming some of the aforementioned issues of classical theories, the CUF was introduced as a generator of structural theories for beams, plates and shells [40]. According to CUF, the

3D displacement field is described as follows:

$$\begin{aligned} &Beam: \quad \boldsymbol{u}^k(x,y,z;t) = F^k_\tau(x,z)\boldsymbol{u}^k_\tau(y;t), \qquad \tau = 1,\dots,M \\ &Plate: \quad \boldsymbol{u}^k(x,y,z;t) = F^k_\tau(z)\boldsymbol{u}^k_\tau(x,y;t), \qquad \tau = 1,\dots,M \\ &Shell: \quad \boldsymbol{u}^k(\alpha,\beta,z;t) = F^k_\tau(z)\boldsymbol{u}^k_\tau(\alpha,\beta;t), \qquad \tau = 1,\dots,M \end{aligned} \tag{3.10}$$

in which F_τ stands for a set of functions of the cross-section coordinates x and z for beams and thickness expansion functions for plate and shell models, respectively, $\boldsymbol{u}_\tau$ represents the generalized displacement vector, M denotes the order of the expansion, t indicates time and the repeated index τ stands for summation. In detail, the parameters F_τ and M are provided by the user as inputs and define the structural theory adopted in the model. Two classes of expansion functions have emerged in recent years as ideal choices due to their various capabilities: the Taylor Expansion (TE) and Lagrange Expansion (LE). When laminated composite structures are analyzed, the Layerwise (LW), based on the LE, and Equivalent-Single-Layer (ESL), using the TE, approaches are adopted. Note that the acronym LEN (LW) and TEN (ESL), used in this thesis, indicate LE and TE of order N assumed in the $x-z$ cross-section or z direction, respectively.

The TE class considers the Taylor series of the kind $x-z$ as cross-sectional or z as thickness expansion functions F_τ. This results in a hierarchical basis function, where the polynomial order N is user-defined. For instance, the first-order Taylor expansion (TE1) for 1D and 2D models is reported below:

$$\begin{aligned} &\text{1D}: \quad \begin{aligned} u_x &= u_{x_1} + xu_{x_2} + zu_{x_3} \\ u_y &= u_{y_1} + xu_{y_2} + zu_{y_3} \\ u_z &= u_{z_1} + xu_{z_2} + zu_{z_3} \end{aligned} \\ &\text{2D}: \quad \begin{aligned} u_x &= u_{x_1} + zu_{x_2} \\ u_y &= u_{y_1} + zu_{y_2} \\ u_z &= u_{z_1} + zu_{z_2} \end{aligned} \end{aligned} \tag{3.11}$$

Classical beam/plate/shell theories may be derived as special cases of the first-order theory by the selective removal of certain terms. For brevity, further details of TE class can be found in [43, 201].

LE models use Lagrange polynomials to build 1D and 2D higher-order theories and the isoparametric formulation is exploited to deals with arbitrary geometries. LE are

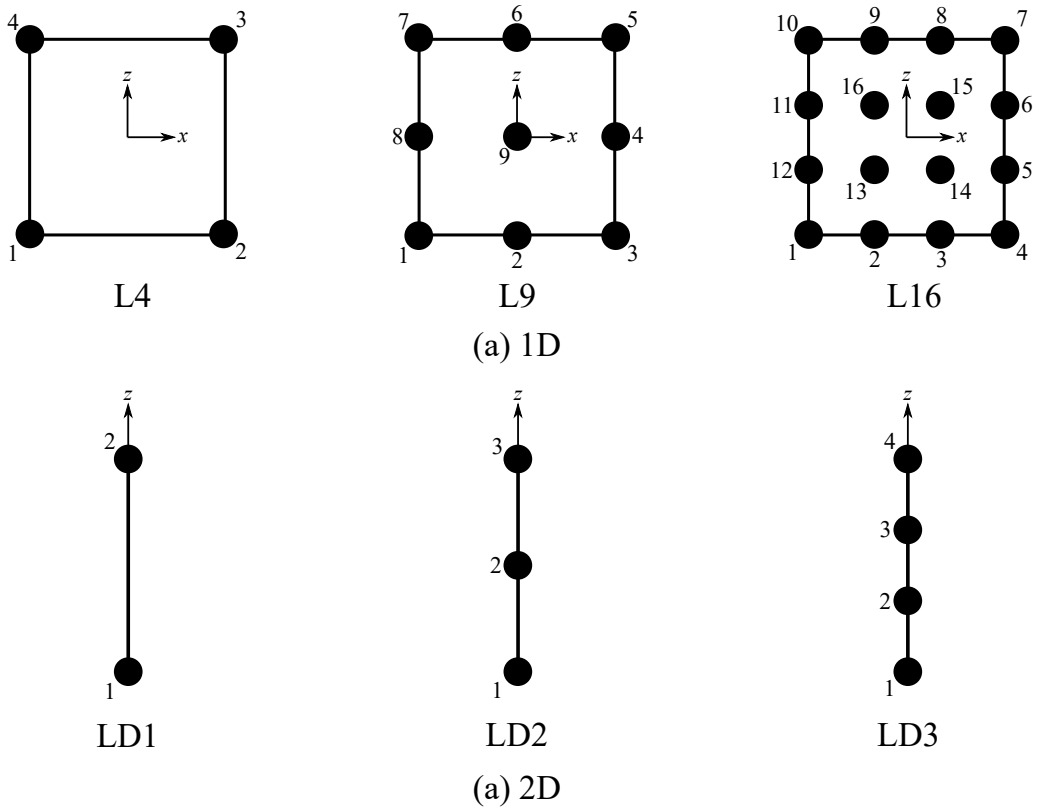

Fig. 3.4 Lagrange expansion on the (a) cross-section (1D) and (b) thickness (2D).

employed as F_τ functions over the cross-section for beams and thickness direction for plates and shells. In this work, three types of polynomial sets were employed for both 1D and 2D models, as shown in Fig. 3.4. In detail, four-point polynomials (L4), nine-point polynomials (L9), and sixteen-point polynomials (L16) were adopted to build linear to higher-order kinematics beam models. On the other hand, the acronym LDN (Lagrange expansion, Displacement-based theory with the order N) will be assumed to refer to specific refined plates or shells. For instance, LD1, LD2, and LD3 represent linear (two-node), quadratic (three-node), and cubic (four-node) Lagrange expansion functions, respectively. They are used in the z-direction in order to generate linear to higher-order kinematics CUF 2D models. For clarity, an illustrative example of the interpolation function is reported below for the case of an L9 beam model:

$$\begin{aligned} F_\tau &= \tfrac{1}{4}(r^2 + rr_\tau)(s^2 + ss_\tau) && \tau = 1,3,5,7 \\ F_\tau &= \tfrac{1}{2}s_\tau^2(s^2 - ss_\tau)(1 - r^2) + \tfrac{1}{2}r_\tau^2(r^2 - rr_\tau)(1 - s^2) && \tau = 2,4,6,8 \\ F_\tau &= (1 - r^2)(1 - s^2) && \tau = 9 \end{aligned} \tag{3.12}$$

in which r and s vary from -1 to +1, while r_τ and s_τ are the coordinates of the 9 points whose numbering and location in the natural coordinate frame are depicted in Fig. 3.4. LE use only displacement unknowns; i.e., it have only displacements as degrees of freedom [202]. This allows us to impose displacement continuity among components in a natural manner and without adopting mathematical artifices. In addition, the LE formulation was considered to implement the Component-Wise method [203–205]. In the CW domain, each component of the structure can be approximated independently via 1D models with higher-order approximation. Generally speaking, this approach divides the cross-section in different sub-domains, for example, stringers and panels, as reported in Fig 3.5.

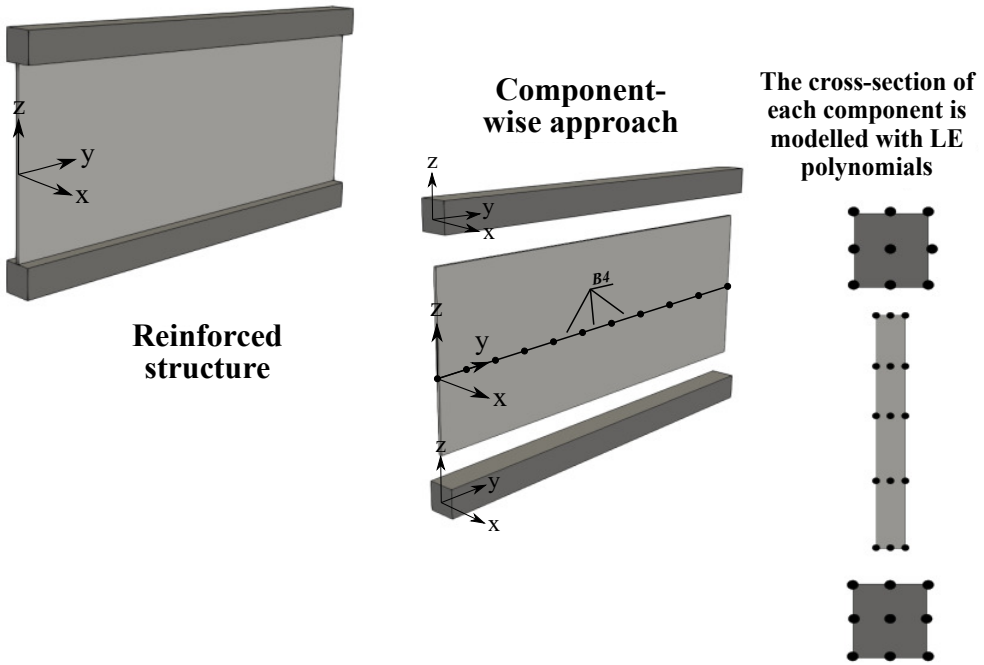

Fig. 3.5 A reinforced structure modelled using the CW approach.

As previously mentioned, ESL and LW approaches are typically employed when dealing with laminated structures. Considering the ESL approach, the cross-section is treated as a single domain in which the cross-sectional functions F_τ are defined and the stresses are computed considering the resulting strains in each layer in the displacement-based models. Therefore, the stiffness matrix is derived through the homogenization technique of the properties of each layer by summing the contributions of each layer. Due to the heterogeneity of multi-layered structures, ESL models lead to continuous transverse deformations across the thickness and discontinuous transverse stresses at the interfaces of the layers. Given such a defect, ESL models are still widely employed due to their intrinsic simplicity and fairly good performance. In detail, ESL theories show reliable

results of global responses (fundamental vibration frequencies, transverse deflections), but they are often inaccurate for 3D stress distribution evaluations. For clarity, Fig. 3.6a illustrates the general behaviour of the primary variables in the z-direction of a 2D (plate or shell) structure.

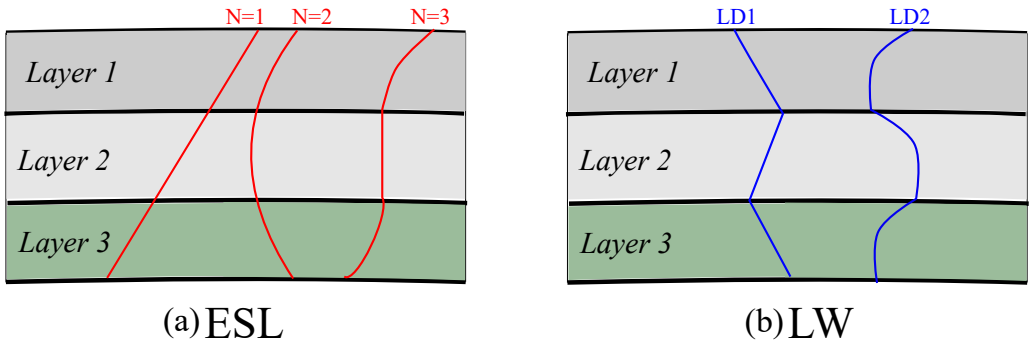

Fig. 3.6 (a) ESL and (b) LW behaviours of the primary variables through-the-thickness of a 2D model.

Differently, LW theories divide and expand the displacement field within each material layer. Therefore, the continuity of displacements is guaranteed at the interface level to accurately evaluate the deformation and stress distributions. In this way, the homogenization is performed at the interface layer. Then, by adopting LE, the displacements on each interpolation are assumed as unknowns, and displacements at each interface obey the compatibility conditions, as depicted in Fig. 3.6b [198]. For completeness, differences in the assembly procedure by using the ESL and LW for a 2D structure are reported in Fig. 3.7.

3.3 Finite Element Method

The FEM is employed to solve the structural problem due to its superior versatility compared to other analytical and numerical approaches [34]. Independently of the used beam, plate and shell model kinematics, the FEM is utilized to discretize the generalized displacement vector along the y-axis (beam) or in the $x-y$ (plate) or $\alpha-\beta$ (shell) plane, as follows:

$$\begin{aligned}
&Beam: \quad \boldsymbol{u}_\tau^k(y;t) = N_i(y)\boldsymbol{q}_{\tau i}^k(t), && i = 1,\ldots,N_n \\
&Plate: \quad \boldsymbol{u}_\tau^k(x,y;t) = N_i(x,y)\boldsymbol{q}_{\tau i}^k(t), && i = 1,\ldots,N_n \\
&Shell: \quad \boldsymbol{u}_\tau^k(\alpha,\beta;t) = N_i(\alpha,\beta)\boldsymbol{q}_{\tau i}^k(t), && i = 1,\ldots,N_n
\end{aligned} \tag{3.13}$$

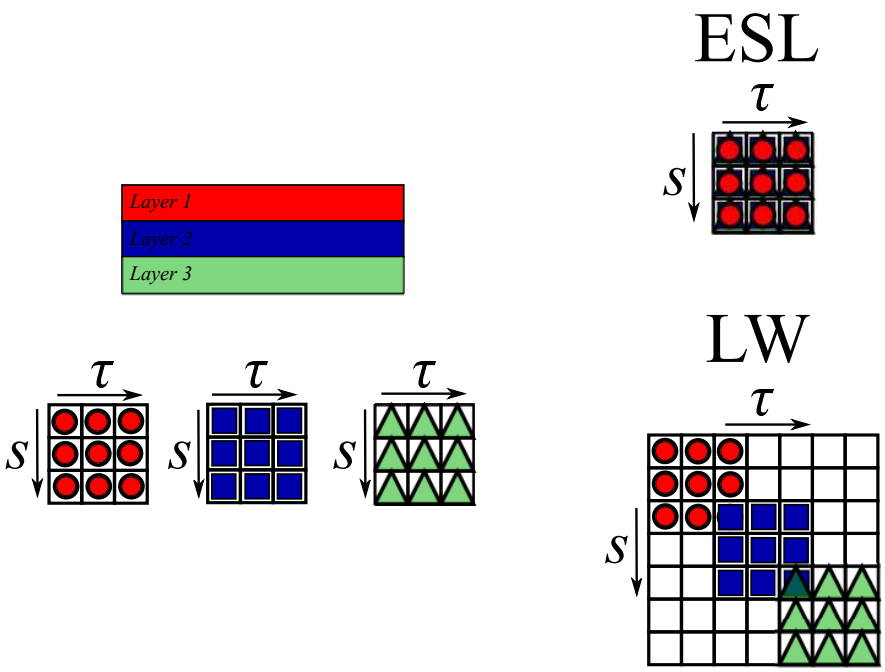

Fig. 3.7 Assembling technique of the stiffness matrix of the 2D model using ESL and LW methods. τ and s stand for the two indexes exploited to assemble the matrices.

where N_i denotes the shape functions, $\boldsymbol{q}_{\tau i}$ represents the unknown nodal variables, N_n stands for the number of nodes per element and the i indicates summation. In this research, classical 1D FEs with two (B2), three (B3) and four nodes (B4), i.e., linear, quadratic and cubic approximation along the beam axis, are employed, whereas the classical 2D FEs with four-node linear (Q4), nine-node quadratic (Q9) and sixteen-node cubic (Q16) are adopted for the shape functions in the $x-y$ or $\alpha-\beta$ plane.

For the sake of completeness, the CUF and FEM model approximation of typical 1D and 2D structures is illustrated in Fig. 3.8. Combining the FE approximation in Eq. 3.13 and CUF in EQ. 3.10, the 3D displacement field becomes:

$$
\begin{aligned}
&\textit{Beam}: \quad \boldsymbol{u}^k(x,y,z;t) = F^k_\tau(x,z)N_i(y)\boldsymbol{q}^k_\tau(t), \qquad \tau = 1,\dots,M \qquad i = 1,\dots,N_n \\
&\textit{Plate}: \quad \boldsymbol{u}^k(x,y,z;t) = F^k_\tau(z)N_i(x,y)\boldsymbol{q}^k_\tau(t), \qquad \tau = 1,\dots,M \qquad i = 1,\dots,N_n \\
&\textit{Shell}: \quad \boldsymbol{u}^k(\alpha,\beta,z;t) = F^k_\tau(z)N_i(\alpha,\beta)\boldsymbol{q}^k_\tau(t), \qquad \tau = 1,\dots,M \qquad i = 1,\dots,N_n
\end{aligned}
\tag{3.14}
$$

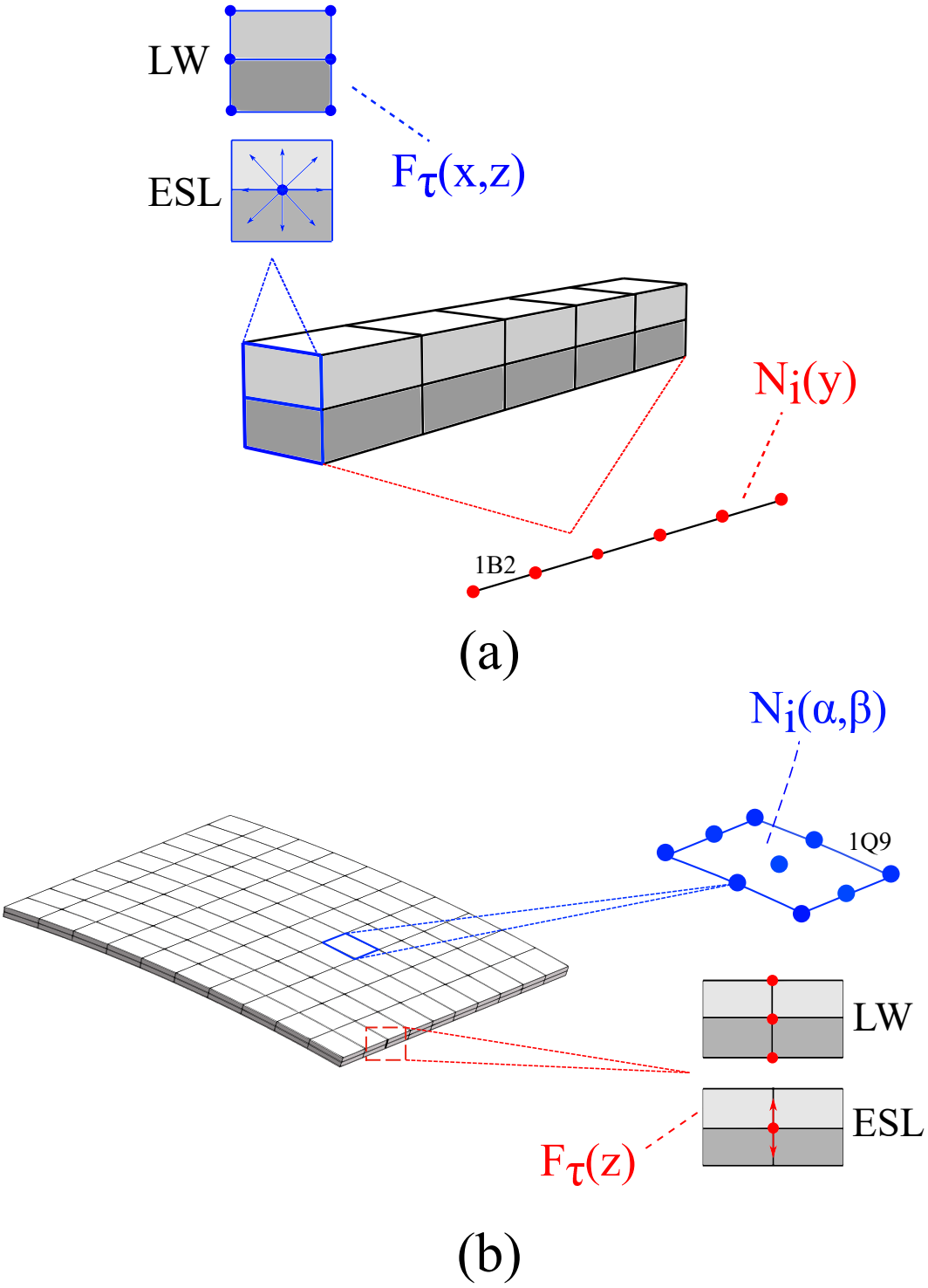

Fig. 3.8 CUF and FEM (a) 1D and (b) 2D model approximations.

Finally, by substituting the CUF (Eq. 3.10) and FEM (Eq. 3.13) equations into Eq. 3.4, the strain vector may be expressed as follows:

$$\boldsymbol{\epsilon}^k = (\boldsymbol{b}_l + \boldsymbol{b}_{nl})(F_\tau^k N_i)\boldsymbol{q}_{\tau i}^k = (\boldsymbol{B}_l^k + \boldsymbol{B}_{nl}^k)\boldsymbol{q}_{\tau i}^k \tag{3.15}$$

where $\boldsymbol{B}_l^k$ and $\boldsymbol{B}_{nl}^k$ stand for the linear and nonlinear algebraic matrices [206].

In the linear thermoelasticity, the elastic strain vector $\boldsymbol{\epsilon}_e^k$ is equal to:

$$\boldsymbol{\epsilon}_e^k = \boldsymbol{\epsilon}^k - \boldsymbol{\epsilon}_T^k \tag{3.16}$$

where $\boldsymbol{\epsilon}^k$ represents the total strain vector, see Eq. 3.15, and $\boldsymbol{\epsilon}_T^k$ is the strain vector due to the temperature change $\Delta T = \mathrm{T} - \mathrm{T}_0$, that is:

$$\boldsymbol{\epsilon}_T^k = \boldsymbol{\alpha}^k \Delta T \tag{3.17}$$

in which T_0 indicates the reference temperature and $\boldsymbol{\alpha}$ stands for the linear thermal expansion coefficients vector. Consequently, it is possible to define a new constitutive law given by:

$$\boldsymbol{\sigma}^k = \boldsymbol{\sigma}_H^k - \boldsymbol{\sigma}_T^k = \boldsymbol{C}^k\boldsymbol{\epsilon}^k - \boldsymbol{\beta}^k\Delta T \tag{3.18}$$

in which the subscript H indicates the quantities relating to Hooke's law, whereas T those relating to thermal deformation. In Eq. 3.18, $\boldsymbol{\beta}^k$ indicates the vector of the stress-temperature moduli. It reads:

$$\boldsymbol{\beta}^k = \boldsymbol{C}^k\boldsymbol{\alpha}^k \tag{3.19}$$

3.4 Nonlinear governing equations and explicit form of matrices

Consider elastic structures that undergo large displacements and rotations. To accurately assess the analysis in these structures, nonlinear analyses must be performed. Therefore, to derive the nonlinear governing equations of the elasticity problem, the PVD is used. It states that for all kinematically admissible virtual displacements, a body is in equilibrium if the virtual work done by the internal stresses and inertial loads equals to the work done by the external loads:

$$\delta L_{int} = \delta L_{ext} - \delta L_{ine} \tag{3.20}$$

where δL_{int}, δL_{ext} and δL_{ine} represent the virtual variation of the strain energy, the virtual variation of the work of external loads and the virtual variation of the inertia loads. Their expressions are given in the explicit form below. The virtual variation of the strain energy is:

$$\begin{aligned}\delta L_{int} &= \int_V \delta {\boldsymbol{\epsilon}^k}^{\mathrm{T}} \boldsymbol{\sigma}^k \, dV = \int_V \delta {\boldsymbol{\epsilon}^k}^{\mathrm{T}} \boldsymbol{C}^k \boldsymbol{\epsilon}^k \, dV = \int_V \delta {\boldsymbol{q}_{sj}^k}^{\mathrm{T}} (\boldsymbol{B}_l^k + 2\boldsymbol{B}_{nl}^k)^{\mathrm{T}} \boldsymbol{C}^k (\boldsymbol{B}_l^k + \boldsymbol{B}_{nl}^k) \boldsymbol{q}_{\tau i}^k \, dV = \\ &= \delta {\boldsymbol{q}_{sj}^k}^{\mathrm{T}} \boldsymbol{K}_0^{ij\tau s k} \boldsymbol{q}_{\tau i}^k + \delta {\boldsymbol{q}_{sj}^k}^{\mathrm{T}} \boldsymbol{K}_{lnl}^{ij\tau s k} \boldsymbol{q}_{\tau i}^k + \delta {\boldsymbol{q}_{sj}^k}^{\mathrm{T}} \boldsymbol{K}_{nll}^{ij\tau s k} \boldsymbol{q}_{\tau i}^k + \delta {\boldsymbol{q}_{sj}^k}^{\mathrm{T}} \boldsymbol{K}_{nlnl}^{ij\tau s k} \boldsymbol{q}_{\tau i}^k \\ &= \delta {\boldsymbol{q}_{sj}^k}^{\mathrm{T}} \boldsymbol{K}_S^{ij\tau s k} \boldsymbol{q}_{\tau i}^k \end{aligned} \tag{3.21}$$

where V is the volume of the body, $\boldsymbol{K}_S^{ij\tau s k}$ represents the secant stiffness matrix, $\boldsymbol{K}_0^{ij\tau s k}$ indicates the linear contribution of $\boldsymbol{K}_S^{ij\tau s k}$ and $\boldsymbol{K}_{lnl}^{ij\tau s k}$, $\boldsymbol{K}_{nll}^{ij\tau s k}$ and $\boldsymbol{K}_{nlnl}^{ij\tau s k}$ are the nonlinear components of order 1 and 2, respectively. In detail, they read:

$$\begin{aligned} \boldsymbol{K}_0^{ij\tau s k} &= \int_V \boldsymbol{B}_l^{k\,\mathrm{T}} \boldsymbol{C}^k \boldsymbol{B}_l^k \, dV \\ \boldsymbol{K}_{lnl}^{ij\tau s k} &= \int_V \boldsymbol{B}_l^{k\,\mathrm{T}} \boldsymbol{C}^k \boldsymbol{B}_{nl}^k \, dV \\ \boldsymbol{K}_{nll}^{ij\tau s k} &= 2 \int_V \boldsymbol{B}_{nl}^{k\,\mathrm{T}} \boldsymbol{C}^k \boldsymbol{B}_l^k \, dV \\ \boldsymbol{K}_{nll}^{ij\tau s k} &= 2 \int_V \boldsymbol{B}_{nl}^{k\,\mathrm{T}} \boldsymbol{C}^k \boldsymbol{B}_{nl}^k \, dV \end{aligned} \tag{3.22}$$

These components are expressed in the form of CUF 3×3 *FNs*. The *FN*s are independent of the theory approximation and may be expanded against F_τ approximation (τ, $s = 1$, ... ,M) and N_i shape functions (i, $j = 1$, ... ,N_n) to derive the final stiffness matrix of any higher-order model. The superscripts i, j, τ, s stand for the four indexes exploited to assemble the matrices. Figure 3.9 depicts the CUF assembly technique to build a matrix of the node, of the element and, finally, the global stiffness matrix $\boldsymbol{K}_S$ by exploiting the *FNs*. For completeness, the nine component of the 3×3 *FN* of the $\boldsymbol{K}_0^{ij\tau s k}[r, c]$ for a plate model are provided below, where r and c denote the row and column number (r,c = 1,2,3), respectively. Although derivation is made for plate models below, it should be emphasized that similar relations hold for beam and shell models. For clarity, the

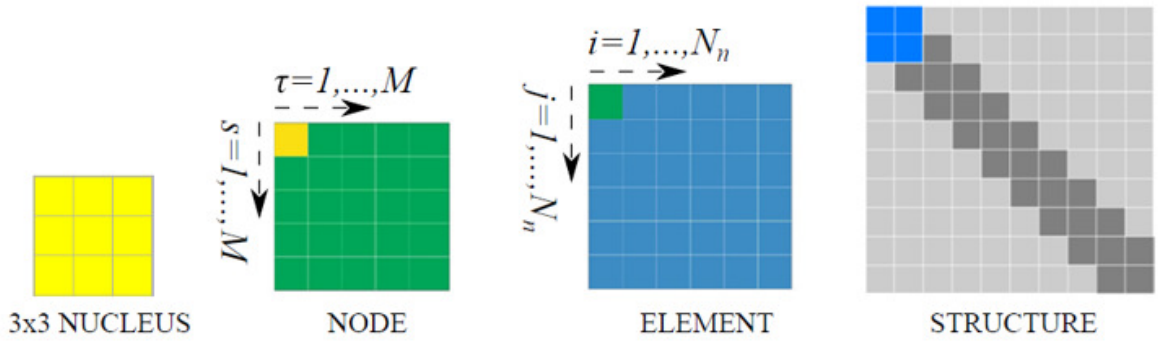

Fig. 3.9 CUF assembly technique.

superscript k was omitted and $< (\cdot) >= \int_V (\cdot)\, dV$.

$$
\begin{aligned}
\boldsymbol{K}_0^{ij\tau s}[1,1] &= < C_{11} F_\tau F_s N_{i,_x} N_{j,_x} > + < C_{44} F_{\tau,_z} F_{s,_z} N_i N_j > + < C_{66} F_\tau F_s N_{i,_y} N_{j,_y} > \\
\boldsymbol{K}_0^{ij\tau s}[1,2] &= < C_{66} F_\tau F_s N_{i,_y} N_{j,_x} > + < C_{12} F_\tau F_s N_{i,_x} N_{j,_y} > \\
\boldsymbol{K}_0^{ij\tau s}[1,3] &= < C_{13} F_\tau F_{s,_z} N_{i,_x} N_j > + < C_{44} F_{\tau,_z} F_s N_i N_{j,_x} > \\
\boldsymbol{K}_0^{ij\tau s}[2,1] &= < C_{12} F_\tau F_s N_{i,_y} N_{j,_x} > + < C_{66} F_\tau F_s N_{i,_x} N_{j,_y} > \\
\boldsymbol{K}_0^{ij\tau s}[2,2] &= < C_{66} F_\tau F_s N_{i,_x} N_{j,_x} > + < C_{55} F_{\tau,_z} F_{s,_z} N_i N_j > + < C_{22} F_\tau F_s N_{i,_y} N_{j,_y} > \\
\boldsymbol{K}_0^{ij\tau s}[2,3] &= < C_{23} F_\tau F_{s,_z} N_{i,_y} N_j > + < C_{55} F_{\tau,_z} F_s N_i N_{j,_y} > \\
\boldsymbol{K}_0^{ij\tau s}[3,1] &= < C_{44} F_\tau F_{s,_z} N_{i,_x} N_j > + < C_{13} F_{\tau,_z} F_s N_i N_{j,_x} > \\
\boldsymbol{K}_0^{ij\tau s}[3,2] &= < C_{55} F_\tau F_{s,_z} N_{i,_y} N_j > + < C_{23} F_{\tau,_z} F_s N_i N_{j,_y} > \\
\boldsymbol{K}_0^{ij\tau s}[3,3] &= < C_{44} F_\tau F_s N_{i,_x} N_{j,_x} > + < C_{33} F_{\tau,_z} F_{s,_z} N_i N_j > + < C_{55} F_\tau F_s N_{i,_y} N_{j,_y} >
\end{aligned}
\tag{3.23}
$$

Similarly, the components of the *FN* of $\boldsymbol{K}_{nll}^{ij\tau s^k}[r,c]$ are:

$$
\begin{aligned}
\boldsymbol{K}_{nll}^{ij\tau s}[r,1] &= <\boldsymbol{u}_{,x}[r]C_{11}F_\tau F_s N_{i,_x}N_{j,_x}> + <\boldsymbol{u}_{,x}[r]C_{44}F_{\tau,_z}F_{s,_z}N_iN_j> + \\
&+ <\boldsymbol{u}_{,x}[r]C_{66}F_\tau F_s N_{i,_y}N_{j,_y}> + <\boldsymbol{u}_{,y}[r]C_{66}F_\tau F_s N_{i,_x}N_{j,_y}> + \\
&+ <\boldsymbol{u}_{,x}[r]C_{12}F_\tau F_s N_{i,_y}N_{j,_x}> + <\boldsymbol{u}_{,z}[r]C_{44}F_\tau F_{s,_z}N_{i,_x}N_j> + \\
&+ <\boldsymbol{u}_{,z}[r]C_{13}F_{\tau,_z}F_s N_iN_{j,_x}> \\
\boldsymbol{K}_{nll}^{ij\tau s}[r,2] &= <\boldsymbol{u}_{,x}[r]C_{12}F_\tau F_s N_{i,_x}N_{j,_y}> + <\boldsymbol{u}_{,x}[r]C_{66}F_\tau F_s N_{i,_y}N_{j,_x}> + \\
&+ <u_{,y}[r]C_{66}F_\tau F_s N_{i,_x}N_{j,_x}> + <\boldsymbol{u}_{,y}[r]C_{55}F_{\tau,_z}F_{s,_z}N_iN_j> + \\
&+ <\boldsymbol{u}_{,y}[r]C_{22}F_\tau F_s N_{i,_y}N_{j,_y}> + <\boldsymbol{u}_{,z}[r]C_{23}F_{\tau,_z}F_s N_iN_{j,_y}> + \\
&+ <\boldsymbol{u}_{,z}[r]C_{55}F_\tau F_{s,_z}N_{i,_y}N_j> \\
\boldsymbol{K}_{nll}^{ij\tau s}[r,3] &= <\boldsymbol{u}_{,x}[r]C_{13}F_\tau F_{s,_z}N_{i,_x}N_j> + <\boldsymbol{u}_{,x}[r]C_{44}F_{\tau,_z}F_s N_iN_{j,_x}> + \\
&+ <\boldsymbol{u}_{,y}[r]C_{55}F_{\tau,_z}F_s N_iN_{j,_y}> + <\boldsymbol{u}_{,y}[r]C_{23}F_\tau F_{s,_z}N_{i,_y}N_j> + \\
&+ <\boldsymbol{u}_{,z}[r]C_{44}F_\tau F_s N_{i,_x}N_{j,_x}> + <u_{,z}[r]C_{33}F_{\tau,_z}F_{s,_z}N_iN_j> + \\
&+ <\boldsymbol{u}_{,z}[r]C_{55}F_\tau F_s N_{i,_y}N_{j,_y}>
\end{aligned}
\tag{3.24}
$$

where $\boldsymbol{u}_{,x}[r]$ represents the r-th component of vector $\frac{\delta \boldsymbol{u}}{\delta x}$; for example, $\boldsymbol{u}_{,x}[2] = u_{y,_x}$. The same applies to $\boldsymbol{u}_{,y}[r]$ and $\boldsymbol{u}_{,z}[r]$. The components of $\boldsymbol{K}_{lnl}^{ij\tau s^k}[r,c]$ are not written here, but they are easily derived from $\boldsymbol{K}_{nll}^{ij\tau s^k}[r,c]$. In fact, it is evident from Eq. 3.22 that $\left(\boldsymbol{K}_{lnl}^{ij\tau s^k}\right)^{\mathrm{T}} = \frac{1}{2}\boldsymbol{K}_{nll}^{ij\tau s^k}$. Finally, the generic component $[r,c]$ of the matrix $\boldsymbol{K}_{nlnl}^{ij\tau s^k}$ is

written as:

$$
\begin{aligned}
2 \times \boldsymbol{K}^{ij\tau s}_{nlnl}[r,c] \; = & < \boldsymbol{u}_{,x}[r]\boldsymbol{u}_{,x}[c]C_{11}F_\tau F_s N_{i,_x}N_{j,_x} > + < \boldsymbol{u}_{,x}[r]\boldsymbol{u}_{,x}[c]C_{44}F_{\tau,_z}F_{s,_z}N_iN_j > + \\
& + < \boldsymbol{u}_{,x}[r]\boldsymbol{u}_{,x}[c]C_{66}F_\tau F_s N_{i,_y}N_{j,_y} > + < \boldsymbol{u}_{,y}[r]\boldsymbol{u}_{,y}[c]C_{66}F_\tau F_s N_{i,_x}N_{j,_x} > + \\
& + < \boldsymbol{u}_{,y}[r]\boldsymbol{u}_{,y}[c]C_{55}F_{\tau,_z}F_{s,_z}N_iN_j > + < \boldsymbol{u}_{,y}[r]\boldsymbol{u}_{,y}[c]C_{22}F_\tau F_s N_{i,_y}N_{j,_y} > + \\
& + < \boldsymbol{u}_{,z}[r]\boldsymbol{u}_{,z}[c]C_{44}F_\tau F_s N_{i,_x}N_{j,_x} > + < \boldsymbol{u}_{,z}[r]\boldsymbol{u}_{,z}[c]C_{33}F_{\tau,_z}F_{s,_z}N_iN_j > + \\
& + < \boldsymbol{u}_{,z}[r]\boldsymbol{u}_{,z}[c]C_{55}F_\tau F_s N_{i,_y}N_{j,_y} > + < \boldsymbol{u}_{,x}[r]\boldsymbol{u}_{,y}[c]C_{12}F_\tau F_s N_{i,_x}N_{j,_y} > + \\
& + < \boldsymbol{u}_{,x}[r]\boldsymbol{u}_{,y}[c]C_{66}F_\tau F_s N_{i,_y}N_{j,_x} > + < \boldsymbol{u}_{,y}[r]\boldsymbol{u}_{,x}[c]C_{12}F_\tau F_s N_{i,_y}N_{j,_x} > + \\
& + < \boldsymbol{u}_{,y}[r]\boldsymbol{u}_{,x}[c]C_{66}F_\tau F_s N_{i,_x}N_{j,_y} > + < \boldsymbol{u}_{,x}[r]\boldsymbol{u}_{,z}[c]C_{13}F_\tau F_{s,_z}N_{i,_x}N_j > + \\
& + < \boldsymbol{u}_{,x}[r]\boldsymbol{u}_{,z}[c]C_{44}F_{\tau,_z}F_s N_iN_{j,_x} > + < \boldsymbol{u}_{,z}[r]\boldsymbol{u}_{,x}[c]C_{13}F_{\tau,_z}F_s N_iN_{j,_x} > + \\
& + < \boldsymbol{u}_{,z}[r]\boldsymbol{u}_{,x}[c]C_{44}F_\tau F_{s,_z}N_{i,_x}N_j > + < \boldsymbol{u}_{,y}[r]\boldsymbol{u}_{,z}[c]C_{23}F_\tau F_{s,_z}N_{i,_y}N_j > + \\
& + < \boldsymbol{u}_{,y}[r]\boldsymbol{u}_{,z}[c]C_{55}F_{\tau,_z}F_s N_iN_{j,_y} > + < \boldsymbol{u}_{,z}[r]\boldsymbol{u}_{,y}[c]C_{55}F_\tau F_{s,_z}N_{i,_y}N_j > + \\
& + < \boldsymbol{u}_{,z}[r]\boldsymbol{u}_{,y}[c]C_{23}F_{\tau,_z}F_s N_iN_{j,_y} >
\end{aligned}
\tag{3.25}
$$

Following the structure of the derivation of the virtual internal strain energy, the virtual variation of the inertial loads may be defined as:

$$
\delta L_{ine} = \int_V \delta \boldsymbol{u}^{k\,\mathrm{T}} \rho \ddot{\boldsymbol{u}}^k \, dV = \delta \boldsymbol{q}^{k\,\mathrm{T}}_{sj} \boldsymbol{M}^{ij\tau s k} \ddot{\boldsymbol{q}}^k_{\tau i} \tag{3.26}
$$

where $\boldsymbol{M}^{ij\tau s k}$ indicates the *FN* of the mass matrix, that is assumed to be linear, ρ denotes the material density, $\ddot{\boldsymbol{q}}^k_{\tau i}$ stands for the nodal acceleration vector and the dot indicates $\delta/\delta t$. The matrix $\boldsymbol{M}^{ij\tau s k}$ only has three components on the diagonal that are not zero, whereas the ones outside the diagonal are null.

$$
\boldsymbol{M}^{ij\tau s k} = \int_v N_j F^k_s \rho N_i F^k_\tau \, dV \tag{3.27}
$$

The *FNs* will be expanded with respect to the indices τ, s, i, j in order to build the global mass matrix $\boldsymbol{M}$.

The virtual variation of the work due to external loads is defined as:

$$\begin{aligned}\delta L_{ext} &= \textstyle\int_V \delta\boldsymbol{u}^{\mathrm{T}}\boldsymbol{g}\, dV + \int_S \delta\boldsymbol{u}^{\mathrm{T}}\boldsymbol{b}\, dS + \int_l \delta\boldsymbol{u}^{\mathrm{T}}\boldsymbol{r}\, dl + \delta\boldsymbol{u}^{\mathrm{T}}P_m = \\ &= \delta\boldsymbol{q}_{sj}^{\mathrm{T}}\left(\textstyle\int_V N_i F_\tau \boldsymbol{g}\, dV + \int_S N_i F_\tau \boldsymbol{b}\, dS + \int_l N_i F_\tau \boldsymbol{r}\, dl + N_i F_\tau P_m\right) = \\ &= \delta\boldsymbol{q}_{sj}^{\mathrm{T}}\boldsymbol{p}_{sj}\end{aligned} \tag{3.28}$$

in which $\boldsymbol{g}$ is the body force acting on the volume V, $\boldsymbol{b}$ is the surface force acting on the surface S, $\boldsymbol{r}$ is the line force acting on a line l, and P_m is a point force acting at a point m. $\boldsymbol{p}_{sj}$ stands for the *FN* of the external equivalent nodal force vector. After the assembly operation, the global external nodal force vector $\boldsymbol{F}$ is obtained.

By substituting Eqs. 3.21, 3.26, and 3.28 into Eq. 3.20, after simple mathematical operations, considering undamped problems and the mass matrix constant, the nonlinear governing equations of the elasticity problem read as:

$$\boldsymbol{M}\ddot{\boldsymbol{q}}(t) + \boldsymbol{K_S}\boldsymbol{q}(t) = \boldsymbol{F}(t) \tag{3.29}$$

The governing equations of the elasticity problem expressed in Eq. 3.29 are now separately considered in the next chapter for geometrically nonlinear static analysis, free vibration analysis around nonlinear equilibrium states and dynamic response analysis.

Chapter 4

Nonlinear static and dynamic formulations

The governing differential equations are expressed by substituting the explicit expressions of the virtual variations of the internal, inertial and external works into the PVD. Several problems are studied and they are derived as particular cases of Eq. 3.29. For clarity, although derivation is performed for plate models in this chapter, it should be underlined that similar relations hold for beam and shell ones.

4.1 Geometrically nonlinear static analysis

When static structural analyses are performed, the contribution of the virtual work of inertial loadings is neglected in the PVD. Hence:

$$\delta L_{int} = \delta L_{ext} \tag{4.1}$$

As a result, after some mathematical operations, the nonlinear static equilibrium equations in a compact vectorial form read as:

$$\boldsymbol{K}_S \boldsymbol{q} - \boldsymbol{F} = 0 \tag{4.2}$$

4.1.1 Tangent stiffness matrix

As far as the tangent stiffness matrix $\boldsymbol{K}_T^{ij\tau s^k}$ is concerned, the linearization of the equilibrium equations has to be performed. Conservative loadings are assumed in this research so that the linearization of the work made by the external loads is null. As a

consequence, the linearization of the internal loads is performed as follows:

$$\begin{aligned}
\delta(\delta L_{int}) &= \textstyle\int_V \delta(\delta{\boldsymbol{\epsilon}^k}^{\mathrm{T}}\boldsymbol{\sigma}^k)\, dV = \int_V(\delta{\boldsymbol{\epsilon}^k}^{\mathrm{T}}\delta\boldsymbol{\sigma}^k) + (\delta(\delta\boldsymbol{\epsilon}^{\mathrm{T}})\boldsymbol{\sigma}^k)\, dV = \\
&= \delta{\boldsymbol{q}_{sj}^k}^{\mathrm{T}} \textstyle\int_V(\boldsymbol{B}_l^k + 2\boldsymbol{B}_{nl}^k)^{\mathrm{T}}\boldsymbol{C}^k(\boldsymbol{B}_l^k + \boldsymbol{B}_{nl}^k)\, dV\delta\boldsymbol{q}_{\tau i}^k + \delta{\boldsymbol{q}_{sj}^k}^{\mathrm{T}} \textstyle\int_V {\boldsymbol{B}_{nl}^*}^{k\mathrm{T}}\boldsymbol{\sigma}^k\, dV\ \delta\boldsymbol{q}_{\tau i}^k = \\
&= \delta{\boldsymbol{q}_{sj}^k}^{\mathrm{T}}(\boldsymbol{K}_0^{ij\tau s k} + 2\boldsymbol{K}_{lnl}^{ij\tau s k} + \boldsymbol{K}_{nll}^{ij\tau s k} + 2\boldsymbol{K}_{nlnl}^{ij\tau s k} + \boldsymbol{K}_{\sigma}^{ij\tau s k})\delta\boldsymbol{q}_{\tau i}^k = \\
&= \delta{\boldsymbol{q}_{sj}^k}^{\mathrm{T}}(\boldsymbol{K}_0^{ij\tau s k} + \boldsymbol{K}_{T1}^{ij\tau s k} + \boldsymbol{K}_{\sigma}^{ij\tau s k})\delta\boldsymbol{q}_{\tau i}^k = \\
&= \delta{\boldsymbol{q}_{sj}^k}^{\mathrm{T}}\boldsymbol{K}_T^{ij\tau s k}\delta\boldsymbol{q}_{\tau i}^k
\end{aligned} \tag{4.3}$$

in which $\boldsymbol{K}_{T1}^{ij\tau s k} = 2\boldsymbol{K}_{lnl}^{ij\tau s k} + \boldsymbol{K}_{nll}^{ij\tau s k} + 2\boldsymbol{K}_{nlnl}^{ij\tau s k}$ stands for the nonlinear contribution of the *FN* of the tangent stiffness matrix due to the linearization of the Hooke's law, $\boldsymbol{K}_0^{ij\tau s k}$ indicates the linear component of the $\boldsymbol{K}_T^{ij\tau s k}$ and $\boldsymbol{K}_{\sigma}^{ij\tau s k} = \boldsymbol{K}_{\sigma_l}^{ij\tau s k} + \boldsymbol{K}_{\sigma_{nl}}^{ij\tau s k}$ represents the so-called geometric stiffness matrix. The complete expression of the matrix ${\boldsymbol{B}_{nl}^*}^k$ is provided below. For clarity, the superscript k was omitted.

$$\boldsymbol{B}_{nl}^* = \begin{bmatrix}
F_\tau F_s N_{i,x} N_{j,x} & F_\tau F_s N_{i,x} N_{j,x} & F_\tau F_s N_{i,x} N_{j,x} \\
F_\tau F_s N_{i,y} N_{j,y} & F_\tau F_s N_{i,y} N_{j,y} & F_\tau F_s N_{i,y} N_{j,y} \\
F_{\tau,z} F_{s,z} N_i N_j & F_{\tau,z} F_{s,z} N_i N_j & F_{\tau,z} F_{s,z} N_i N_j \\
F_\tau F_{s,z} N_{i,x} N_j + F_{\tau,z} F_s N_i N_{j,x} & F_\tau F_{s,z} N_{i,x} N_j + F_{\tau,z} F_s N_i N_{j,x} & F_\tau F_{s,z} N_{i,x} N_j + F_{\tau,z} F_s N_i N_{j,x} \\
F_{\tau,z} F_s N_i N_{j,y} + F_\tau F_{s,z} N_{i,y} N_j & F_{\tau,z} F_s N_i N_{j,y} + F_\tau F_{s,z} N_{i,y} N_j & F_{\tau,z} F_s N_i N_{j,y} + F_\tau F_{s,z} N_{i,y} N_j \\
F_\tau F_s N_{i,x} N_{j,y} + F_\tau F_s N_{i,y} N_{j,x} & F_\tau F_s N_{i,x} N_{j,y} + F_\tau F_s N_{i,y} N_{j,x} & F_\tau F_s N_{i,x} N_{j,y} + F_\tau F_s N_{i,y} N_{j,x}
\end{bmatrix} \tag{4.4}$$

For completeness, the $\boldsymbol{K}_{\sigma}^{ij\tau s^k}$ contribution in terms of FN is expressed as follows:

$$\begin{aligned}\boldsymbol{K}_{\sigma}^{ij\tau s^k} = \int_V (&\sigma_{xx}^k F_{\tau}^k F_s^k N_{i,x} N_{j,x} + \sigma_{yy}^k F_{\tau}^k F_s^k N_{i,y} N_{j,y} + \sigma_{zz}^k F_{\tau,z}^k F_{s,z}^k N_i N_j + \sigma_{xy}^k F_{\tau}^k F_s^k N_{i,x} N_{j,y} + \\ &+\sigma_{xy}^k F_{\tau}^k F_s^k N_{i,y} N_{j,x} + \sigma_{xz}^k F_{\tau}^k F_{s,z}^k N_{i,x} N_j + +\sigma_{xz}^k F_{\tau,z}^k F_s^k N_i N_{j,x} + \sigma_{yz}^k F_{\tau,z}^k F_s^k N_i N_{j,y} + \\ &+\sigma_{yz}^k F_{\tau}^k F_{s,z}^k N_{i,y} N_j) \boldsymbol{I}\, dV\end{aligned} \tag{4.5}$$

where $\boldsymbol{I}$ denotes the 3×3 identity matrix.

4.1.2 Newton-Raphson linearization scheme

In this research, geometrical nonlinear equations are expressed in a TL framework and computed with a NR linearization scheme based on the arc-length constraint [207]. The NR-based solution algorithms are the most commonly employed routines for solving nonlinear problems. They are iterative solution schemes and can be used under either displacement, load control or sophisticated numerical procedure. According to the NR approach, Eq. 4.2 is written as:

$$\boldsymbol{\varphi}_{res} = \boldsymbol{K}_S \boldsymbol{q} - \boldsymbol{F} = 0 \tag{4.6}$$

in which $\boldsymbol{\varphi}_{res}$ denotes the vector of the residual nodal forces (unbalanced nodal force vector). Equation 4.6 may be linearized by expanding $\boldsymbol{\varphi}_{res}$ in Taylor's series about a known solution $(\boldsymbol{q}, \boldsymbol{F})$. It reads:

$$\boldsymbol{\varphi}_{res}(\boldsymbol{q} + \delta\boldsymbol{q}, \boldsymbol{F} + \delta\boldsymbol{F}) = \boldsymbol{\varphi}_{res}(\boldsymbol{q}, \boldsymbol{F}) + \frac{\partial \boldsymbol{\varphi}_{res}}{\partial \boldsymbol{q}} \delta\boldsymbol{q} + \frac{\partial \boldsymbol{\varphi}_{res}}{\partial \boldsymbol{F}} \delta\lambda \boldsymbol{F}_{ref} = 0 \tag{4.7}$$

where $\frac{\partial \boldsymbol{\varphi}_{res}}{\partial \boldsymbol{q}} = \boldsymbol{K}_T$, $-\frac{\partial \boldsymbol{\varphi}_{res}}{\partial \boldsymbol{F}}$ stands for the matrix $\boldsymbol{I}$ and it was assumed that the load varies directly with the vector of the reference loadings $\boldsymbol{F}_{ref}$, that it has a rate of change equal to the load parameter λ, i.e., $\boldsymbol{F} = \lambda \boldsymbol{F}_{ref}$. For clarity, the reference loading represents the initial load value. Therefore, we can rewrite in compact form:

$$\boldsymbol{K}_T \delta\boldsymbol{q} = \delta\lambda \boldsymbol{F}_{ref} - \boldsymbol{\varphi}_{res} \tag{4.8}$$

Since the load-scaling parameter, λ, is considered a variable, an additional governing equation is required and this is provided by a constraint relationship $c(\delta\boldsymbol{q}, \delta\lambda)$ to give

the final system as:

$$\begin{cases} \boldsymbol{K}_T \delta \boldsymbol{q} = \delta\lambda \boldsymbol{F}_{ref} - \boldsymbol{\varphi}_{res} \\ c(\delta \boldsymbol{q}, \delta\lambda) = 0 \end{cases} \tag{4.9}$$

Different incremental methods may be implemented depending on the constraint equation assumed. For instance, one can impose the condition $\delta\lambda = 0$ or $\delta\boldsymbol{q} = 0$, corresponding to the load-control and displacement-control methods. However, these methods fail in the presence of highly nonlinear behaviours, e.g., snap-through or snap-back behaviour. In the present thesis, a method of a path-following type based on the arc-length scheme is implemented, and the constraint condition involves both displacement and load parameters.

The path-following constraint was employed for the first time in the CUF by Pagani and Carrera [208]. The details, along with the adopted notation, of the path-following constraint method are shown in Fig. 4.1. In detail:

- $\delta^n_m(\cdot)$ indicates the finite variation, where m is the number of reached load step and n the iteration within the m^{th} load step. It can be stated that $\delta^n_m(\cdot) = (\cdot)^n_m - (\cdot)^{n-1}_m$ and $(\cdot)_m = (\cdot)_{m-1} + \sum_n \delta^n_m(\cdot)$;
- $n = 0$ represents the initial condition, so that $\delta^0_m \boldsymbol{q}$ is the initial linear solution and $\delta^0_m \lambda$ denotes the initial increment of the load parameter;
- $\boldsymbol{\varphi}^n_{m_{res}}$ indicates the vector of the residual nodal forces at the n^{th} iteration (of the m^{th} load step).
- $\boldsymbol{t}^n_m = \boldsymbol{t}^{n-1}_m + \delta^n_m \boldsymbol{t} = \boldsymbol{t}^{n-1}_m + (\delta^n_m \boldsymbol{q} + \delta^n_m \lambda\, \boldsymbol{F}_{ref})$ relates the current solution to the previous one.

Consequently, the equilibrium reached at each iteration is obtained by the intersection of the linearized governing equation and the constraint equation $c(\delta\boldsymbol{q}, \delta\lambda) = 0$. The arc-length method as developed by Crisfield [209] is used. Thus, the initial arc-length value Δl^0_m is equal to the radius of a sphere, representing the constraint relationship. It means that $|\boldsymbol{t}^n_m|$ is equal to the square of the arc-length. Therefore, the system of equation expressed in Eq. 4.9 becomes:

$$\begin{cases} \boldsymbol{K}_T\, \delta^n_m \boldsymbol{q} = \delta^n_m \lambda\, \boldsymbol{F}_{ref} - \boldsymbol{\varphi}^n_{m_{res}} \\ \\ \boldsymbol{t}^{n^T}_m \boldsymbol{t}^n_m = (\Delta l^0_m)^2 \end{cases} \tag{4.10}$$

This procedure would require the inversion of the tangent stiffness matrix, which could be

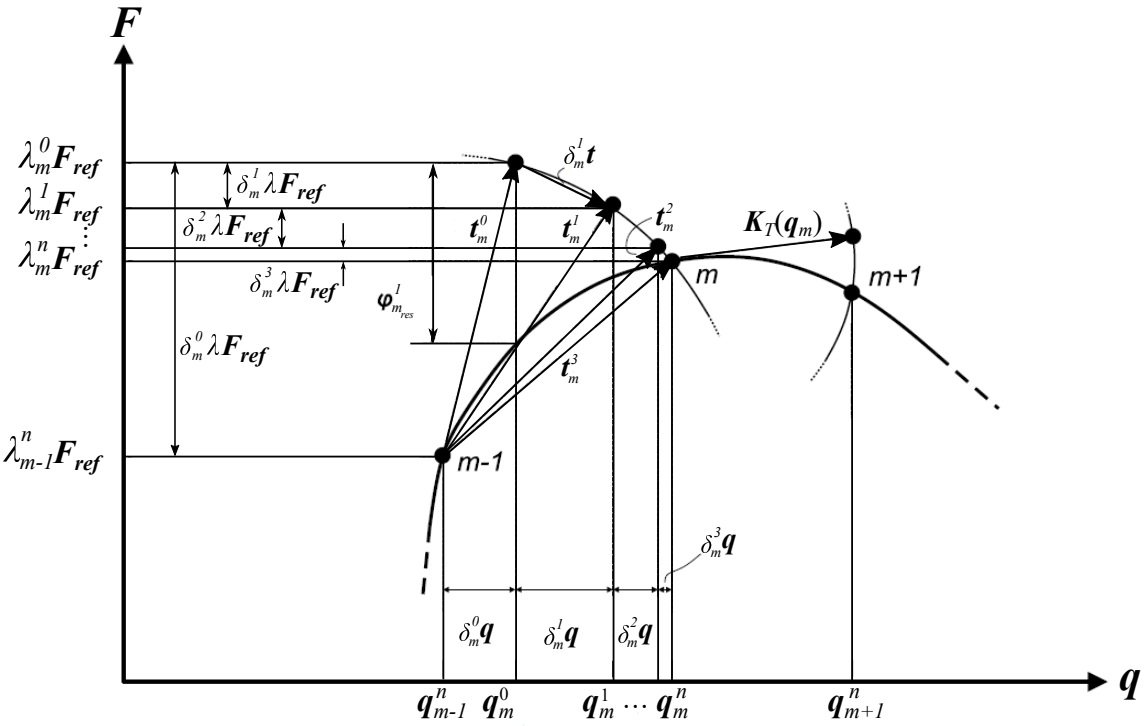

Fig. 4.1 The adopted incremental scheme of arc-length type.

computationally heavy. For this reason, the Batoz and Dhatt [210] approach is employed, and the finite displacement vector could be rewritten as:

$$\delta_m^n \boldsymbol{q} = \delta_m^n \lambda \, \bar{\boldsymbol{q}}_m^n + \delta_m^n \hat{\boldsymbol{q}} \tag{4.11}$$

in which $\bar{\boldsymbol{q}}_m^n$ and $\delta_m^n \hat{\boldsymbol{q}}$ denote the solutions of the linear systems below:

$$\begin{cases} \boldsymbol{K}_T \, \bar{\boldsymbol{q}}_m^n = \mathbf{F}_{ref} \\ \\ \boldsymbol{K}_T \, \delta_m^n \hat{\boldsymbol{q}} = -\boldsymbol{\varphi}_{m_{res}}^n \end{cases} \tag{4.12}$$

Thus, introducing Eq. 4.11 into the system Eq. 4.10, the following equation can be obtained.

$$a \, (\delta_m^n \lambda)^2 + 2 \, b \, \delta_m^n \lambda + c = 0 \tag{4.13}$$

in which:

$$
\begin{aligned}
a &= \bar{\boldsymbol{q}}_m^{n^{\mathrm{T}}}\, \bar{\boldsymbol{q}}_m^n + \boldsymbol{F}_{ref}^{\mathrm{T}}\, \boldsymbol{F}_{ref} \\
b &= (\boldsymbol{q}_m^{n-1} - \boldsymbol{q}_{m-1})^{\mathrm{T}}\, \bar{\boldsymbol{q}}_m^n + \bar{\boldsymbol{q}}_m^{n^{\mathrm{T}}}\, \delta_m^n \hat{\boldsymbol{q}} + (\lambda_m^{n-1} - \lambda_{m-1})\, \boldsymbol{F}_{ref}^{\mathrm{T}} \boldsymbol{F}_{ref} \\
c &= \left((\boldsymbol{q}_m^{n-1} - \boldsymbol{q}_{m-1}) + \delta_m^n \hat{\boldsymbol{q}}\right)^{\mathrm{T}} \left((\boldsymbol{q}_m^{n-1} - \boldsymbol{q}_{m-1}) + \delta_m^n \hat{\boldsymbol{q}}\right) + \\
&\quad + (\lambda_m^{n-1} - \lambda_{m-1})^2\, \boldsymbol{F}_{ref}^{\mathrm{T}} \boldsymbol{F}_{ref} - (\Delta l_m^0)^2
\end{aligned}
\tag{4.14}
$$

Equation (4.13) returns two solutions of the load parameter $\delta_m^n \lambda$, so the problem arises which of the solutions should be chosen. The solution that gives a positive angle is the one to choose, being the one that allows us to calculate the next solution If both solutions give positive angles, the appropriate one is the closest to the linearized solution of Eq. (4.13), i.e., $\delta_m^n \lambda = -\frac{c}{b}$. In the case of snap-back behaviours, a sign function of the predictor load factor was implemented. In the present research, the solution closest to the one of the linearized constraint equation, $\delta_m^n \lambda_{cl}$. $\delta_m^n \lambda_{cl}$ is computed by linearizing the constraint relationship $c(\delta \boldsymbol{q}, \delta\lambda) = 0$, as done for the equilibrium equations. An iterative cycle in each load step allows to reach the convergence of the solution, satisfying that the ratio between the calculated displacement increment and the previous one is less than a certain predefined tolerance, and then continue with the next step. For the sake of completeness, the explicit linearization of the constraint equation is provided in [207].

4.2 Trivial-linearized and full nonlinear vibration analysis

The characterization of the natural frequencies variation of beam, plate and shell structures for progressively increasing applied compression loadings is an engineering problem that attracts considerable interest. Because the modal behaviours of structures are not a property of the geometric and mechanical characteristics but are properties of the equilibrium states, eigenfrequencies and eigenmodes may suffer abrupt aberrations in deep nonlinear regimes [211]. Several changes in dynamic responses through structural parameter variations are usually characterized in plots of the eigenvalue loci over the parameter range of interest. The most important mode aberration phenomena concern the mode jumping, crossing and veering, among others. These phenomena have been extensively studied and observed in the literature. For instance, particular interest was

given to the phenomenon of veering. One of the first occurrences of the veering in the literature is due to Leissa [212]. The author demonstrated the occurrence of this behaviour by applying the Ritz-Galerkin method to the classical eigenvalue problem to compute the free natural frequencies of a clamped rectangular membrane. Then, many other authors analytically found or experimentally observed veering phenomenon. For example, Doll and Mote [213] studying vessels under pressure, Nair and Durvasula [214] in the study of plate vibrations and important contributions on the relations between eigenvalue veering and mode localization were provided by Pierre [215] and Natsiavas [216]. In these works, the perturbation method was applied to carry out these investigations in order to predict the occurrence of strong localization and eigenvalue loci veering, which are two manifestations of the same phenomenon. In detail, mode veering is characterized by the sharp transition of two loci of converging eigenvalue to new trajectories. After veering, each locus continues on the path before followed by the other. In addition to the rapid change in sensitivity to eigenvalues, it has long been known that the mode shapes undergo violent changes as they veer, described elegantly by Leissa [212]: "*figuratively speaking, a dragonfly one instant, a butterfly the next, and something indescribable in between*". Therefore, it is of fundamental importance to have a tool that may accurately predict and describe how the vibration modes change for each state of equilibrium.

In this context, vibration analyses are performed around a linearized (*non-trivial*) equilibrium state along the nonlinear curve. For reasons of clarity, the superscript k was omitted in this section.

$$\begin{aligned}\delta(\delta L_{int} + \delta L_{ine} - \delta L_{ext}) = \delta \boldsymbol{q}_{sj}^{\mathrm{T}}(\boldsymbol{K}_0^{ij\tau s} + \boldsymbol{K}_{T1}^{ij\tau s} + \boldsymbol{K}_{\sigma}^{ij\tau s})\delta \boldsymbol{q}_{\tau i} + \delta \boldsymbol{q}_{sj}^{\mathrm{T}} \boldsymbol{M}^{ij\tau s} \delta \ddot{\boldsymbol{q}}_{\tau i} = \\ = \delta \boldsymbol{q}_{sj}^{\mathrm{T}} \boldsymbol{K}_T^{ij\tau s} \delta \boldsymbol{q}_{\tau i} + \delta \boldsymbol{q}_{sj}^{\mathrm{T}} \boldsymbol{M}^{ij\tau s} \delta \ddot{\boldsymbol{q}}_{\tau i} = 0\end{aligned} \tag{4.15}$$

In order to derive Eq. 4.15, the mass matrix is considered linear and $\delta^2 L_{ext} = 0$ (loading is conservative).

In summary, the present methodology for studying vibrations around nonlinear equilibrium states may be explained in the following steps:

- Firstly, the static geometrical nonlinear problem is solved by using the NR method based on the arc-length scheme.
- Once the nonlinear equilibrium curve is computed, the $\boldsymbol{K}_T$ is calculated in each states of interest, as illustrated in Fig. 4.2, where $\alpha = \arctan(\Delta P/\Delta u)$.
- After that, by considering the incremental linearized equilibrium condition of Eq. 4.15 and assuming harmonic displacements around *non-trivial* equilibrium states

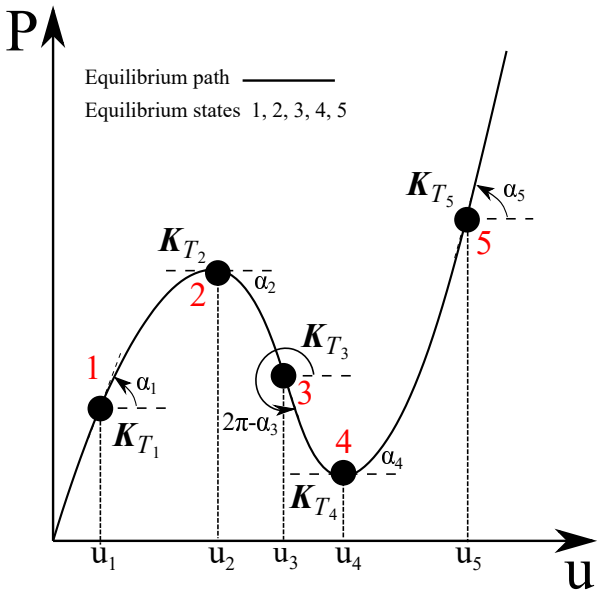

Fig. 4.2 $\boldsymbol{K}_T$ in specific equilibrium states of the nonlinear equilibrium path.

along the nonlinear path,

$$\begin{aligned} \delta\boldsymbol{q}_{\tau i}(t) &= \delta\widetilde{\boldsymbol{q}}_{\tau i}e^{i\omega t} \\ \delta\ddot{\boldsymbol{q}}_{\tau i}(t) &= -\omega^2\delta\widetilde{\boldsymbol{q}}_{\tau i}e^{i\omega t} \end{aligned} \tag{4.16}$$

the equations of motion are simplified into linear eigenvalue problems from which it is possible to compute natural frequencies and mode shapes:

$$(\boldsymbol{K}_T^{ij\tau s} - \omega^2\boldsymbol{M}^{ij\tau s})\delta\widetilde{\boldsymbol{q}}_{\tau i} = 0 \tag{4.17}$$

where ω is the natural frequency and $\delta\widetilde{\boldsymbol{q}}_{\tau i}$ represent the eigenvector.

- For clarity, it is important to highlight how the nonlinear vibrations investigated in this work show low amplitudes; as a consequence, it is legitimate to adopt a linearization around the state of equilibrium for the resolution of these problems.

If the complete form of the tangent stiffness matrix is used, the method is called full nonlinear approach. Differently, in the case of small rotations and linear stable pre-buckling, a simplified method, called trivial linearized approach, based on the linearization around *trivial* ($\boldsymbol{q} = 0$) equilibrium state is employed. In this case, the tangent stiffness matrix $\boldsymbol{K}_T^{ij\tau s}$ may be approximated as the sum of the linear stiffness

$\left(\boldsymbol{K}_0^{ij\tau s} = \boldsymbol{K}_S^{ij\tau s}(\boldsymbol{q}_{\tau i} = 0)\right)$ and the linear geometric (pre-stress) contribution ($\boldsymbol{K}_{\sigma_l}^{ij\tau s}$):

$$\boldsymbol{K}_T^{ij\tau s} \approx \boldsymbol{K}_0^{ij\tau s} + \lambda \boldsymbol{K}_{\sigma_l}^{ij\tau s} \tag{4.18}$$

in which λ stands for the increasing load factor. The trivial linearized method is performed by substituting Eq. 4.18 in Eq. 4.15, where the $\boldsymbol{K}_{T1}$ tends to 0 because the δq are small.

If thermal loadings are considered, a new constitutive law and definition of the geometric stiffness matrix are required, see Chapter 3. In detail:

$$\begin{aligned}
\delta L_{\text{int}} &= \textstyle\int_V \delta \boldsymbol{\epsilon}_e{}^{\mathrm{T}}(\boldsymbol{C}\boldsymbol{\epsilon} - \boldsymbol{\beta}\Delta T)\, dV = \int_V \delta \boldsymbol{q}_{sj}{}^{\mathrm{T}} \boldsymbol{B}^{\mathrm{T}}(\boldsymbol{C}\boldsymbol{B}\boldsymbol{q}_{\tau i} - \boldsymbol{\beta}\Delta T)\, dV = \\
&= \textstyle\int_V \delta \boldsymbol{q}_{sj}{}^{\mathrm{T}} \boldsymbol{B}^{\mathrm{T}}(\boldsymbol{C}\boldsymbol{B}\boldsymbol{q}_{\tau i})\, dV - \int_V \delta \boldsymbol{q}_{sj}{}^{\mathrm{T}} \boldsymbol{B}^{\mathrm{T}}(\boldsymbol{\beta}\Delta T)\, dV = \\
&= \delta \boldsymbol{q}_{sj}{}^{\mathrm{T}} \boldsymbol{K}_S^{ij\tau s} \boldsymbol{q}_{\tau i} - \delta \boldsymbol{q}_{sj}{}^{\mathrm{T}} \boldsymbol{F}_{T\,sj}
\end{aligned} \tag{4.19}$$

$$\begin{aligned}
\delta(\delta L_{int}) &= \textstyle\int_V \delta(\delta \boldsymbol{\epsilon}^{\mathrm{T}})\boldsymbol{\sigma}_l\, dV = \int_V \delta \boldsymbol{q}_{sj}{}^{\mathrm{T}} \boldsymbol{B}_{nl}^{*\,\mathrm{T}} \boldsymbol{\sigma}_l\, dV = \delta \boldsymbol{q}_{sj}{}^{\mathrm{T}} \int_V \boldsymbol{B}_{nl}^{*\,\mathrm{T}} \boldsymbol{C}\boldsymbol{\epsilon}\, dV\ \delta \boldsymbol{q}_{\tau i} + \\
&- \delta \boldsymbol{q}_{sj}{}^{\mathrm{T}} \int_V \boldsymbol{B}_{nl}^{*\,\mathrm{T}} \boldsymbol{\beta}\Delta T\, dV\ \delta \boldsymbol{q}_{\tau i} = \delta \boldsymbol{q}_{sj}{}^{\mathrm{T}} \boldsymbol{K}_\sigma \delta \boldsymbol{q}_{\tau i} - \delta \boldsymbol{q}_{sj}{}^{\mathrm{T}} \boldsymbol{K}_{\sigma T} \delta \boldsymbol{q}_{\tau i}
\end{aligned} \tag{4.20}$$

in which $\boldsymbol{F}_{T\,sj}$ is the thermal load vector, that is an artificial force for modelling thermal expansion and the $\boldsymbol{K}_{\sigma T}$ represents the new term of the geometric stiffness matrix due to the thermal contribution. For clarity, it should be emphasized once again that only linear contributions are taken into account.

In the CUF domain, it is possible to consider both a coupled and uncoupled formulation performing static, quasi-static, and dynamic analyses and apply any static, dynamic, or transient thermal loads. The reader is referred to [217] for a detailed description of thermoelastic analyses using the CUF. In this work, for simplicity, high-speed thermo-mechanical loads have not been considered. Therefore, it has been possible to adopt a dynamic uncoupled thermoelasticity formulation. In particular, a constant thermal load on the entire structure was applied in the following thermal analyses.

4.3 Transient analysis

In the more general case, both internal, external and inertial energy contributions are accounted for. Therefore, for time response analyses, the PVD holds:

$$\delta L_{int} = \delta L_{ext} - \delta L_{ine} \tag{4.21}$$

where in the FEM form the undamped dynamic problem becomes:

$$\boldsymbol{M}\ddot{\boldsymbol{q}}(t) + \boldsymbol{K_S}\boldsymbol{q}(t) = \boldsymbol{F}(t) \tag{4.22}$$

A numerical technique is required in order to compute the solution of this equation in the time domain.

Over the years, many research efforts have focused on improving effective algorithms that can accurately perform dynamic analyses. However, in practical analysis of dynamic responses, we are interested in some effective numerical methods, that may be divided in two main categories: 1. direct integration and 2. mode superposition. Regarding the direct integration method, the equation is integrated employing a step-by-step numerical procedure [34]. The term "*direct*" means that no transformation of the equations is carried out prior to the numerical integration. Direct integrations schemes are very effective and widely utilized for both linear and nonlinear dynamic problems. Nevertheless, long computational times can be required and could be affected by possible instability due to increasing errors. On the other hand, one of the main advantages of the mode superposition method is that the system of equations is formulated in modal coordinates and eventually decoupled.

Various direct time integration techniques are widely used. In particular, the scheme of step-by-step time integration is frequently adopted to carry out transient analyses. The dynamic algorithm chosen can be explicit or implicit. Explicit schemes, for example, the central difference method, are adopted for fast analysis, such as crash simulations. These methods compute the equilibrium state of a system at a later time than the system state at that time. There are no convergence criteria to check and no iterations using this approach. Nevertheless, the explicit scheme is only conditionally stable and requires an extremely small time step to maintain numerical stabilities. The implicit method, for example Houbolt, and Newmark methods, is used for analyses involving small accelerations. In this scheme, the solution is found by computing an equation in which both the current and the last state of the system are involved. Each time increment is solved slowly since iterations are needed to obtain the convergence, i.e., the global equilibrium. The reader is referred to [218, 219] for meticulous reviews of these methods. For many problems, such as structural vibration analyses, an implicit method is usually preferred. In dynamic structural applications, excluding impact analysis, interest is typically focused only on the low modes because the high modes usually do not indicate the real behaviour of the initial problem and for computational efficiency reasons. To thoroughly investigate these modes, an implicit unconditionally stable method is generally used. For these schemes, time steps are selected independent of stability aspects.

However, some form of numerical damping must be considered in these algorithms to damp out the spurious participation of the higher modes in dynamic responses in order to facilitate the convergence solution during the iteration.

In the present thesis, we adopt both the mode superposition approach [34] and direct integration algorithms. In detail, the time integration algorithm used to describe the dynamic responses is the Newmark method [220]. However, this method may not be unconditionally stable in a highly nonlinear regime. Therefore, for these cases, the Hilber-Hughes-Taylor (HHT)-α method [221] is implemented into the presented formulation to stabilize the time integration process under highly nonlinear effects.

4.3.1 Mode superposition method

Thanks to the accuracy of the modal analysis carried out using the CUF, the mode superposition method is advantageous in dynamic analysis when the Newmark method is too computationally expensive. The undamped dynamic equilibrium, Eq. 4.22, may be written in modal coordinates by employing the following transformation:

$$\boldsymbol{q}(t) = \boldsymbol{\Phi}\boldsymbol{x}(t) \tag{4.23}$$

in which $\boldsymbol{\Phi}$ is a $DOFs \times m$ matrix containing m $\boldsymbol{M}$-orthonormalized eigenvectors and $\mathbf{x}(t)$ indicates a time-dependent vector of order m.

The transformation matrix $\boldsymbol{\Phi}$ must be non-singular (i.e., rank($\boldsymbol{\Phi}$) = m) to have a unique relation between any vectors $\boldsymbol{q}$ and $\boldsymbol{x}$. In detail, an effective transformation matrix is setted employing the solution of the undamped free-vibration equations of motion, that is reduced into linear or nonlinear eigenvalue problems by assuming harmonic solutions. Briefly, the eigenproblem of the m-$DOFs$ system under consideration gives the m eigensolutions $(\omega_1^2, \boldsymbol{\Phi}_1)$, $(\omega_2^2, \boldsymbol{\Phi}_2)$, ... , $(\omega_m^2, \boldsymbol{\Phi}_m)$, in which ω_i denote the corresponding natural frequencies (rad/s).

We define a matrix $\boldsymbol{\Phi}$) containing the eigenvectors Φ_i in the columns and a diagonal matrix $\boldsymbol{\Omega}^2$ that stores the second power of the natural periods ω_i^2. Furthermore, since the eigenvectors are $\boldsymbol{M}$-orthogonal, we may prove that:

$$\boldsymbol{\Phi}^{\mathrm{T}}\boldsymbol{K}_S\boldsymbol{\Phi} = \boldsymbol{\Omega}^2, \qquad \boldsymbol{\Phi}^{\mathrm{T}}\boldsymbol{M}\boldsymbol{\Phi} = \boldsymbol{I} \tag{4.24}$$

The equilibrium equations without damping are:

$$\ddot{\boldsymbol{x}}(t) + \boldsymbol{\Omega}^2\boldsymbol{x}(t) = \boldsymbol{\Phi}^{\mathrm{T}}\boldsymbol{F}(t) \tag{4.25}$$

Equation 4.25 is a system of m individual equations of the form:

$$\begin{cases} \ddot{x}_i(t) + \omega_i^2 x_i(t) = r_i(t) \\ r_i(t) = \boldsymbol{\Phi}_i^T \boldsymbol{F}(t) \end{cases} \qquad i = 1, 2, ..., m \tag{4.26}$$

with initial conditions defined as:

$$x(0) = \boldsymbol{\Phi}^{\mathrm{T}} \boldsymbol{M} \boldsymbol{q}(0), \qquad \dot{x}(0) = \boldsymbol{\Phi}^{\mathrm{T}} \boldsymbol{M} \dot{\boldsymbol{q}}(0) \tag{4.27}$$

The solution of each Eq. 4.26 is obtained by introducing the well-known Duhamel integral:

$$x_i(t) = \frac{1}{\omega_i} \int_0^t r_i(\tau) sin\omega_i(t-\tau)\ \mathrm{d}\tau + \alpha_i sin\omega_i t + \beta_i cos\omega_i t \tag{4.28}$$

in which α_i and β_i are derived from the initial conditions (Eq. 4.27). By considering this procedure, the contributions to the response for each mode are evaluated. Of course, the accuracy of the solution will depend on the number m. The complete response $\boldsymbol{q}(t)$ is defined by superposition of the response in each mode as follows:

$$\boldsymbol{q}(t) \sum_{i=1}^{m} \boldsymbol{\Phi}_i x_i(t) \tag{4.29}$$

However, the essence of the mode superposition method is that, generally, only a small fraction of the total number of decoupled equations has to be considered to achieve good approximate solutions. Typically, only the first n equations of motion in Eq. 4.26 need to be used, with $n \ll m$.

4.3.2 Newmark method

Equation 4.22 gives a system of algebraic equations in the time domain. The resolution can involve the use of a time integration algorithm, e.g., the Newmark approach. This method, widely employed in structural dynamics, belongs to the family of direct integration methods. For completeness, the equation of motion at time $t + \Delta t$ and its solution is given below.

$$\boldsymbol{M} \ddot{\boldsymbol{q}}_{t+\Delta t} + \boldsymbol{K}_S \boldsymbol{q}_{t+\Delta t} = \boldsymbol{F}_{t+\Delta t} \tag{4.30}$$

The step-by-step solution of Eq. 4.30 is derived by considering the following assumptions for the velocities and displacements within the time step Δt:

$$\begin{aligned} \dot{\boldsymbol{q}}_{t+\Delta t} &= \dot{\boldsymbol{q}}_t + [(1-\delta)\ddot{\boldsymbol{q}}_t + \delta\ddot{\boldsymbol{q}}_{t+\Delta t}]\Delta t \\ \boldsymbol{q}_{t+\Delta t} &= \boldsymbol{q}_t + \dot{\boldsymbol{q}}_t\Delta t + [(\tfrac{1}{2}-\alpha)\ddot{\boldsymbol{q}}_t + \alpha\ddot{\boldsymbol{q}}_{t+\Delta t}]\Delta t^2 \end{aligned} \tag{4.31}$$

in which α and δ stand for parameters that are determined to obtain integration accuracy stability. In the present work, δ= 0.5 and α= 0.25 are assumed for the related constants. By introducing the trapezoidal rule, $\dot{\boldsymbol{q}}_{t+\Delta t}$ and $\ddot{\boldsymbol{q}}_{t+\Delta t}$ are calculated from Eq. 4.31 in terms of $\boldsymbol{q}_{t+\Delta t}$. Then, we solve for each time step:

$$\widehat{\boldsymbol{K}}_S \boldsymbol{q}_{t+\Delta t} = \widehat{\boldsymbol{F}}_{t+\Delta t} \tag{4.32}$$

where:

$$\begin{aligned} \widehat{\boldsymbol{K}}_S &= \boldsymbol{K}_S + \tfrac{1}{\alpha(\Delta t)^2}\mathbf{M} \\ \widehat{\boldsymbol{F}} &= \boldsymbol{F} + \tfrac{1}{\alpha(\Delta t)}\boldsymbol{M}\dot{\boldsymbol{q}}_t + \tfrac{1}{2\alpha}\boldsymbol{M}\ddot{\boldsymbol{q}}_t \end{aligned} \tag{4.33}$$

This procedure is repeated for all the time steps. For the sake of brevity, the Newmark complete solution procedure is reported in [34].

4.3.3 HHT-α method

The Newmark method, especially the trapezoidal rule, is the most widely adopted in practical dynamic analyses. This integration algorithm is generally the most effective because it is a single-step scheme and a second-order accurate procedure. This algorithm that is not dissipative and has no amplitude decay is acceptable in any engineering problem. Nevertheless, the trapezoidal rule that is known to be unconditionally stable in linear analyses may become unstable in nonlinear dynamic analysis when very large deformations and long-time responses are studied. To overcome this limit, numerical damping is introduced to assure energy conservation or decays. These methods are called generalized α-algorithms [222]. In this research, the implicit time integration scheme used to derive the nonlinear dynamic responses is the Hilber-Hughes-Taylor (HHT)-α algorithm, that represents a formulation able to stabilize the time integration process under highly nonlinear effects. The latter method allows possessing numerical damping to suppress any spurious growth of high-frequency response. This implicit method is a second-order accurate dissipative method that has much high-frequency dissipation with little low-frequency damping. It is important to highlight that if $\alpha = 0$, this method

reduces to the Newmark algorithm. In summary, the resolution of nonlinear dynamic equations, Eq. 4.22, solved by employing an opportune Newton-Raphson method and the HHT-α scheme, is provided below.

Considering the values known at the time t, the corresponding ones at $t + \Delta t$ are calculated using the HHT-α methodology, which was formulated by Hilber *et al.* [221]. In detail, the equation of motion is expressed as follows:

$$\boldsymbol{M}\ddot{\boldsymbol{q}}_{t+\Delta t} + (1+\alpha)\boldsymbol{K}_S\boldsymbol{q}_{t+\Delta t} - \alpha\boldsymbol{K}_S\mathbf{q}_t = (1+\alpha)\boldsymbol{F}_{t+\Delta t} - \alpha\boldsymbol{F}_t \tag{4.34}$$

In order to obtain approximate step-by-step solutions of Eq. 4.30, the classical Newmark assumptions for velocities and displacements within the time step Δt are introduced.

$$\begin{aligned} \dot{\boldsymbol{q}}_{t+\Delta t} &= \dot{\boldsymbol{q}}_t + [(1-\gamma)\ddot{\boldsymbol{q}}_t + \gamma\ddot{\boldsymbol{q}}_{t+\Delta t}]\Delta t \\ \boldsymbol{q}_{t+\Delta t} &= \boldsymbol{q}_t + \dot{\mathbf{q}}_t\Delta t + [(\tfrac{1}{2}-\beta)\ddot{\boldsymbol{q}}_t + \beta\ddot{\boldsymbol{q}}_{t+\Delta t}]\Delta t^2 \end{aligned} \tag{4.35}$$

where $\beta = (1-\alpha)^2/4$ and $\gamma = (1-2\alpha)/2$. The parameters α, β and γ control the accuracy, stability and numerical dissipation characteristics. As described by Hilber *et al.* [221], to use adequate numerical damping properties in the higher modes while at the same time ensuring that the lower modes are not affected too strongly, a value of $-1/3 \leq \alpha \leq 0$ has to be employed.

The resolution of the presented numerical algorithm adopted to perform nonlinear dynamic analysis can be described in the following steps:

1. Form stiffness $\boldsymbol{K}_S$ and mass matrix $\boldsymbol{M}$;
2. Set the initial conditions;
3. **For each time step:**
   (a) Starting condition:

$$\begin{aligned} \ddot{\boldsymbol{q}}_{t+\Delta t} &= 0 \\ \boldsymbol{q}_{t+\Delta t} &= \boldsymbol{q}_t + \dot{\boldsymbol{q}}_t\Delta t + \ddot{\boldsymbol{q}}_t(1/2-\beta)\delta^2 + \ddot{\boldsymbol{q}}_{t+\Delta t}\beta\Delta t^2 \\ \dot{\boldsymbol{q}}_{t+\Delta t} &= \ddot{\boldsymbol{q}}_t + \ddot{\boldsymbol{q}}_t(1-\gamma)\Delta + \ddot{\boldsymbol{q}}_{t+\Delta t}\gamma\Delta t \end{aligned} \tag{4.36}$$

(b) Form residual load vector $\mathbf{R}_{t+\Delta t}$:

$$\boldsymbol{R}_{t+\Delta t} = (1+\alpha)\boldsymbol{F}_{t+\Delta t} - \alpha\boldsymbol{F}_t - (1+\alpha)\boldsymbol{r}_{t+\Delta t} + \alpha\boldsymbol{r}_t - \boldsymbol{M}\ddot{\boldsymbol{q}}_{t+\Delta t} \tag{4.37}$$

where $\boldsymbol{r}$ represent the internal forces.

(c) Newton-Raphson iteration convergence:

i. **while** $||\boldsymbol{R}_{t+\Delta t}|| \geq Tol$ **do**

ii. Calculate tangent stiffness matrix $\boldsymbol{K}_T$;

iii. Solve for incremental acceleration $\Delta\ddot{\boldsymbol{q}}_{t+\Delta t}$:

$$[(\boldsymbol{M} + \boldsymbol{K}_T\beta\Delta t^2(1+\alpha)]\Delta\ddot{\boldsymbol{q}}_{t+\Delta t} = \boldsymbol{R}_{t+\Delta t} \tag{4.38}$$

iv. Calculate new acceleration, velocity and displacement vectors:

$$\begin{aligned} \ddot{\boldsymbol{q}}_{t+\Delta t} &= \ddot{\boldsymbol{q}}_{t+\Delta t} + \Delta\ddot{\boldsymbol{q}}_{t+\Delta t} \\ \dot{\boldsymbol{q}}_{t+\Delta t} &= \dot{\boldsymbol{q}}_{t+\Delta t} + \Delta\ddot{\boldsymbol{q}}_{t+\Delta t}\gamma\Delta t \\ \boldsymbol{q}_{t+\Delta t} &= \boldsymbol{q}_{t+\Delta t} + \Delta\ddot{\boldsymbol{q}}_{t+\Delta t}\beta\Delta t^2 \end{aligned} \tag{4.39}$$

v. Calculate new residual load vector.

$$\boldsymbol{R}_{t+\Delta t} = (1+\alpha)\boldsymbol{F}_{t+\Delta t} - \alpha\boldsymbol{F}_t - (1+\alpha)\boldsymbol{r}_{t+\Delta t} + \alpha\boldsymbol{r}_t - \boldsymbol{M}\ddot{\boldsymbol{q}}_{t+\Delta t} \tag{4.40}$$

vi. **end while**

(d) Next time step.

4.4 Need of higher-order and full nonlinear models

First, geometrically nonlinear static analyses were performed on isotropic and laminated composite shells, emphasizing the potentiality of the presented full nonlinear approach to compute the interlaminar 3D stress state in large displacement/rotation fields. In addition, the effectiveness of various geometrically nonlinear strain approximations, such as the full nonlinear and the classical von Kármán strains, is evaluated. Then, the results derived from the large-deflections and post-buckling analyses of laminated plates highlight the differences between the classical and refined structural theories. Finally, the nonlinear transient response of several beam structures considering various loadings

and boundary conditions are presented. Results show the need to adopt LE theories and full nonlinear strain models in order to capture the complex behaviours. Of course, the interest is also focused on the capability of the presented approach to carry out enhanced analyses of complex problems with very low computational efforts.

4.4.1 Stress distribution evaluation

Isotropic pinched cylindrical shell (static analysis)

A cylindrical shell under transverse loadings is considered as first analysis case. Regarding the boundary conditions, the vertical deflection and the rotation about the β-axis are restrained along its longitudinal edges and a clamped constraint is imposed in $\beta = 0$. Figure 4.3 illustrates this considered structure, including its geometrical parameters, L = 3.048 m, R_α = 1.016 m, and t = 0.03 m. The material data are: $E = 20.685{\times}10^6$ N/m^2 and $\nu = 0.3$. The nonlinear static analysis of this case has already been analyzed by Sze

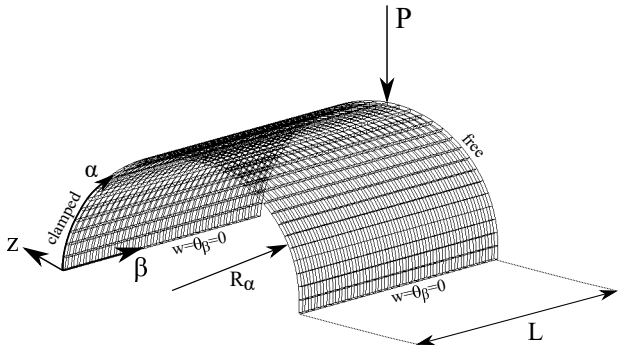

Fig. 4.3 Geometric properties, boundary and loading conditions of the isotropic pinched cylindrical shell.

et al. [223] and Wu *et al.* [224]. Nevertheless, only nonlinear equilibrium curves were analyzed and no through-the-thickness stress benchmarks were yet provided.

Firstly, convergence analyses on the surface finite element mesh is performed in order to carry out accurate evaluations. Figure 4.4 depicts the transverse deflections for different 2D shells, and from 100Q9 to 1600Q9 elements are employed for the in-plane discretization, while 1LD2 is adopted in the z-axis. In addition, Table 4.1 provides the transverse displacements for various models and loads, along with the total degrees of freedom (DOFs). The results given Fig. A.13 and Table 4.1 show that the kinematics 32×32Q9 is a good approximation for the surface mesh. Furthermore, another convergence study on the expansion functions in z-direction is needed for an accurate evaluation of the 3D stress fields, which include the circumferential normal stress $\sigma_{\alpha\alpha}$ and transverse

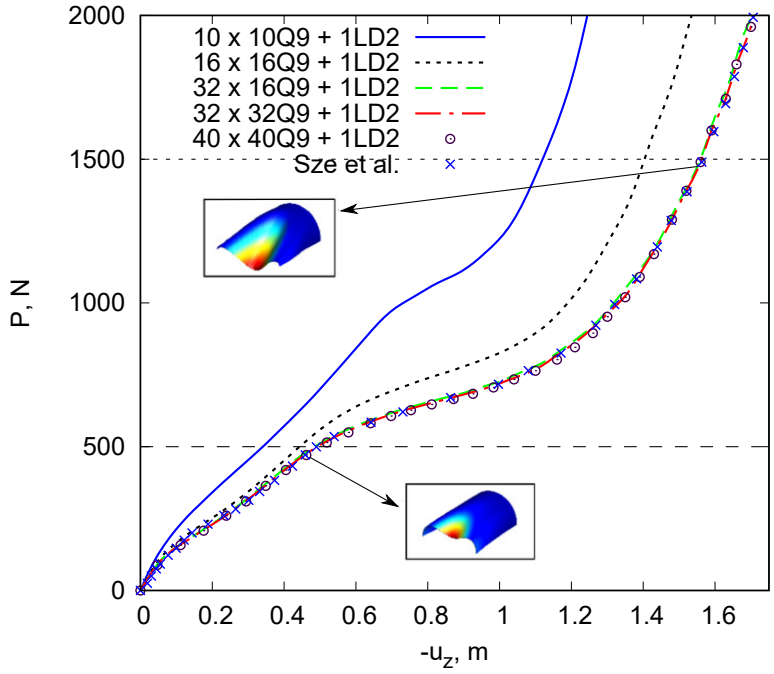

Fig. 4.4 Nonlinear equilibrium path for the isotropic pinched cylindrical shell structure, including convergence analyses on the surface mesh approximation.

Model	DOFs	$-u_z$		
		500 N	1500 N	2000 N
10x10Q9+1LD2	3969	0.34	0.73	1.24
16x16Q9+1LD2	9801	0.44	1.40	1.53
32x16Q9+1LD2	19305	0.49	1.55	1.70
32x32Q9+1LD2	38025	0.50	1.57	1.72
40x40Q9+1LD2	59049	0.50	1.57	1.72

Table 4.1 Transverse displacements [m] of the loading point for various shell models. Isotropic pinched cylindrical shell structure.

shear stress $\sigma_{\beta z}$. In particular, both LE and TE functions are used and compared. Figure 4.5 and 4.6 displays the stress distributions for various expansion orders. Table

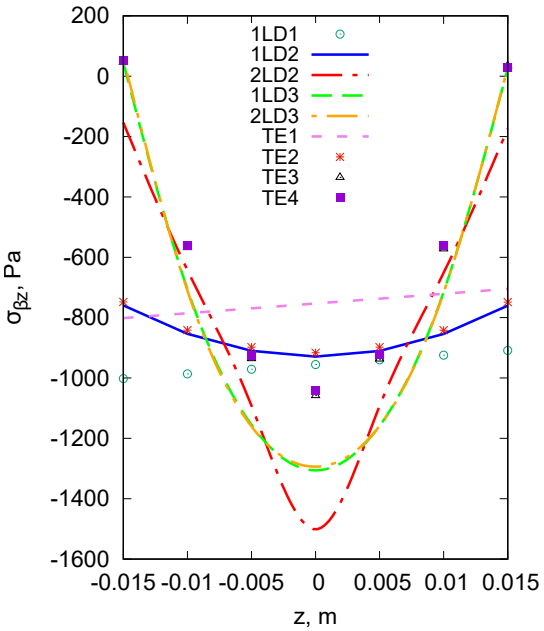

Fig. 4.5 Transverse shear stress, $\sigma_{\beta z}$, distributions through thickness for various TE and LE functions at the middle point of the isotropic pinched cylindrical shell subjected to P = 500 N.

4.2 provides the comparison of the circumferential normal and transverse shear stress values for various shell theories and loads. Clearly, it is observed that at least one LD3 kinematics should be employed to accurately compute the stresses. It is possible to state that the 1LD3 model is convergent with the higher-order 2LD3 model and, therefore, to consider these values accurate. Results suggest that a low-order model is sufficient to predict the circumferential normal stress, while a higher-order model is mandatory to accurately evaluate the transverse shear stress component. In addition, Fig. 4.7 plots the through-the-thickness circumferential normal and transverse shear stresses for two loads. The stress distributions of both TE1 and with 1LD3 models are shown to underline the different capabilities of the two shell theories in detecting accurate stress distributions. The linear interpolation given by the TE1 approximation is not enough to catch the parabolic distribution of transverse shear stresses, as highlighted in Fig. 4.7d. In fact, at least 1LD3 must be considered for a correct description of the current problem.

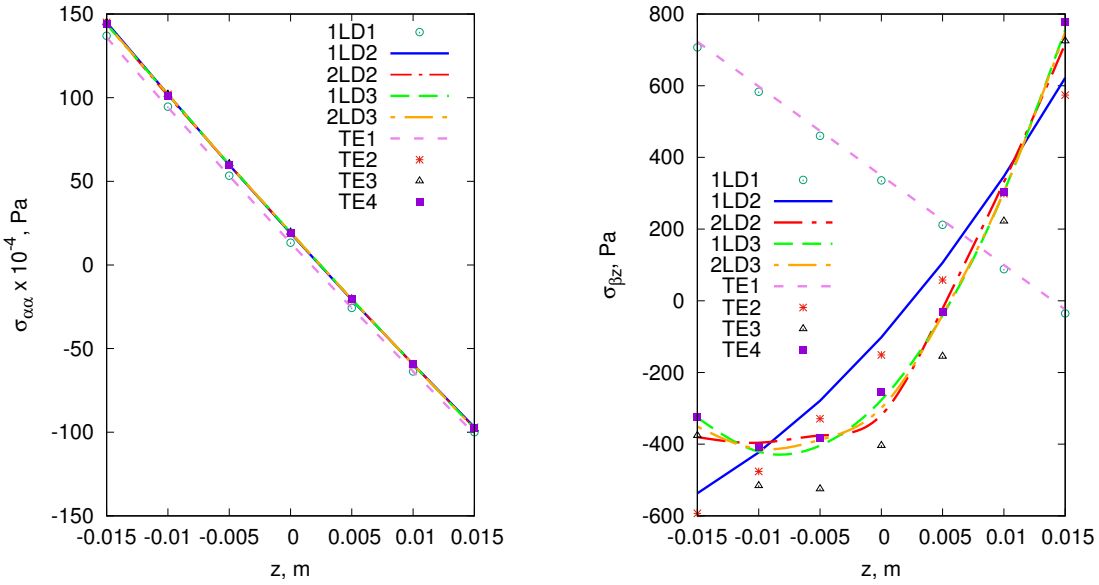

(a) $\sigma_{\alpha\alpha}$ (b) $\sigma_{\beta z}$

Fig. 4.6 Variation of stress distributions through thickness for various TE and LE functions at the middle point of the isotropic pinched cylindrical shell subjected to P = 1500 N.

Theory	DOFs	$\sigma_{\alpha\alpha} \times 10^{-4}$, [Pa]		$\sigma_{\beta z}$, [Pa]	
		500 N	1500 N	500 N	1500 N
TE1	25350	-10.72	-100.75	-753.08	349.29
TE2	38025	-9.80	-97.12	-916.36	-151.02
TE3	50700	-9.85	-97.88	-1058.51	-404.04
TE4	63375	-9.85	-97.87	-1042.43	-254.80
1LD1	25350	-10.72	-100.74	-955.35	355.90
1LD2	38025	-9.80	-97.11	-928.97	-102.39
2LD2	63375	-9.84	-97.62	-1501.40	-318.89
1LD3	50700	-9.85	-97.87	-1302.05	-287.32
2LD3	88725	-9.85	-97.87	-1299.74	-290.58

Table 4.2 Circumferential normal and transverse shear stresses of the isotropic pinched cylindrical shell for various expansion theories and loads at $\alpha = 1.595$ m, $\beta = 1.524$ m and at $z = 0.015$ m for the $\sigma_{\alpha\alpha}$ and at $z = 0.0$ m for the $\sigma_{\beta z}$

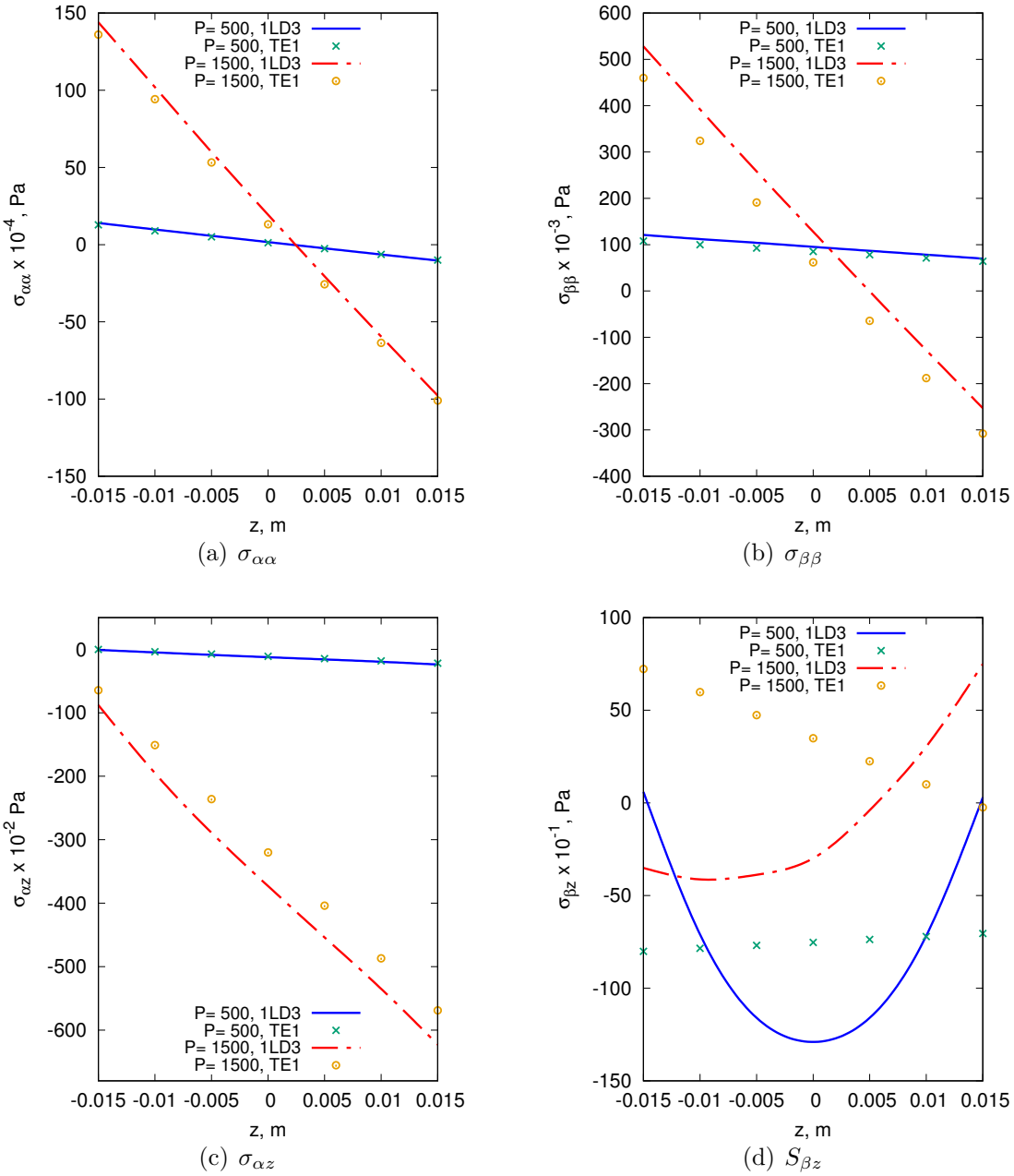

(a) $\sigma_{\alpha\alpha}$ (b) $\sigma_{\beta\beta}$

(c) $\sigma_{\alpha z}$ (d) $S_{\beta z}$

Fig. 4.7 The distribution of normal (a, b) and transverse shear (c, d) stresses in the z-axis for two load values for the isotropic pinched cylindrical shell at the middle point.

Composite hinged shell (static analysis)

As a further case, a composite hinged shell subjected to a central transverse force P is studied. The structure has the following geometrical characteristics, L = 508 mm, R_α = 2540 mm, θ = 0.1 rad. The material data of this laminated hinged shell involves E_L= 3300 MPa, E_T= 1100 MPa, G_{LT}= 660 MPa, G_{TT}= 660 MPa and ν_{LT}=ν_{TT}= 0.25. The lamination sequences are $[0°, 90°, 0°]$, $[90°, 0°, 90°]$ and $[45°, 0°, -45°]$, and the thickness equals 12.7 mm.

First, convergence studies on the in-plane 2D shell model is performed in order to perform accurate static analyses. Then, stress investigations are carried out for different expansion orders. Figure 4.8 shows the transverse displacements for different in-plane FE mesh, and the elements from 25Q9 to 225Q9 are employed for the surface discretization, while only 1LD2 is used in each layer in the z-direction. The nonlinear response curves are divided into the regions A, B and C, as shown in Fig. 4.8c. In addition, transverse displacements values for the three laminations for different in-plane mesh and loads are provided in Table 4.3, including the number of DOFs. As a consequence, the 10×10Q9

Model	DOFs	-u_z [mm]									
		$[0°, 90°, 0°]$				$[90°, 0°, 90°]$		$[45°, 0°, -45°]$			
		500 N (A)	500 N (B)	500 N (C)	2000 N	500 N	2000 N	500 N (A)	500 N (B)	500 N (C)	2000 N
5 x 5Q9 + 3LD2	2541	2.521	14.629	24.601	29.821	2.125	27.069	2.620	18.074	22.097	29.296
10 x 10Q9 + 3LD2	9261	2.701	15.698	25.092	30.492	2.062	27.701	2.879	17.296	22.691	30.220
15 x 15Q9 + 3LD2	20181	2.702	15.700	25.092	30.495	2.066	27.709	2.883	17.307	22.706	30.221
Sze *et al.* [223]	-	2.697	15.727	25.124	30.506	2.061	27.722	-	-	-	-

Table 4.3 Transverse displacements values of the composite hinged shell for various in-plane mesh approximation and loads at α = 254 mm, β = 254 mm and z = 6.35 mm.

mesh will be considered as converged discretization and, therefore, it is adopted for the following stress analyses. Both ESL and LW models are adopted and compared using different expansion functions in the z-direction. Figure 4.9 depicts the comparison for different kinematic theories for the stress assessment. The corresponding stress values are tabulated in Table 4.4 for different shell theories. As suggested by the results, the LW model should be exploited to accurately predict the stress distribution. Results highlight that the ESL model with a low-order model is enough to evaluate the circumferential normal stress, while it is inaccurate to predict the transverse shear stress component. Figures 4.10, 4.11 and 4.12 show the circumferential normal and transverse shear stresses in the thickness direction for different loads and for the three different staking sequences.

As previously done, the stresses computed using both ESL and LW models with 4LD3 are illustrated to show the different capabilities of the two approaches. According to Fig. 4.10d, ESL models are not able to accurately evaluate the transverse shear stresses.

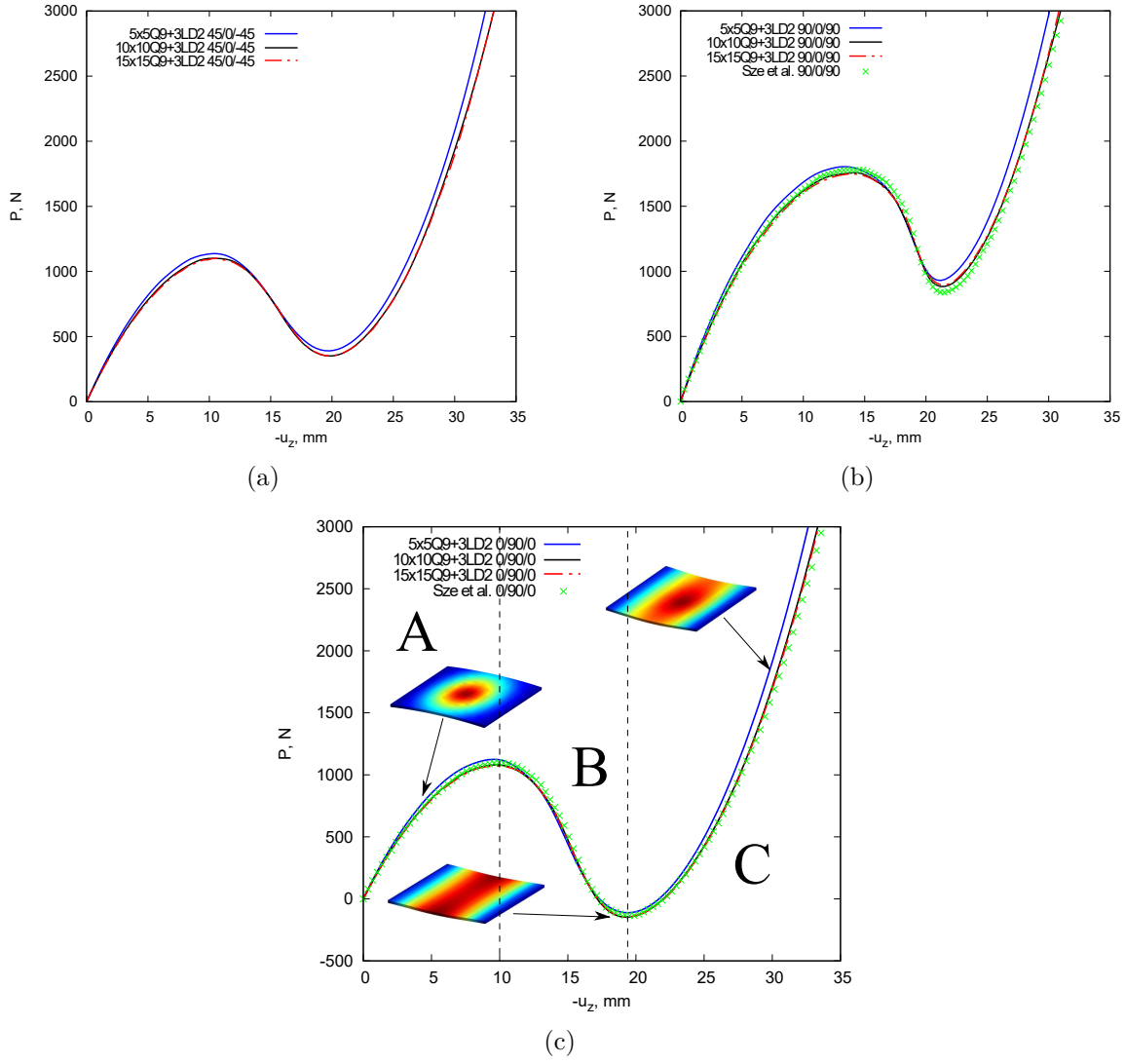

Fig. 4.8 Nonlinear equilibrium curves of the composite hinged shell under transverse loadings, including the convergence analysis on in-plane mesh numbers. Lamination sequences: (a) $[45°, 0°, -45°]$, (b) $[90°, 0°, 90°]$, (c) $[0°, 90°, 0°]$.

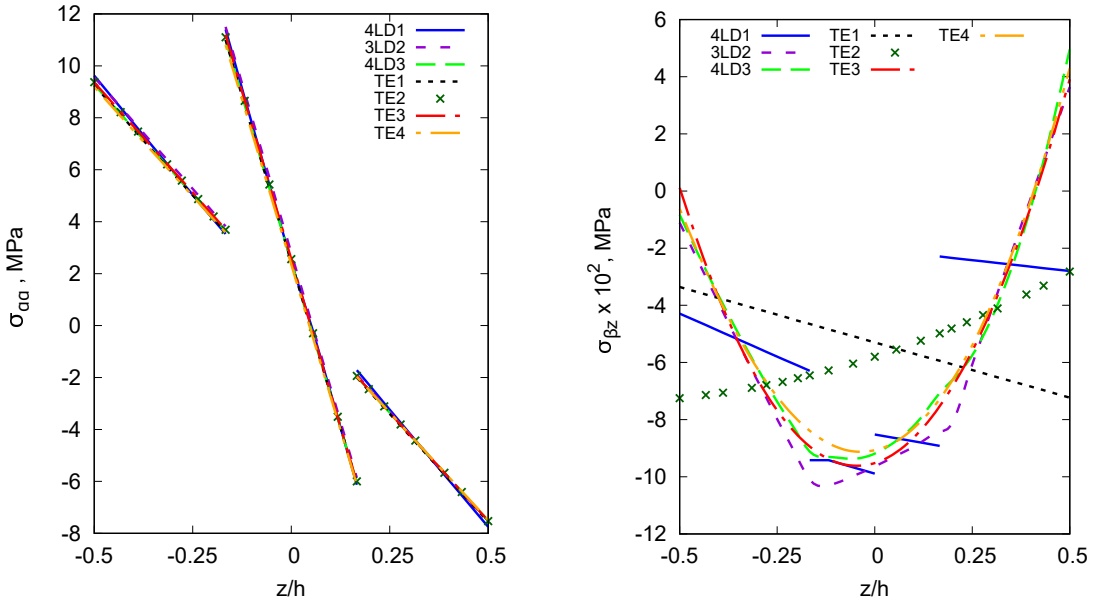

(a) $\sigma_{\alpha\alpha}$ (b) $\sigma_{\beta z}$

Fig. 4.9 Convergence analyses of the composite hinged cylindrical shell under P = 2000 N for stresses evaluation at $\alpha = 254$ mm and $\beta = 127$ mm. Comparison of various orders of both Lagrange expansion functions in the thickness direction and Taylor expansions. Lamination sequence: $[0°, 90°, 0°]$.

Theory	DOFs	$[0°, 90°, 0°]$		$[90°, 0°, 90°]$		$[45°, 0°, -45°]$	
		$\sigma_{\alpha\alpha}$ [MPa]	$\sigma_{\beta z}$ [MPa×10^{-2}]	$\sigma_{\alpha\alpha}$ [MPa]	$\sigma_{\beta z}$ [MPa×10^{-2}]	$\sigma_{\alpha\alpha}$ [MPa]	$\sigma_{\beta z}$ [MPa×10^{-2}]
		2000 N	2000 N	2000 N	2000 N	1500 N	1500 N
TE1	2646	-7.563	-5.299	-21.264	-2.135	-11.840	-3.360
TE2	3969	-7.533	-5.802	-21.301	-2.530	-11.817	-3.607
TE3	5292	-7.510	-9.518	-21.214	-4.211	-11.796	-5.919
TE4	6615	-7.480	-9.069	-21.215	-4.231	-11.172	-6.260
4LD1	6615	-7.749	-9.899	-21.470	-3.861	-12.072	-5.932
3LD2	9261	-7.545	-9.635	-21.218	-3.998	-11.857	-5.943
4LD3	17199	-7.05	-9.192	-21.220	-4.157	-11.792	-5.949

Table 4.4 Circumferential normal stress and transverse shear stresses of the composite hinged shell for various theories and loads at $\alpha = 254$ mm, $\beta = 127$ mm and $z = 6.35$ mm for $\sigma_{\alpha\alpha}$ and $z = 0$ mm for $\sigma_{\beta z}$.

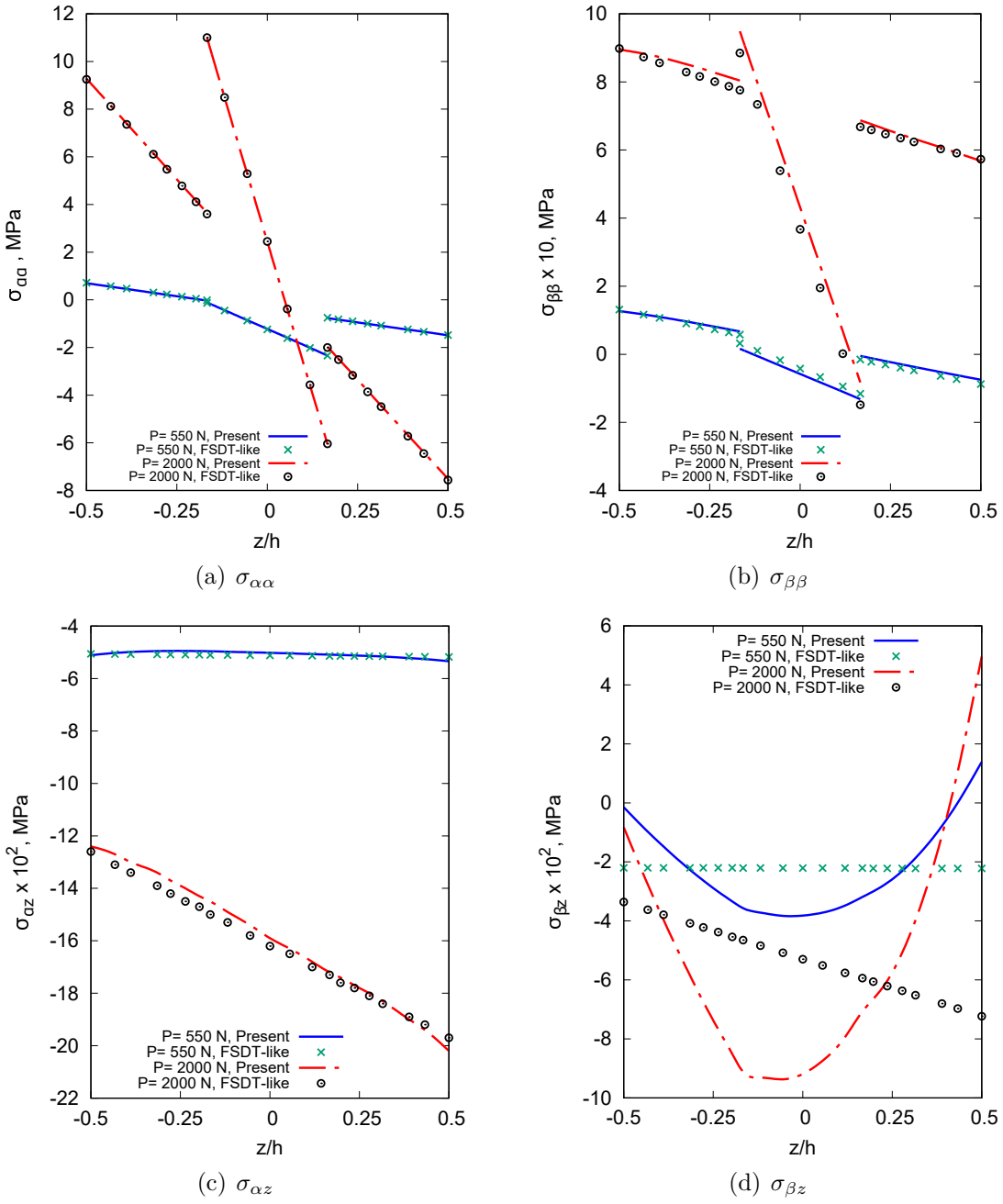

(a) $\sigma_{\alpha\alpha}$ (b) $\sigma_{\beta\beta}$

(c) $\sigma_{\alpha z}$ (d) $\sigma_{\beta z}$

Fig. 4.10 Through-the-thickness stress for various load values at $\alpha = 254$ mm and $\beta = 127$ mm of the composite hinged shell. Lamination sequence $[0°, 90°, 0°]$.

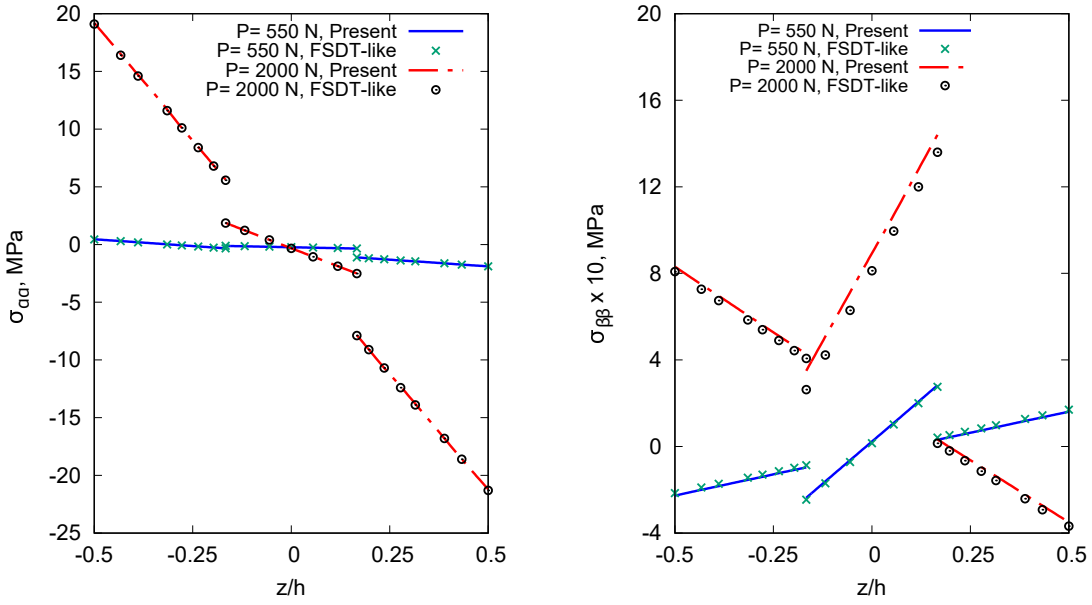

(a) $\sigma_{\alpha\alpha}$

(b) $\sigma_{\beta\beta}$

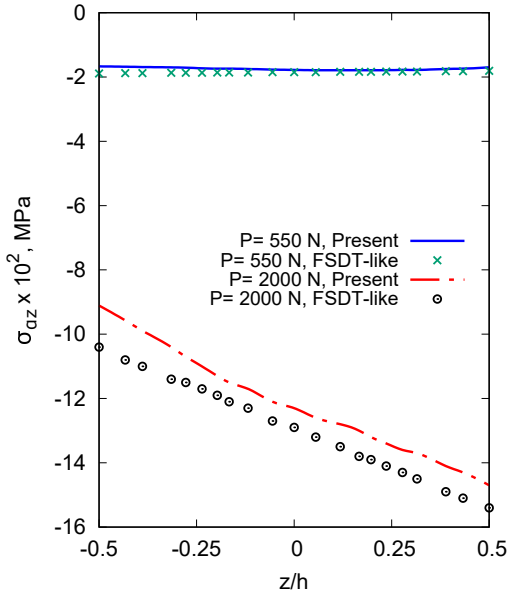

(c) $\sigma_{\alpha z}$

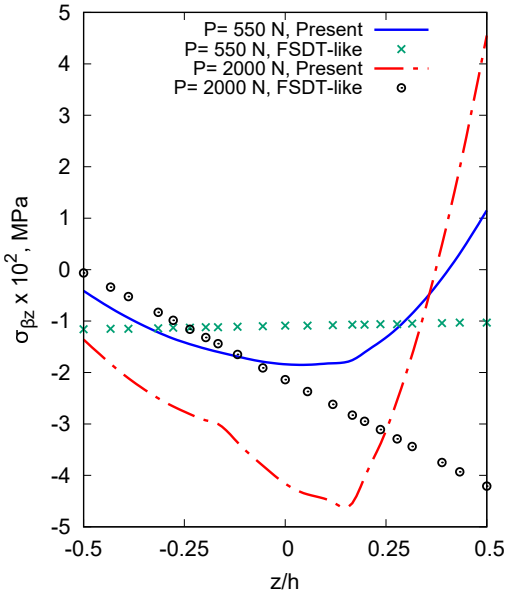

(d) $\sigma_{\beta z}$

Fig. 4.11 Through-the-thickness stress for various load values at $\alpha = 254$ mm and $\beta = 127$ mm of the composite hinged shell. Lamination sequence $[90°, 0°, 90°]$.

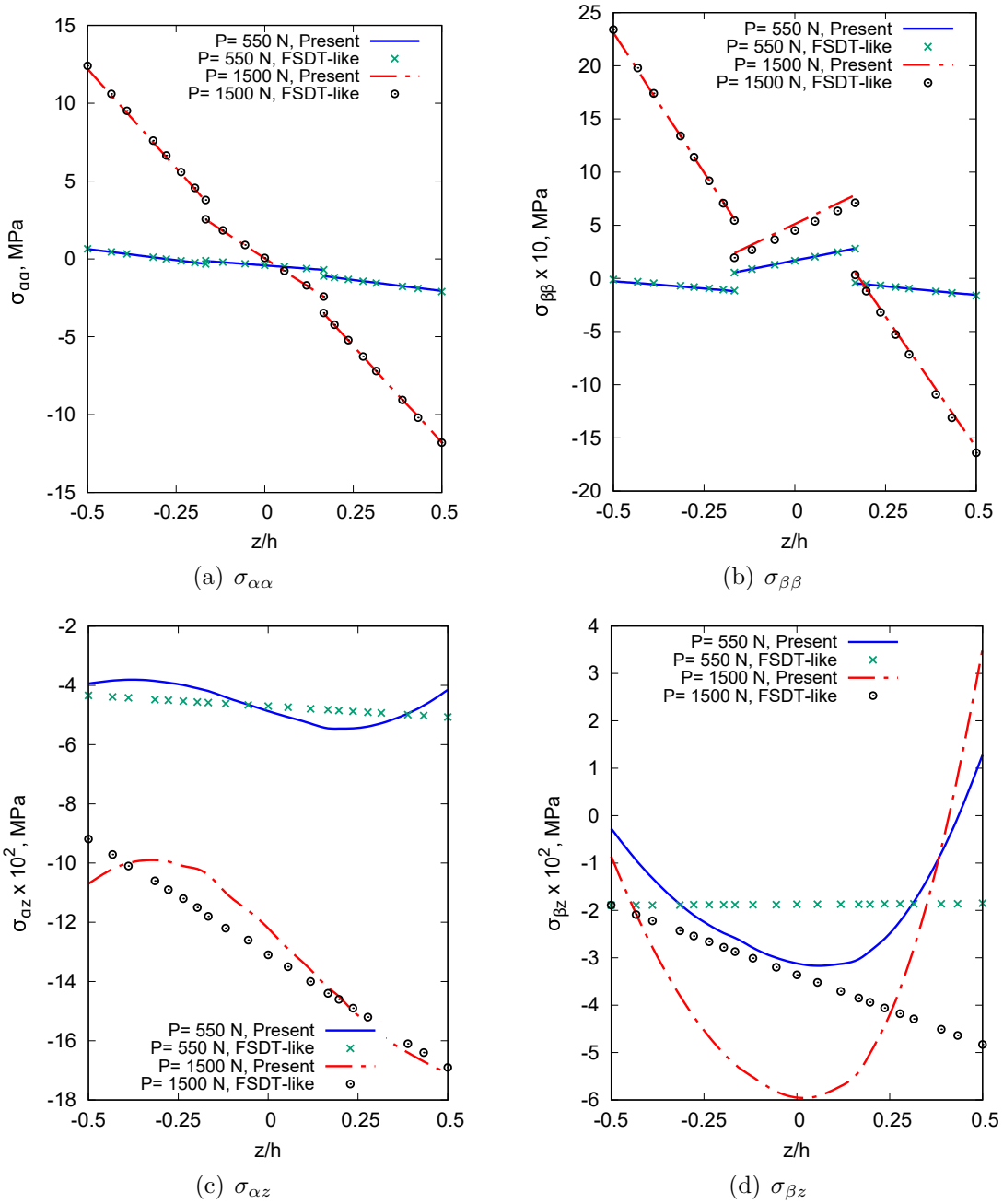

(a) $\sigma_{\alpha\alpha}$ (b) $\sigma_{\beta\beta}$

(c) $\sigma_{\alpha z}$ (d) $\sigma_{\beta z}$

Fig. 4.12 Through-the-thickness stress for various load values at $\alpha = 254$ mm and $\beta = 127$ mm of the composite hinged shell. Lamination sequence $[45°, 0°, -45°]$.

Next, another stress analysis is performed considering the hinged shell structure with stacking sequence $[90°, 0°, 90°]$ subjected to a line force in $\alpha = 254$ mm, $z = 6.35$ mm. Figure 4.13 shows the nonlinear equilibrium path of the composite hinged shell subjected to the line force. Finally, for the sake of completeness, the circumferential normal and

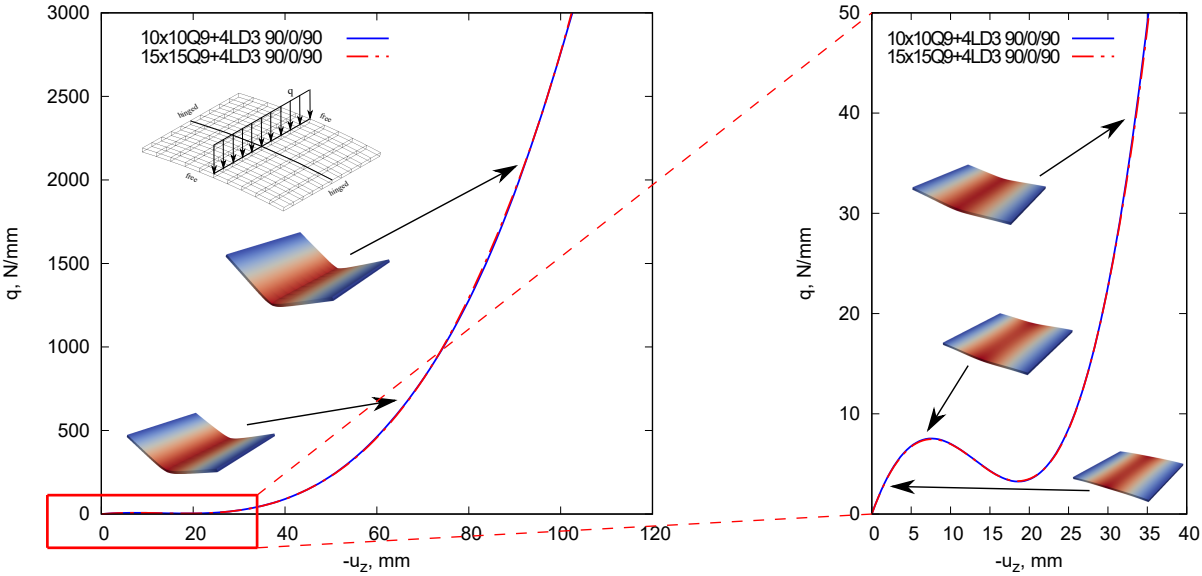

Fig. 4.13 Nonlinear equilibrium trend of the composite hinged shell under line loadings. Stacking sequence $[90°, 0°, 90°]$.

transverse shear stresses in the z-direction for a line load conditions are plotted in Fig. 4.14.

Solid square cross-section beam under sinusoidal loading (dynamic analysis)

A simply supported square cross-section beam was analyzed as the first dynamic example, see Fig. 4.15. The square cross-section has the following geometrical characteristics: sides are equal to 0.1 m, span-to-height ratio L/h is equal to 100. The whole structures has the following material data: E= 69 GPa, ν= 0.33 and ρ= 2700 kg/m^3. This structure is modelled by means of 10B4 finite elements along the y-axis and a quadratic approximation is used on the cross-section (L9). The structure is loaded with a single harmonic load applied at the center of the mid-span section:

$$P_z(t) = P_{z_0} sin(\omega t) \tag{4.41}$$

where P_{z_0}= -1000 N is the amplitude of the sinusoidal load, whereas ω= 7 rad/s is the angular frequency.

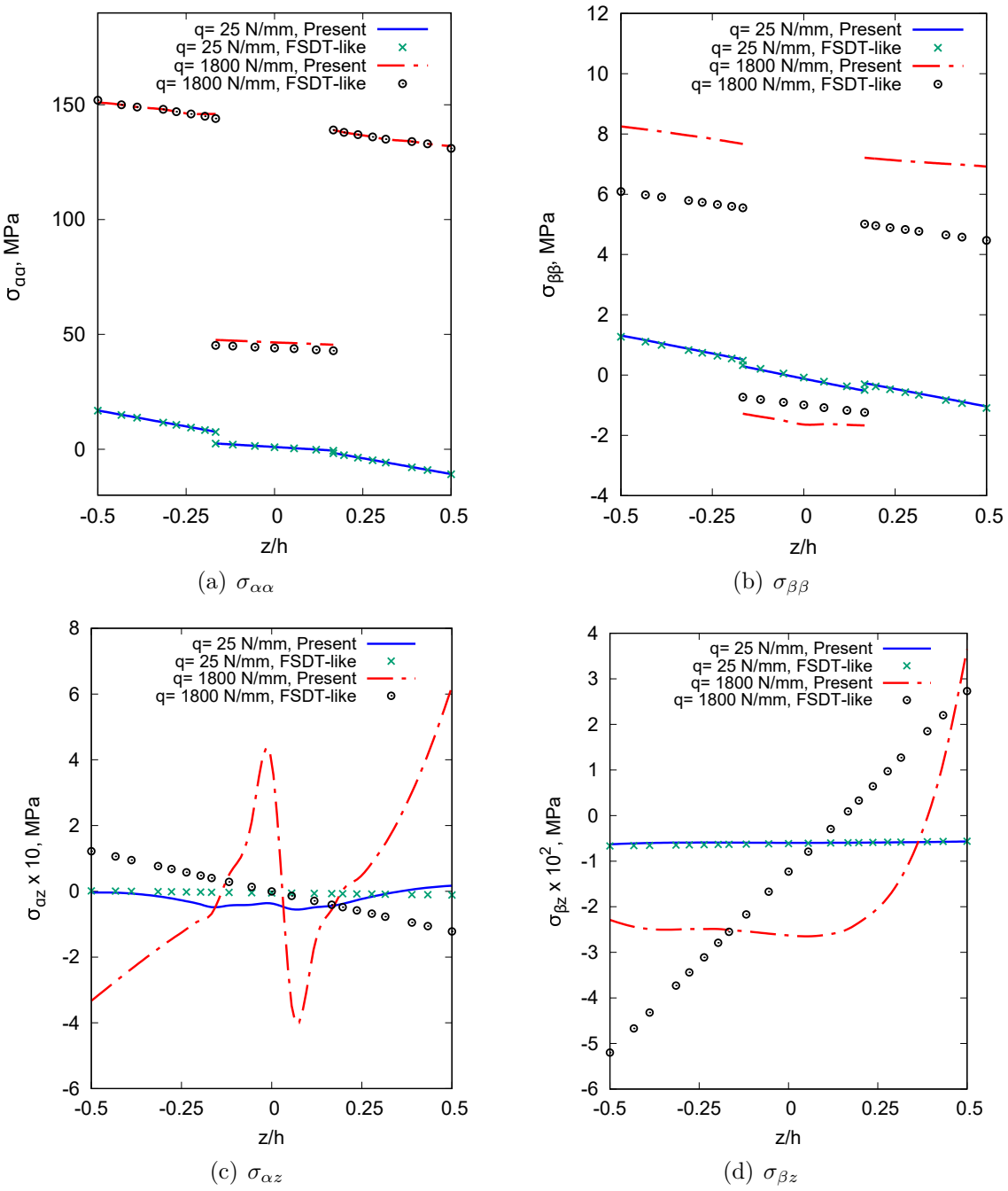

(a) $\sigma_{\alpha\alpha}$ (b) $\sigma_{\beta\beta}$

(c) $\sigma_{\alpha z}$ (d) $\sigma_{\beta z}$

Fig. 4.14 Stress distribution versus z of the composite hinged shell under line loading for different loads at $\alpha = 127$ mm and $\beta = 254$ mm. Lamination sequence $[90°, 0°, 90°]$.

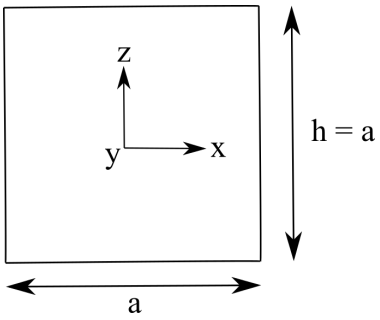

Fig. 4.15 Compact square cross section.

The dynamic response is analyzed using both the Newmark method and the mode superposition method over the time interval [0,8] s. 2000 steps (dt= 0.004 s) are chosen to perform direct time integration via the Newmark method. Instead, in the case of the mode superposition method, zero initial conditions are used and a convergence study on the number of modes to be used is necessary. Figure 4.16 shows the transverse displacement as a function of the time in the middle of the structure for different number of modes. It is noted that only 3 modes are sufficient for this type of analysis. The

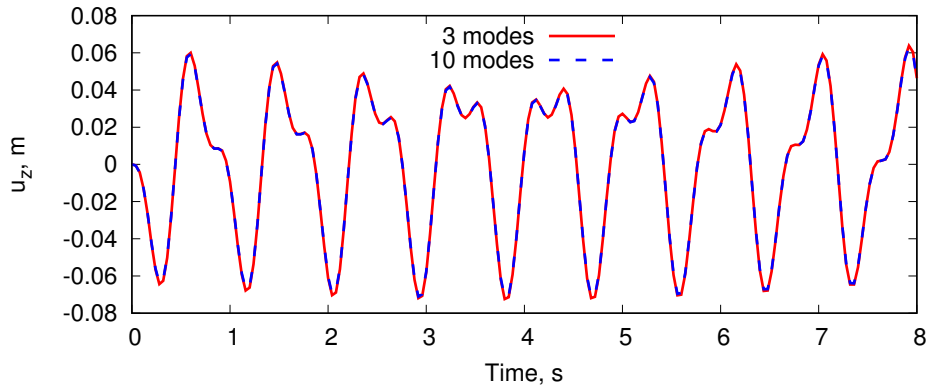

Fig. 4.16 Convergence study of the number of modes for the mode superposition method. Square beam under sinusoidal load.

comparison between the mode superposition and the Newmark method is shown, instead, in Fig. 4.17, including the comparison with the reference results [225, 226]. These results confirm the validity of the two methods, which are effective when displacement response is necessary. It should be mentioned that, since only 3 modes are enough to guarantee the effectiveness of the mode superposition, for this analysis, this method should be preferred because it is convenient in terms of computational costs.

In addition, also an evaluation of stresses is provided. First, convergence analyses on the dt and modes for the evaluation of the stresses are performed and illustrated in

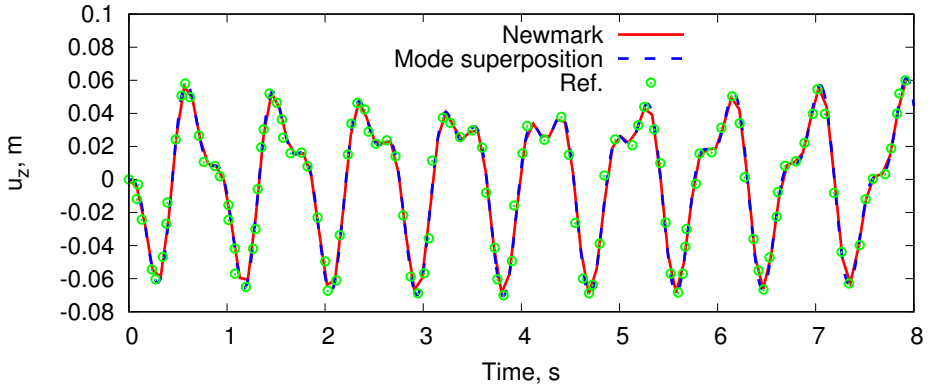

Fig. 4.17 Transverse displacement at the mid-span section by using the mode superposition method (3 modes) and Newmark method (dt= 0.004 s) see Ref. [225,226]. Square beam under sinusoidal load.

Figs. 4.18a and 4.18b. Figure 4.18c shows the comparison between the two methods for the shear stress, σ_{yz}, distributions as a function of the time. From Fig. 4.18, it can be noticed that there is a slight difference between the two resolution methods. The mode superposition allows us to evaluate stress using relatively few and correct mode shapes calculated by the proposed model. Furthermore, the resulting analyses indicate that using the mode superposition method there is a considerable time saving even for a simple model like this. This last aspect is very important to underline because it gives us a significant computational gain when dealing with more complicated structures. For completeness, a comparison between the results obtained with the present method and the MSC Nastran solid model [227] solutions is carried out in order to provide a validation of the proposed approach. In particular, both the axial stress, σ_{yy}, and shear stress, σ_{yz}, with respect to the time are shown in Fig. 4.19. It should be noted that by employing the present method, it is possible to accurately derive the stress distributions with a significant computational advantage than Nastran solid model due to a noticeable reduction in degrees of freedom (DOFs) (1488 vs 6102).

For the sake of completeness, the convergence analysis, see Fig. 4.20, for the cross-section discretization using both LE and TE theories is also reported. As a result, the cross-section of the structure was modelled with a cubic LE approximation on the cross-section (L16). Sixteen-point (L16) polynomials are considered, which lead to cubic displacement field approximations over the beam cross-section and, therefore, a better evaluation of stresses. From this figure, it is clear that a low-order model is sufficient to evaluate the normal stress σ_{yy}, whereas a high-order model is needed to accurately predict the transverse shear stress component. For example, the linear interpolation provided

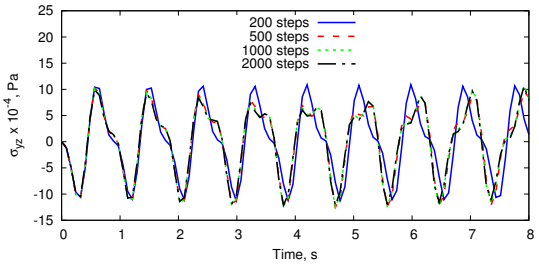

(a) Convergence analysis on the dt for the Newmark method

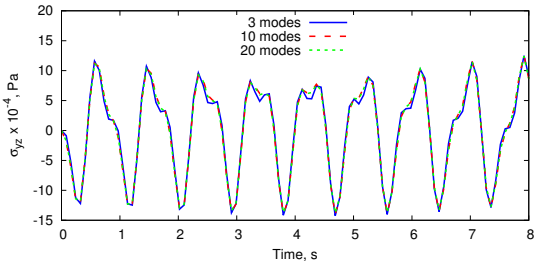

(b) Convergence analysis on the number of modes for the mode superposition method

%

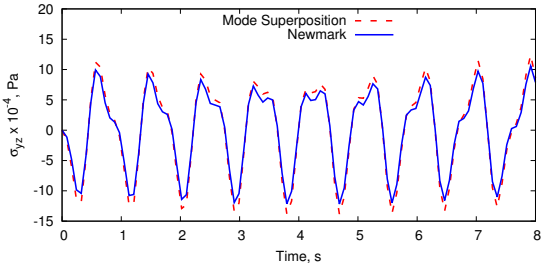

(c) Comparison between the Newmark method (500 steps) and the mode superposition method (10 modes)

Fig. 4.18 Shear stress distributions at a quarter of the beam (x=z=0) versus time. Square beam under sinusoidal load.

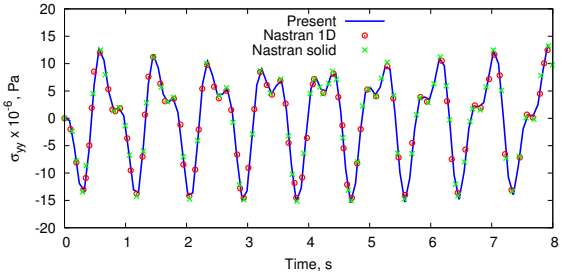

(a) σ_{yy} at x=0 m, z= 0.05 m

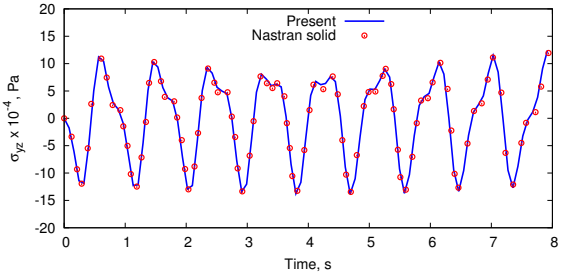

(b) σ_{yz} at x=0 m, z= 0 m

Fig. 4.19 Axial and shear stress distributions at a quarter of the beam versus time. Comparison between the present method and MSC Nastran solid model results. Square beam under sinusoidal load.

by the TE1 approximation is, clearly, not enough to catch the parabolic distribution of the transverse shear stress σ_{yz}. Axial and shear stress trends in the thickness direction

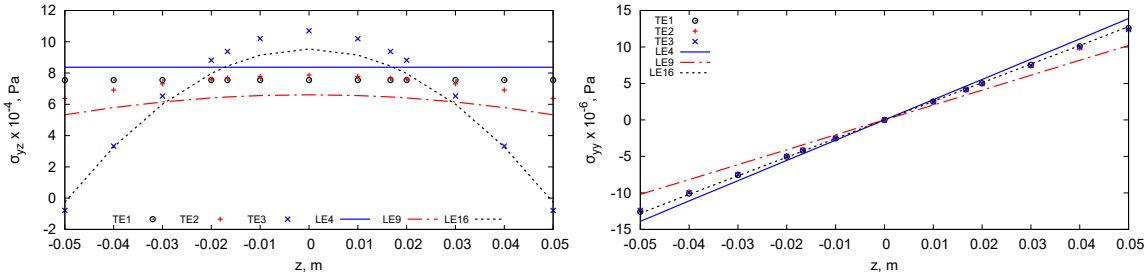

Fig. 4.20 Through-the-thickness stress distribution at a quarter of the beam at t = 0.6 s for different LE and TE theories. Square beam under sinusoidal load.

at a quarter of the beam, $y = L/4$, are shown in Fig. 4.21 at $t = 0.6$ s and $t = 4$ s using the mode superposition method. Furthermore, in these figures stress distributions adopting a theory based on linear interpolation (*FSDT-like*) is also provided, showing how inaccurate this theory is for evaluating transverse shear stress.

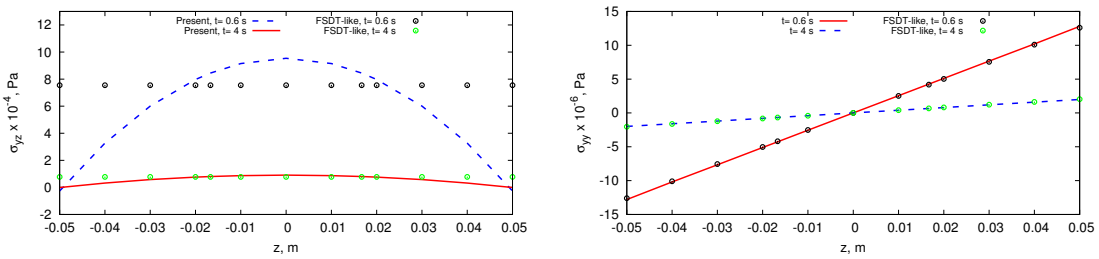

Fig. 4.21 Through-the-thickness distribution of axial, σ_{yy}, and transverse, σ_{yz}, stress components at a quarter of the beam at different times. Square beam under sinusoidal load. Mode superposition using 10 modes. LE16 beam model.

Thin-walled rectangular beam (dynamic analysis)

The transient analysis of a cantilever thin-walled rectangular cross-section beam is presented as the second dynamic example. This model, illustrated in Fig. 4.22, has the following dimensions: a = 1 m, L = 10 m, width-to-height ratio equal to 10 and t = 0.005 m. The material data are: $E = 69$ GPa, $\nu = 0.33$ and $\rho = 2700$ kg/m^3. This structure is relatively short and will incur into cross-sectional deformations, so higher-order theories are necessary. As a consequence, this structure is modelled by employing 10 B4 finite elements along the y-axis and 10L9 in the cross-section by using the CW methodology.

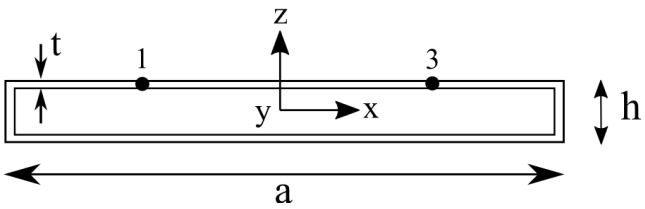

Fig. 4.22 Thin-walled rectangular cross-section.

A time-dependent sinusoidal loading with amplitude P_{z_0} = -10000 and angular frequency $\omega = 30$ rad/s is applied at point 1 at $y = L/4$. Dynamic response analyses are performed over the interval [0,1.5] s, using both the mode superposition method and Newmark method. Convergence studies prove that an appropriate time step for the Newmark method is $dt = 3{\times}10^{-3}$ s (500 steps) [225]. As in the previous case, convergence analyses on the number of modes to use for the mode superposition method are carried out. Transverse displacements as a function of the time for the different number of modes and the comparison between the Newmark method and mode superposition and reference solutions [225] at points 1 are provided in Figs. 4.23a and 4.23b. Consequently, 35 modes

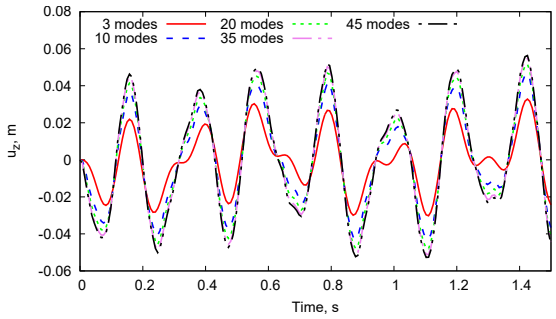

(a) Effect of the number of modes

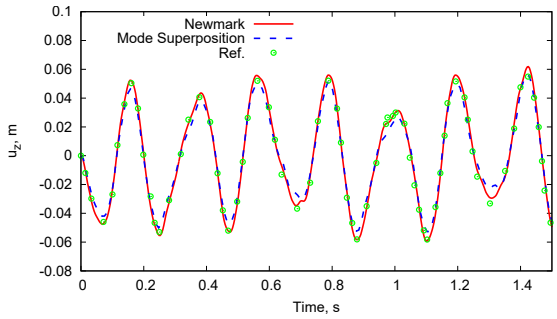

(b) Mode superposition (35 modes) vs Newmark method ($dt = 3\text{x}10^{-3}$ s) and Ref. [225]

Fig. 4.23 Transverse displacements of point 1 as a function of the time. Thin-walled rectangular beam subjected to sinusoidal loading.

turn out to be an appropriate number for the evaluation of transverse displacements.

The second part of this analysis deals with stress assessment. In particular, new convergence analyses on the number of modes is necessary using the mode superposition method for a correct stress investigation. Figure 4.24 shows the shear stress with respect to the time for the several number of modes. The results suggest that more modes should be considered for stress assessment. In particular, 100 modes are needed in this case to perform a correct analysis. The axial and shear stress distribution over the time at x= 0.495 m and $y = L/2$ is depicted in Fig. 4.25. For clarity, only the mode superposition

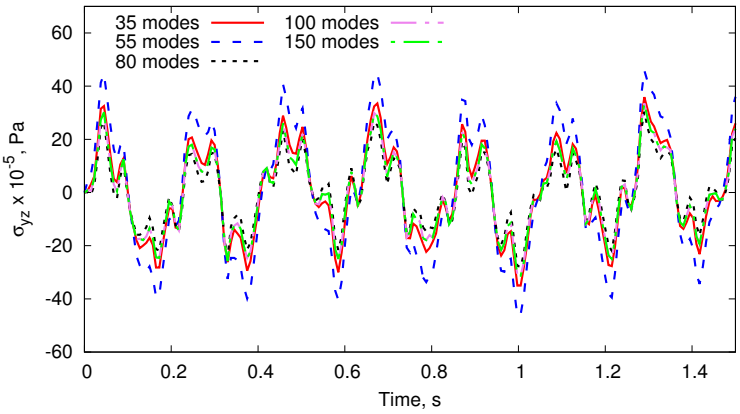

Fig. 4.24 Convergence analyses on the modes number for stress analyses using the mode superposition method. Thin-walled rectangular beam subjected to sinusoidal loading.

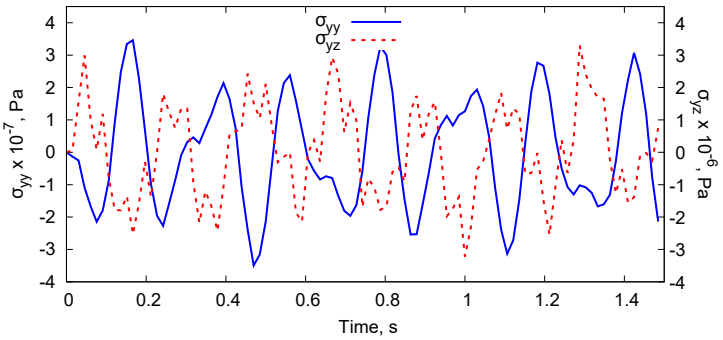

Fig. 4.25 The distribution of the axial (at x=0.495 m, z=0.0475 m) and shear (at x=0.495 m, z=0 m) stresses at the mid-span section vs time adopting the mode superposition method. Thin-walled rectangular beam under sinusoidal loading.

method is adopted for the evaluation of stresses due to the significant advantage in terms of computational cost and accuracy of results. Convergence analyses for several discretization theories on the cross-section are also provided in Fig. 4.26, where both TE and LE theories are used. As a results, it appears that a low-order theory is sufficient to evaluate normal stresses, while an high-order is mandatory to accurately compute transverse shear stresses. For completeness, axial and shear stress distributions in the z-direction for different times are presented in Fig. 4.27, including also the comparison between the L9 beam model and the results obtained employing a theory based on linear interpolation (*FSDT-like*).

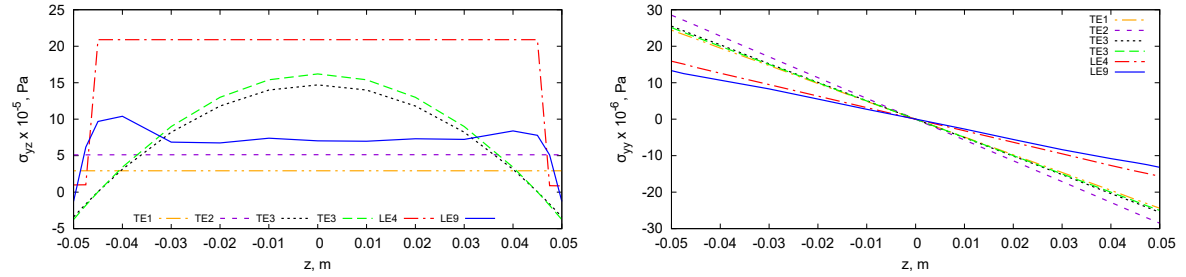

Fig. 4.26 Stress distributions in the z-direction at the mid-span section and $x = 0.495$ m at t = 1.3 s for various LE and TE theories. Thin-walled rectangular beam under sinusoidal loading.

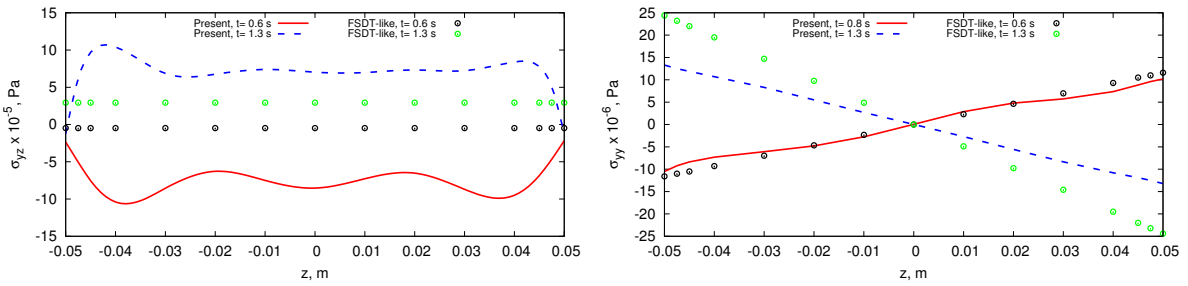

Fig. 4.27 Through-the-thickness axial and shear stress distribution at the mid-span section and x=0.495 m at $t = 0.6$ s and $t = 1.3$ s for σ_{yz} and at $t = 0.8$ s and $t = 1.3$ s for σ_{yy} considering the mode superposition method (100 modes). Thin-walled rectangular beam under sinusoidal loading.

Wing-box structure (dynamic analysis)

Transient analyses of a cantilever wing-box is investigated as the next dynamic case. The structure has the following dimensions: L = 3 m, b = 1 m, h = 0.5 m, the thickness (t) of the panels is equal to 2×10^{-3} m and the spar caps area is $A_s = 1.6\times10^{-3}$ m^2. An isotropic material was considered with the following properties: E= 75 GPa, ν= 0.33 and ρ= 2770 kg/m^3. The structure is modelled with 10B4 finite elements along the

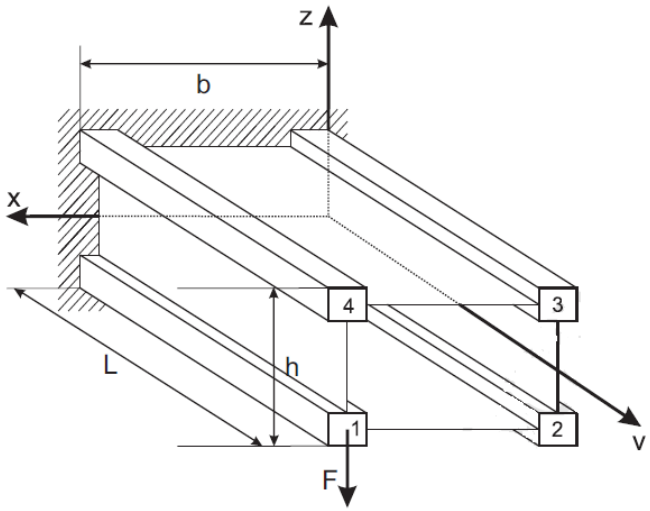

Fig. 4.28 Wing-box model.

y-axis 8L9 in the cross-section. The wing-box is reported in Fig. 4.28, in which it is also indicate the loading condition. In particular, a sinusoidal load having amplitude P_0 = 10000 N and angular frequency ω = 3 rad/s is applied in the stringer 1 at $y = L$.

First, transverse displacements over the time at the load application point are plotted in Fig. 4.29 for various theories considering the Newmark scheme. Moreover, the maximum displacements at the middle of the stringer 1 at t= 0.5 s are tabulated in Table 4.5 for various theories. From these results, it evident that LE is a good choice to use for the following investigations.

Convergence studies for both the Newmark (dt) and mode superposition method (number of modes) are necessary in order to perform accurate analyses, see Fig.s 4.30a and 4.30b. Instead, the comparison between the Newmark scheme, mode superposition method and reference results [226] is provided in Fig. 4.30c.

Next, analyses of the stresses, axial load and mean shear flow are presented. These studies require a more refined model, and, after convergence analyses, we have chosen to use 52L9, whereas 150 modes are considered for the mode superposition method. The distributions of the axial load in the upper stringer, P, at $y = 0$, and mean shear

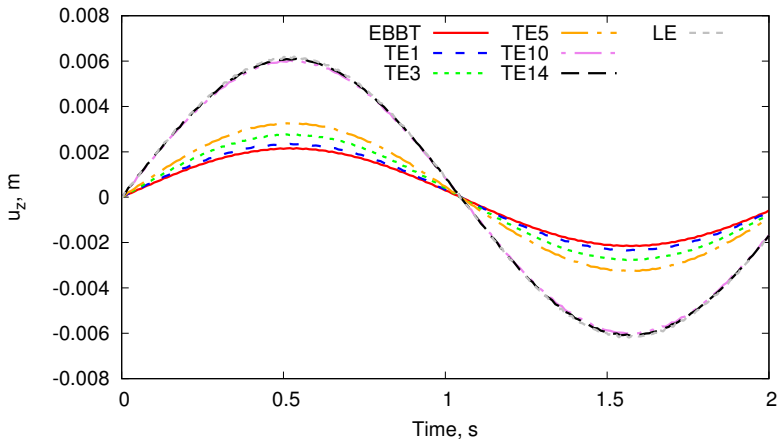

Fig. 4.29 Transverse displacements vs time at the load application point using the Newmark algorithm (dt= 0.01 s) for several theories. Wing-box structure.

Theory	Stringer 1
-	$u_{z_{max}}$ [mm]
EBBT	2.17
TE 1	2.36
TE 3	2.78
TE 5	3.28
TE 10	6.07
TE 14	6.11
L9	6.19

Table 4.5 Maximum transverse displacements at the middle of the stringer 1 employing various theories at t= 0.5 s and using the Newmark scheme. Wing-box structure.

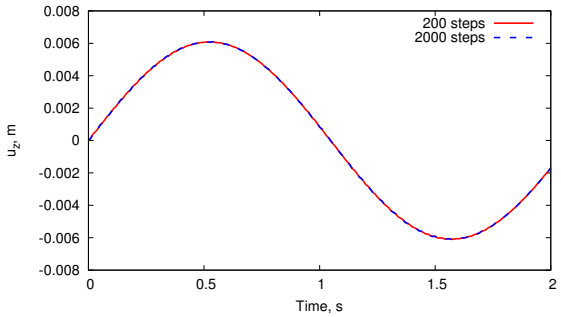

(a) Convergence for the dt

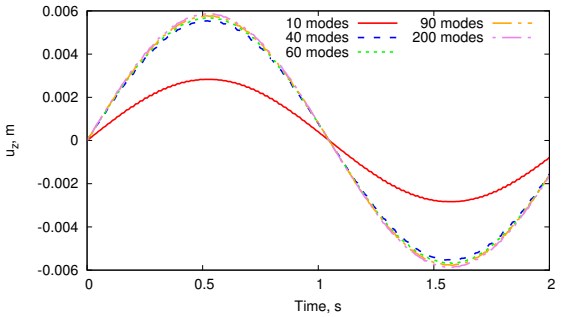

(b) Convergence study for the number of modes

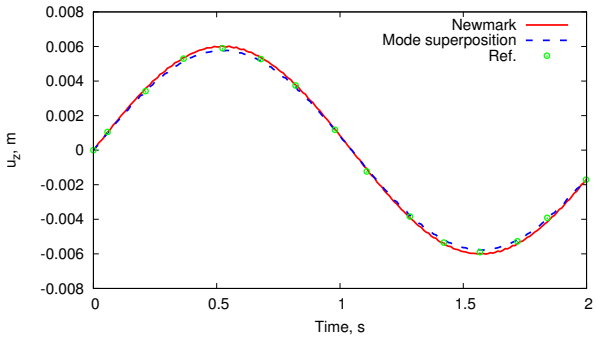

(c) Newmark method (dt= 0.01 s) vs mode superposition (90 modes) and Ref. [226]

Fig. 4.30 Transverse displacements with respect to the time at the load application point. Wing-box structure.

flows in the panel, q, at $y = L/4$, as a function of the time are illustrated in Fig. 4.31. For completeness, the through-the-thickness axial and shear stress distributions for two

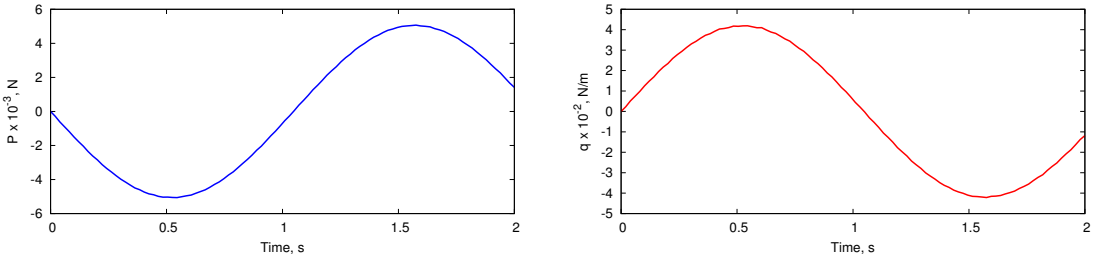

(a) P in the upper stringer at $y = 0$ m (b) q in the panel, at $y = 0.9$ m

Fig. 4.31 Time-dependent axial load (P) and mean shear flows (q) using the mode superposition method (150 modes). Wing-box structure.

times are reported in Fig. 4.32, showing the difference with the results obtained using a *FSDT-like* theory.

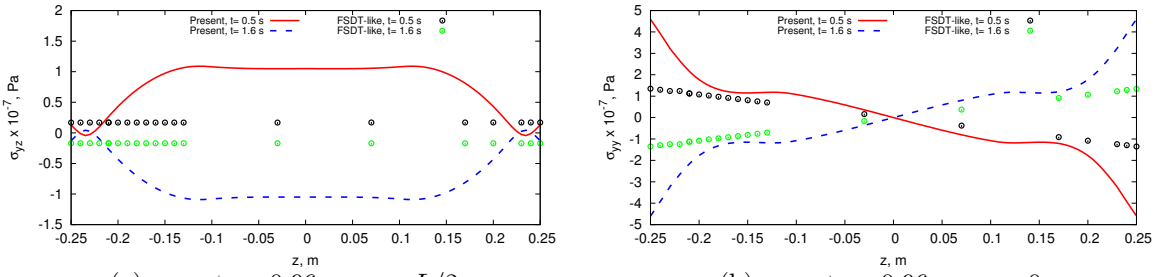

(a) σ_{yz} at x=0.96 m, $y = L/2$ (b) σ_{yy} at x=0.96 m, $y = 0$

Fig. 4.32 Through-the-thickness axial and shear stress distribution employing the mode superposition method (150 modes). Wing-box structure.

Composite plate subjected to a step loading (dynamic analysis)

The next study case concerns a four-layer square composite plate under step loading of intensity 1 N/mm^2. The geometric characteristics of the plate are the same as in the previous isotropic case. The material data of this structure are the following: $E_1 = 525000$ N/mm^2, $E_2 = E_2 = 21000$ N/mm^2, $G_{12} = G_{13} = G_{23} = 10500$ N/mm^2, $\nu_{12} = 0.25$ and $\rho = 800$ kg/m^3. Both cross-ply $[0°/90°/90°/0°]$ and angle-ply $[45°/-45°/45°/-45°]$ plate are analyzed. In addition, both clamped-clamped and simply-supported boundary conditions are adopted in the following analyses. The structure is modelled adopting 12×12Q9 for the in-plane mesh approximation, whereas only 1LD3 is employed in each layer in the z-direction.

The response histories of the cross-ply and angle-ply laminated plate are illustrated in Figs. 4.33, 4.34 and 4.35, again in terms of displacements and stresses, and compared with the solution found in the literature [228] and obtained using the Abaqus software.

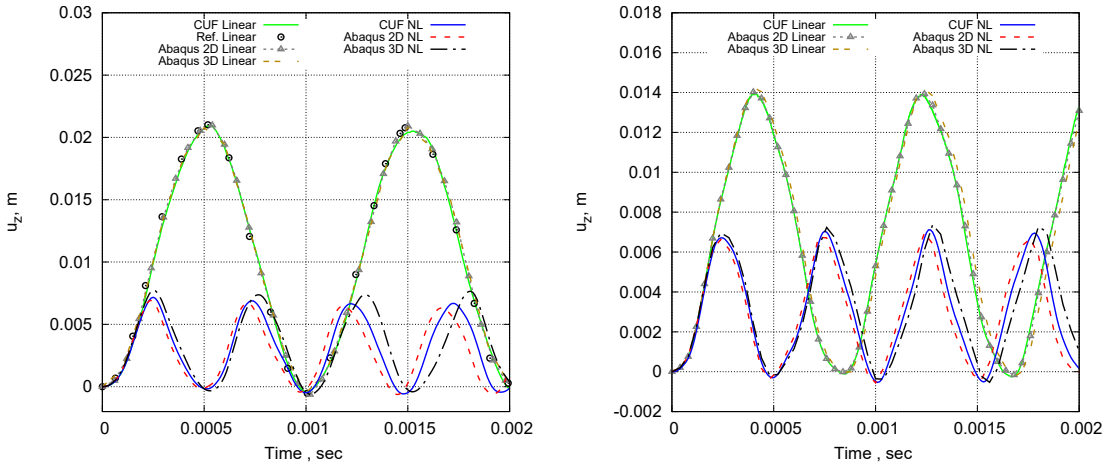

(a) 0/90/90/0 (b) 45/-45/45/-45

Fig. 4.33 Nonlinear dynamic response of the simply-supported composite plate. a/h = 50. Ref. [228].

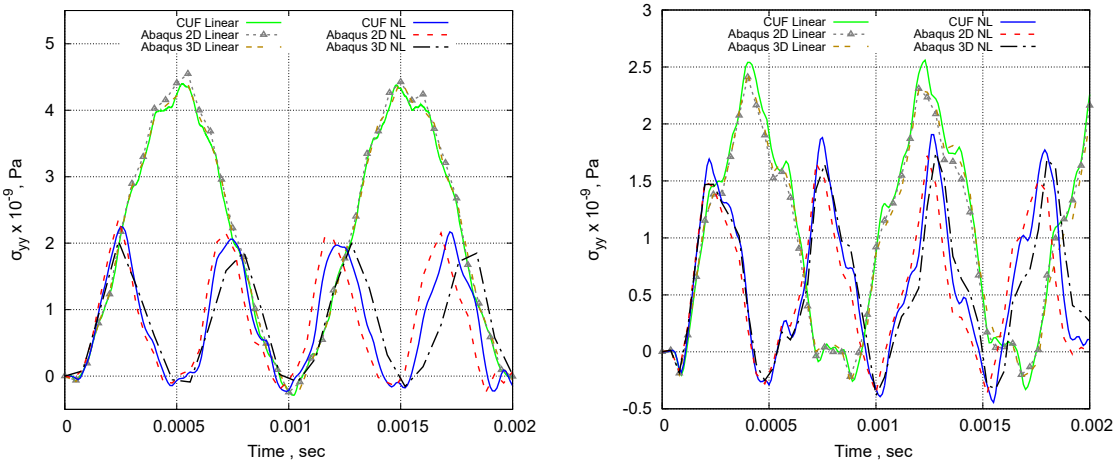

(a) 0/90/90/0 (b) 45/-45/45/-45

Fig. 4.34 σ_{yy} versus time of the simply-supported composite plate. a/h = 50.

Once more it is seen that the predictions of the presented nonlinear approach are broadly verified by comparison with the solution present in available literature and obtained using the commercial software Abaqus: such comparison is close for both deflections and stresses.

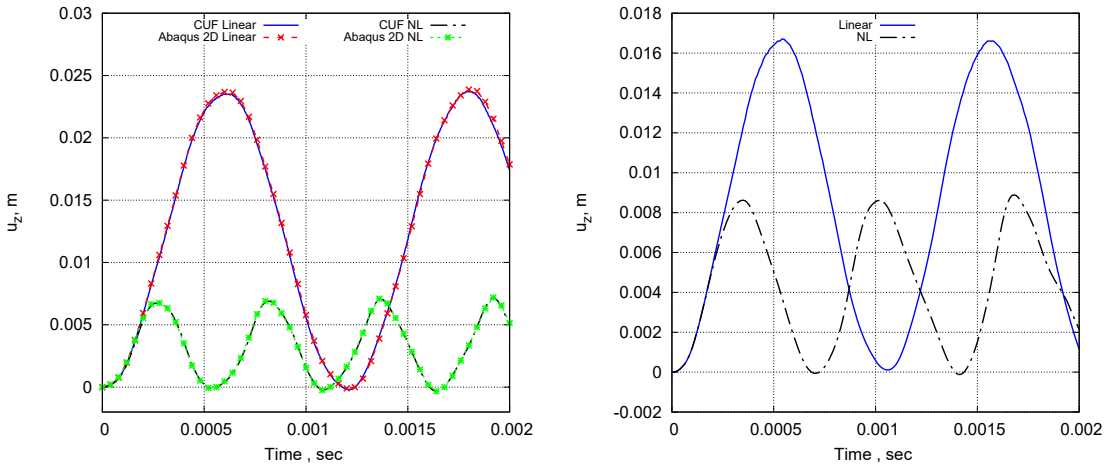

(a) 0/90/90/0 (b) 45/-45/45/-45

Fig. 4.35 Nonlinear dynamic response of the clamped-clamped composite plate. a/h = 50.

Next, we investigated the dynamics of a thick plate structure, in which the ratio a/h = 10 is considered. Figure 4.36 displays the dynamic response of the clamped-clamped composite [0°/90°/90°/0°] plate. Figure 4.37 illustrates the axial stress distribution over the time for various expansion orders. Furthermore, through-the-thickness stress distributions for several TE and LE functions are provided in Fig. 4.38. Finally, the deformed configuration and the displacement and stress contours based on the CUF 2D nonlinear model (12×12Q9+4LD3) at the $t = 5\times10^{-4}$ sec for the clamped-clamped composite [0°/90°/90°/0°] plate with a/h = 10 are depicted in Fig. 4.39.

4.4.2 Influence of geometrically nonlinear strain measures

Isotropic cylindrical structure (static analysis)

A clamped-clamped thin-walled cylindrical shell subjected to a transverse force is analyzed as the first assessment in order to evaluate the effect of the considered geometrically nonlinear strain model. Due to the symmetry of the structure, only one eighth of the entire model is analyzed. The geometrical and material data come from the book of Flügge [229]. In particular, they are: L = 600 in, t = 3 in, R = 300 in, $E = 3\times10^6$ psi and $\nu = 0.3$. The cylindrical structure is subjected to large deflections due to a transverse load P applied, as illustrated in Fig. 4.40.

First, convergence studies on the surface finite element mesh and different kinematic expansion functions in the thickness direction are needed to perform an accurate

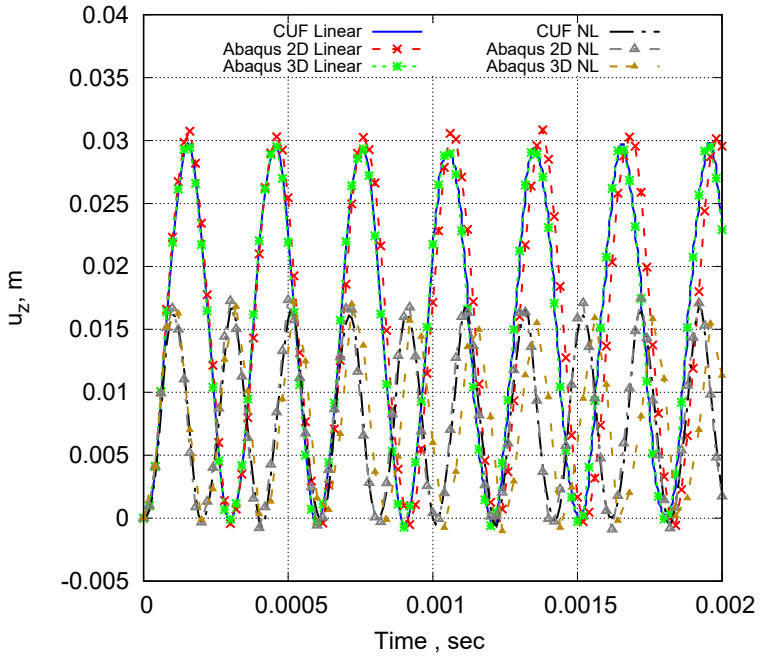

Fig. 4.36 Nonlinear dynamic response of the clamped-clamped composite [0°/90°/90°/0°] plate. a/h = 10.

comparison between the numerical results of different nonlinear strain approximations. Specially, we evaluate the nonlinear equilibrium path of the clamped-clamped thin-walled cylindrical shell structure for various in-plane meshes and LE functions in the z-direction. Figure 4.41a compares the equilibrium curves at the loading point for different CUF 2D shell elements, in which the in-plane meshes from 64Q9 to 400Q9 FEs are employed. In addition, the analysis using one LD1, LD2 or LD3 are illustrated in Fig. 4.41b. The results was validated with those obtained by Pagani *et al.* [230], where the same structure was analyzed using higher-order 1D beam elements. Moreover, the transverse displacement values for various CUF shell models and loads, along with the DOFs, are reported in Table 4.6. As evident from Fig. 4.41 and Table 4.6, to carry out an accurate static nonlinear response analysis and demonstrate the effects of the various nonlinear strain terms below, the structure should be modelled by employing 16×16Q9 for the in-plane mesh approximation and only 1LD2 in the thickness direction.

Figure 4.42 shows the nonlinear equilibrium curves of the cylindrical shell structure subjected to a transverse load for various geometrically nonlinear strain models at the loading point, including some deformed configurations. Basically, different nonlinear strain terms of the operator $\boldsymbol{b}_{nl}$ in Eq. 3.4 are activated in each geometrically nonlinear CUF shell theory. In essence, black dots in Fig. 4.42 denote the activated nonlinear strain terms. For instance, the analysis with all nonlinear terms involved (i.e., 3D full

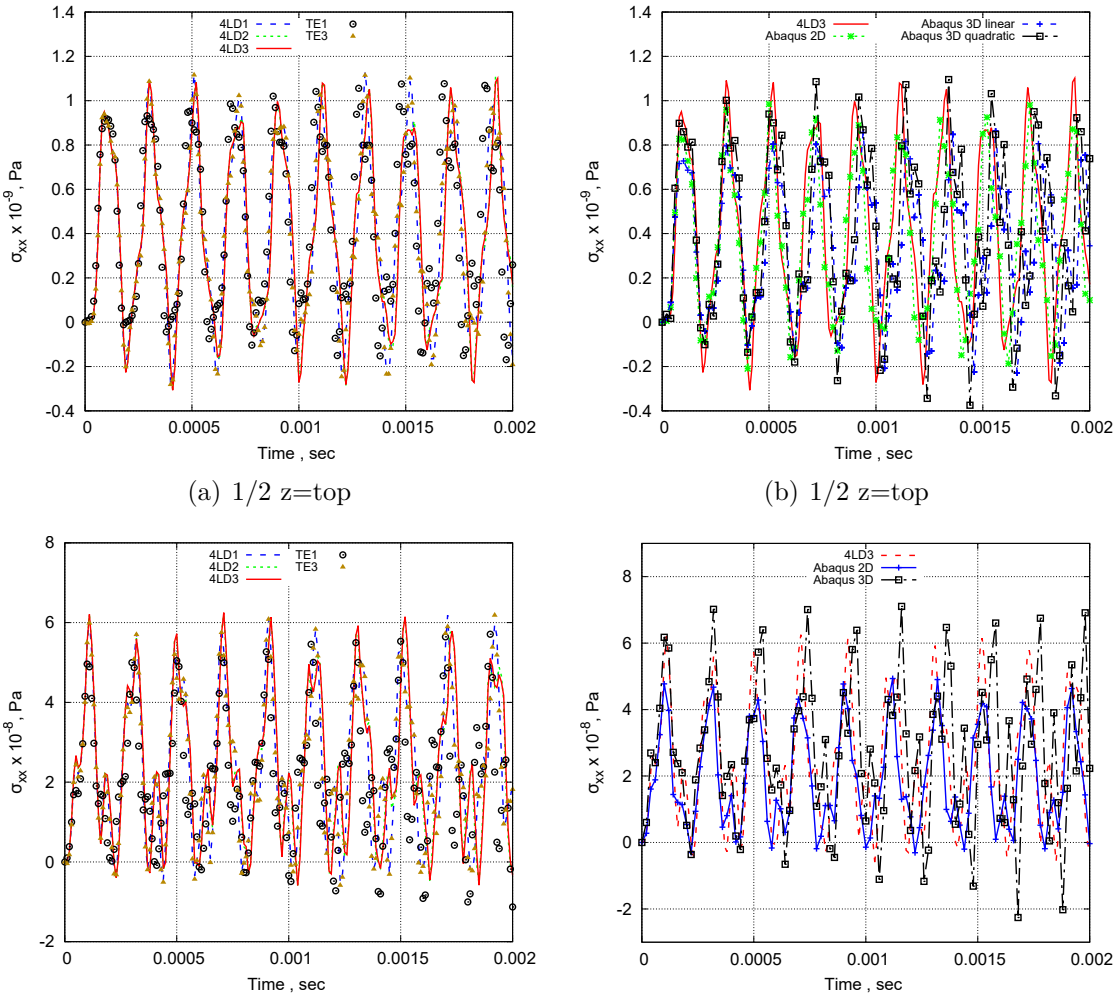

(a) 1/2 z=top (b) 1/2 z=top

(c) 1/4 z=top (d) 1/4 z=top

Fig. 4.37 σ_{xx} versus time. Clamped-clamped composite [0°/90°/90°/0°] plate. a/h = 10.

CUF shell models	DOFs	-u_z	
		2.5×10^5 lb	15×10^5 lb
8 x 8Q9 + 1LD2	2601	18.5	48.1
12 x 12Q9 + 1LD2	5625	21.8	50.8
16 x 16Q9 + 1LD2	9801	22.9	52.0
20 x 20Q9 + 1LD2	15129	22.9	52.1
Ref. [230]	10920	23.1	52.4

Table 4.6 Transverse displacement values [in] of the cylindrical structure for different models and loads at the load point.

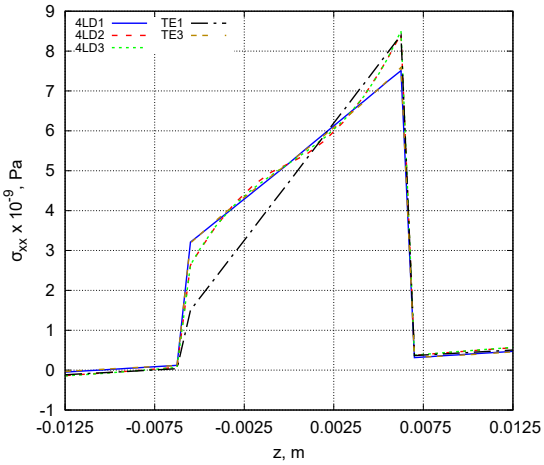

(a) σ_{xx}

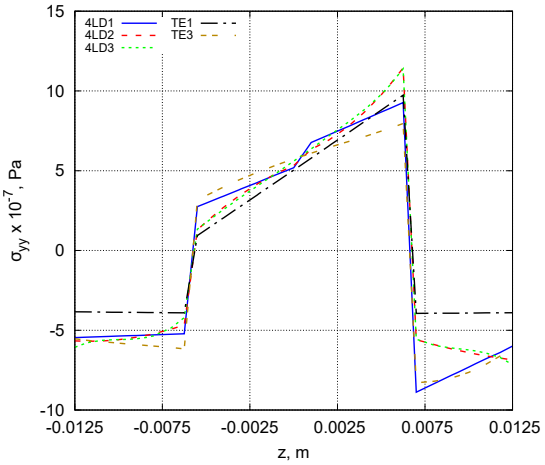

(b) σ_{yy}

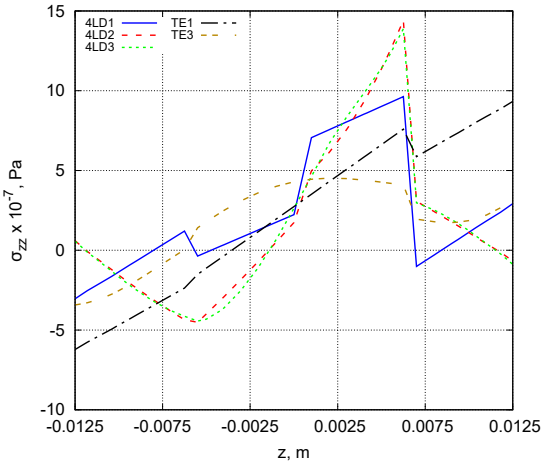

(c) σ_{zz}

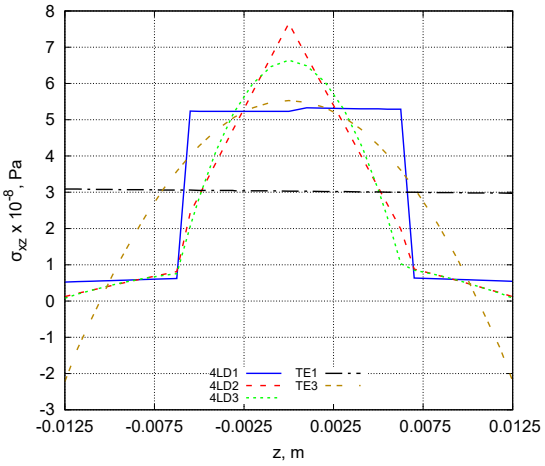

(d) σ_{xz}

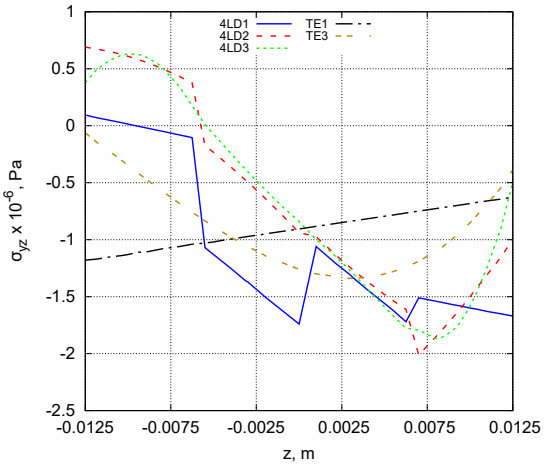

(e) σ_{yz}

Fig. 4.38 Through-the-thickness nonlinear stress distribution at $t = 5{\times}10^{-4}$ sec. Clamped-clamped composite [0°/90°/90°/0°] plate. a/h = 10.

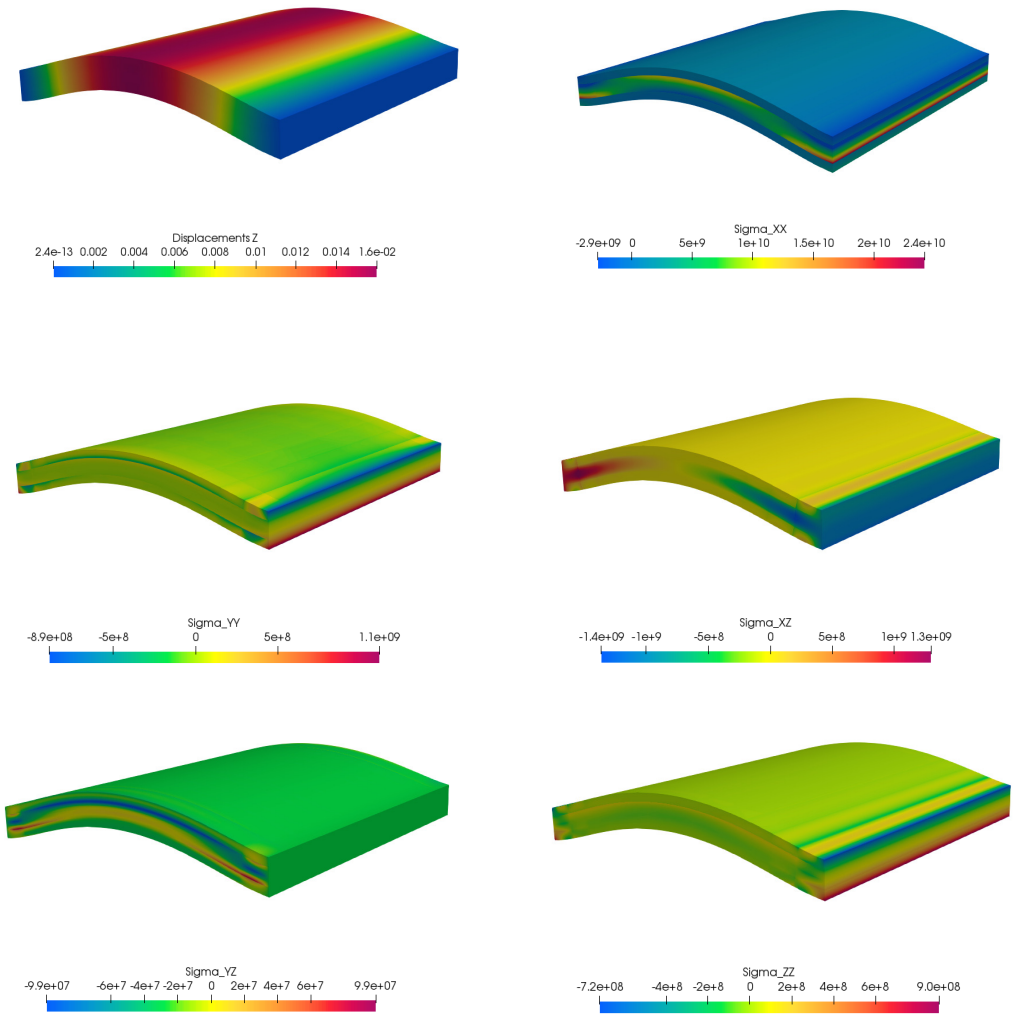

Fig. 4.39 Contour plots at $t = 5\times10^{-4}$ sec. Clamped-clamped composite [0°/90°/90°/0°] plate. a/h = 10.

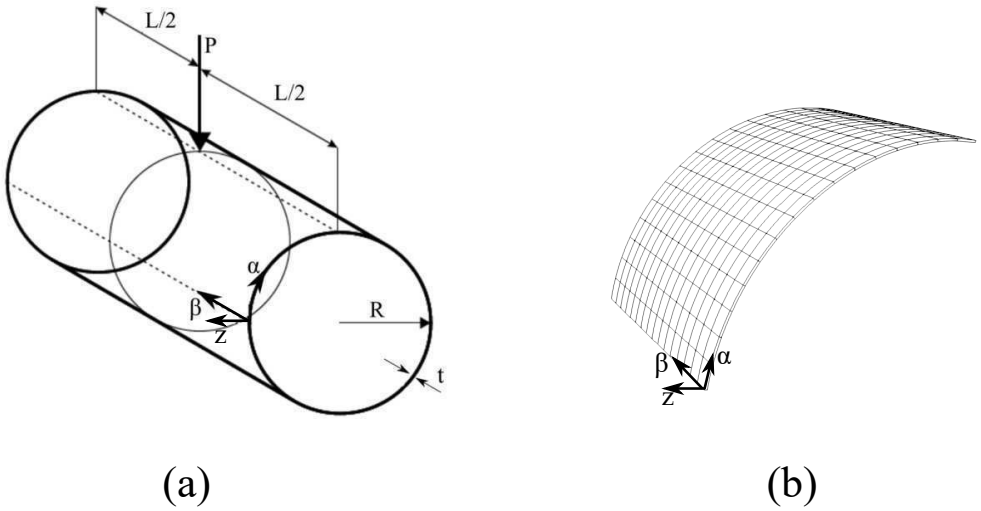

Fig. 4.40 Illustration of (a) the entire cylindrical shell structure subjected to transverse loadings and (b) surface mesh approximations of the model considered.

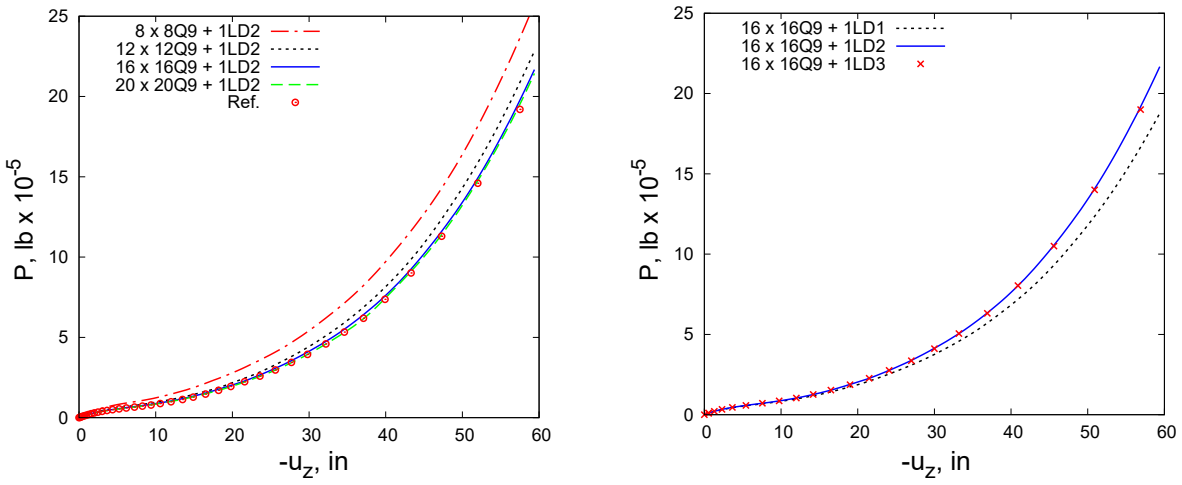

(a) Mesh approximation

(b) Kinematic expansion

Fig. 4.41 Convergence analyses of the clamped cylindrical shell.

GL nonlinear strain) is abbreviated as the “Full", while that with all nonlinear terms excluded indicates “linear" analysis. The “1DVK" and “2DVK" analyses indicate the von Kármán assumptions corresponding to 1D and 2D models. Instead, the analyses including nonlinear shear effects will be referred to as “1DVKs" and “2DVKs". Analysis

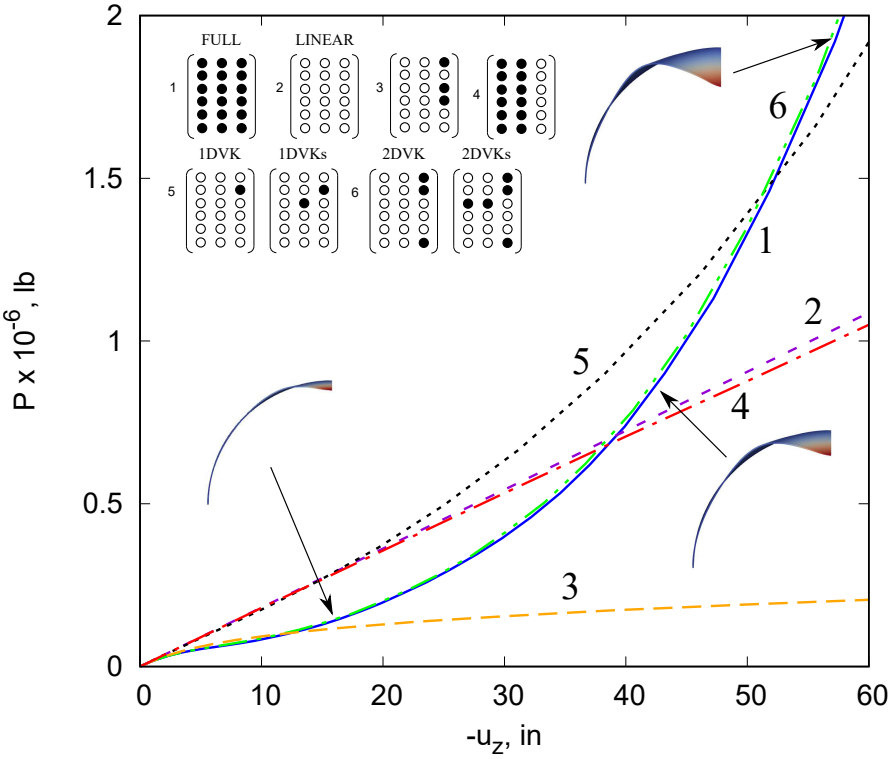

Fig. 4.42 Nonlinear equilibrium curves at the loading point of the cylindrical shell structure subjected to transverse loading for various geometrically nonlinear models.

case number 4 demonstrate that neglecting the higher-order derivatives of the transverse displacement component u_z (the third column of matrix $\boldsymbol{b}_{nl}$) affects the accuracy of the nonlinear solution. In fact, the curve is very similar to that of linear analysis (case number 2). As for the von Kármán models, cases 5 and 6 are the solutions for the traditional sets of 1D and 2D approximations. In particular, the 2DVK curve is very similar to the 3D full geometrically nonlinear solution, even for moderate and large displacement and rotation fields. On the other hand, the 1DVK case leads to a noticeably different curve than the FULL theory. In particular, this curve follows the linear solution until $u_z = 20$ in. The displacement predicted by the 1DVK (and 1DVKs) is greater than the linear case. It is important to underline that including or not the nonlinear shear terms in the von Kármán approximation leads to almost the same results. For the sake of completeness, adopting a symmetrical model, such as an one-eighth of the whole cylindrical structure

as in this case, can not provide accurate results when non-symmetrical load conditions or composite structures with complex laminations are considered.

Composite cylindrical structure (static analysis)

The next analysis deals with a clamped composite cylindrical shell structure subjected to compressive and transverse loadings, see Fig. 4.43. The vertical deflection and the rotation about the β-axis are restrained along its longitudinal edges. This composite cylindrical shell has the following stacking sequence [90°, 0°, 90°]. In the same figure, the boundary conditions and applied loads are depicted. The considered structure has

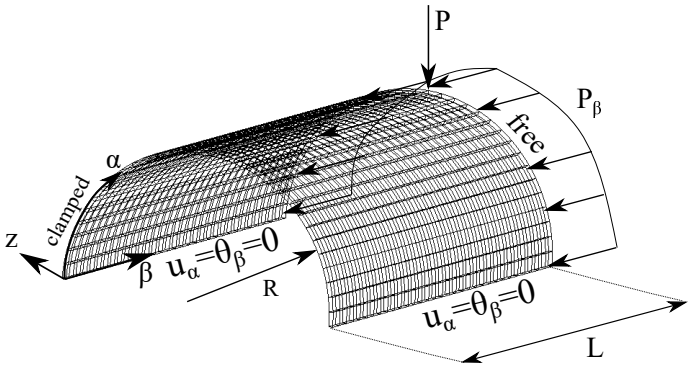

Fig. 4.43 Representation of the composite cylindrical shell structure under compressive and transverse loadings.

the following geometric data: L = 3.048 m, R_α = 1.016 m, and the thickness equal to 0.03 m. Each layer is made up of an orthotropic material with the following properties: $E_L = 2068.5\times10^4$ N/m^2, $E_T = 517.125\times10^4$ N/m^2, $G_{LT} = 795.6\times10^4$ N/m^2 and $\nu_{LT} = \nu_{TT} = 0.3$.

First, convergence analyses of the in-plane mesh approximation are carried out to achieve accurate static nonlinear response evaluations. In the thickness direction, only 1LD2 for each layer is employed. Figure 4.44 shows the transverse displacements versus applied loadings at the loading point for various CUF shell models, in which the in-plane meshes from 256Q9 to 1600Q9 FEs are considered. The nonlinear equilibrium path are split into two regions A and B. Moreover, the transverse displacement values for various models and loads, including the DOFs, are given in Table 4.7. As a result, the composite structure is well modelled by using 32×32Q9 for the in-plane mesh approximation and only 1LD2 for each layer in the z-direction.

Figure 4.45 provides the nonlinear equilibrium curves of the composite cylindrical shell under compressive and transverse loads based on different kinds of nonlinear strain approximations at the loading point. Particular interest is focused on the comparison

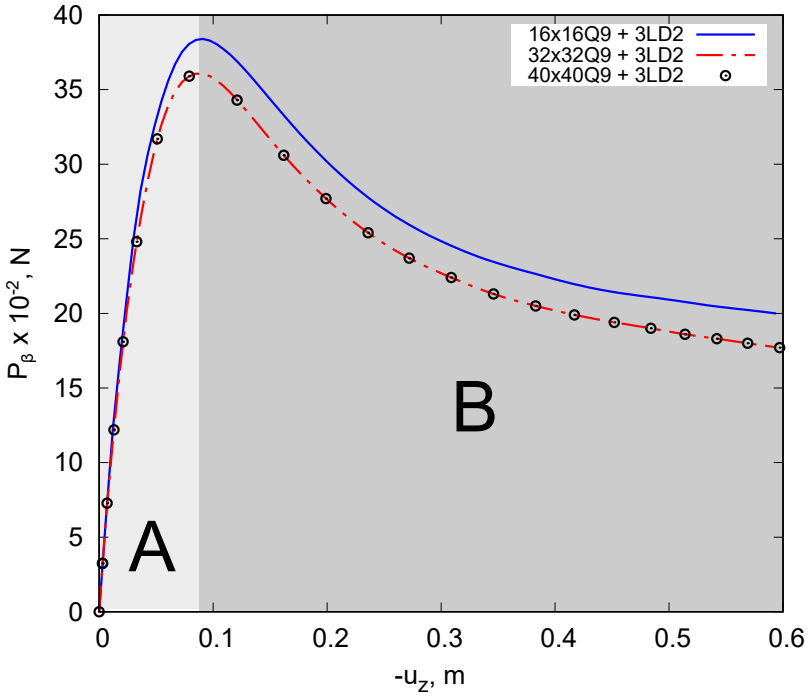

Fig. 4.44 Convergence analysis of the composite cylindrical shell under compression and transverse loadings. Comparison of various surface mesh approximations. $P_0/P_{\beta_0} = 0.1515$.

CUF shell model	DOFs	$-u_z$ [m]		
		$[90°, 0°, 90°]$		
		1800 N	2500 N in A	2500 N in B
16 x 16Q9 + 3LD2	22869	0.021	0.030	0.304
32 x 32Q9 + 3LD2	88725	0.020	0.033	0.236
40 x 40Q9 + 3LD2	137781	0.020	0.033	0.236

Table 4.7 Transverse displacement values of the composite cylindrical shell subjected to compression and transverse loadings for different models and loads at the load point. $P_0/P_{\beta_0} = 0.1515$.

between FULL, 2DVK and 2DVKs solutions in the regime of moderate and large displacements and rotations. It should be highlighted from Fig. 4.45 that the classical

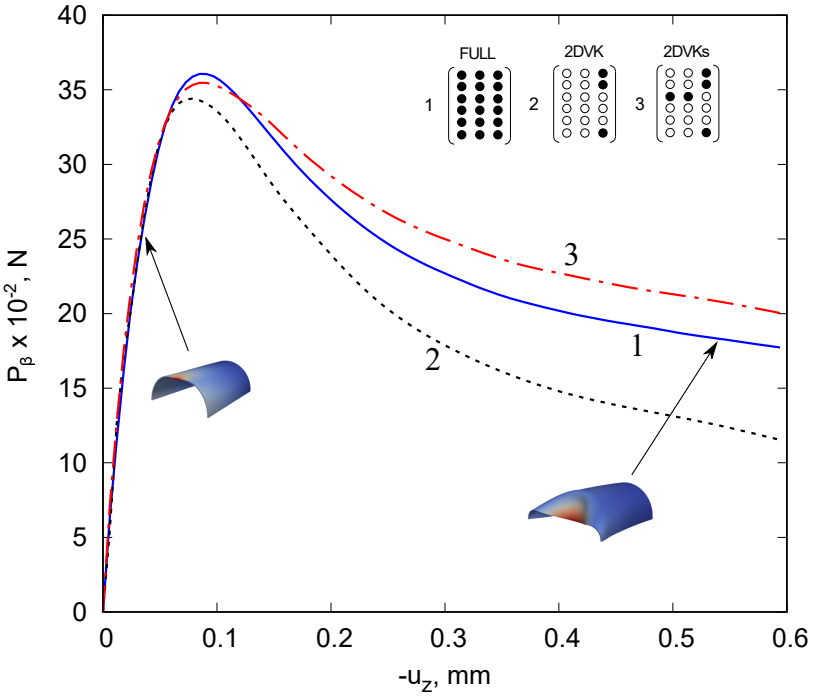

Fig. 4.45 Equilibrium trends at loading point of the composite cylindrical shell subjected to compressive and transverse loadings for several geometrically nonlinear models. P_0/P_{β_0} = 0.1515.

approximation of the von Kármán strains with nonlinear shear effects leads to less conservative results in the post-buckling regime than the FULL solution. On the contrary, curve 2 (the 2DVK solution) provides a more conservative solution.

Cantilever open channel-section beam with different initial deformations (dynamic analysis)

Finally, a cantilever open channel-section beam is investigated in the following analysis case. Figure 4.46 shows the structure geometry, with L = 1 m, a = h = 0.01 m and t = 0.001 m, and the initial deflection configurations considered. The beam has an elastic modulus (E) equals to 70 GPa, ν = 0.3 and ρ = 2700 kg/m^2. Along the y-axis, the structure is discretized by using 20 B4 beam elements. The cross-section discretization is achieved by using 11 LE9. The nonlinear dynamic analyses are carried out by adopting the HHT-α integration scheme with α = -0.1 and a time step of Δt = 0.01 sec.

The static equilibrium trends of the open channel-section beam structure are plotted in Fig. 4.47, where the displacement of the point V is evaluated. As predictable, the von

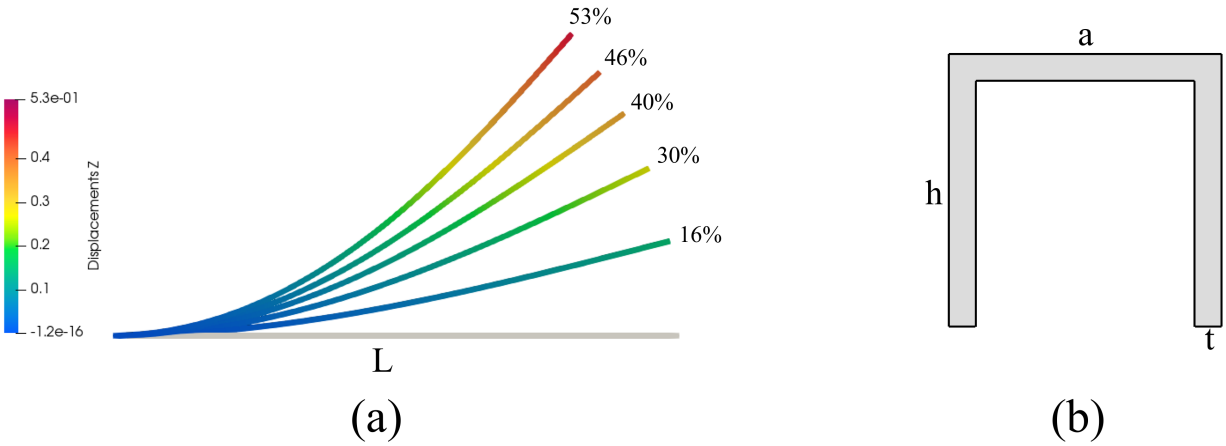

Fig. 4.46 (a) Different initial conditions; (b) Open channel-section beam.

Kármán models provide evident differences compared to the LE full solution, particularly for moderate/large deformations. On the other hand, the curves obtained using the TE kinematic theory lead to similar results to the LE full one.

The nonlinear transient response of the open channel-section structure considering different initial deflection configurations is presented in the following figures. In detail, from 16% (small deformation) to 53% of (moderate deflection) are analyzed in order to show the effect of the amplitudes and the importance of using both an appropriate nonlinear kinematic theory. Results of the dynamic response analysis are illustrated in Fig. 4.48. It can be noted that considering an initial amplitude of 46%, see Fig. 4.48e the periodicity of the response is lost, showing important nonlinear behaviours due to the deformability of the section ($x - z$ plane). Increasing the initial amplitude to 56%, this behaviour is even more noticeable as displayed in Fig. 4.48g.

Finally, the comparison of different theories considering the initial deflection of 53% is reported in Fig. 4.49. The results suggest that adopting a classical von Kármán nonlinear model or a TE theory lead to not accurate solutions. Therefore, the LE full models are mandatory to accurately investigate the dynamic response of open channel-section in moderate/large deformations, in which highly nonlinear effects occur.

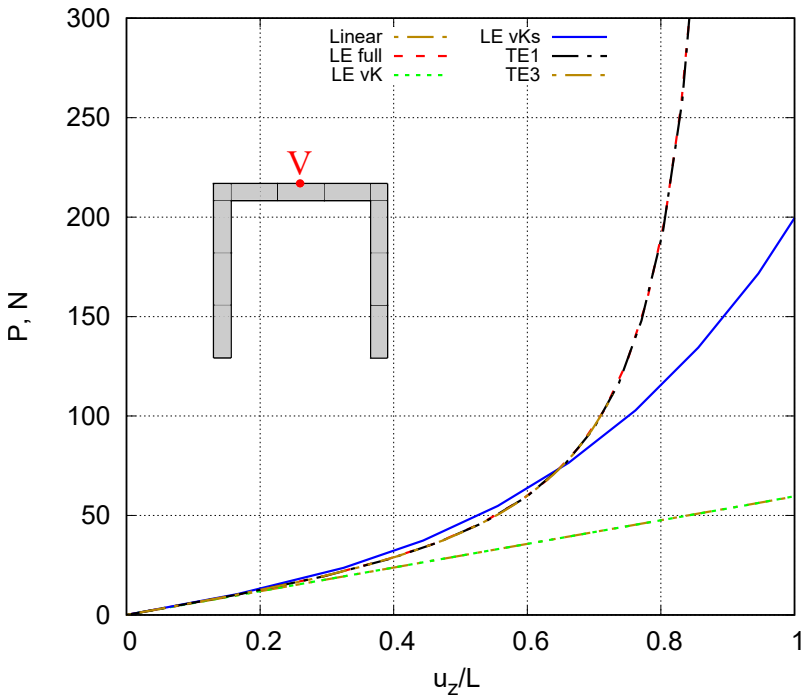

Fig. 4.47 Equilibrium curves considering different theories. Open channel-section beam.

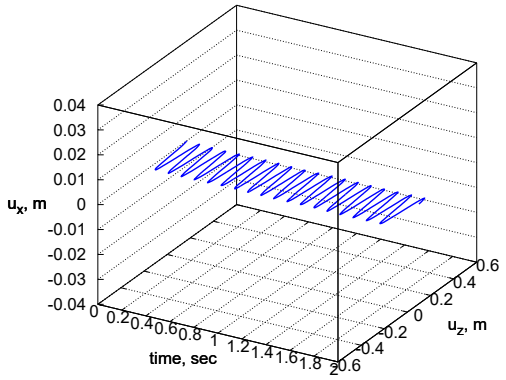

(a) 16%

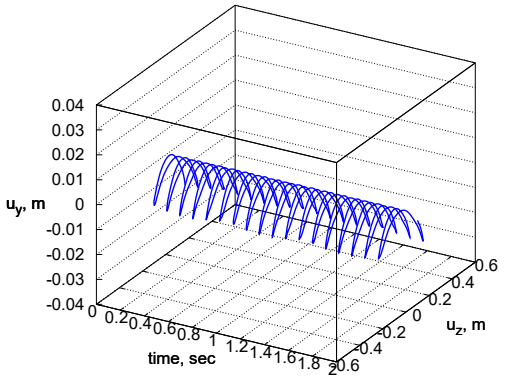

(b) 16%

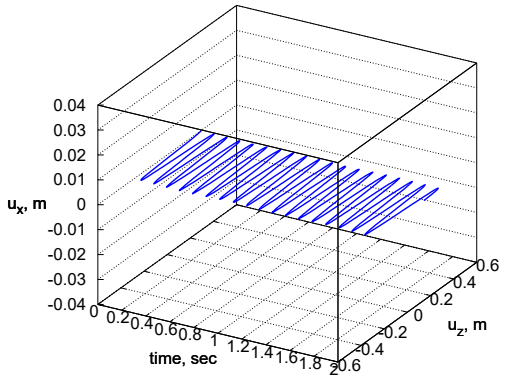

(c) 30%

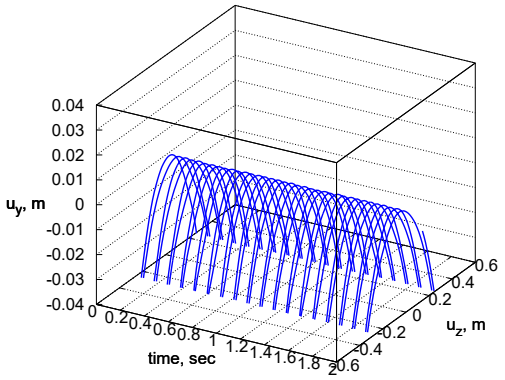

(d) 30%

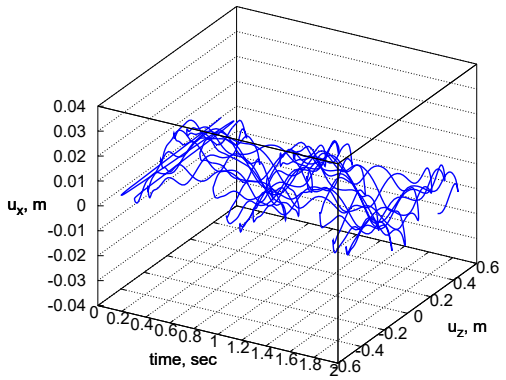

(e) 46%

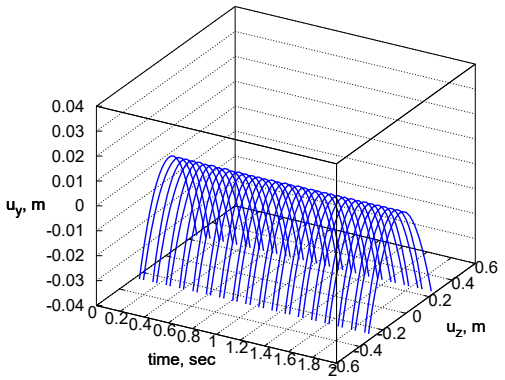

(f) 46%

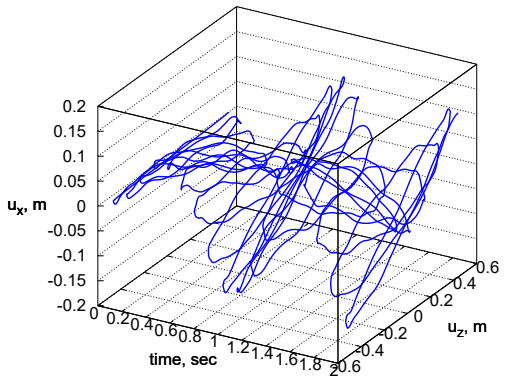

(g) 53%

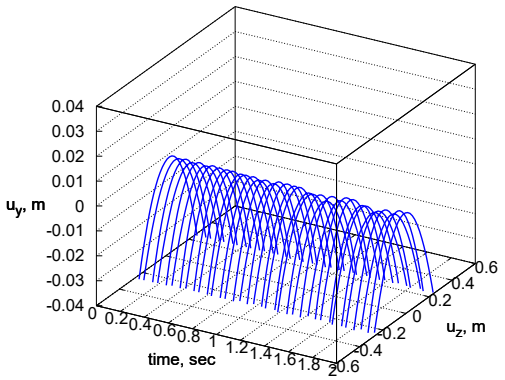

(h) 53%

Fig. 4.48 3D plots for different initial deflection configurations. LE full model. Open channel-section beam.

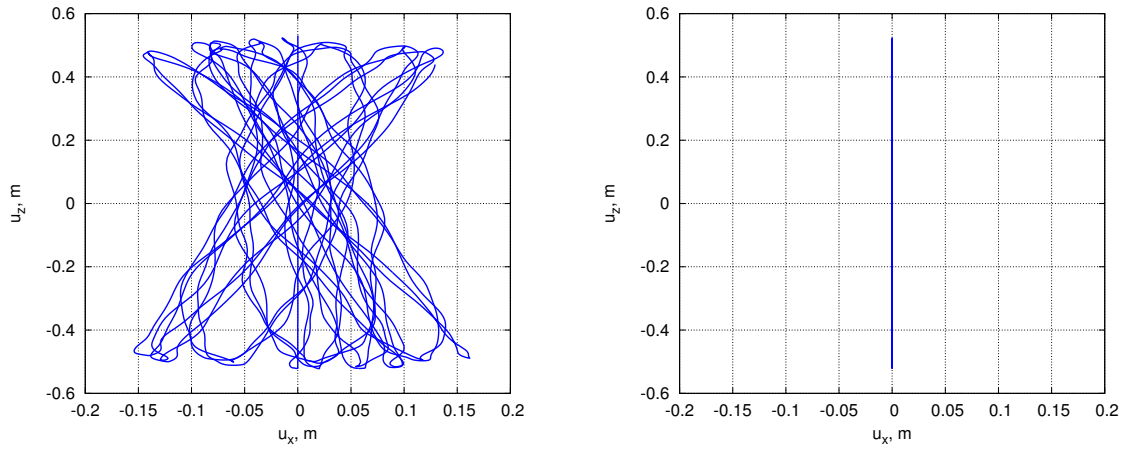

(a) LE Full

(b) LE vK

(c) TE1

(d) TE3

Fig. 4.49 Comparison of different theories considering the 53% of initial deflection. Open channel-section beam.

Chapter 5

Numerical results

Based on the formulations and results given in previous chapters, this section discusses selected nonlinear and linearized vibration analyses of isotropic, classical composite and VAT composite beam, plate and shell structures. Vibration behaviours of loaded structures in their quasi-static nonlinear equilibrium are shown. In detail, a novel numerical approach to explore the critical loads and the natural frequencies variation for progressively increasing loadings of several structures subjected to mechanical or thermal loadings is presented. For clarity, it is important to re-emphasize the fact that damping has been neglected in this work. The effect of damping on computed response depends on the type and loading duration of the dynamic analysis. Damping is important for long duration loadings (such as earthquakes), and is critical for loadings (such as rotating machinery) that continually add energy to the structure.

5.1 Frequency-amplitude dependence

First of all, a simple pendulum, illustrated in Fig. 5.1, is considered to underline the significant amplitude-dependence for the frequency. The pendulum has the following geometric data: L = 0.5 m, L_0 = L/2, t = 0.01 m. The structure is initially at rest and left to oscillate under the action of the constant gravitational field (g). The analysis is performed adopting the HHT-α method with α = -0.1 and a time step Δt = 0.01 sec. The beam structure is modelled by adopting 15 L9 on the cross-section ($x - z$) and 1 B3 finite element along the beam axis (y). This mesh approximation was obtained after convergence analyses not reported here for brevity. The time response considering different values of the initial angular displacement amplitude (θ) is provided below, including the comparison with results obtained using the analytical approach.

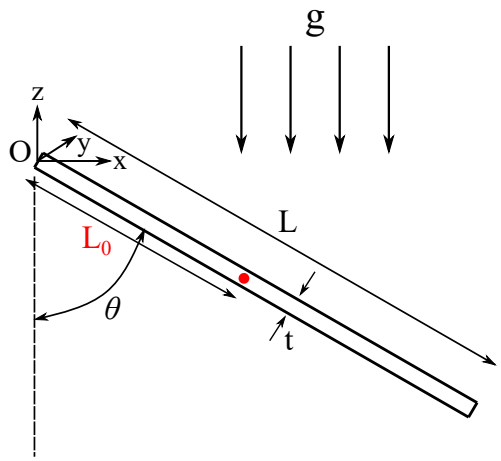

Fig. 5.1 A representative initial configuration of the pendulum.

Figure 5.2 provides the nonlinear time response of the pendulum for different initial angular displacement amplitudes, including the comparison with the analytical solution. For completeness, the nonlinear differential equation for a physical pendulum, with distributed mass (M), oscillating in the constant gravitational field of the Earth is expressed as follows:

$$\ddot{\theta} + \omega^2 sin(\theta) = 0 \tag{5.1}$$

where the frequency of oscillation is $\omega = \sqrt{\frac{g}{L'}}$, $L' = \frac{I}{ML_0}$ represents the equivalent length and $I = \frac{ML^2}{3}$ stands for the moment of inertia of this structure.

The results obtained through the presented nonlinear formulation exhibit an excellent correlation with the reference solution, allowing validation of the methodology. In addition, also a comparison between the linear and nonlinear formulation is carried out, showing that as the initial amplitude increases the differences between the two formulations are present. In particular, already for a $\theta = 30°$, some discrepancies underline the need to use nonlinear formulations to accurately describe the problem. For the sake of completeness, the calculated velocity and acceleration in z-direction at the tip of the structure with respect to time are provided in Figs. 5.3 and 5.4. The frequency of oscillation of the pendulum versus the initial angular displacement amplitude is plotted in Fig. 5.5. A significant reduction of the frequency of oscillation of the pendulum can be observed for progressive increasing initial angular displacement amplitudes. The results show how the frequency varies for different amplitudes due to the fact that the equilibrium to which it is linked changes. Therefore, it is essential to calculate the equilibrium condition correctly, adopting a nonlinear formulation. The work of the thesis focused on this last

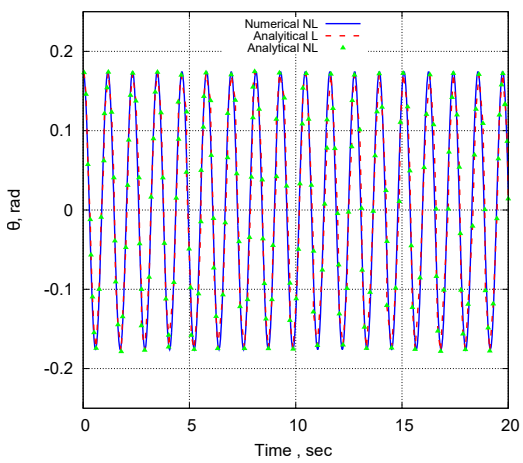

(a) $\theta = 10°$

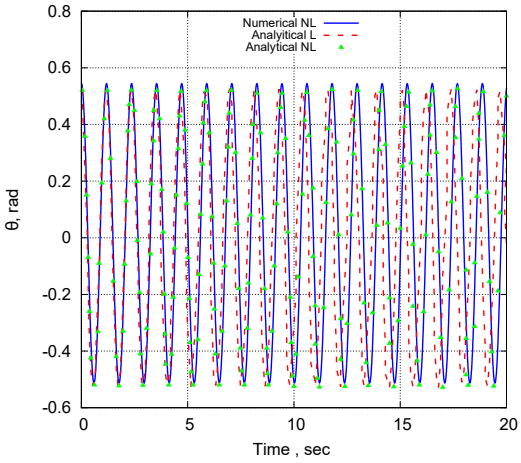

(b) $\theta = 30°$

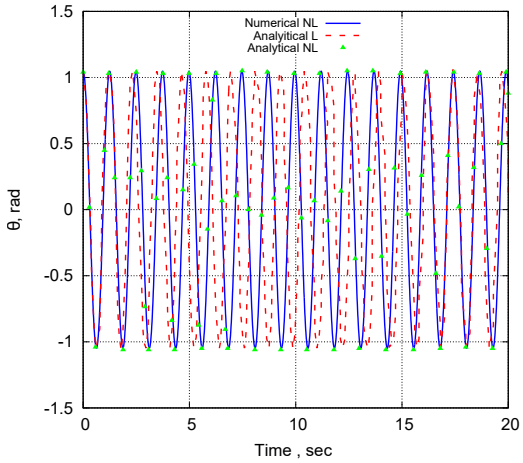

(c) $\theta = 60°$

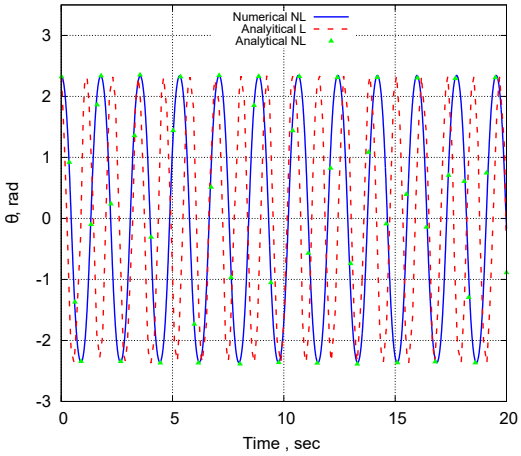

(d) $\theta = 135°$

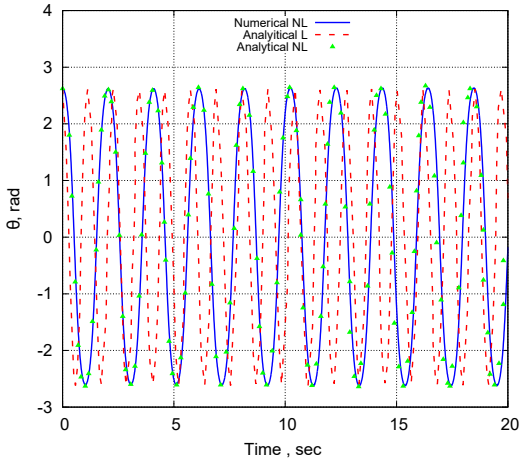

(e) $\theta = 150°$

Fig. 5.2 Time response for different initial angular displacement amplitudes of the pendulum.

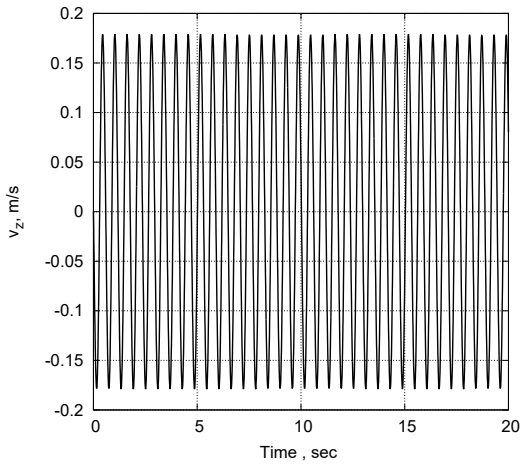

(a) $\theta = 30°$

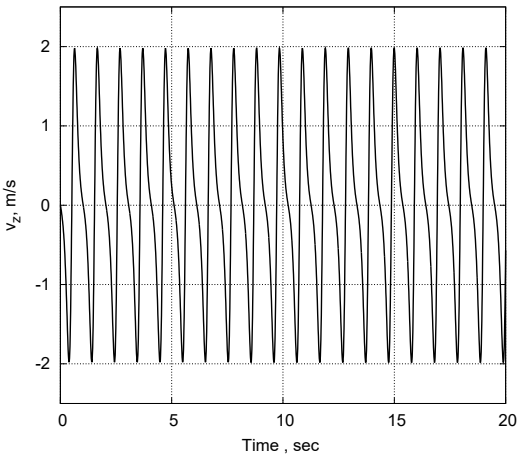

(b) $\theta = 150°$

Fig. 5.3 v_z vs t for the pendulum.

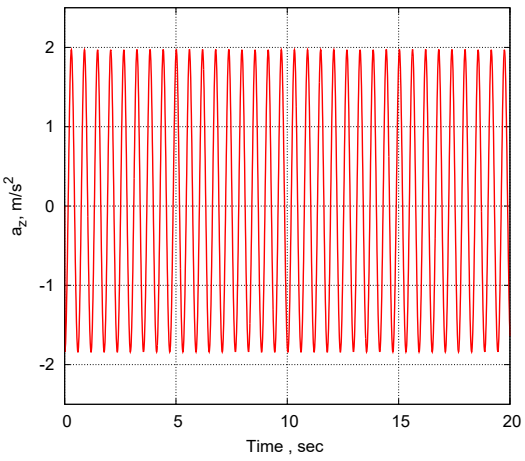

(a) $\theta = 30°$

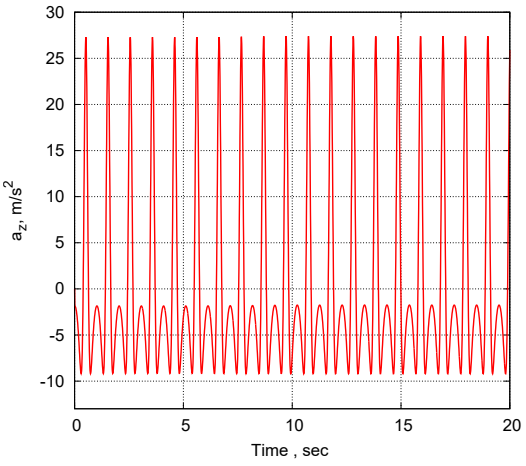

(b) $\theta = 150°$

Fig. 5.4 a_z vs t for the pendulum.

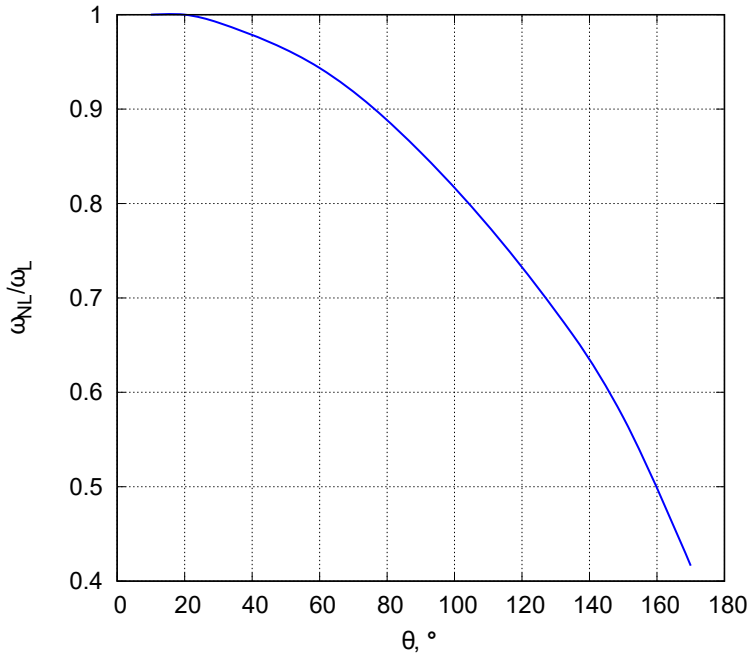

Fig. 5.5 Frequency of oscillation versus initial angular displacement amplitude for the pendulum.

aspect, providing a tool able to characterize the vibrations of various loaded structures accurately.

5.2 Nonlinear and linearized vibration analysis

In the following section, vibration behaviours of isotropic and composite structures in geometrical nonlinear equilibrium states are presented. In particular, the natural frequency variation and mode change is discussed. Various numerical examples are investigated for beam, plate and shell problems dominated by flexure and compression, considering different boundary conditions and mechanical or thermal loadings. Particular emphasis is related to the ability of the present novel approach to provide a numerical methodology to predict critical buckling loads, to characterize the variation of natural frequencies for progressively increasing loads and to have an efficient means for the verification of the experimental VCT results. For completeness, the Mixed Interpolation of Tensorial Components (MITC) technique was considered when necessary to overcome shear and membrane locking phenomenon. For the sake of brevity, readers are referred to [231] for a detailed description of the MITC implementation in the CUF domain. For clarity, in some of the following analyses the results are presented in non-dimensional

form using the following equation:

$$\widetilde{\omega} = \omega \left(\frac{a^2}{h} \sqrt{\frac{\rho}{E_2}} \right) \tag{5.2}$$

5.2.1 Unstiffened and stiffened metallic plate structures

As a first investigation of vibrations, various metallic plate structures under compression are analyzed. First of all, two benchmark cases are considered in order to validate the proposed methodology. In particular, these structures have the following geometrical characteristics: a) *plate 1*: width (a) is 355 mm, length (b) equal to 355 mm and the thickness (t) is 2 mm; b) *plate 2*: a = b = 200 mm and t = 1.955 mm. The boundary conditions of these two plates are shown in Fig. 5.6. In detail, clamped-clamped-simply supported-simply supported (CCSS) for *plate 1* and clamped-clamped-clamped-free (CCCF) for *plate 2* are assumed, respectively. Both plates have the following material data, $E = 70$ GPa, $\nu = 0.33$ and $\rho = 2780$ kg/m^3.

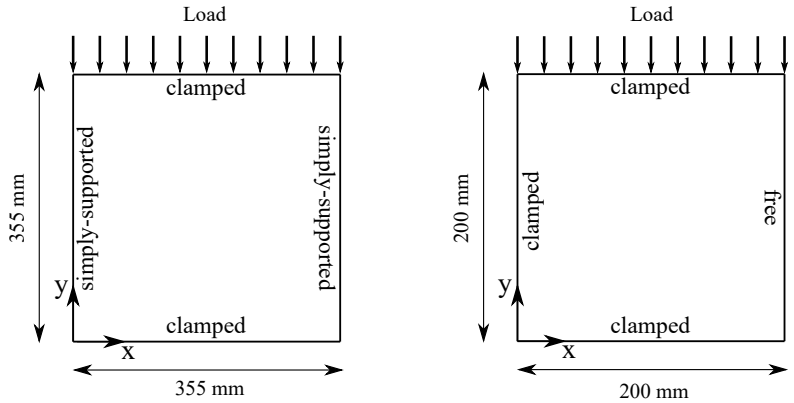

Fig. 5.6 Geometry and boundary conditions of the metallic plate structures.

In order to perform accurate investigations, convergence analyses are carried out. As a consequence, at least 10×10Q9 for the in-plane mesh approximation and only one LD2 in the z-direction must be employed for the convergent model. These convergence analyses are not reported here for the sake of brevity. However, the convergence performance of the proposed finite elements can be appreciated in [16].

Figure 5.7 provides the linear and nonlinear equilibrium trends of the metallic plate structures subjected to compression. It is important to highlight that in the case of nonlinear analysis a defect load applied at the middle of the plates along the z-axis, F_d = 0.01 N, was considered to simulate geometrical imperfections. Figure 5.8 illustrates

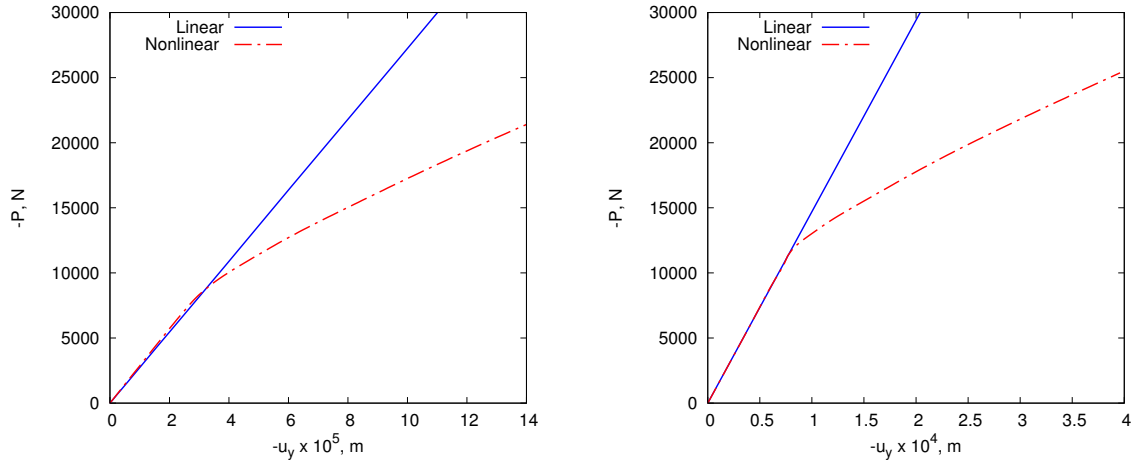

(a) *Plate 1* (b) *Plate 2*

Fig. 5.7 Linear and nonlinear equilibrium curves of metallic plate structures subjected to compression.

the natural frequencies variation as a function of the compressive loadings via the trivial linearized solution. In particular, for *plate 2*, both tensile and compressive loads are applied. For completeness, the characteristics first four free vibration mode shapes of the *plate 1* and the first five free vibration mode shapes of the *plate 2* are depicted in Fig. 5.9 and Fig. 5.10. On the other hand, the variation of natural frequencies with respect to the compressive loadings by using the full nonlinear approach is illustrated in Fig. 5.11.

Table 5.1 provides the metallic plates' buckling load values compared with the experimental results available in the literature [80, 82]. For clarity, results come from a simple linearized buckling analysis, in which the tangent stiffness is approximated as the sum of the linear matrix and the geometric stiffness resulting from linear stress state. Discrepancies between the numerical solution based on the current approach and experimental buckling load are expressed as a percentage difference. Basically, the

Models	*Plate 1*		*Plate 2*	
	Buckling Load [kN]	%Err	Buckling Load [kN]	%Err
Present solution	10.28	2.80	11.85	1.82
Exp. Measurement [80, 82]	10.00	-	12.07	-

Table 5.1 First linearized critical bucking loads of metallic plate structures.

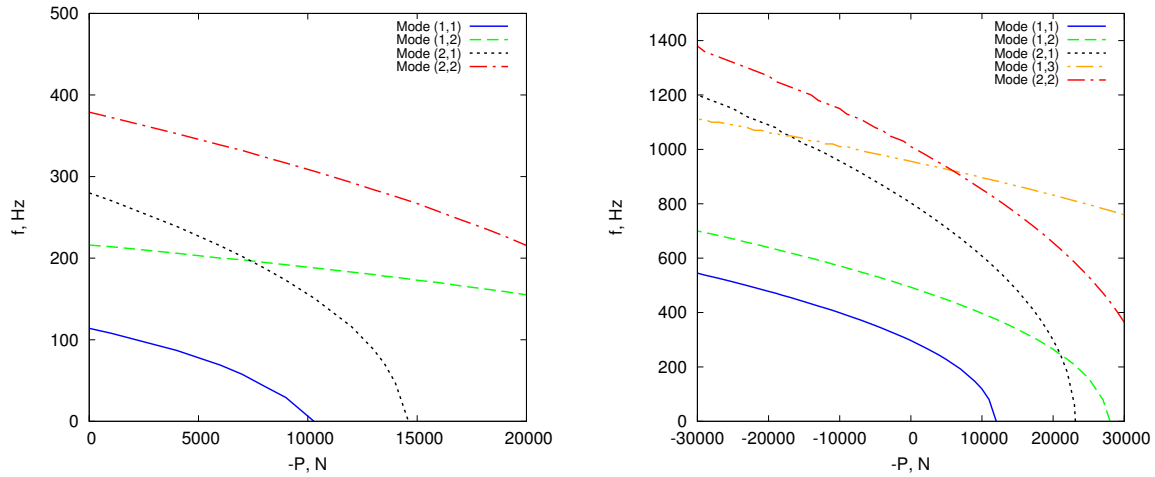

(a) *Plate 1* (b) *Plate 2*

Fig. 5.8 The variation of natural frequencies vs increasing compressive loadings through the trivial linearized approach for metallic plate structures.

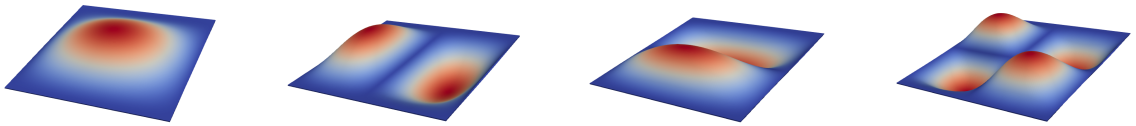

(a) Mode (1,1) (b) Mode (1,2) (c) Mode (2,1) (d) Mode (2,2)

Fig. 5.9 Mode shapes of the first four free-vibrations for the metallic *plate 1*.

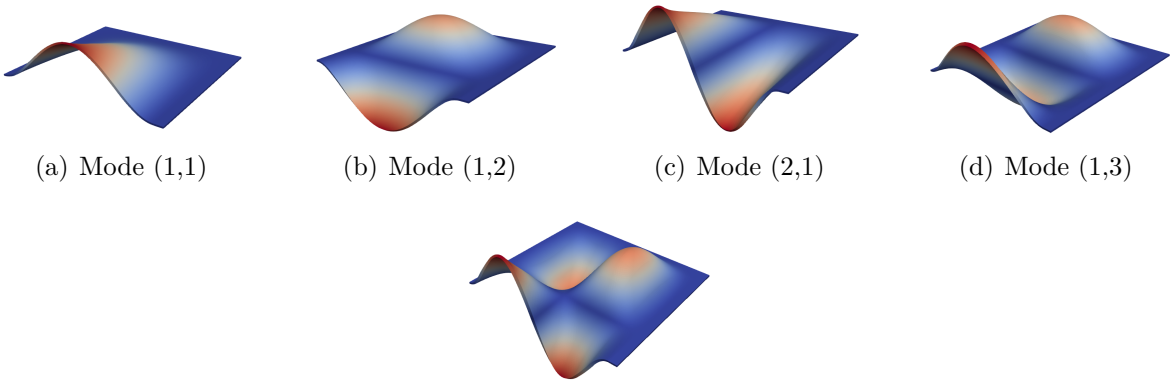

(a) Mode (1,1) (b) Mode (1,2) (c) Mode (2,1) (d) Mode (1,3)

(e) Mode (2,2)

Fig. 5.10 Mode shapes of the first five free-vibrations for the metallic *plate 2*.

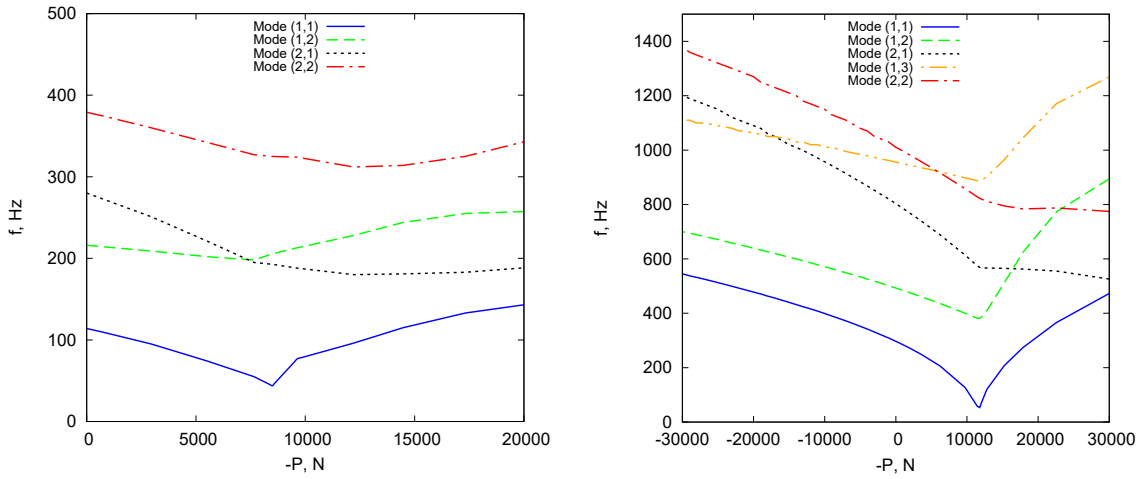

(a) *Plate 1* (b) *Plate 2*

Fig. 5.11 The variation of natural frequencies vs compressive loadings via the full nonlinear approach for metallic plate structures.

discrepancy of the critical load measured using the proposed methodology is minimal compared to the experimental solution.

Figure 5.12 shows the comparison between the variation of natural frequencies for progressively increasing loadings computed through the trivial linearized solution, the full nonlinear approach and experimental results. The results in Fig. 5.12 demonstrate that the approach based on the trivial linearized solution allows one to characterize the variation of the frequency of these benchmark cases at lower levels of the compressive loadings with accuracy. The deviation of the linear results from the nonlinear and experimental ones becomes remarkable for higher compressive loading levels. Particularly, it can be observed that the frequency of the first vibration mode tends to zero at the buckling load value by considering the trivial linearized approach. On the contrary, the nonlinear and experimental solutions shown different behaviours. Basically, the first vibration mode reaches a minimum value near the buckling load value, and after the buckling, the frequencies increase. This definite change in the slope of the frequencies indicates a criterion for the buckling load prediction. The difference between the trivial linearized solution and full nonlinear approach is due to the nonlinear effects of the post-buckling. The results calculated using the proposed nonlinear virtual VCT approach provide an excellent correlation with the experimental ones, allowing to predict the buckling load and to evaluate the variation of natural frequencies in the nonlinear regime with high reliability. The small discrepancies between the numerical and experimental

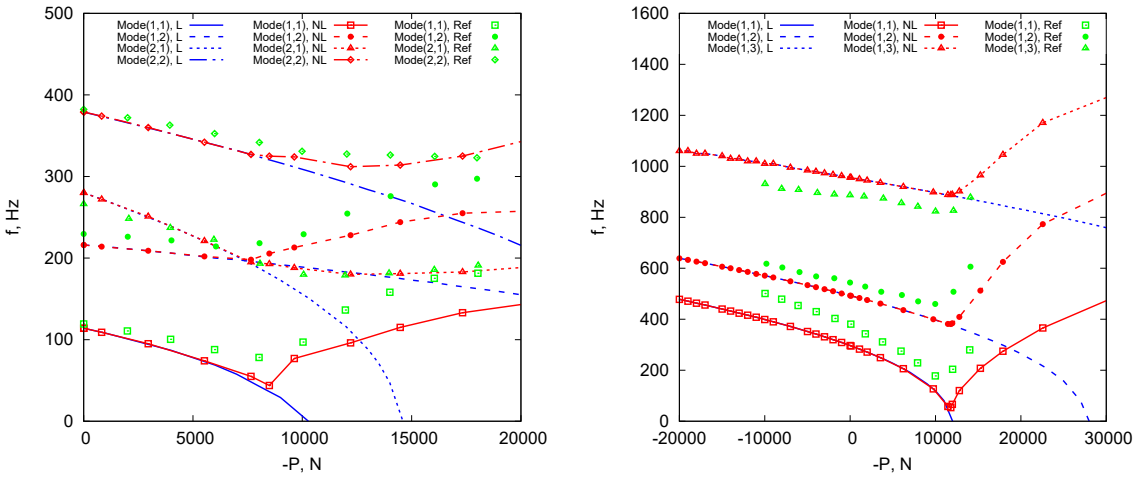

(a) *Plate 1* [80] (b) *Plate 2* [82]

Fig. 5.12 Comparison between the natural frequencies variation for increasing compressive loadings through the trivial linearized solution, the full nonlinear approach and experimental results for metallic plate structures.

solutions are probably due to variations between the actual boundary conditions employed during the test and the numerical constraints and initial geometric imperfections.

Furthermore, considering the case of *Plate 1*, the effect of stiffeners on natural frequency and instability is provided. In detail, Fig. 5.13a illustrates the nonlinear equilibrium curves for three different cases, without stiffener and with stiffeners of different sizes, $d = 4$ mm and 7 mm, respectively. In addition, the linearized buckling load values, represented by the horizontal line, are reported in this graph. A sketch of the geometry and mesh adopted is shown in Fig. 5.13b. The natural frequencies variation for progressively increasing loading is provided in Fig. 5.14. For all cases, the comparison between the trivial linearized approach and the full nonlinear one is presented, and the trend of the frequencies in postbuckling regimes is evaluated, showing important crossing and veering phenomena. For clarity, the effect of the stiffener is depicted in Fig. 5.15, in which the natural frequency variation of the first vibration mode for all cases is plotted. For completeness, the MAC graphical representation are reported in Fig. 5.16, showing significant changes with increasing load. In addition, Fig. 5.17 reports the mode shapes of the first 6 natural frequencies in order to demonstrate the capability of the proposed formulation to also takes into account the deformation of the stiffener.

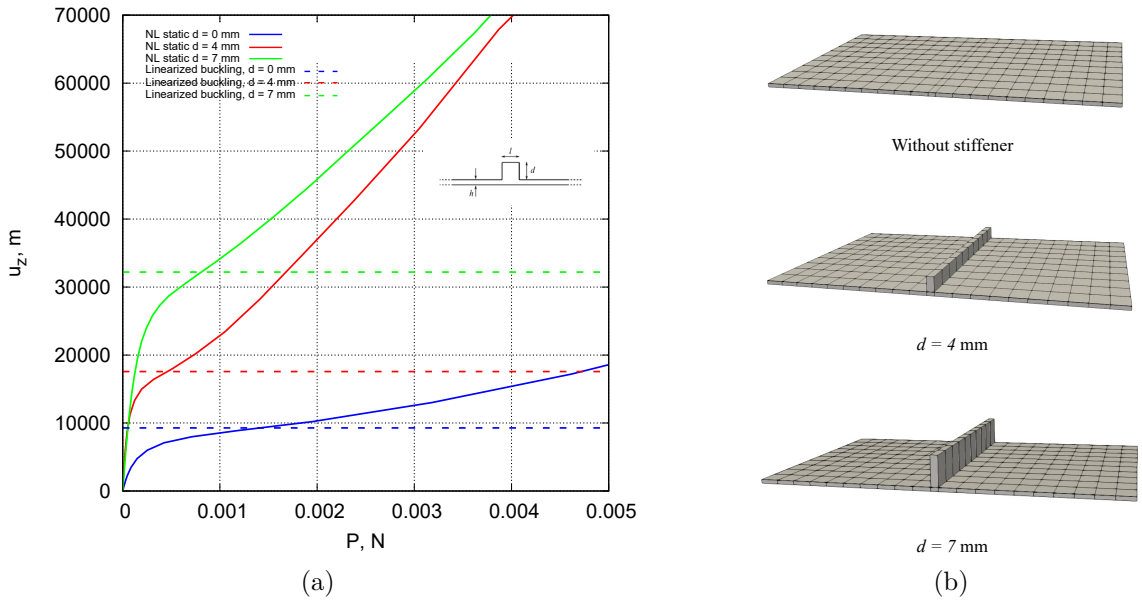

(a) (b)

Fig. 5.13 (a) Nonlinear equilibrium curves; (b) Representation of the geometry and mesh adopted for the unstiffened and stiffened plate structures.

5.2.2 Square VAT composite plate

A 2-layer $[0° + < 0°/15° > \ / \ 90° + < 0°/15° >]$ square VAT composite plate is considered as the following case. This VAT structure has the following geometrical data: a = b = 1 m and h = 2 mm. The material properties of the lamina are provided in Table 5.2. As regards the boundary conditions, simply-supported conditions are applied to all

E_1 [GPa]	$E_2 = E_3$ [GPa]	$G_{12} = G_{13}$ [GPa]	G_{23} [GPa]	$\nu_{12} = \nu_{13}$	ν_{23}	ρ [kg/m^3]
250	6.25	5.125	3.25	0.24	0.49	1

Table 5.2 Material properties of the square VAT composite plate under uniform axial compression.

the edges, i.e., $x = 0$, a has $v = w = 0$ whereas $y = 0$, b satisfies $u = w = 0$. The square plate is subjected to an uniform axial compression in x-direction as illustrated in Fig. 5.18.

First of all, a convergence analysis is needed for carrying out an accurate investigation. For this square plate model, the convergence is achieved by employing at least 18×18Q9 for the in-plane mesh approximation and only one LD1 in each layer in the z-direction. The equilibrium path for the 2-layer $[0° + < 0°/15° > \ / \ 90° + < 0°/15° >]$ square

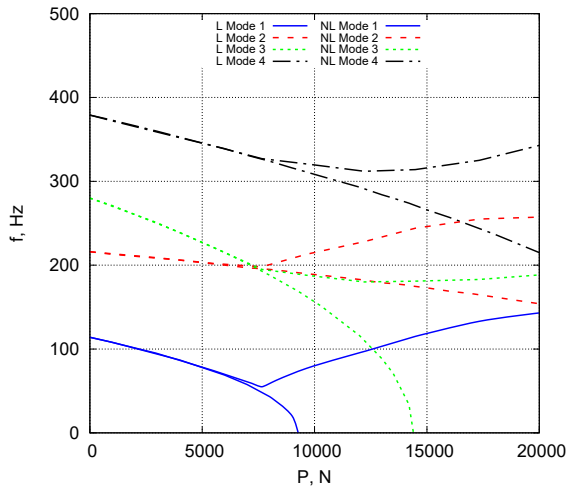

(a) $d = 0$ mm

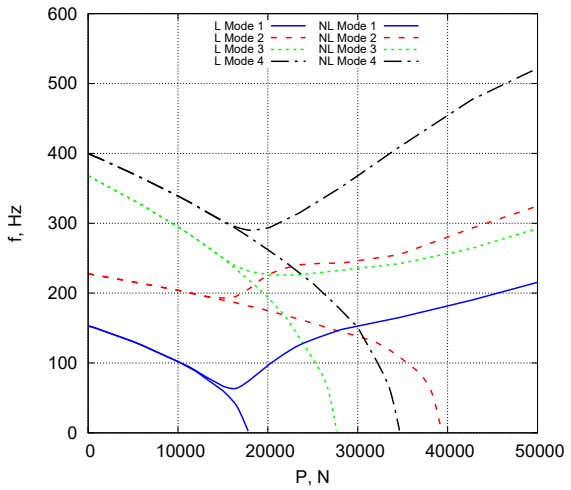

(b) $d = 4$ mm

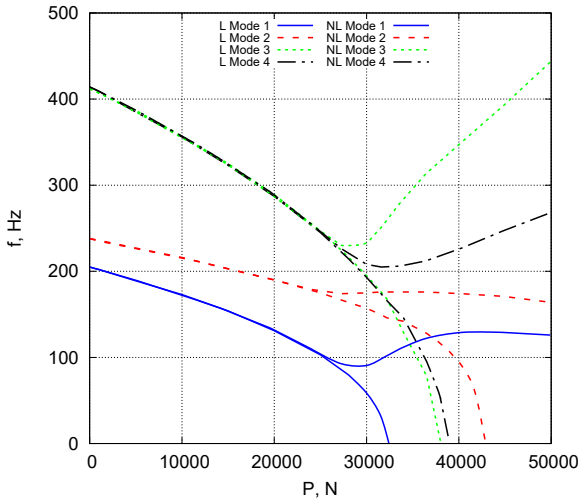

(c) $d = 7$ mm

Fig. 5.14 Natural frequency variation versus compressive loadings for unstiffened and stiffened plate structures.

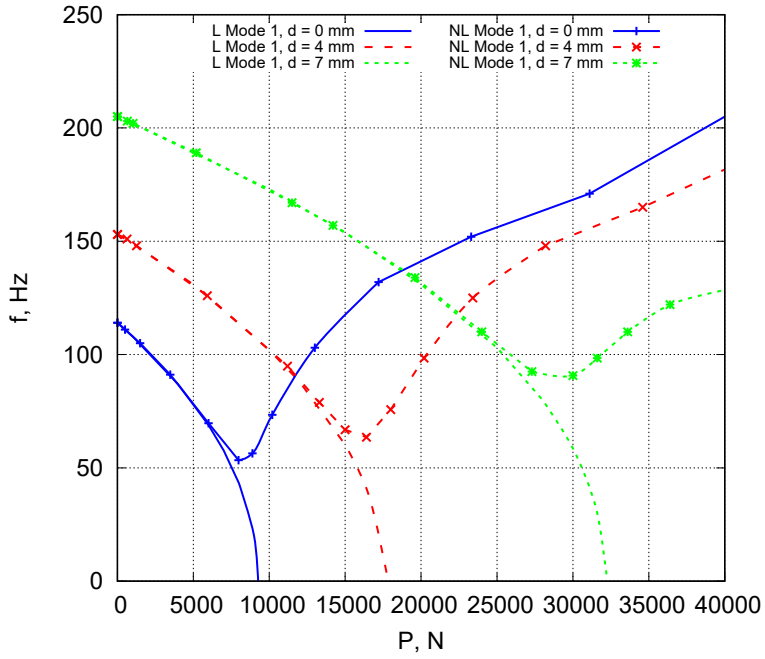

Fig. 5.15 Effect of the stiffener in the variation of the first natural frequency.

VAT composite plate is displayed in Fig. 5.19, which plots the normalized values of the displacement at the center of the plate versus the applied compressive load. For completeness, solutions obtained using the commercial code Abaqus is also provided for this first case for comparison and validation reasons. In detail, both the ABQ 2D shell model (18×18 S8R) and the ABQ 3D solid model (54×54×2 C3D20R) are used. The results demonstrate that the CUF 2D nonlinear model agrees well with the ABQ solutions. In addition, also the linear CUF 2D load-deflection curve and the linear buckling load value, representing by the horizontal line, are depicted in Fig. 5.19. In particular, the linear critical buckling load (P_{cr}) value is equal to 546.53 N/m. For the sake of clarity, it is important to underline that the considered structure does not show any bifurcation because of the coupling between the membrane and bending stiffness due to material non-symmetry. Nevertheless, it is quite common in the literature to identify the linearized buckling loads with the first eigenvalues of the stiffness matrix.

Figure 5.20 illustrates the deformed configuration with the displacements contours based on the CUF 2D NL model and ABQ 3D solid model at the fixed load $N_x = 2130.71$ N/m for the square VAT plate under compressive loads. Furthermore, the values of the first ten free vibration modes obtained using the CUF and ABAQUS are tabulated in Table 5.3, whereas the most relevant mode shapes are depicted in Fig. 5.21-5.27.
Figure 5.28 and 5.29 show the natural frequencies variation versus compressive loading via trivial linearized solution and via full nonlinear solution, respectively. Furthermore,

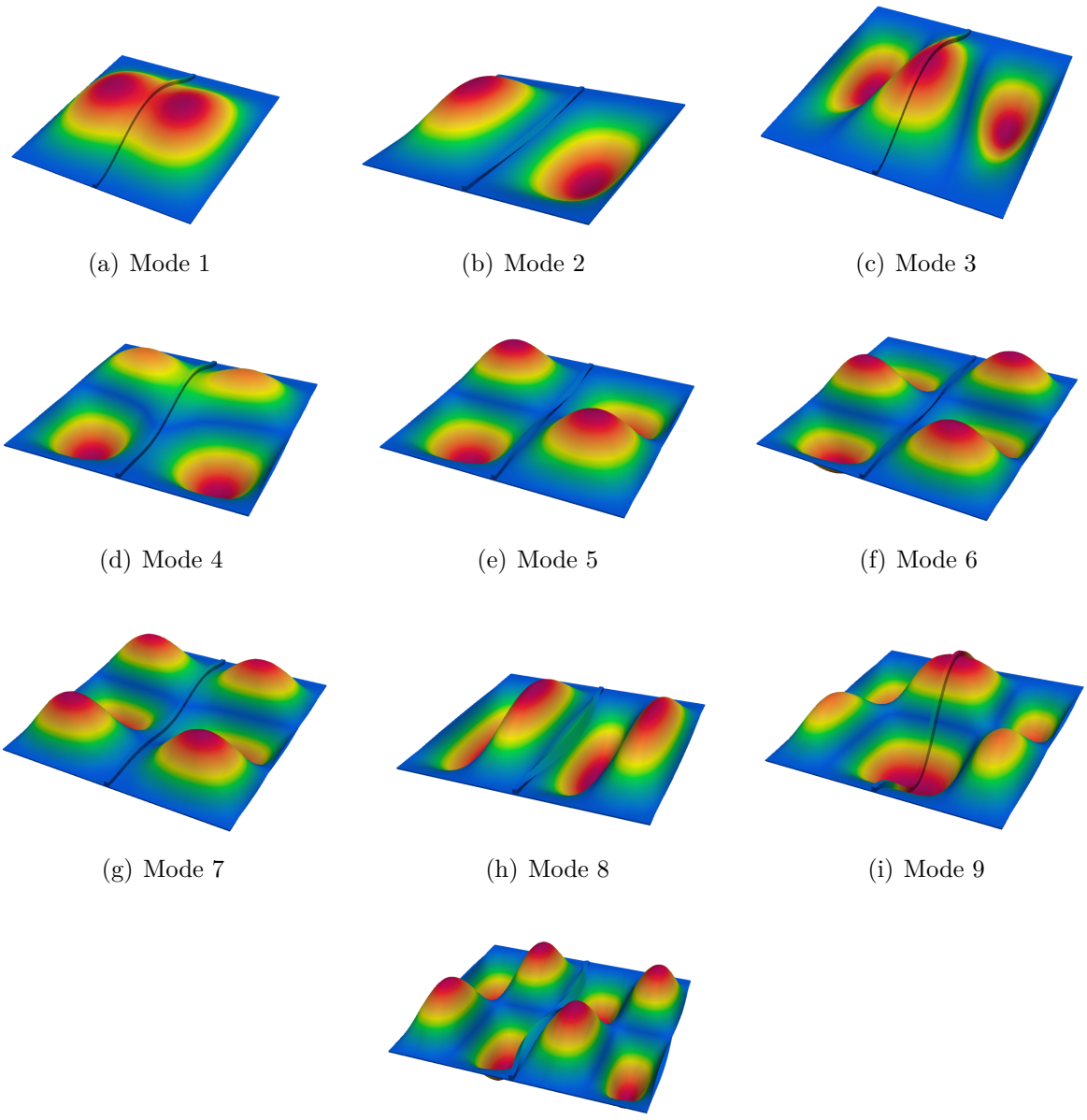

(a) Mode 1 (b) Mode 2 (c) Mode 3

(d) Mode 4 (e) Mode 5 (f) Mode 6

(g) Mode 7 (h) Mode 8 (i) Mode 9

(j) Mode 10

Fig. 5.16 Mode shapes of the first ten free-vibration for the stiffened plate structure. $d =$ 7 mm.

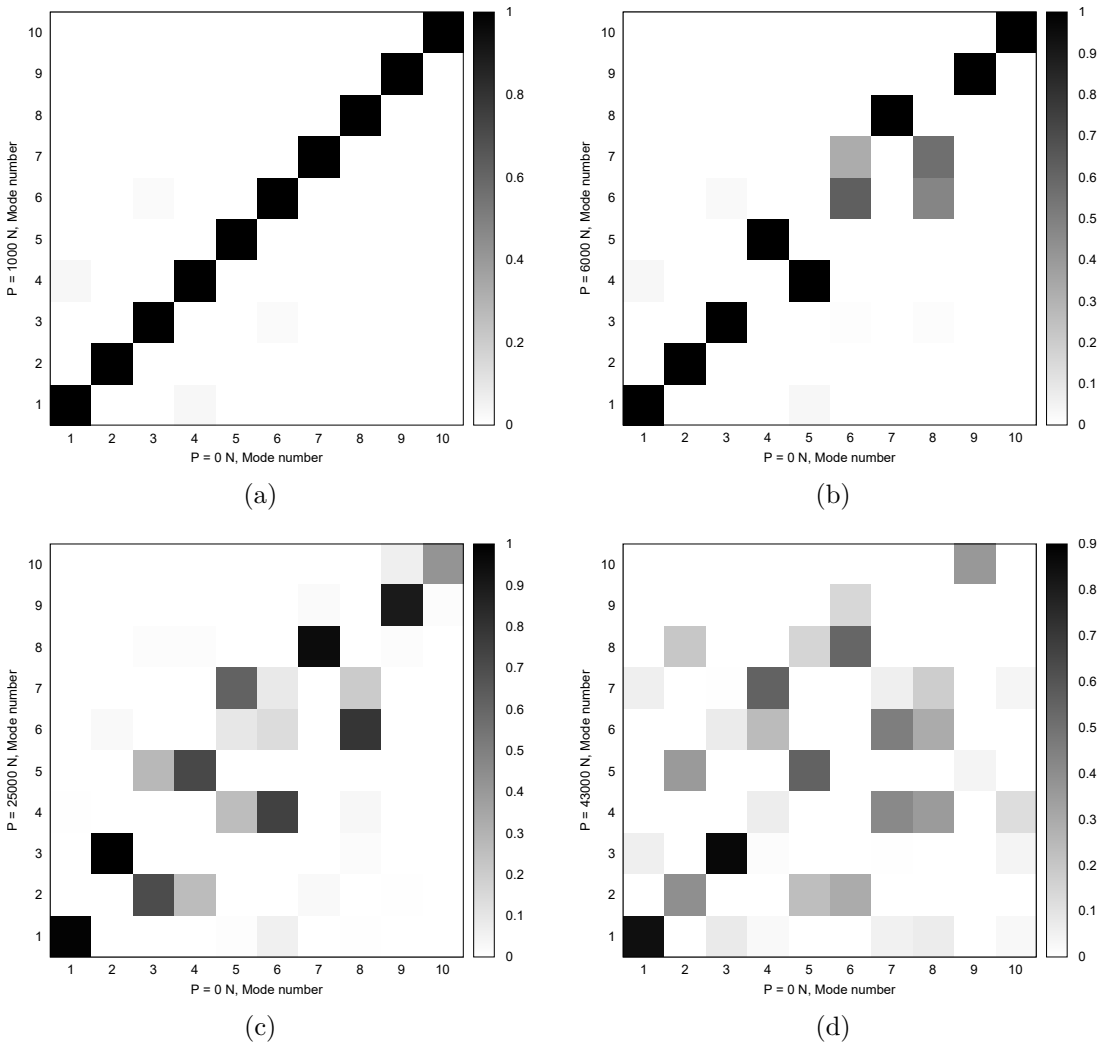

Fig. 5.17 MAC representations between the modes of the undeformed structure and deformed one for the stiffened plate subjected to compressive loadings. $d = 4$ mm.

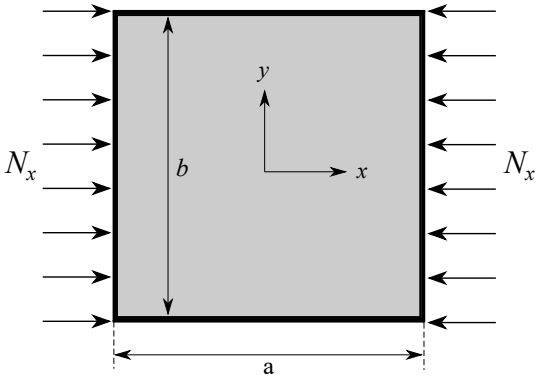

Fig. 5.18 Geometry and loading case of the square VAT plate subjected to uniform axial compression.

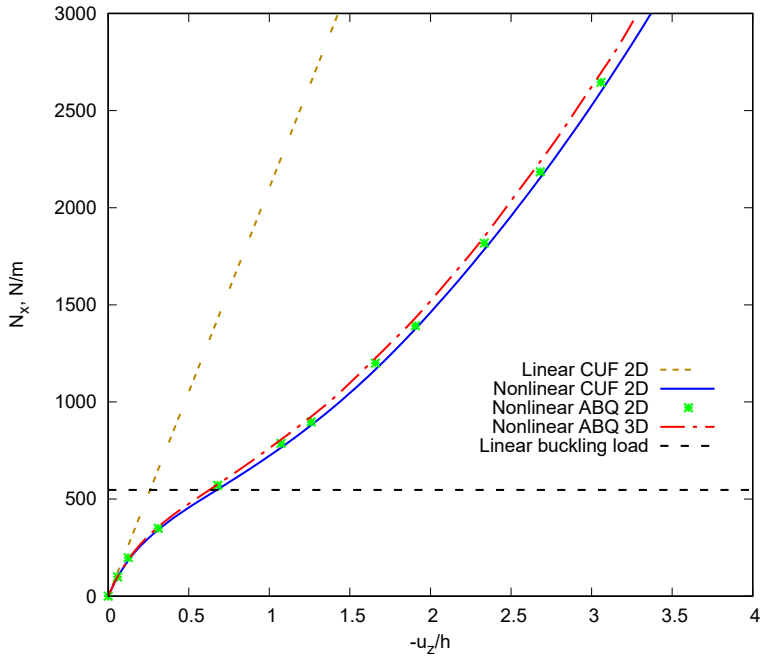

Fig. 5.19 Equilibrium curve of the square VAT composite plate subjected to uniform axial compression. CUF model makes use of LD1 kinematics and 18×18Q9 FE mesh approximation.

Mode number	CUF	Abaqus
1	1.95	1.93
2	5.18	5.13
3	5.18	5.13
4	7.67	7.58
5	10.94	10.76
6	10.99	10.82
7	12.89	12.69
8	12.89	12.69
9	17.23	16.93
10	19.21	18.83

Table 5.3 First ten free non-dimensional natural frequencies of the square VAT plate. Comparison between CUF 2D NL 18×18Q9+LD1 and ABQ 3D solid NL 54×54×2 C3D20R model.

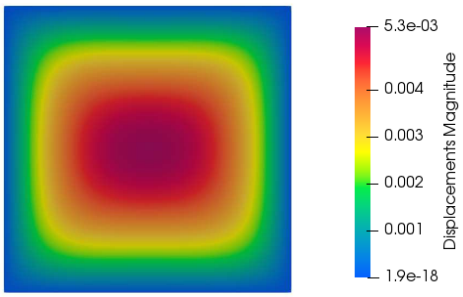

(a) 2D CUF NL model

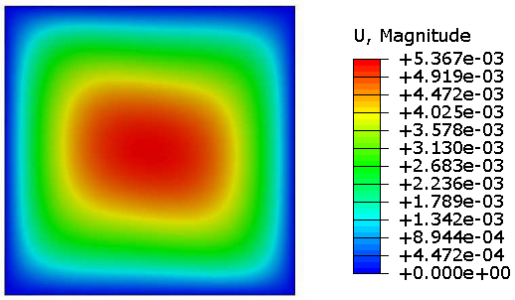

(b) ABQ 3D solid NL model

Fig. 5.20 Comparison of displacement contours at the fixed load of $N_x = 2130.71$ N/m for the square VAT composite plate under uniform axial compression. (a) CUF 2D NL 18×18Q9+LD1; (b) ABQ 3D solid NL 54×54×2 C3D20R model.

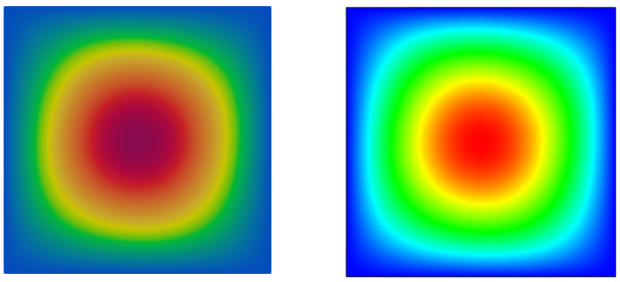

(a) CUF (b) ABQ

Fig. 5.21 Mode 1 for the square VAT plate with simply-supported edge conditions. $N_x = 0$ N/m.

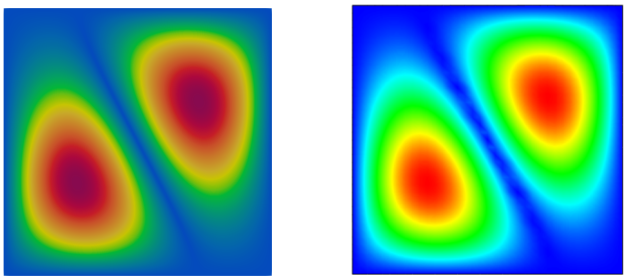

(a) CUF (b) ABQ

Fig. 5.22 Mode 3 for the square VAT plate with simply-supported edge conditions. $N_x = 0$ N/m.

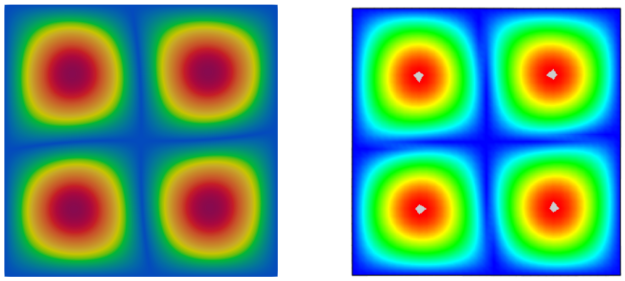

(a) CUF (b) ABQ

Fig. 5.23 Mode 4 for the square VAT plate with simply-supported edge conditions. $N_x = 0$ N/m.

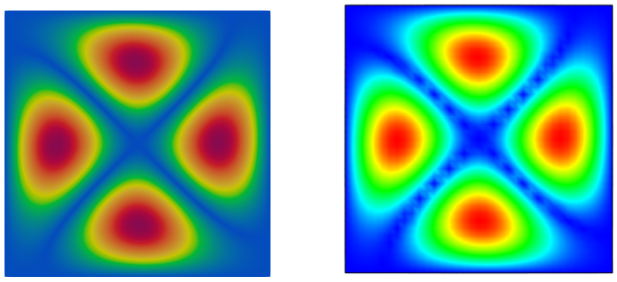

(a) CUF (b) ABQ

Fig. 5.24 Mode 5 for the square VAT plate with simply-supported edge conditions. $N_x = 0$ N/m.

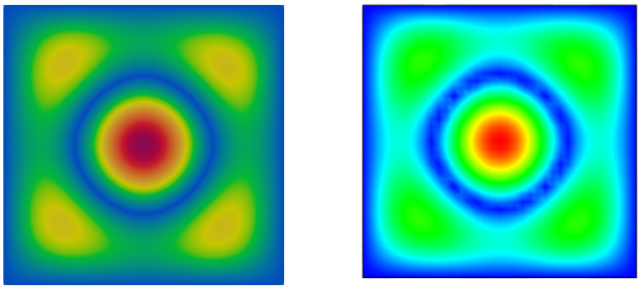

(a) CUF (b) ABQ

Fig. 5.25 Mode 6 for the square VAT plate with simply-supported edge conditions. N_x = 0 N/m.

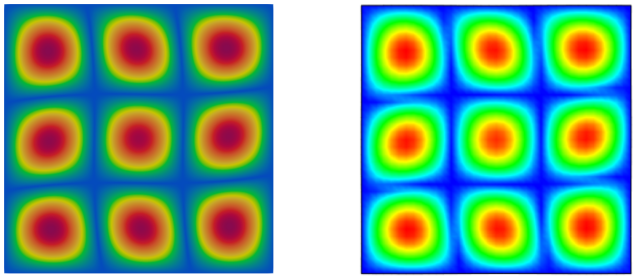

(a) CUF (b) ABQ

Fig. 5.26 Mode 9 for the square VAT plate with simply-supported edge conditions. N_x = 0 N/m.

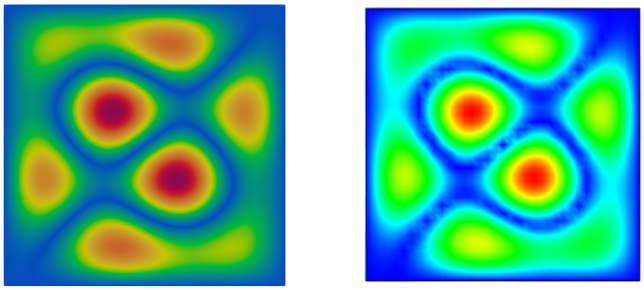

(a) CUF (b) ABQ

Fig. 5.27 Mode 10 for the square VAT plate with simply-supported edge condition. N_x = 0 N/m.

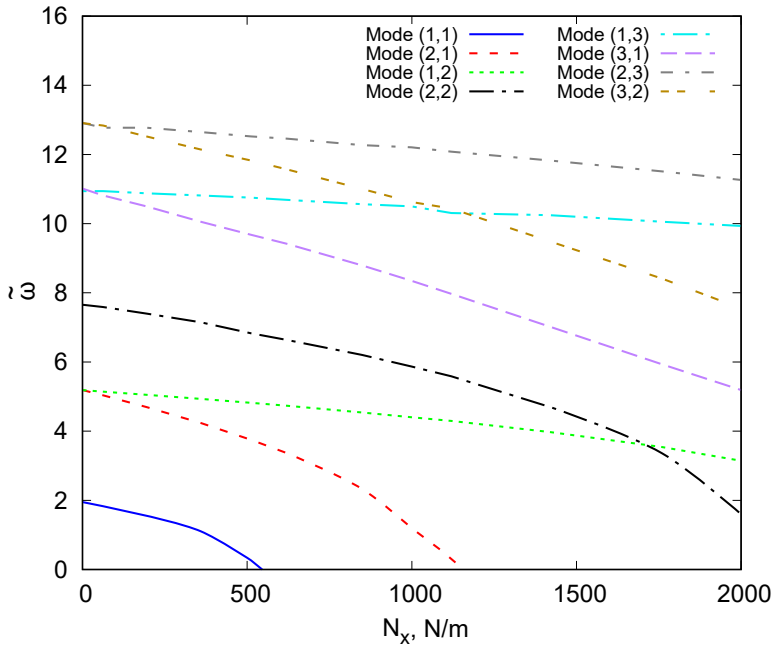

Fig. 5.28 Non-dimensional natural frequencies variation versus compressive loading via trivial linearized solution for the square VAT composite plate with simply-supported edge conditions.

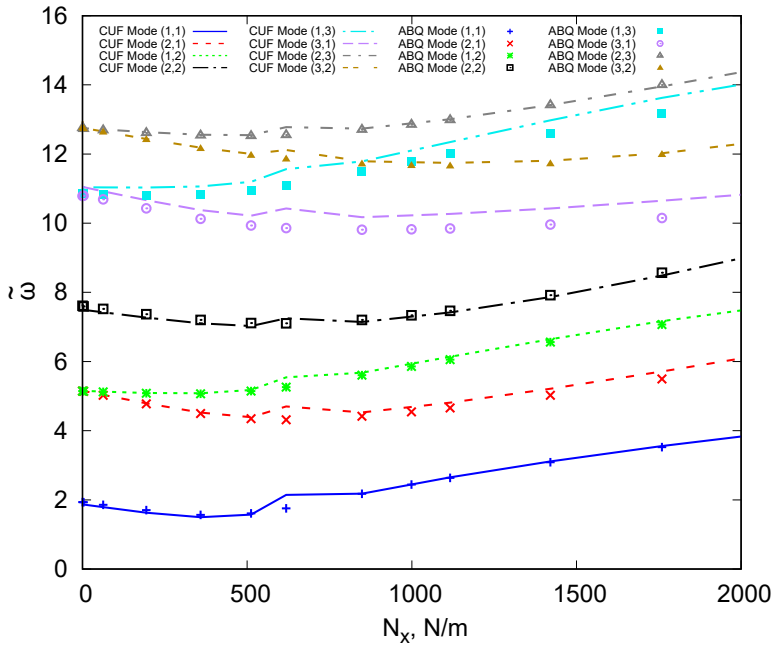

Fig. 5.29 Non-dimensional natural frequencies variation versus compressive loading via full nonlinear solution for the square VAT composite plate with simply-supported edge conditions.

the comparison between the variation of the natural frequencies obtained via the trivial linearized and via full nonlinear approach is reported in Fig. 5.30. This figure illustrates

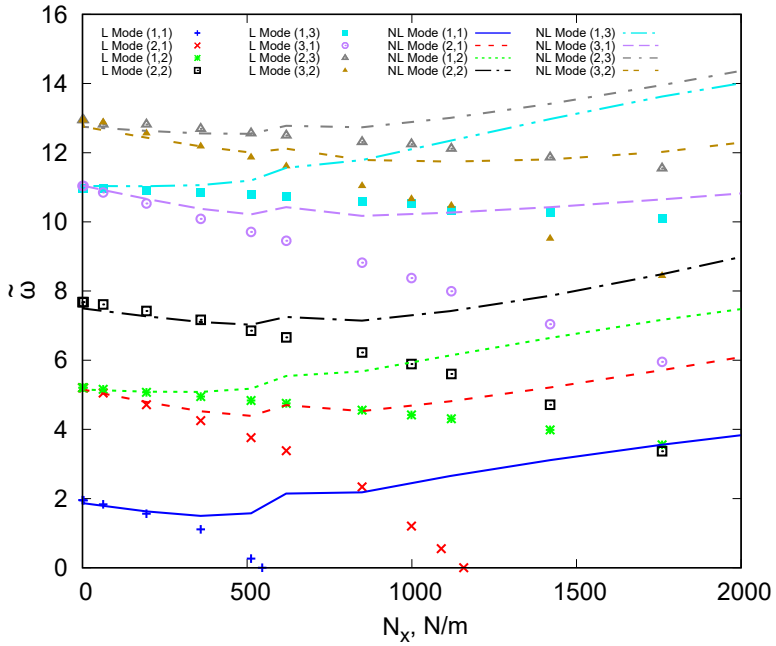

Fig. 5.30 Comparison between the variation of the non-dimensional natural frequencies via trivial linearized solution and full nonlinear approach for the square VAT composite plate under compressive loadings.

the trend of the linearized and nonlinear frequencies associated with the first eight modes. In the case of the linear analysis, it can be pointed out that the first natural frequency, mode (1,1), disappears when the buckling phenomenon occurs within the structure. Thus, the first mode has a null frequency in correspondence with the buckling load as the tangent stiffness is singular. On the other hand, in the case of nonlinear analysis, different behaviour is observed. In fact, no vibration mode reaches zero frequency. In particular, the mode (1,1) reaches a minimum and then it increases in the post-buckling regime. This change in slope shows an instability behaviour, but the buckling phenomena are irrelevant in this case. The results suggest that a nonlinear approach should be adopted to carry out accurate virtual VCT analyses with the aim of predicting the buckling and characterizing the natural frequencies variation. For completeness, the first eight vibration mode shapes of the square VAT composite plate structure at $N_x = 3.47$ N/m are depicted in Fig. 5.31. Readers are invited to compare these modes with those shown in Figs. 5.21-5.27 (trivial state, i.e. N_x =0); mode aberration is evident.

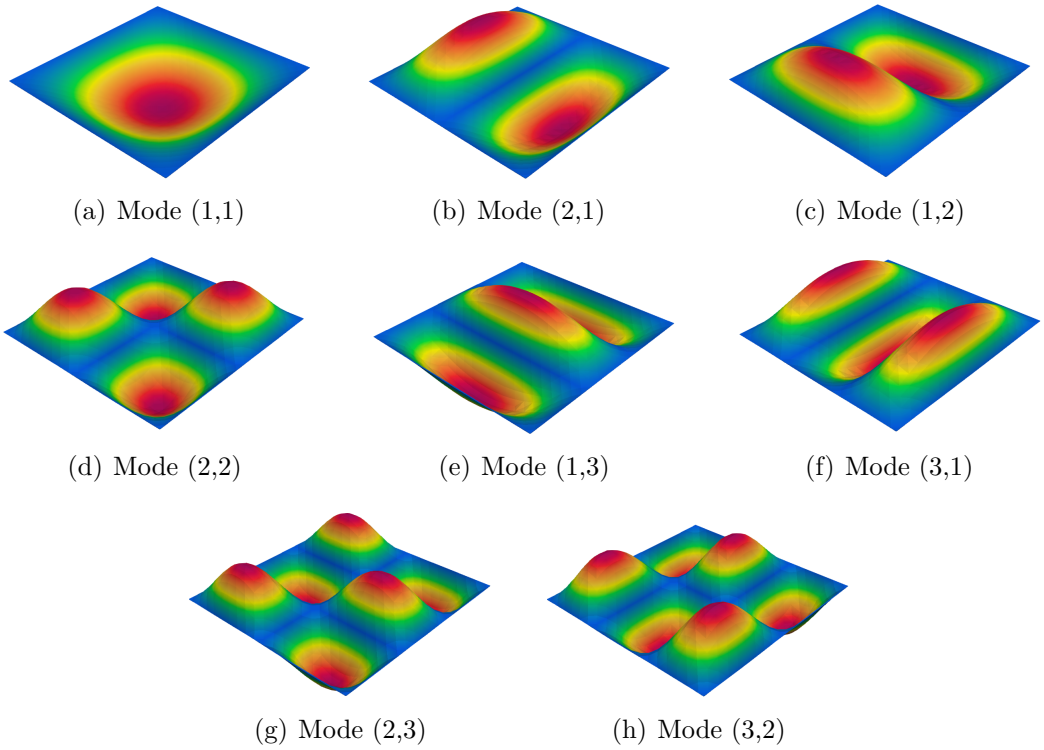

(a) Mode (1,1) (b) Mode (2,1) (c) Mode (1,2)

(d) Mode (2,2) (e) Mode (1,3) (f) Mode (3,1)

(g) Mode (2,3) (h) Mode (3,2)

Fig. 5.31 Characteristics first eight vibration mode shapes for the square VAT composite plate. $N_x = 3.47$ N/m.

5.2.3 Rectangular VAT composite plate

A rectangular VAT composite plate structure with 4 layers $[0° \pm < 0°/15° >]_2$ is studied as a third example. The structure has the following geometrical data: length (a) equal to 0.2 m, the width (b) is 0.05 m and a total thickness (h) of 0.002 m. This VAT plate is subjected to compression in the x-direction, N_x, as illustrated in Fig. 5.32. All the plate edges are simply-supported, i.e, $x = 0$, a satisfy $v = w = 0$, whereas $y = 0$, b have $w = 0$ at $z = 0$. In addition, a further constraint, $u = v = 0$ is applied in the central point of the plate to avoid the rigid body motion of the structure. The lamina properties are: $E_1 = 220$ GPa, $E_2 = E_3 = 5.5$ GPa, $G_{12} = G_{13} = 3.3$ GPa, $G_{12} = 2.75$ and $\nu_{12} = \nu_{13} = 0.25$. For clarity, the analysis are conducted considering a density ρ equal to 1 kg/m^3.

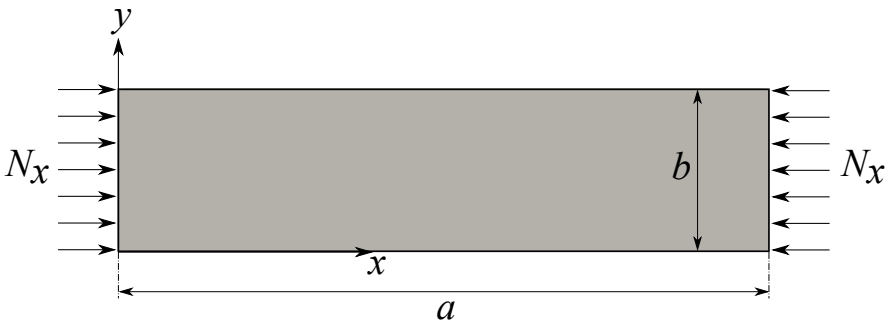

Fig. 5.32 Geometry of the rectangular VAT plate structure under compression.

As before, convergence analyses on the discretization of the model was carried out. As a consequence, the convergent model is obtained by adopting at least 20×5Q9 for the surface mesh approximation and only 1LD1 in each layer in the z-direction. Figure 5.33 plots the equilibrium trends of the rectangular VAT plate calculated by the CUF 2D linear model, CUF 2D nonlinear model, and, for comparison reasons, employing the ABQ 3D solid nonlinear model. In addition, some linearized buckling load values, representing by the horizontal lines, calculated with the CUF method are also provided in this figure (Fig. 5.33). In detail, the first linearized critical buckling load value (P_{cr}) turns out to be equal to 2.31×10^5 N/m. Although there are no bifurcations in the problem under consideration, the buckling must be identified as the point at which the change in slope in the equilibrium curve is no longer acceptable for the given problem. In this case, the linearized buckling has a purely mathematical and not physical meaning. As depicted in Fig. 5.33, the equilibrium path computed by using the presented methodology has a excellent correlation compared to the solution obtained with the commercial code Abaqus. The small discrepancies that can be observed in the equilibrium curves are mainly due to the different applications of the variable angle of the laminations. In fact,

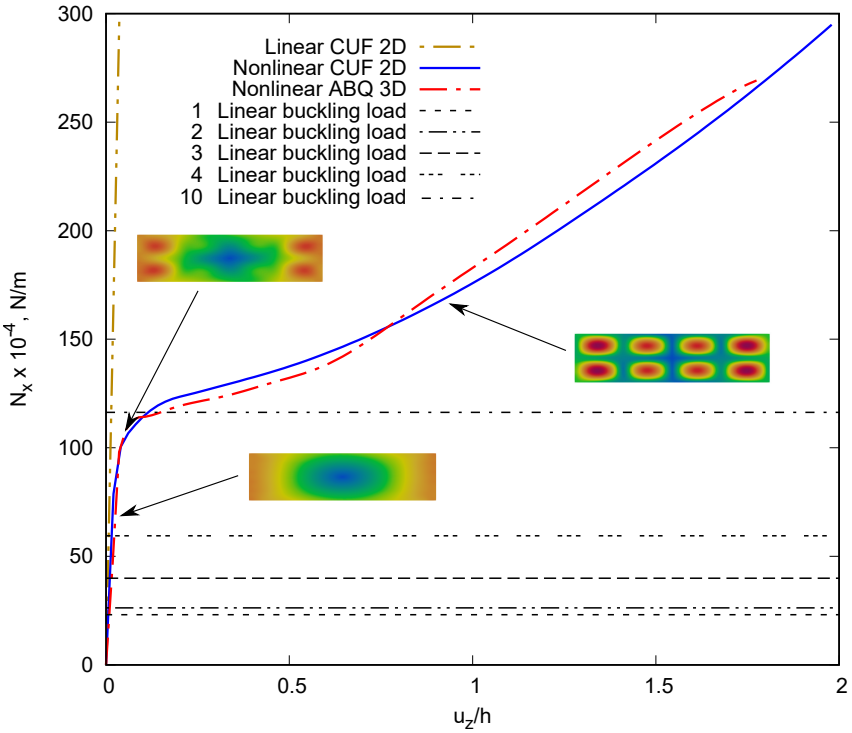

Fig. 5.33 Equilibrium trends for the rectangular VAT plate subjected to compression through the CUF 2D L model, CUF 2D NL model and ABQ 3D NL model.

the application of VAT is applied to each element in Abaqus, whereas it is performed for each gauss point in CUF, giving the possibility of having greater accuracy. For completeness, the convergent ABQ model adopted in this case is discretized with a fine mesh (60×15×4) by using C3D20R elements to overcome the mesh instability problem due to the hourglassing. A particular deformed configuration with the displacements contours based on the CUF 2D NL model and ABQ 3D solid model at the fixed $N_x = 2.1\times10^6$ N/m for the rectangular VAT plate is shown in Fig. 5.34.

Figure 5.35 provides the variation of natural frequencies versus compressive loadings by using the trivial linearized solution. On the other hand, the natural frequencies variation for progressively increasing compressive loadings via the full nonlinear approach is displayed in Fig. 5.36. In addition, the comparison between the variation of the non-dimensional natural frequencies for progressively increasing loadings via trivial linearized and full nonlinear approach is represented in Fig. 5.37. The results displayed in this figure show that even for small load values an important difference is presented between the two trends of the frequencies. The results suggest that a nonlinear approach is mandatory to perform accurate vibration analysis and, in particular, to have a reliable buckling prediction. In fact, it can be noted from Fig. 5.37 that employing a trivial

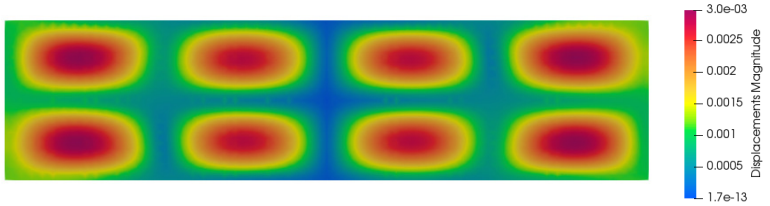

(a) 2D CUF NL model

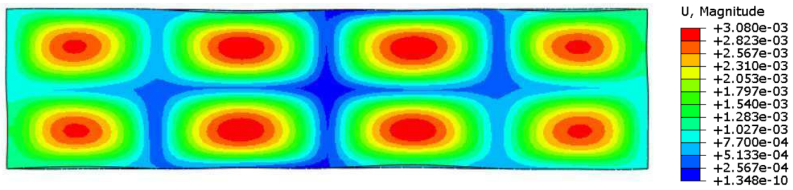

(b) ABQ 3D solid NL model

Fig. 5.34 Comparison of transverse displacement contours at the fixed$N_x = 2.1\times10^6$ N/m for the rectangular VAT plate under compression. (a) CUF 2D NL 20×5Q9+LD1 model; (b) ABQ 3D solid NL 60×15×4 C3D20R model.

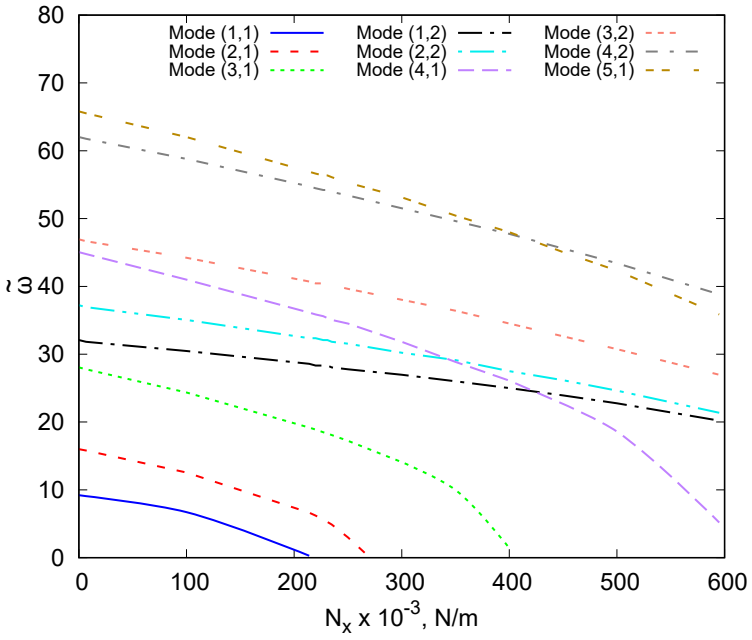

Fig. 5.35 The variation of non-dimensional natural frequencies vs compressive loadings via the trivial linearized approach for the simply-supported rectangular VAT plate.

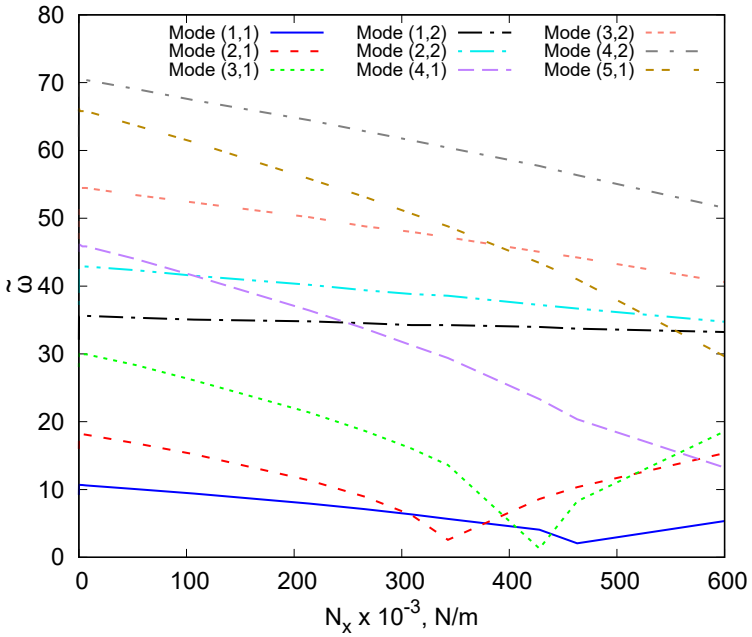

Fig. 5.36 The variation of non-dimensional natural frequencies vs compressive loadings through the full nonlinear approach for the simply-supported rectangular VAT plate.

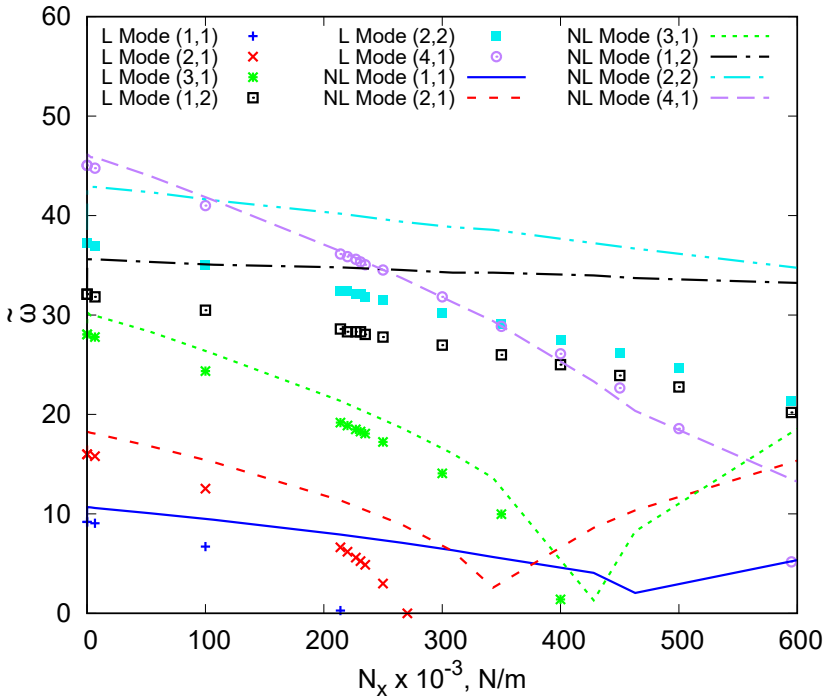

Fig. 5.37 Comparison between the non-dimensional natural frequencies variation computed via the trivial linearized solution and full nonlinear approach for the simply-supported rectangular VAT plate.

approach the natural frequency of the mode (1,1) tends to zero at the linearized buckling load. On the contrary, the nonlinear solutions exhibit a different behaviour. In detail, the mode (2,1) reaches a minimum at about 3.7×10^5 N/m, after that the frequency increase in the post-buckling regime. This particular behaviour, already discussed in the literature in numerous nonlinear studies on different panels [54, 232–234], demonstrates that the natural frequencies increase after the structure had buckled due to the nonlinear effect of post-buckling distortions. This definite change in the slope of the frequency represents a criterion for the nonlinear buckling prediction. Furthermore, it is clear that crossing and veering phenomena are completely unforeseen by the trivial linearized approach. Results computed employing the presented nonlinear virtual VCT prove the potentialities of this methodology to calculate the buckling load of the structure and to characterize the variation of natural frequencies in a large nonlinear regime with high reliability. Finally, for completeness, the first six vibration mode shapes of the rectangular VAT plate at the trivial solution $N_x = 0$ N/m and in far nonlinear regime $N_x = 1.83\times10^6$ N/m are illustrated in Figs. 5.38 and 5.39, respectively. The readers is invited to compare these modes; various crossing phenomena occur and mode aberration is evident.

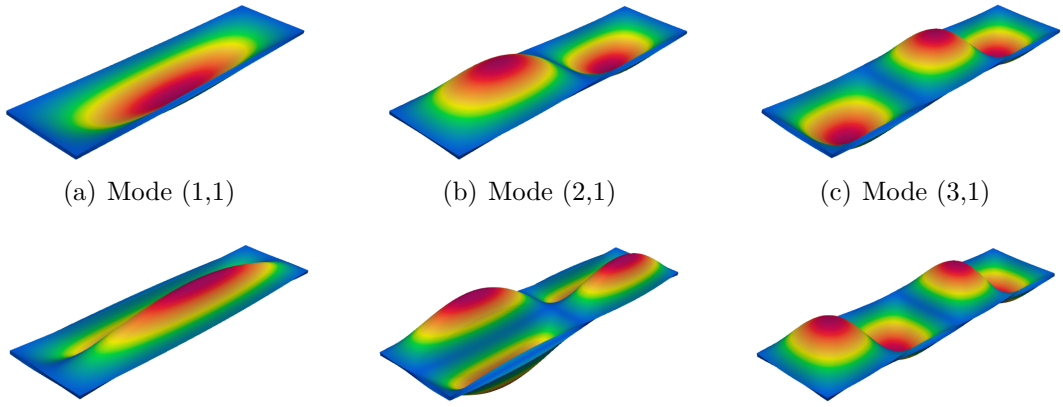

(a) Mode (1,1) (b) Mode (2,1) (c) Mode (3,1)

(d) Mode (1,2) (e) Mode (2,2) (f) Mode (4,1)

Fig. 5.38 Mode shapes of the first six vibrations for the rectangular VAT structure. $N_x = 0$ N/m.

5.2.4 Metallic and composite pinched cylindrical shell

The next analysis concerns a clamped cylindrical shell subjected to a pinching force. The geometric and material data are the same as for the structure studied in 4.4.1 and A.1.5. Besides an isotropic structure, a laminate one with stacking sequence $[90°, 0°, 90°]$ is also considered. The present structure is modelled using 32×32Q9 for the in-plane mesh and

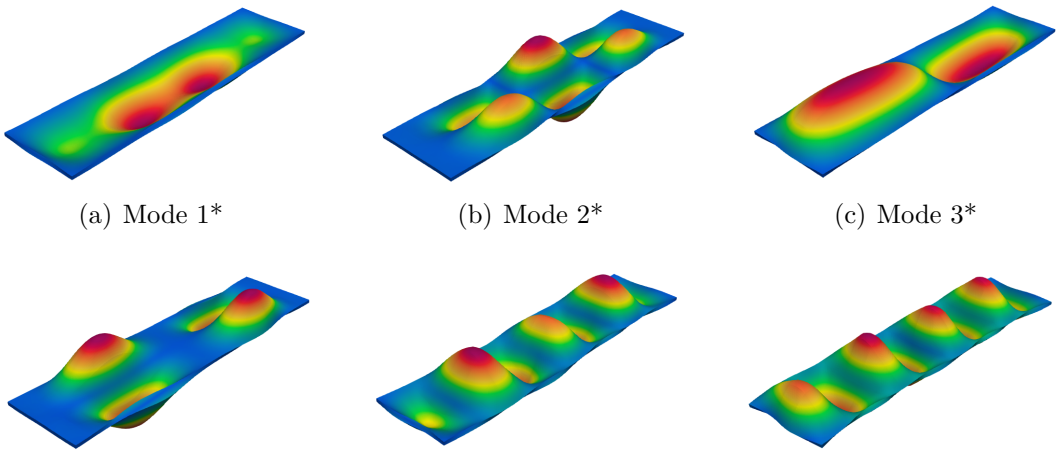

(a) Mode 1* (b) Mode 2* (c) Mode 3*

(d) Mode 4* (e) Mode 5* (f) Mode 6*

Fig. 5.39 Mode shapes of the first six vibrations for the rectangular VAT structure. N_x = 1.83×10^6 N/m.

one LD3 in the z-direction for the isotropic model, whereas 3LD3 kinematics are adopted for the through-the-thickness of the composite shell.

Figure 5.40 illustrates the quasi-static equilibrium curve for the studied isotropic and composite shell models, including some of the most relevant deformed configurations. At each step of the nonlinear equilibrium curve, free-vibrations are computed, adopting the local tangent stiffness of the deformed configuration. In Table 5.4, the natural frequency values for the first three mode shapes as a function of the transverse displacements are shown. The values of u_z are referred to Fig. 5.40. Figure 5.41 depicts the trends of the first

Isotropic				Composite			
$-u_z$	$f_1/\sqrt{\rho}$	$f_2/\sqrt{\rho}$	$f_3/\sqrt{\rho}$	$-u_z$	$f_1/\sqrt{\rho}$	$f_2/\sqrt{\rho}$	$f_3/\sqrt{\rho}$
0.00	56.82	56.55	95.44	0.00	44.05	51.77	90.76
0.24	47.59	50.32	86.43	0.13	40.78	48.38	82.61
0.57	29.99	44.38	81.90	0.63	21.16	37.75	65.98
1.11	16.89	39.11	59.14	1.12	20.41	42.85	48.93
1.36	24.43	44.54	52.44	1.46	21.13	42.04	48.06
1.48	22.68	45.23	52.63	1.58	20.77	37.84	48.39

Table 5.4 Natural frequencies [Hz/(kg/m^3)] for different transverse displacement [m]. Isotropic and composite pinched cylindrical shells.

six natural frequencies with respect to the transverse displacement. It can be observed that the natural frequencies decrease as the load rises. In these plots, we underline the

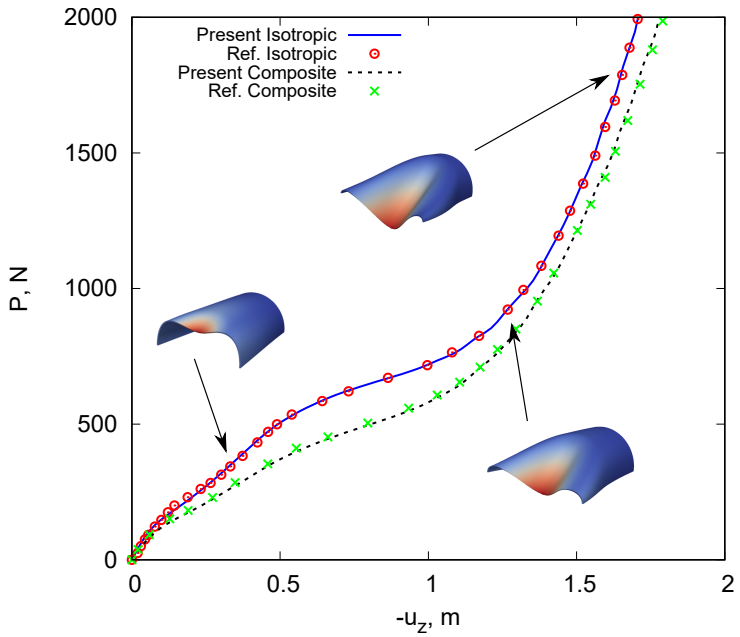

Fig. 5.40 Equilibrium curves of the isotropic and composite pinched cylindrical shell subjected to an end pinching force.

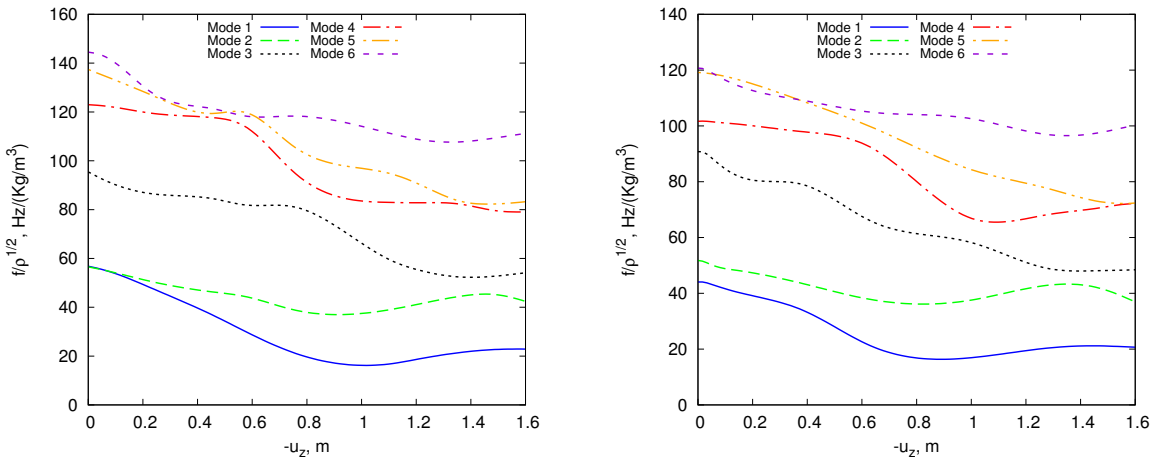

Fig. 5.41 Natural frequencies from modes 1 to 6. (a) Isotropic and (b) composite pinched cylindrical shell subjected to an end pinching force for progressively increasing displacements.

crossing between mode 5 and mode 6, some veering phenomena and the interaction with mode 4 in both isotropic and composite results. Moreover, the change of these mode shapes all along the quasi-static equilibrium path of the pinched composite structure is shown in Figs. 5.42 and 5.43. The most significant MAC graphical representations are

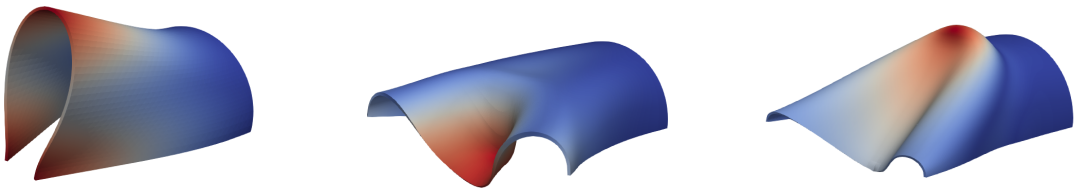

(a) $u_z = 0$ m (b) $u_z = 0.63$ m (c) $u_z = 1.58$ m

Fig. 5.42 First mode shape of the composite pinched cylindrical shell subjected to a pinching force for progressively increasing displacements.

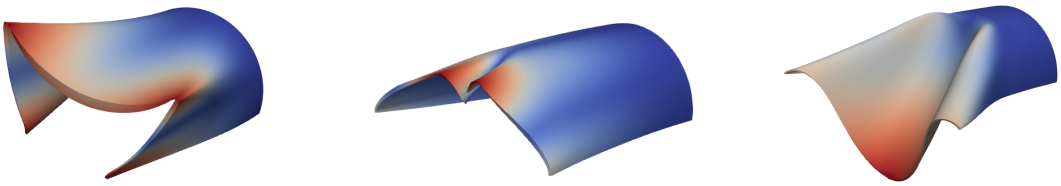

(a) $u_z = 0$ m (b) $u_z = 0.63$ m (c) $u_z = 1.58$ m

Fig. 5.43 Second mode shape of the composite pinched cylindrical shell subjected to a pinching force for progressively increasing displacements.

illustrated in Fig. 5.44. MAC is a scalar indicating correspondence between two sets of mode shapes, see [235, 236]. Different values of the nonlinear analysis are reported in comparison with the linear case ($u_z = 0$ m). This figures compare the first 10 modes for progressively increasing displacements. As reported by these graphical representations, natural modes for a low load (Fig. 5.44a) are identical to those related to the linear case ($u_z = 0$ m); i.e., all the MAC values in the diagonal are equal to 1. In Figs. 5.44b to 5.44d, the state is entirely nonlinear; in fact, dark boxes are all different from 1. This suggests that the structure shows a significant nonlinear influence, so the mode aberration analysis is crucial to predict the dynamic behaviours accurately.

In addition, the analysis for the composite pinched cylindrical shell subjected to compressive and transverse loads is also provided. The geometry, the constraints and the loading conditions are shown in Fig. 5.45a. Moreover, Fig. 5.45b illustrates the equilibrium curve (compressive load P_β versus transverse displacement). In this case,

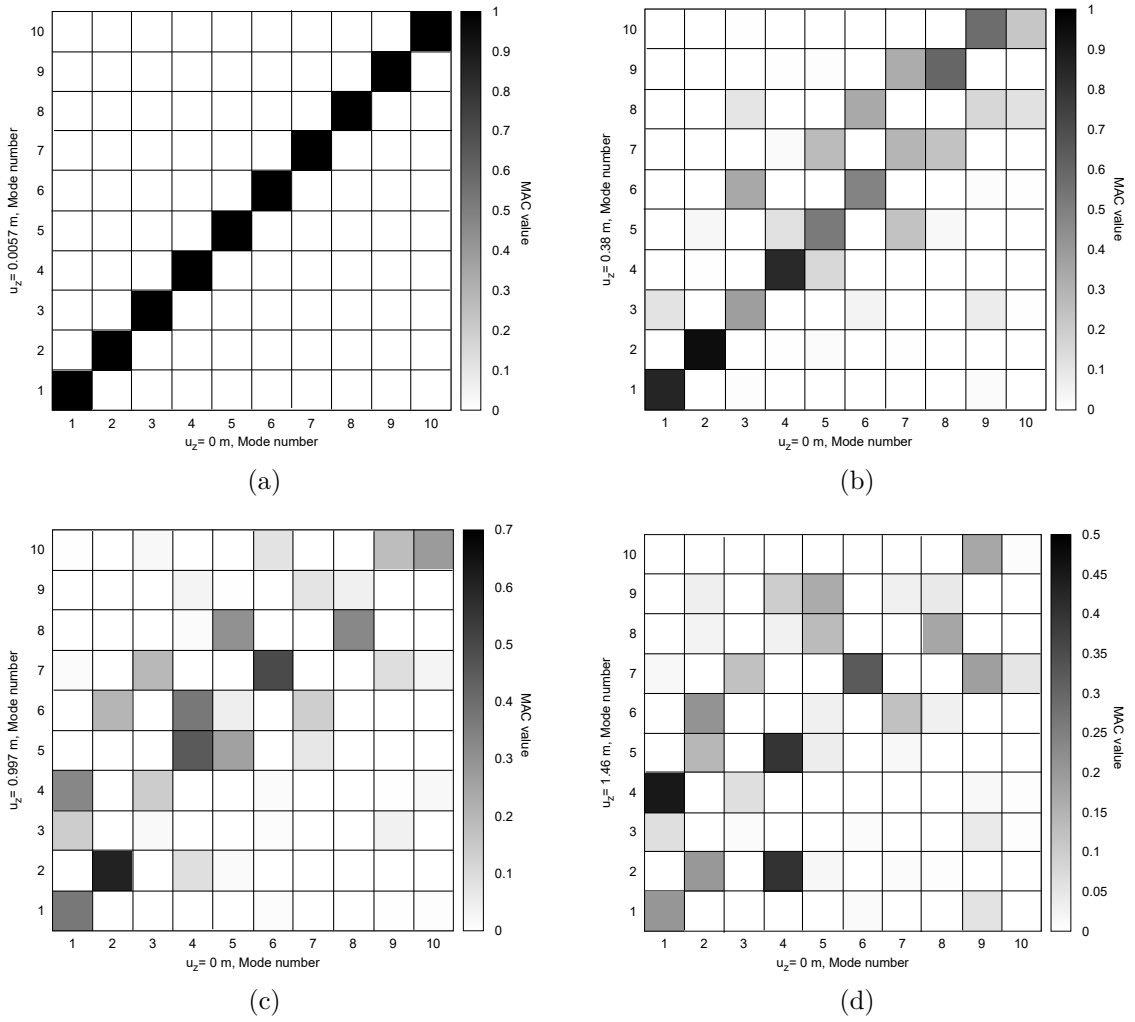

Fig. 5.44 MAC values between the modes of the undeformed structure and those of the deformed structure for the composite pinched cylindrical shell.

the compressive-transverse load ratio is equal to 66. The trends of the first five natural

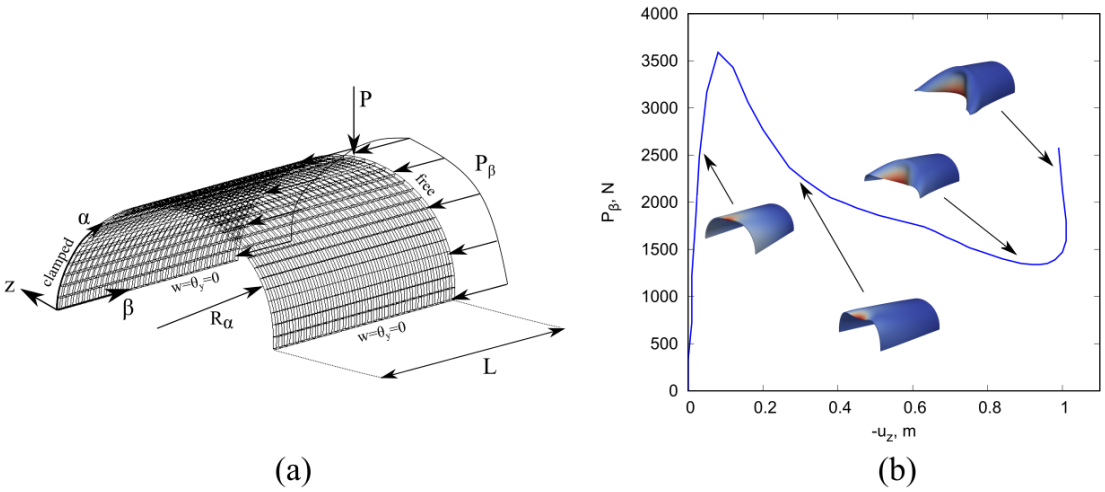

Fig. 5.45 (a) Composite pinched cylindrical shell subjected to compressive and transverse loads. (b) Equilibrium curve at the transverse load point.

frequencies with respect to the transverse displacement is reported in Fig. 5.46. Figures 5.47 and 5.48 display the evolution of some important mode as a function of the quasi-static equilibrium path of the composite pinched cylindrical shell under compressive and transverse loads. Finally, the MAC graphical representations are shown in Fig. 5.49. From the Figs. 5.46, 5.47 and 5.48, it is clear that the natural frequencies and, therefore, the relative modal shapes undergo a considerable change with the progressive increase of the nonlinear quasi-static analysis. Moreover, it can be observed some important phenomena, e.g., the interaction between mode 3, 4 and 5, the veering at $u_z = 0.169$ m, and the crossing at $u_z = 0.60$ m between modes 1 and 2.

5.2.5 Curved panel subjected to transverse loadings

As a further example, a hinged curved panel subjected to a transverse load P is analyzed. The geometric and material properties of the isotropic model are $E = 3102.75$ MPa and $\nu = 0.3$, with L = 508 mm, $R_\alpha = 2540$ mm, $\theta = 0.1$ rad and t = 12.7 mm, whereas those of composite $[90°/0°/90°]$ structure are the same as for the case in 4.4.1. The present structure is discretized employing 10×10Q9 for the surface mesh and 2LD3 in the thickness direction for the isotropic model, while 4LD3 kinematics are used in the through-the-thickness of the composite one.

Figure 5.50 shows the nonlinear equilibrium path of the hinged curved panel subjected to a transverse load for both isotropic and composite configurations, including deformed

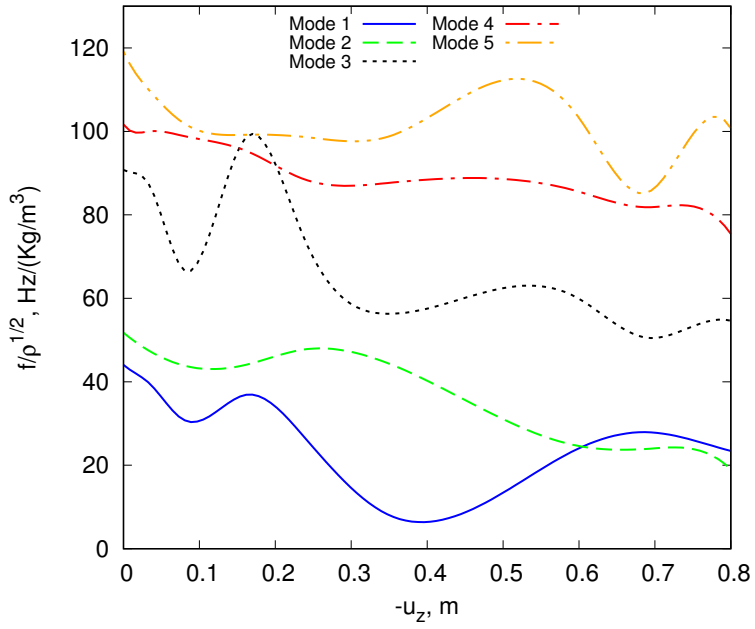

Fig. 5.46 Natural frequencies from modes 1 to 5. Composite pinched cylindrical shell subjected to compressive and transverse loads.

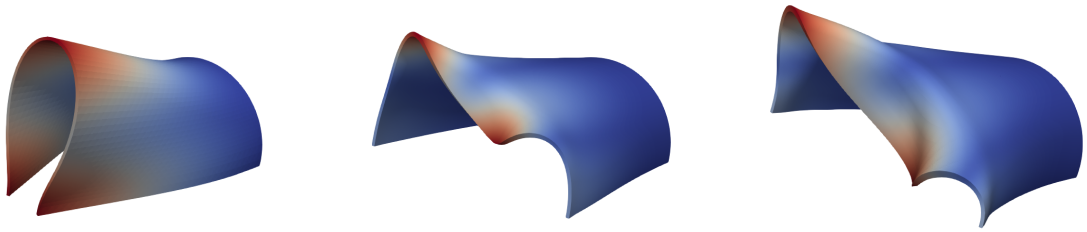

(a) $u_z = 0$ m (b) $u_z = 0.346$ m (c) $u_z = 0.690$ m

Fig. 5.47 First mode shape of the composite pinched cylindrical shell subjected to compressive and transverse loads for progressively increasing displacements.

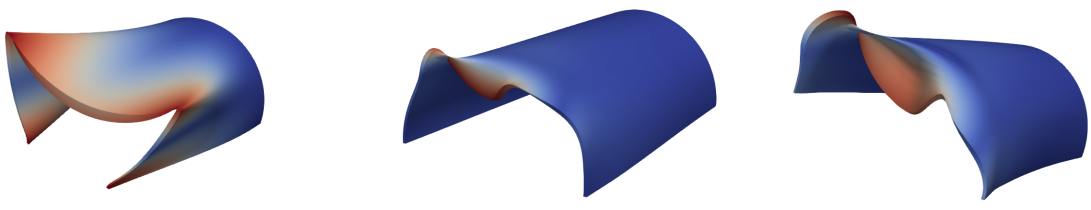

(a) $u_z = 0$ m (b) $u_z = 0.346$ m (c) $u_z = 0.690$ m

Fig. 5.48 Second mode shape of the composite pinched cylindrical shell subjected to compressive and transverse loads for progressively increasing displacements.

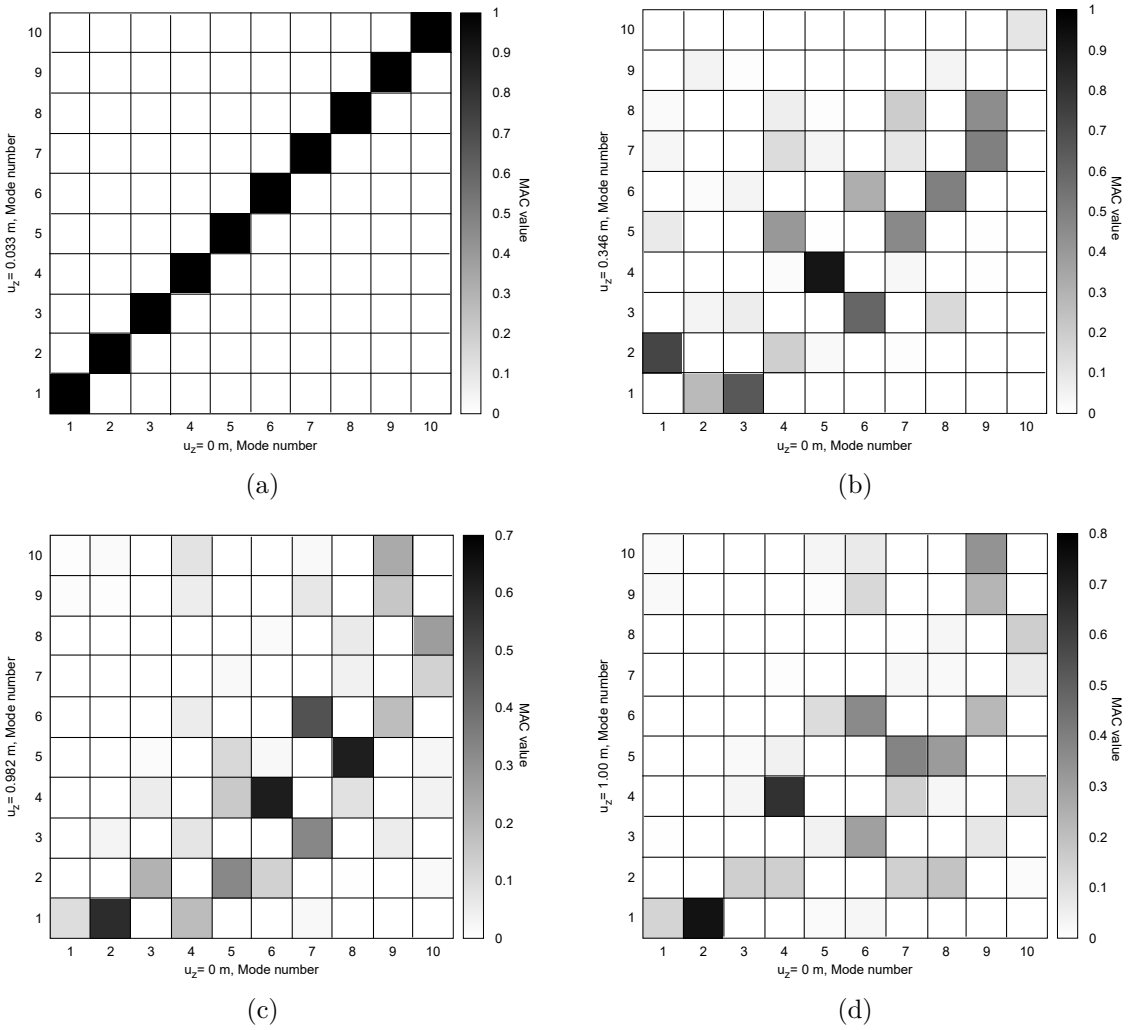

Fig. 5.49 MAC values between the modes of the undeformed structure and those of the deformed structure for the composite pinched cylindrical shell subjected to compressive and transverse loads.

configurations of some nonlinear states. Figure 5.51 and Table 5.5 show the distribution

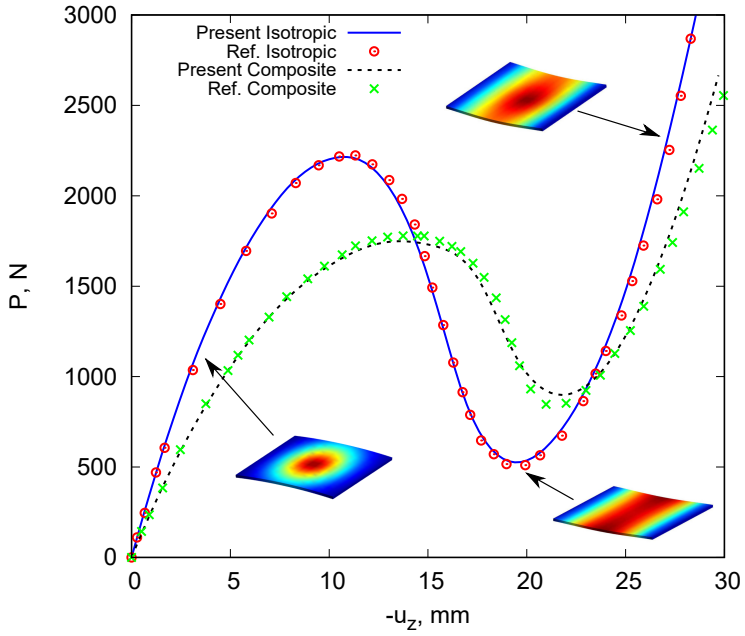

Fig. 5.50 Nonlinear equilibrium curves of the isotropic and composite hinged curved panel under transverse load.

and values of the natural frequencies of the first five and three modes, respectively. It

Isotropic				Composite			
$-u_z$	$f_1/\sqrt{\rho}\times10^5$	$f_2/\sqrt{\rho}\times10^5$	$f_3/\sqrt{\rho}\times10^5$	$-u_z$	$f_1/\sqrt{\rho}\times10^5$	$f_2/\sqrt{\rho}\times10^5$	$f_3/\sqrt{\rho}\times10^5$
0.00	10.67	11.88	16.30	0.00	9.71	10.46	13.97
0.49	10.39	11.72	16.07	0.37	9.56	10.39	13.87
4.2	8.10	10.28	14.39	4.45	7.65	9.47	12.75
10.30	1.79	6.75	11.47	17.60	2.26	3.81	10.30
15.50	5.54	1.86	8.89	21.75	1.71	3.44	10.74
25.82	9.93	8.65	14.82	27.23	6.99	7.17	13.50

Table 5.5 Natural frequency values [Hz/(kg/mm^3)] for different transverse displacements [mm] for the isotropic and composite hinged curved panel.

can be observed that natural frequencies, illustrated in Fig. 5.51, gradually decreases with the increasing load and, then, they rise. In particular, it is important to highlight the crossing between mode 1 and mode 2 (Fig. 5.51a) at $u_z = 13.10$ mm, with the consequent change of the mode shapes. Figures 5.52 and 5.53 provide the evolution of these modes with respect to the quasi-static equilibrium path of the isotropic hinged model. Furthermore, MAC representations are presented in Fig. 5.54, showing a

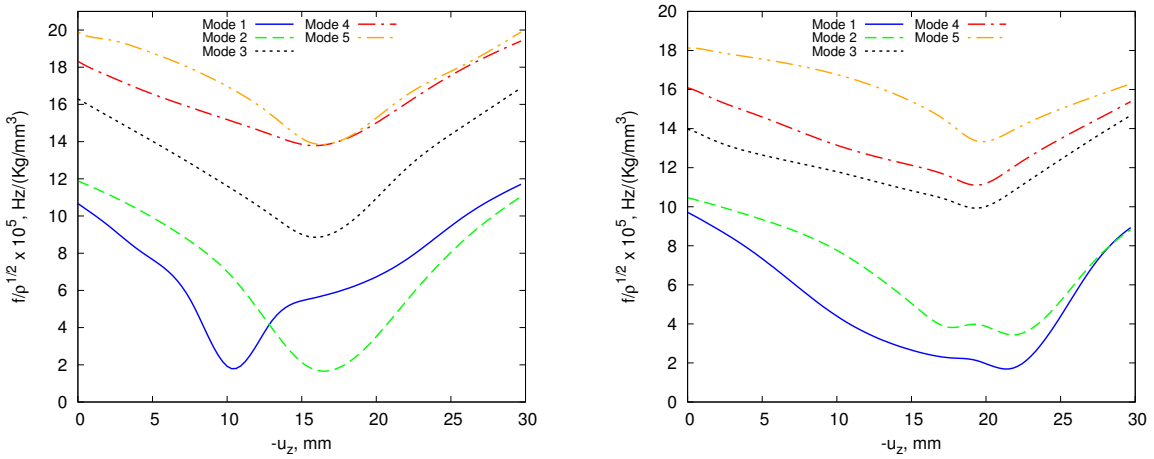

(a) (b)

Fig. 5.51 The variation of first five natural frequencies. (a) Isotropic and (b) composite hinged curved panel under transverse loadings.

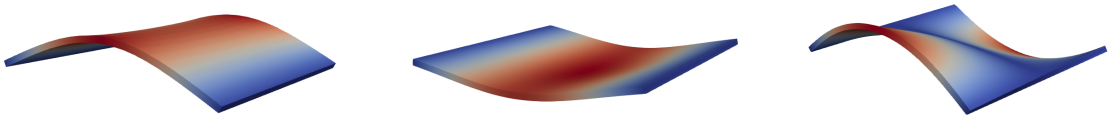

(a) $u_z = 0$ mm (b) $u_z = 10.32$ mm (c) $u_z = 21.95$ mm

Fig. 5.52 Mode shape of the first natural frequency of the isotropic hinged curved panel under transverse load for increasing displacements.

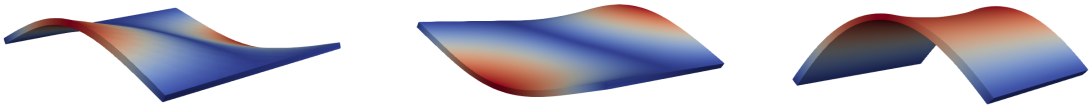

(a) $u_z = 0$ mm (b) $u_z = 10.32$ mm (c) $u_z = 21.95$ mm

Fig. 5.53 Mode shape of the second natural frequency of the isotropic hinged curved panel under transverse load for increasing displacements.

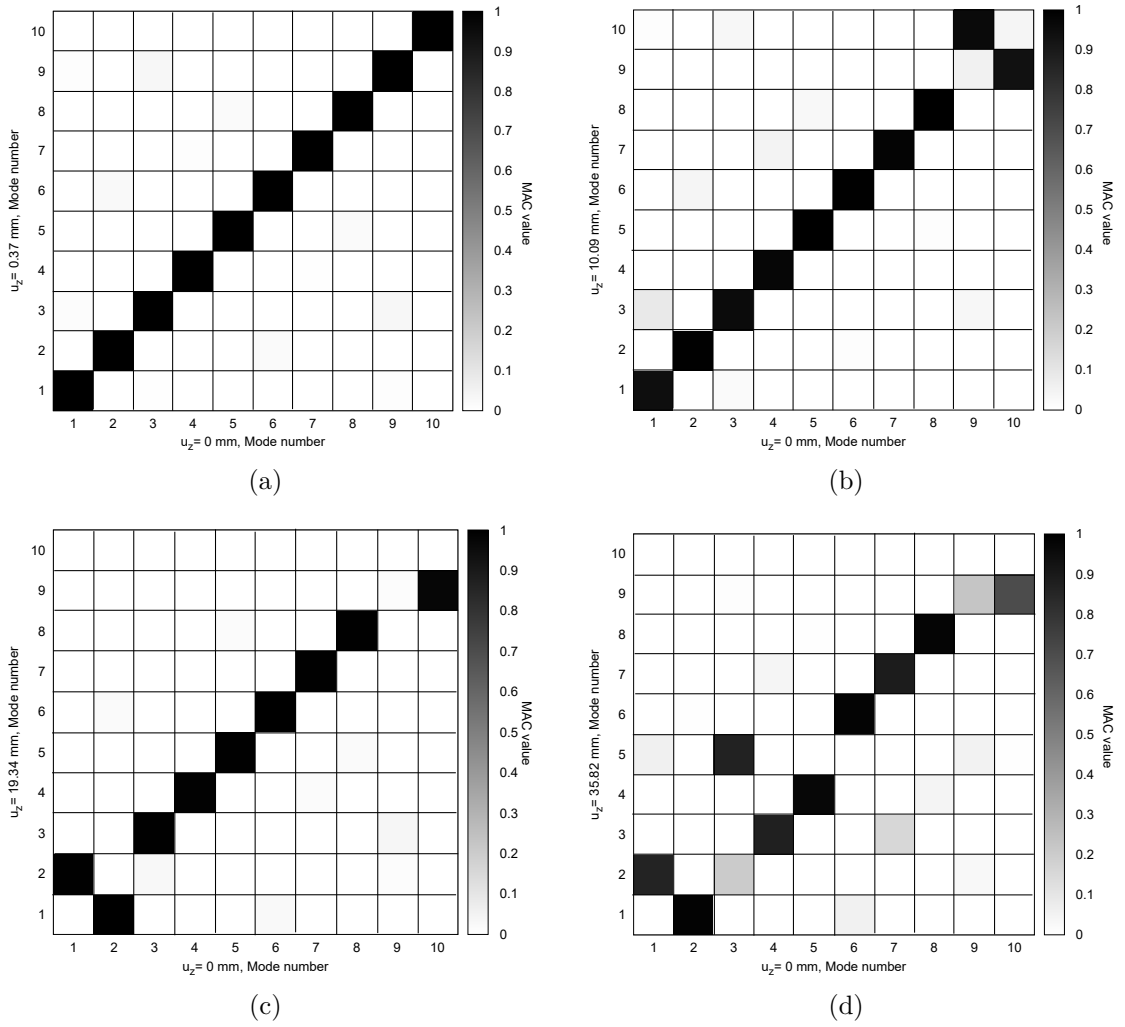

Fig. 5.54 MAC representations between the modes of the undeformed structure and deformed one for the isotropic hinged curved panel.

significant mode change for progressively increasing displacements.

In addition, for the sake of completeness, the isotropic hinged curved panel under compression and transverse load is also studied. In this case, the compressive-transverse load ratio is equal to 22. The nonlinear equilibrium curve and the loading conditions of this further case are depicted in Fig. 5.55. Figure 5.56 provides the the first five natural

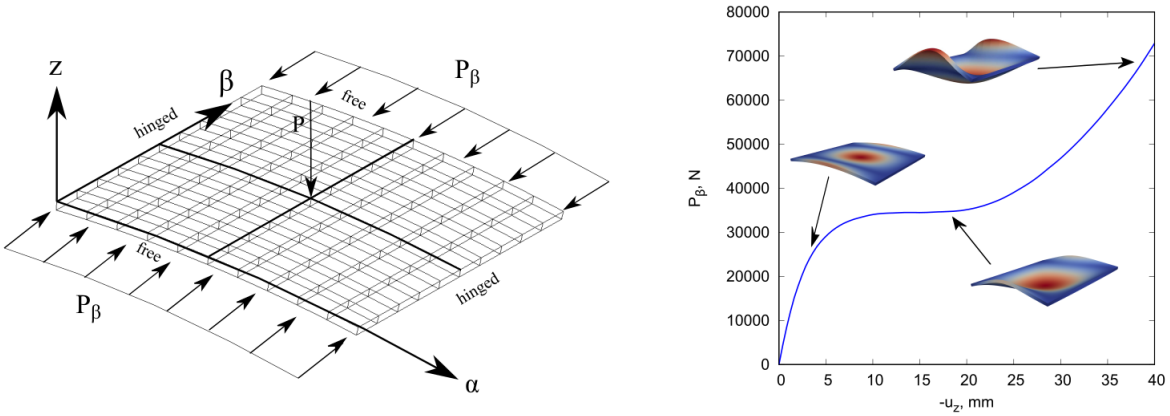

Fig. 5.55 (a) Isotropic hinged curved panel under compression and transverse loadings. (b) Equilibrium path at the transverse loading point.

frequencies trend with respect to transverse displacements. It can be noted that there are two important phenomena, e.g., the crossing between mode 3 and mode 4 at u_z= 2.39 mm, and the veering one between mode 3 and mode 5 at u_z= 28.58 mm. Figures 5.57, 5.58 and 5.59 report the modes evolution as a function of the quasi-static equilibrium curve of the isotropic hinged curved panel under compression and transverse load. Furthermore, the MAC values for this last example are represented in Fig. 5.60, in which a more significant mode change for progressively increasing displacements compared to the case with only the transverse load can be observed.

5.2.6 Curved panel subjected to compressive loadings

Different curved panels subjected to compressive loadings are analyzed as subsequent examples. The investigated models have the following geometric data: L = 355 mm, a = 355 mm, t = 2 mm. The representation of the curved panel with R/a = 5 is illustrated in Fig. 5.61. Regarding the boundary conditions, the constraints are the same considered for the plate 1 in the previous case. The material properties for these curved panels are: E = 70 GPa, ν = 0.33 and ρ = 2780 kg/m^3. The convergent model for these curved

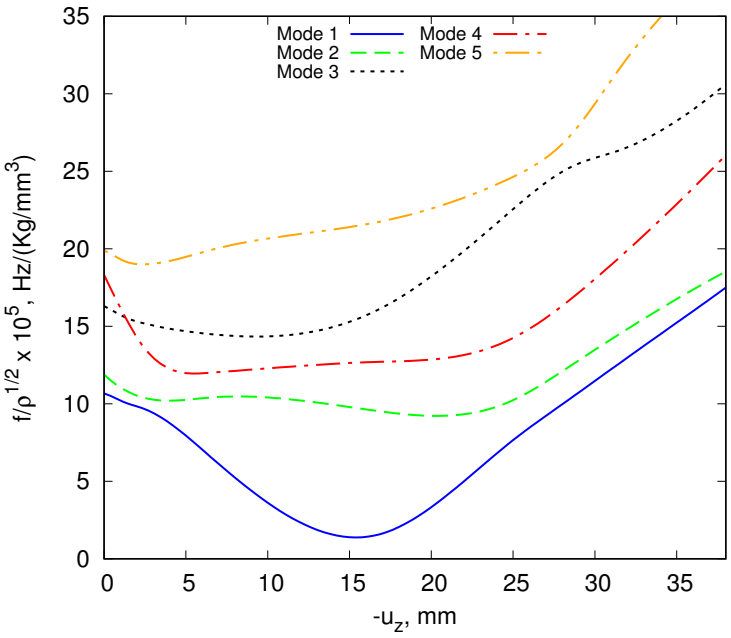

Fig. 5.56 The variation of the first five natural frequencies for the isotropic hinged curved panel under compression and transverse loadings.

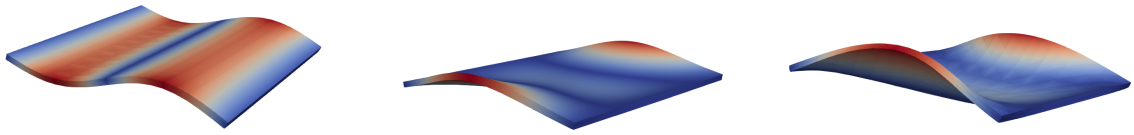

(a) $u_z = 0$ mm (b) $u_z = 6.44$ mm (c) $u_z = 38.80$ mm

Fig. 5.57 Third mode shape of the isotropic hinged curved panel subjected to compression and transverse loadings.

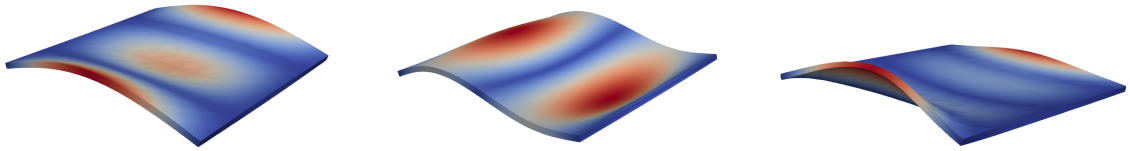

(a) $u_z = 0$ mm (b) $u_z = 6.44$ mm (c) $u_z = 38.80$ mm

Fig. 5.58 Fourth mode shape of the isotropic hinged curved panel subjected to compression and transverse loadings.

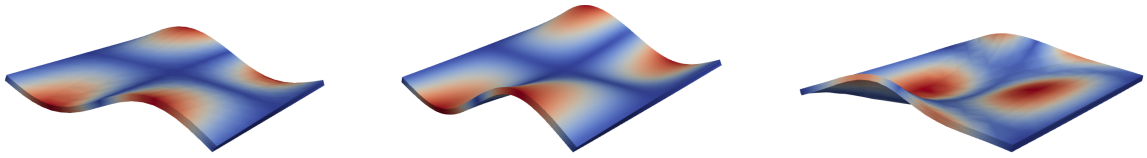

(a) $u_z = 0$ mm (b) $u_z = 6.44$ mm (c) $u_z = 38.80$ mm

Fig. 5.59 Fifth mode shape of the isotropic hinged curved panel subjected to compression and transverse loadings.

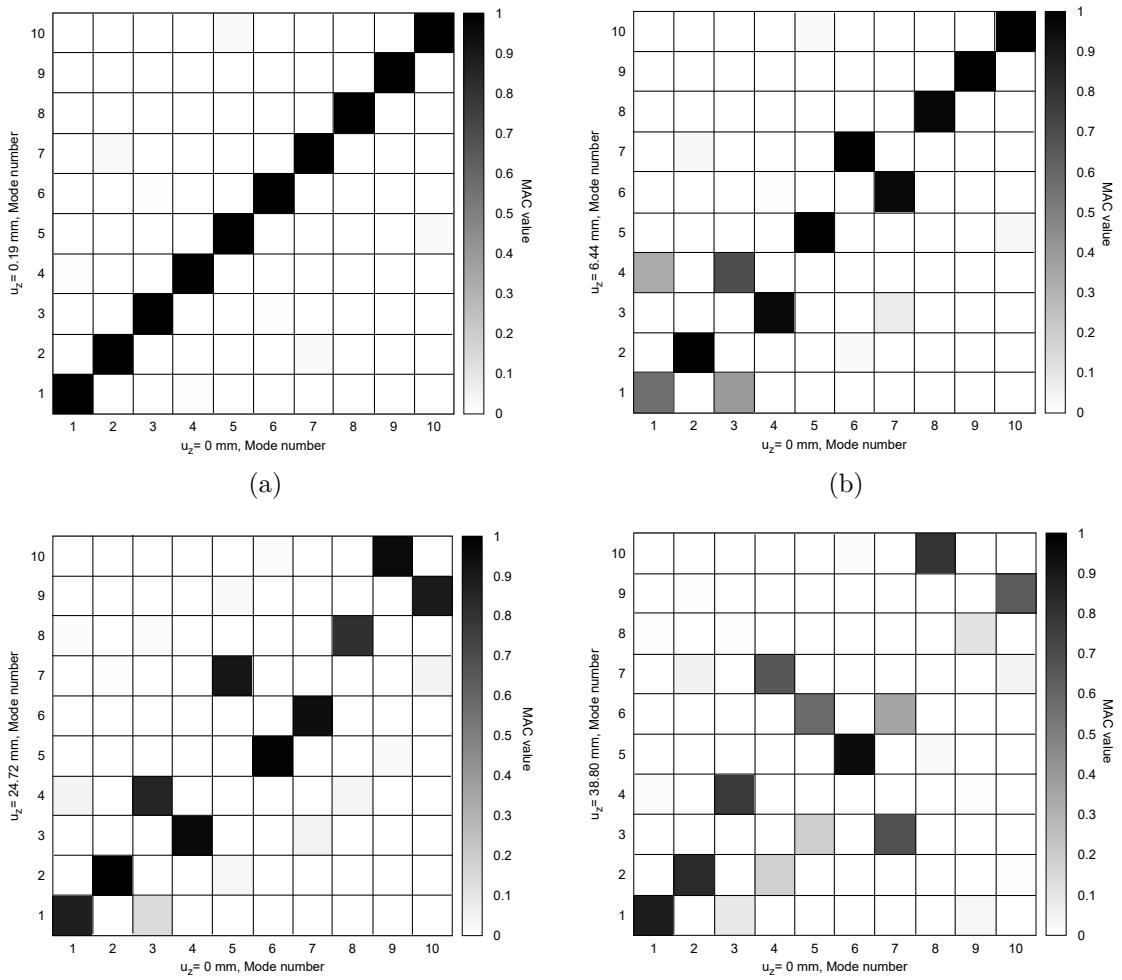

Fig. 5.60 MAC representations between the modes of the undeformed structure and deformed one for the isotropic hinged curved panel under compression and transverse load.

panel structures is reached employing 10×10Q9 for the in-plane mesh approximation and only one LD2 in the thickness direction.

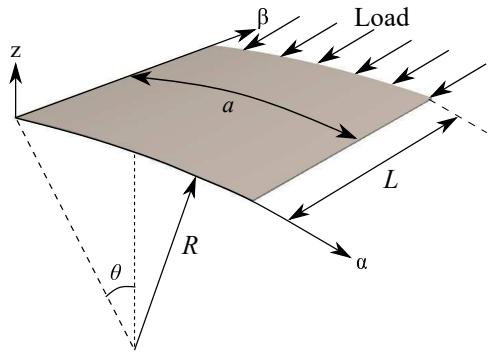

Fig. 5.61 Curved panel with R/a = 5 subjected to compressive load.

The nonlinear quasi-static analysis has been performed for different values of R/a to evaluate the effect of the curvature. In contrast, VCT is only shown for the case R/a = 5 for the sake of brevity. Figure 5.62a depicts the quasi-static equilibrium curves for the investigated metallic curved panels considering different R/a values. In detail, the equilibrium path of the curved panel case with R/a = 5 with some of the most relevant deformed configurations is reported in Fig. 5.62b. For different states of interest, the

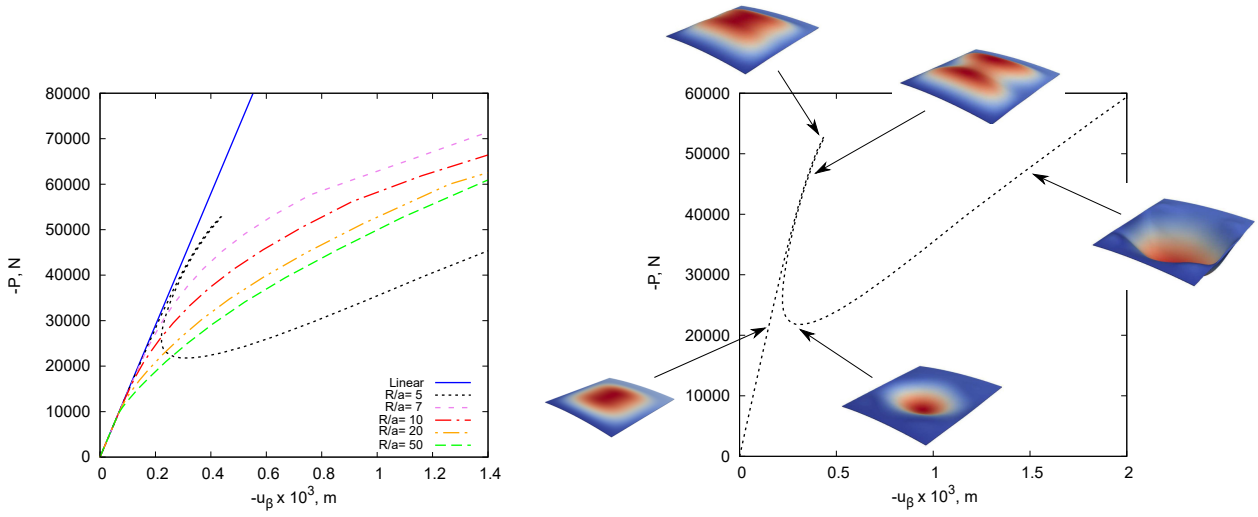

Fig. 5.62 Equilibrium curve of the curved panels subjected to compressive load. (a) Different curvatures; (b) R/a = 5.

trend of the first ten natural frequencies with respect to the progressive load by means of the trivial linearized solution is provided in Fig. 5.63a. Instead, the natural frequency

variation of mode 1 versus compressive loading via full nonlinear solution is depicted in Fig. 5.63b. It can be observed that considering the nonlinearity, the trend of the

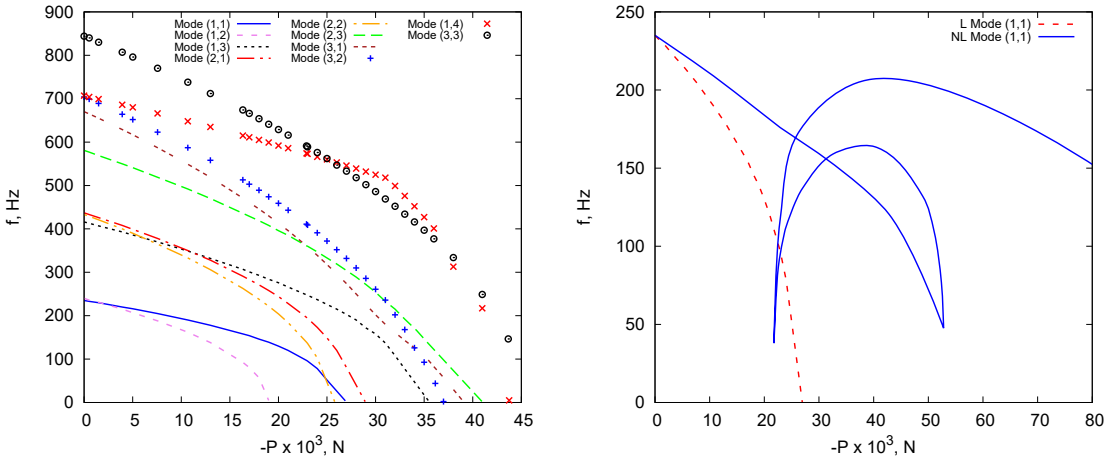

(a) (b)

Fig. 5.63 Natural frequency variation versus compressive loading via (a) trivial linearized solution and (b) full nonlinear solution (NL) vs trivial linearized solution (L) for mode (1,1). Curved panel with R/a = 5.

natural frequencies is very complex. The nonlinear variation of the natural frequencies was divided into three parts, Fig. 5.64, to plot more modes and have a better and clearer representation. The characteristics first ten vibration mode shapes of the curved panel with R/a = 5 at P = 0 N are provided in Fig. 5.65. As a result, it is possible to evaluate the complex trend of the natural frequencies with respect to the higher progressive compressive loadings and to predict the linear and nonlinear buckling load by performing a nonlinear study.

5.2.7 VAT composite hinged shell subjected to snap-through

A VAT composite hinged shell under compression and transverse load is investigated. This shell consists of 3 layers with the following lamination: $[90° + < 0°/45° > \ / \ 0° + < 0°/45° > \ / \ 90° + < 0°/45° >]$. This structure has: L = 508 mm, R_α = 2540 mm, θ = 0.1 rad and the thickness (h) equal to 12.7 mm. The material properties of the considered structure are: E_1 = 3300 MPa, $E_2 = E_3$ = 1100 MPa, $G_{12} = G_{13}$ = 660 MPa, and $\nu_{12} = \nu_{13}$ = 0.25. For clarity, the analysis are conducted considering a density ρ equal to 1 kg/m^3. All nodal displacements are restrained along the hinged edges. The present shell is modelled using 10×10Q9 for the in-plane mesh approximation and 1LD2 in each layer in the z-direction.

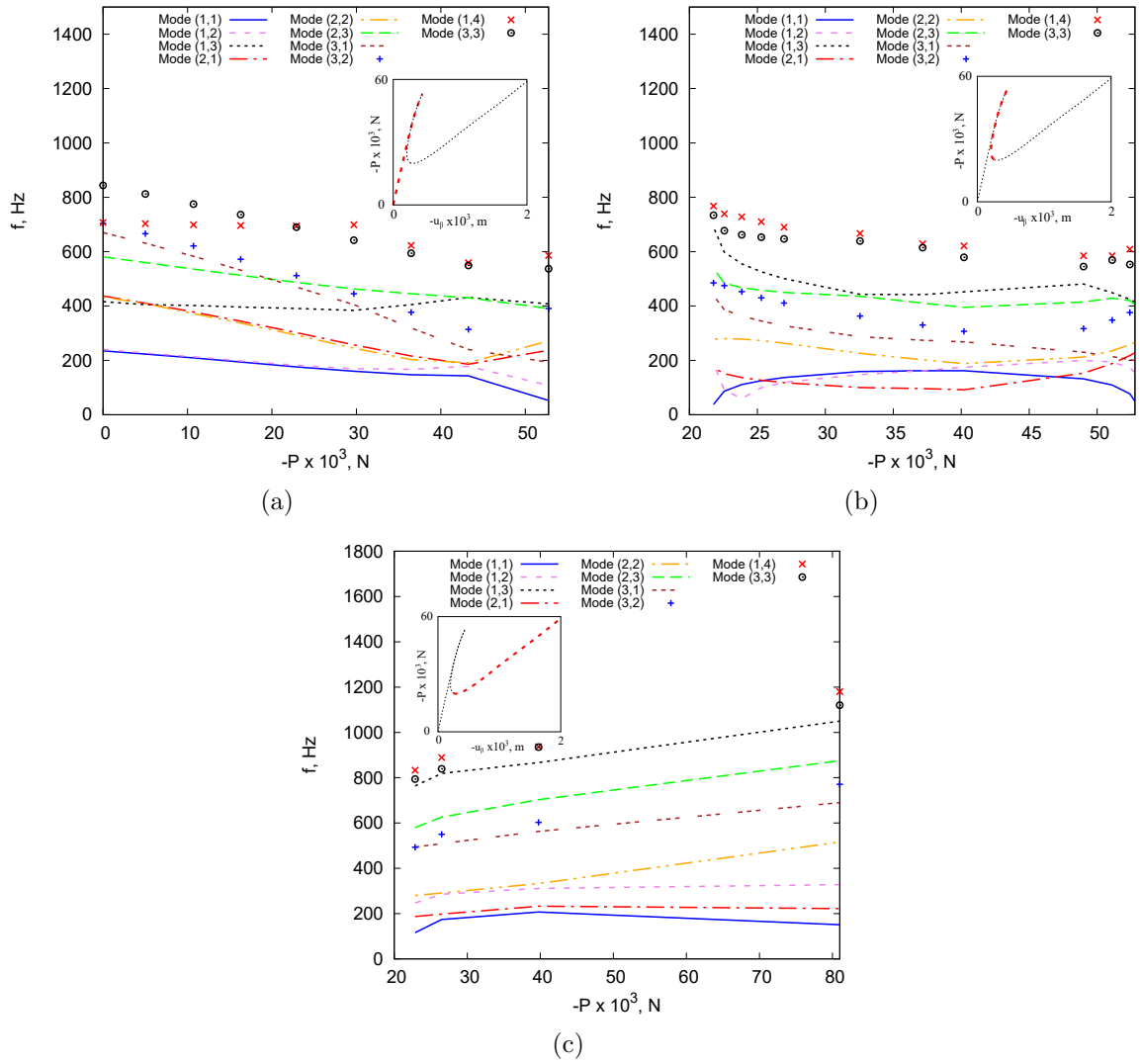

Fig. 5.64 Nonlinear variation of the natural frequencies all along the quasi-static equilibrium path. Curved panel with R/a = 5.

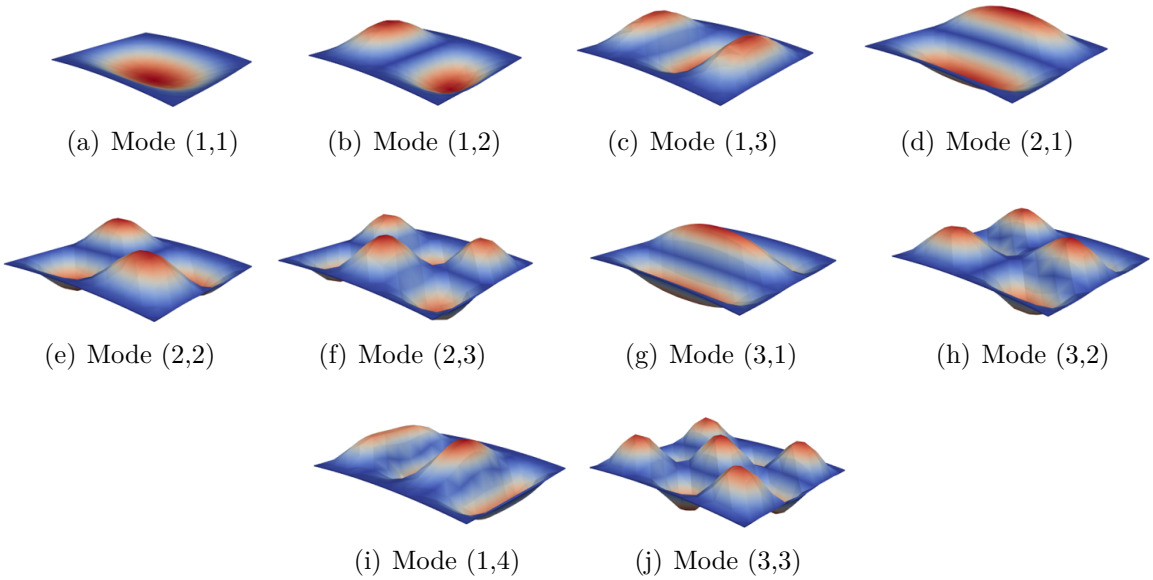

(a) Mode (1,1) (b) Mode (1,2) (c) Mode (1,3) (d) Mode (2,1)

(e) Mode (2,2) (f) Mode (2,3) (g) Mode (3,1) (h) Mode (3,2)

(i) Mode (1,4) (j) Mode (3,3)

Fig. 5.65 Characteristics first ten free vibration mode shapes for the curved panel with R/a = 5.

The transverse displacements at the middle of the shell with respect to the compressive load P_β, considering the ratio $P_{\beta_0}/P_0 = 2.2$, are displayed in Fig. 5.66, including also the linearized buckling load value ($P_{cr} = 2.07$ N/mm). Particularly, some representative points with the relative angle at which the local tangent stiffness is computed are reported in this graph. Basically, at each step, free vibration analyses are conducted, as presented in Section 4.2, by using the tangent stiffness matrix obtained in the previous nonlinear static analysis.

Figure 5.67 provides the variation of natural frequencies as a function of compressive loadings through the trivial linearized solution, whereas the natural frequencies variation evaluated by using the full nonlinear approach is depicted in Fig. 5.68. For clarity reasons, a comparison between the variation of the first two natural frequencies employing the two approaches is presented in Fig. 5.69. In this figure, the red dots and the relative numbers refer to those represented in Fig. 5.66. The results suggest that for this type of structure in order to provide the correct trend of the natural frequencies is mandatory to consider a full nonlinear method. In detail, two peaks of the blue line, see Fig. 5.69, denote the linear (1.25 N/mm) and nonlinear (5.30 N/mm) buckling loads, respectively. For completeness, the first ten vibration mode shapes of the hinged VAT composite structures are shown in Fig. 5.70. Finally, a MAC representation is displayed in Fig. 5.71, in which the first 10 modes at the state 3 and 5, see Fig. 5.69 are compared; the

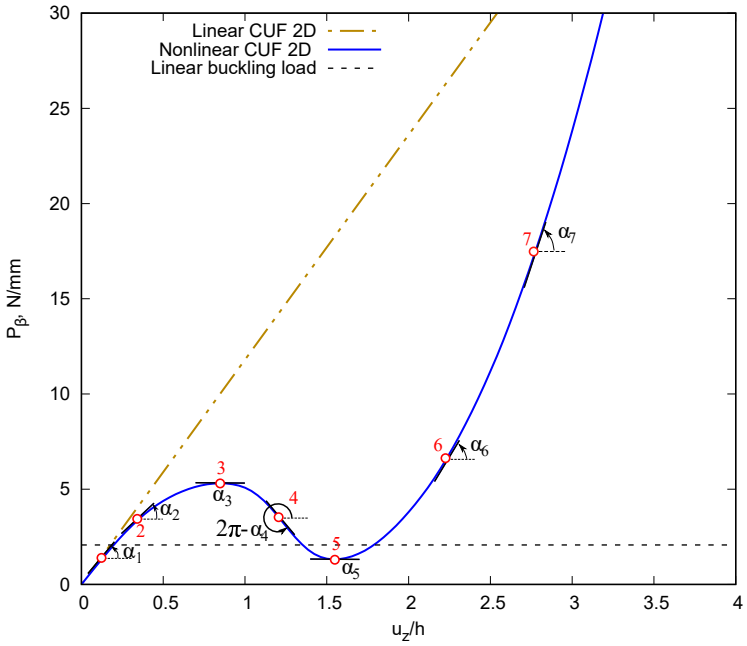

Fig. 5.66 Equilibrium trend at the middle of the VAT composite hinged shell under compression and transverse load.

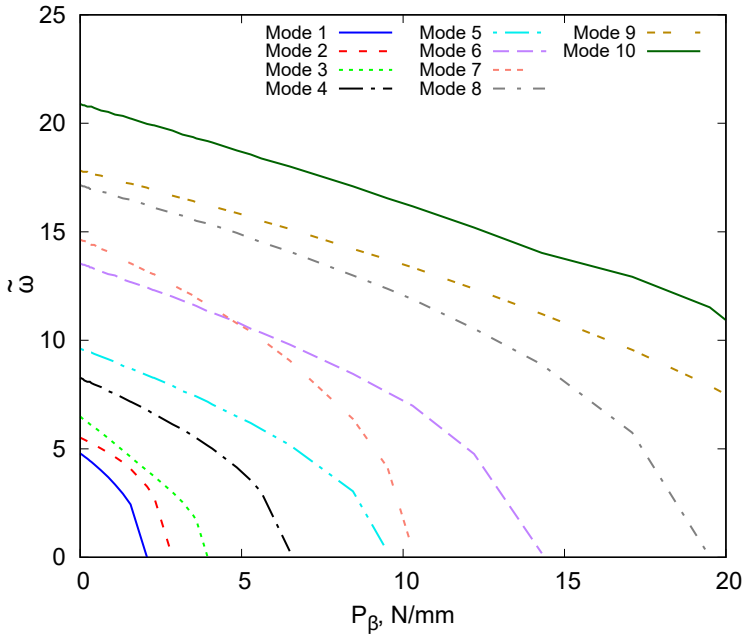

Fig. 5.67 The variation of non-dimensional natural frequencies vs compressive loadings through the trivial linearized solution for the VAT composite hinged shell under compression and transverse load.

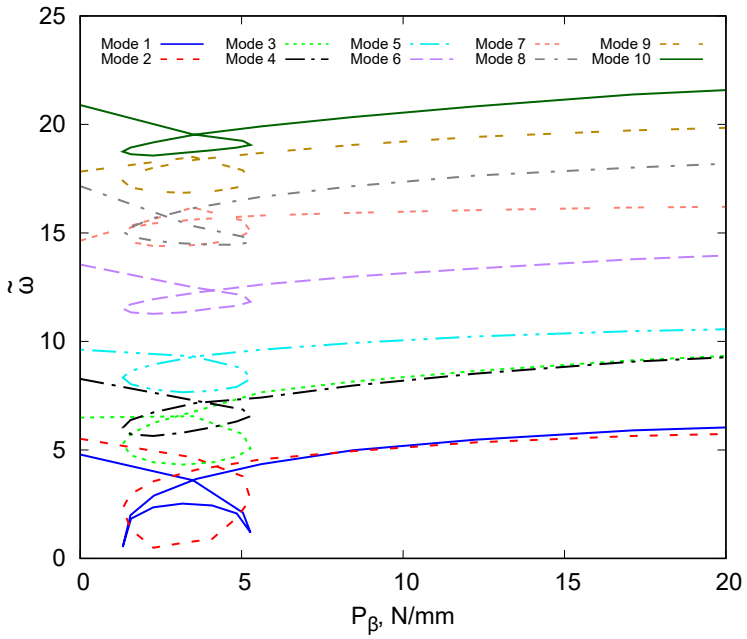

Fig. 5.68 The variation of non-dimensional natural frequencies vs compressive loadings via full nonlinear approach for the VAT composite hinged shell under compression and transverse load.

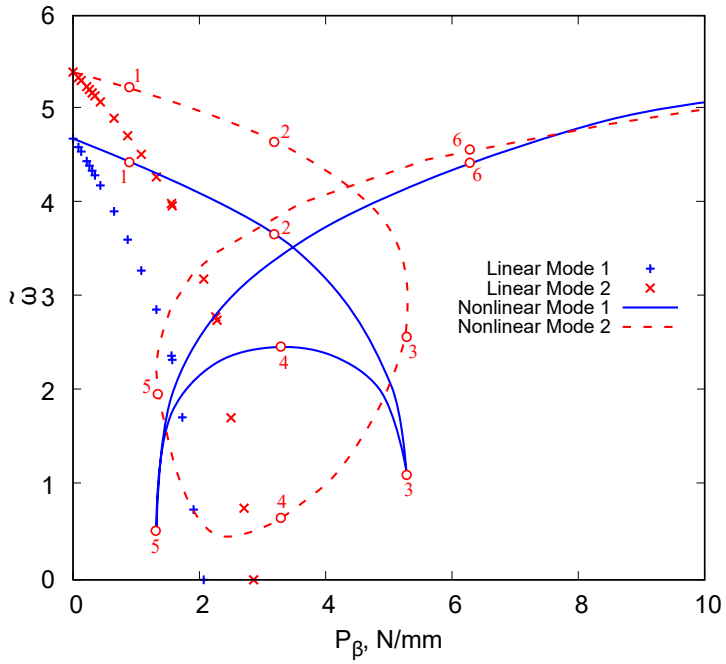

Fig. 5.69 Comparison between the trivial linearized and full nonlinear approaches for the variation of the first two non-dimensional natural frequencies for the VAT composite hinged shell under compression and transverse loadings.

natural modes at state 3 are identical to those relating to state 5, with the exception of modes 7 and 8 which exhibit a crossing phenomena.

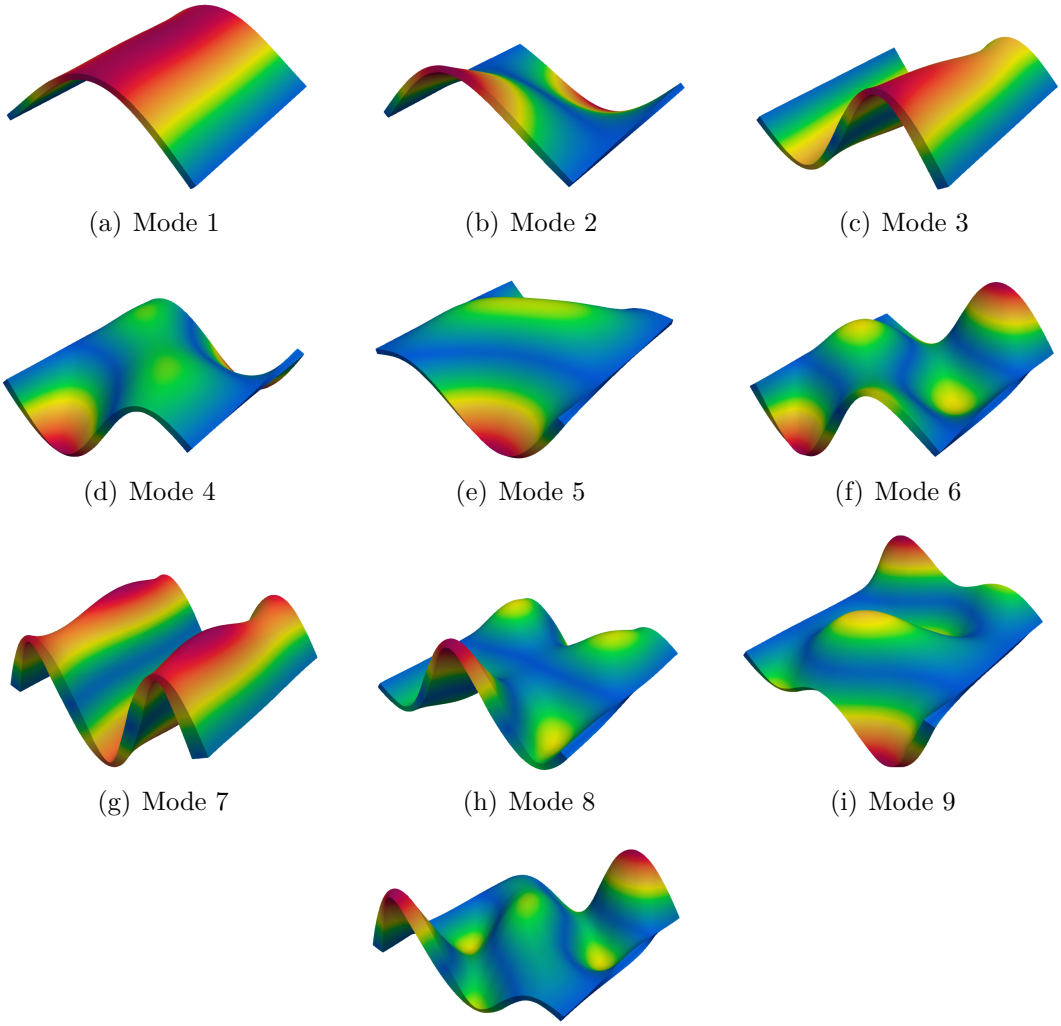

(a) Mode 1 (b) Mode 2 (c) Mode 3

(d) Mode 4 (e) Mode 5 (f) Mode 6

(g) Mode 7 (h) Mode 8 (i) Mode 9

(j) Mode 10

Fig. 5.70 Mode shapes of the first ten free-vibration for the VAT composite hinged shell subjected to compression and transverse load.

5.2.8 Curved panel under internal pressure and axial compression

The following case regards the vibration analysis of a simply-supported curved shell structure subjected to internal pressure and compressive loadings, illustrated in Fig. 5.72. Particular interest is devoted to show the effect of the ratios between the Young moduli

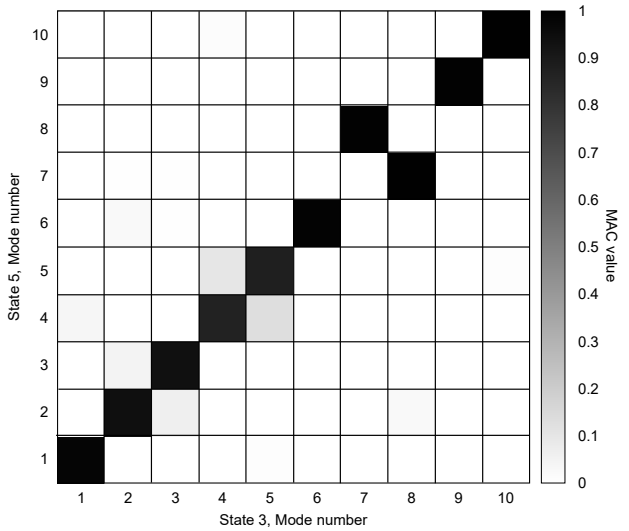

Fig. 5.71 MAC representation between the modes of the state 3 and state 5 for the VAT composite hinged shell subjected to compression and transverse load.

of the loading domain and the research object (E_L/E_R) and the internal pressure (P_{inner}). The structure consists of a aluminium curved panel with the following geometrical and material properties: 508 × 508 × 12.7mm (arclength × width × thickness), two loading areas are 508 × 20 × 12.7mm, attached to two opposite sides of the panel, $\mathrm{E_R} = 70.0 \times 10^3 \mathrm{N/mm^2}$, $\nu = 0.33$, $\rho = 2700 \mathrm{kg/m^3}$, radius $\mathrm{R}_\alpha = 2540.01$mm and a central angle $\theta = 0.2$. The reason for these two loading parts is related to the fact that in real working conditions, a uniform axial pressure requires the application of a pair of opposing fasteners on the edges of the curved shell. After convergence studies, not reported here for the sake of brevity, the structure is modelled by employing 10×10Q9 for the in-plane mesh, while 2LD3 are used in the z-direction. In addition, the loading part is discretized by adopting 1×10Q9 + 2LD3.

Effect of E_L/E_R

Various kinds of attached loading parts strongly and directly influence the original boundary condition of the structure. Five different values of E_L/E_R are evaluated: 1, 10, 500, 1000, 2000, considering $P_{inner} = 1$ MPa, $\theta = 0.2$, $R_\alpha = 2540.01$ mm. Figures 5.73 and 5.74 illustrate the effect of these different ratio value on the trend of the natural frequencies for increasing axial compressive loadings. As evident from Fig.5.73(a), the frequencies of mode 1 and mode 3 decrease as P_{axial} increases. It is observed how the first buckling mode corresponds with the first vibration mode which reaches zero for a bucking load equal to about 250 MPa. In addition, Fig. 5.73(b) shows a veering phenomenon

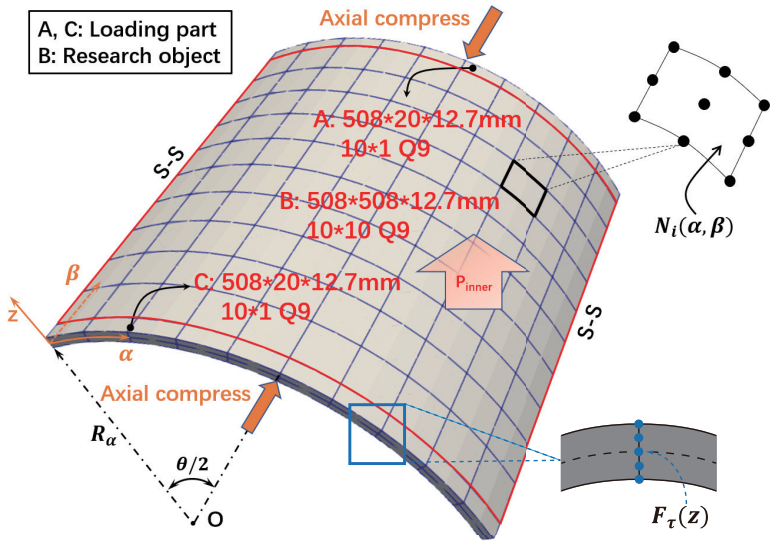

Fig. 5.72 Geometrical description of the isotropic curved shell under internal pressure (P_{inner}) and axial compression (P_{axial}),including the FE discretization and CUF kinematics.

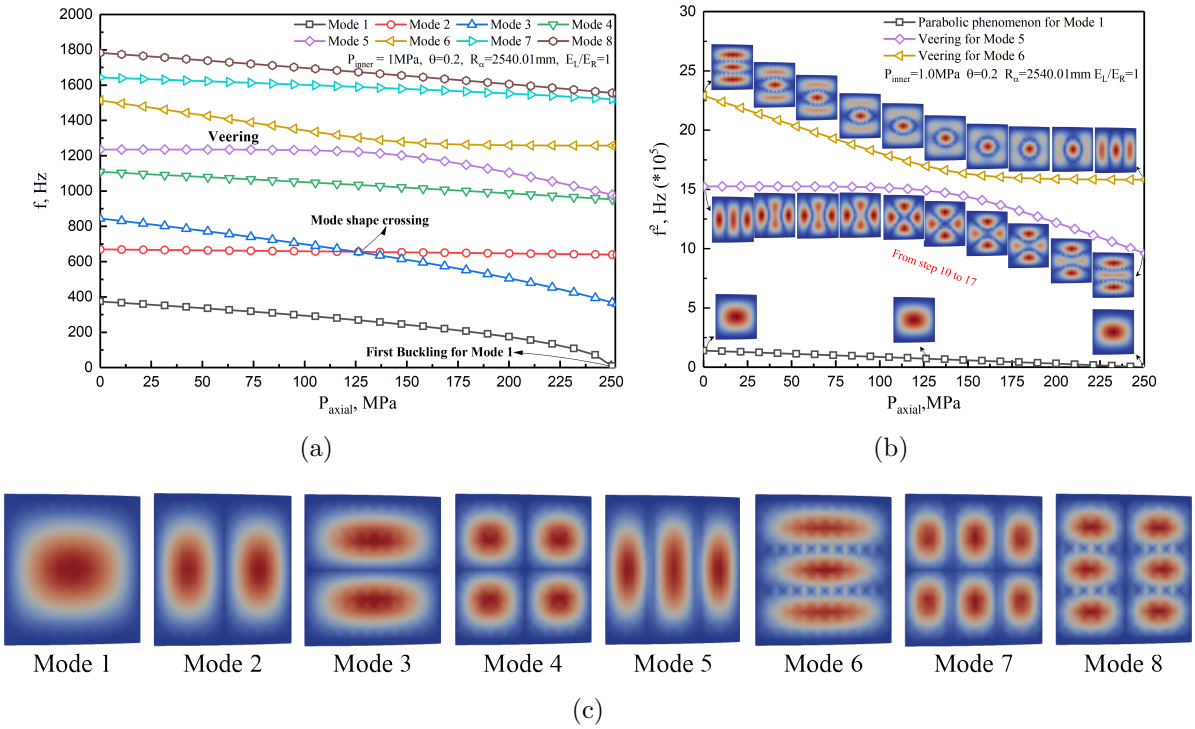

Fig. 5.73 (a) Natural frequencies variation, (b) Parabolic and veering phenomenon and (c) Mode shapes of the first eight free vibrations, considering $E_L/E_R = 1$, $P_{inner} = 1$ MPa, $\theta = 0.2$, $R_\alpha = 2540.01$ mm. Curved panel under internal pressure and axial compression.

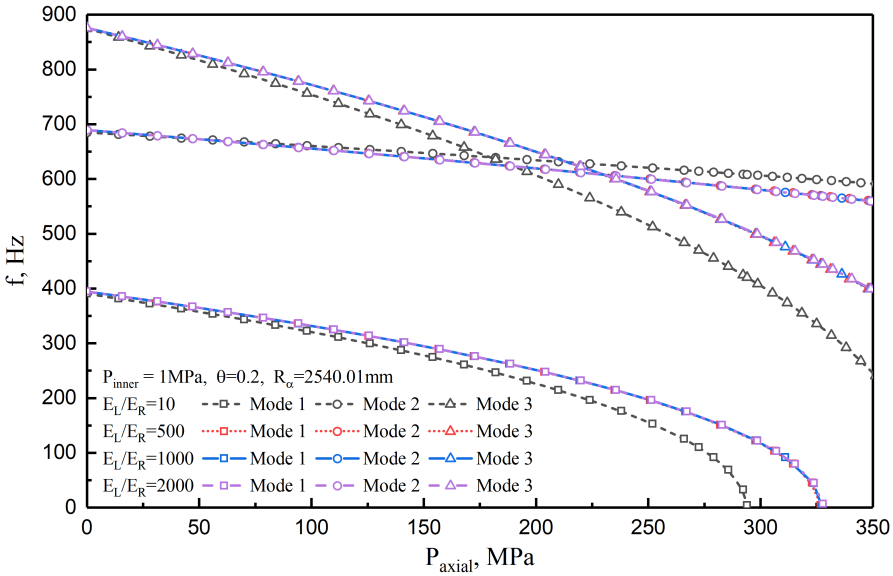

Fig. 5.74 Effect of different E_L/E_R on the natural frequencies variation, considering fixed $P_{inner} = 1$ MPa, $\theta = 0.2$, $R_\alpha = 2540.01$ mm. Curved panel under internal pressure and axial compression.

between modes 5 and 6 and a parabolic behaviour of mode 1. From Fig. 5.74, we see how for all the ratios the buckling mode shape turns out to be that of mode 1 and the the E_L/E_R make a difference to vibration frequencies of the shell structure, reaching convergence for the ratio values: 500, 1000, 2000.

Since uniform pressure has to be applied to the structure, it is not an ideal way to impose a point load on each node of the side surface to generate uniform pressure in terms of numerical simulation. On the other hand, the lateral surface of the curved shell cannot always hold itself as a smooth surface with the axial compression directly applied to the sides in real situations. Some unpredictable conditions, such as shrinking or expansion, occur during the loading process. A point load on the midpoint of the side surface of the loading part is applied by choosing an appropriate ratio E_L/E_R that are able to theoretically generate uniform pressure. Figure 5.75 shows different loading application on the sides after adding the loading parts considering different E_L/E_R. Clearly, lower E_L/E_R results in stress concentration and irregular displacements in the axial direction. By combining Figs. 5.74 and 5.75, $E_L/E_R = 1000$ is enough to generate uniform axial pressure on the structure.

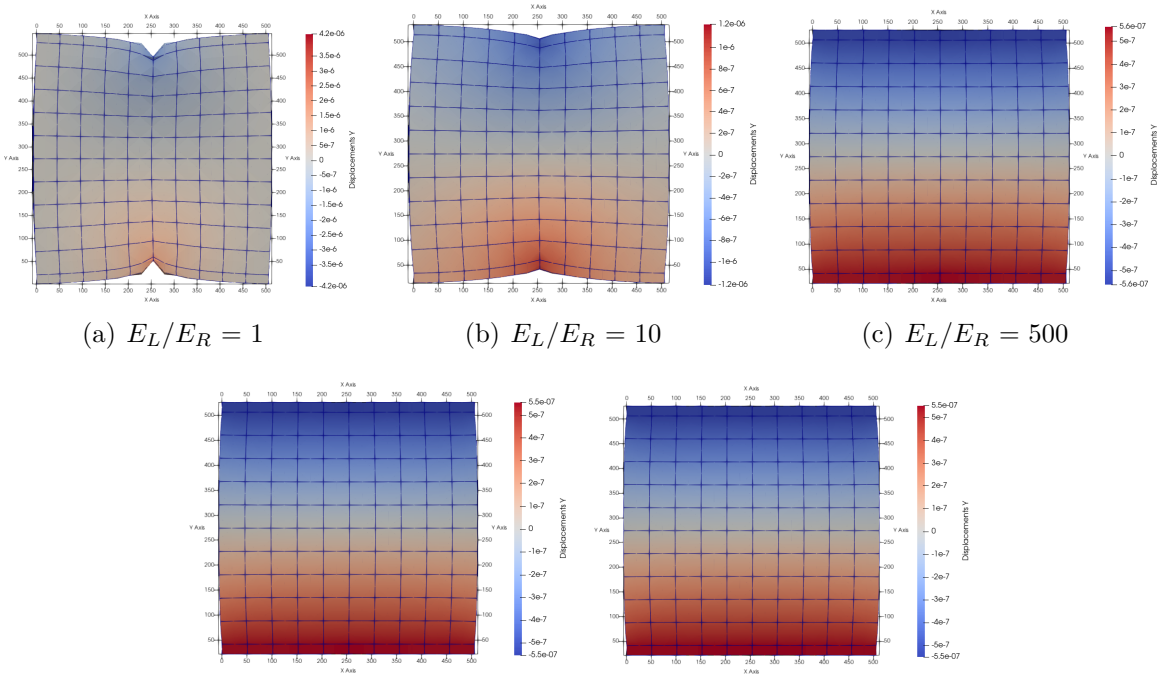

(a) $E_L/E_R = 1$ (b) $E_L/E_R = 10$ (c) $E_L/E_R = 500$

(d) $E_L/E_R = 1000$ (e) $E_L/E_R = 2000$

Fig. 5.75 Different effect of the E_L/E_R in the application of the compressive load. Curved panel under internal pressure and axial compression with fixed $P_{inner} = 1$ MPa, $\theta = 0.2$, $R_\alpha = 2540.01$ mm.

Effect of the P_{inner}

Four different values of P_{inner} (i.e., 0, 0.1, 0.5 and 1 MPa) are considered in order to evaluate how the internal pressure affects the natural frequencies. The corresponding natural frequencies variation, mode shapes and the relevant phenomena that occur are illustrated in Figs. 5.76-5.79, considering $E_L/E_R = 1000$, $\theta = 0.2$, $R_\alpha = 2540.01$ mm.

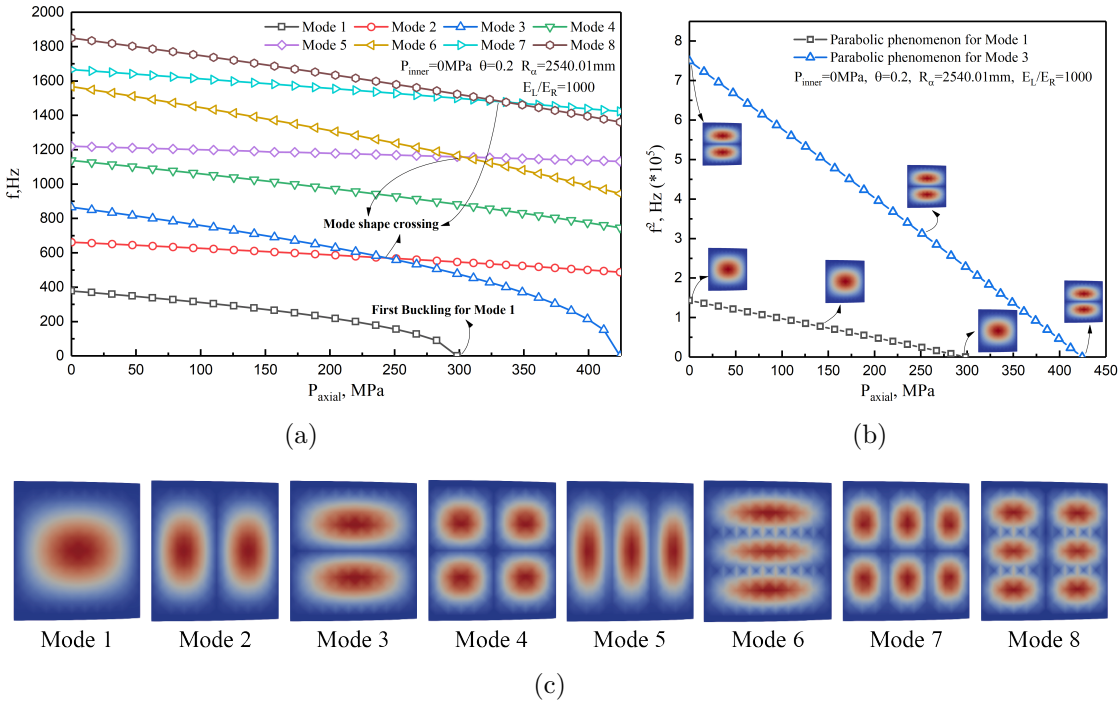

Fig. 5.76 (a) Natural frequencies variation, (b) Parabolic and veering phenomenon and (c) Mode shapes of the first eight free vibrations, considering $E_L/E_R = 1000$, $P_{inner} = 0$ MPa, $\theta = 0.2$, $R_\alpha = 2540.01$ mm. Curved panel under internal pressure and axial compression.

Results suggest that for all value of P_{inner}, the first buckling mode turns out be that of mode 1. A crossing phenomenon occurs between mode 2 and mode 3, and between mode 7 and mode 8. An interesting aspect is that when we increase the P_{inner} to 0.5 MPa, the veering phenomenon between mode 5 and mode 6 starts appearing. Figure 5.79 shows how the veering phenomenon becomes more evident considering a $P_{inner} = 1$ MPa, i.e., the gap between these two lines becomes wider. In Fig. 5.79(b), veering occurs between mode 5 and mode 6 and the mode shapes between mode 5 and mode 6 start switching from steps 17 to 23. Figure 5.80 provides the natural frequencies variation of the first 3 modes for different P_{inner}. Clearly, the increasing application of the P_{inner} increases the values of the natural frequencies.

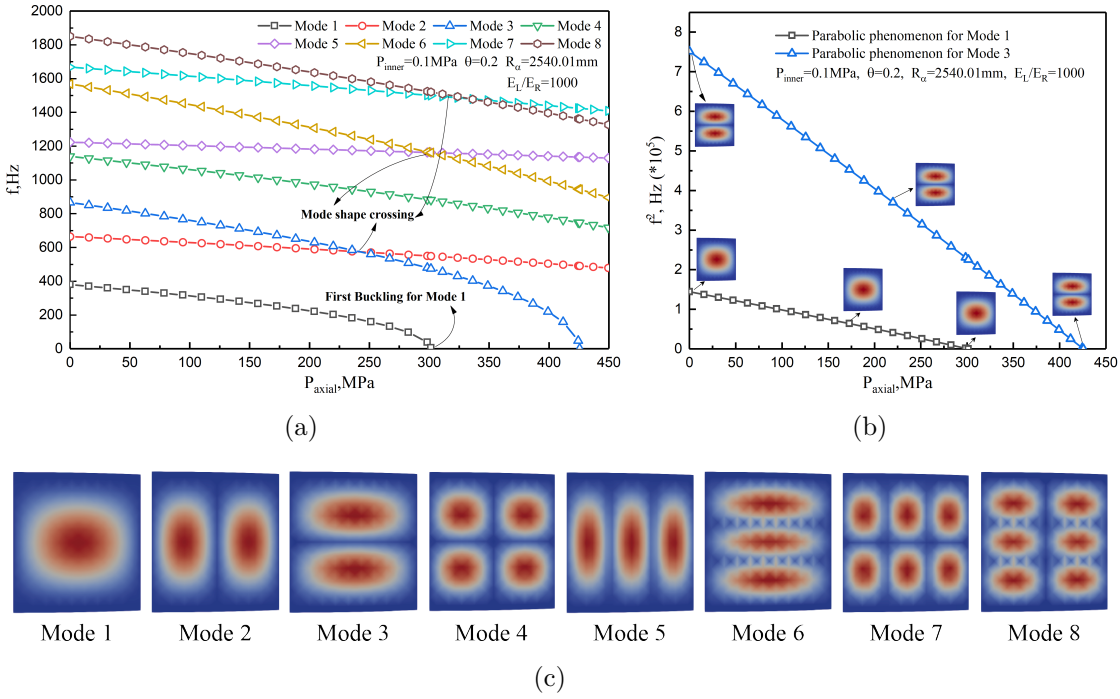

Fig. 5.77 (a) Natural frequencies variation, (b) Parabolic and veering phenomenon and (c) Mode shapes of the first eight free vibrations, considering $E_L/E_R = 1000$, $P_{inner} = 0.1$ MPa, $\theta = 0.2$, $R_\alpha = 2540.01$ mm. Curved panel under internal pressure and axial compression.

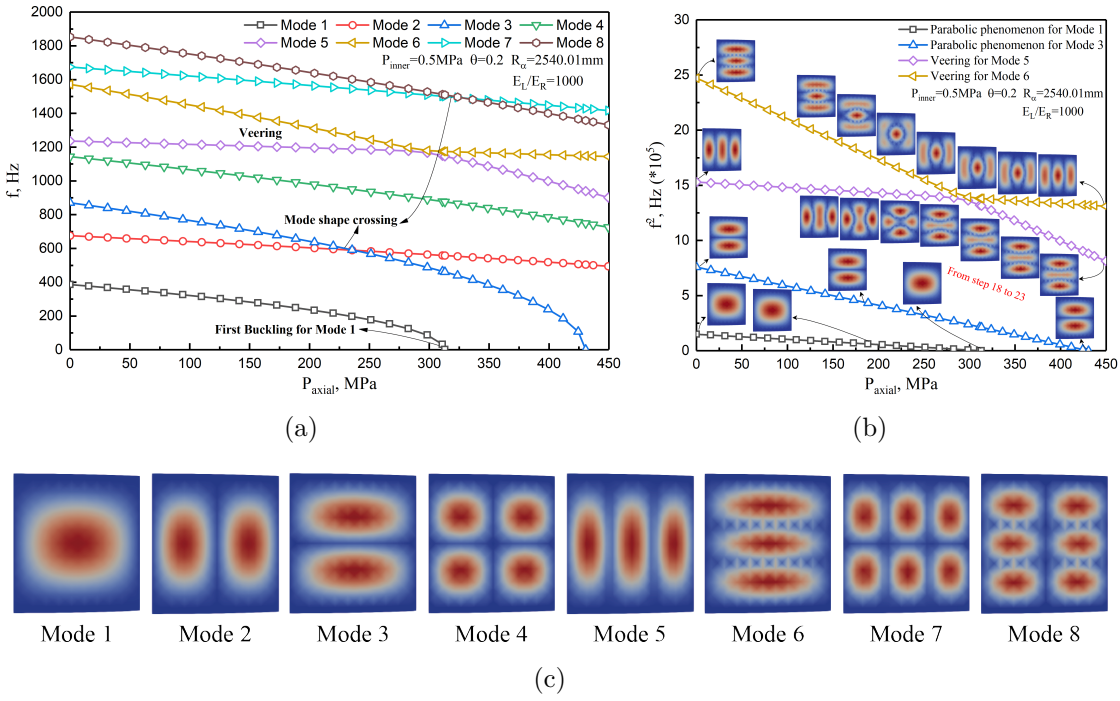

Fig. 5.78 (a) Natural frequencies variation, (b) Parabolic and veering phenomenon and (c) Mode shapes of the first eight free vibrations, considering $E_L/E_R = 1000$, $P_{inner} = 0.5$ MPa, $\theta = 0.2$, $R_\alpha = 2540.01$ mm. Curved panel under internal pressure and axial compression.

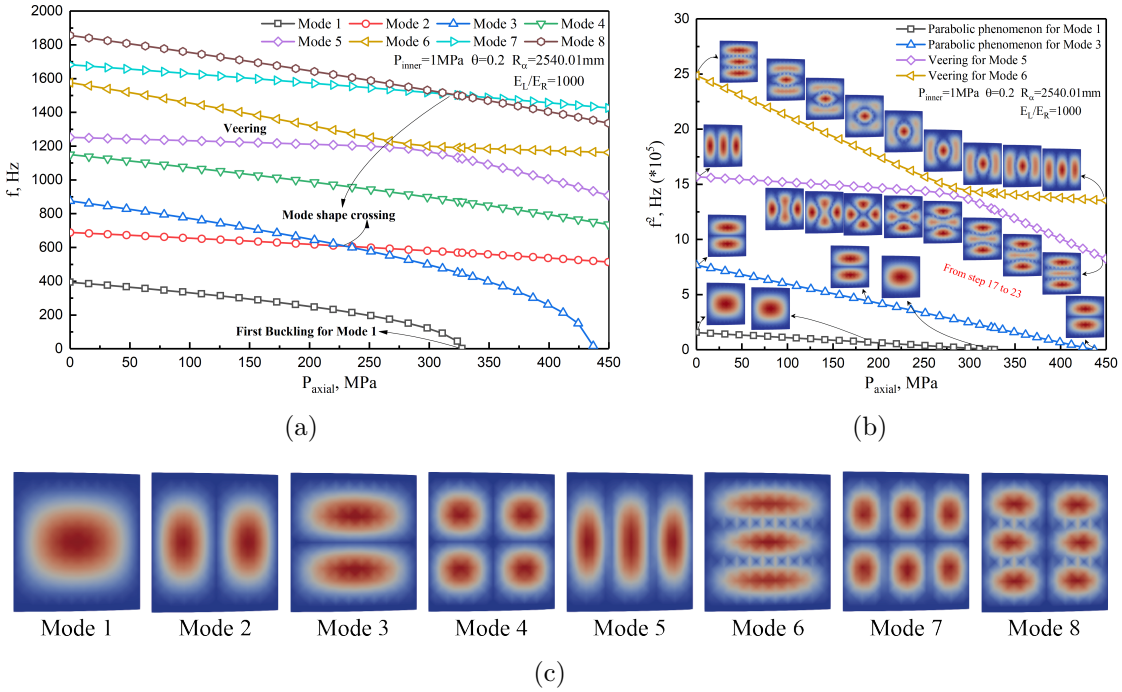

Fig. 5.79 (a) Natural frequencies variation, (b) Parabolic and veering phenomenon and (c) Mode shapes of the first eight free vibrations, considering $E_L/E_R = 1000$, $P_{inner} = 1$ MPa, $\theta = 0.2$, $R_\alpha = 2540.01$ mm. Curved panel under internal pressure and axial compression.

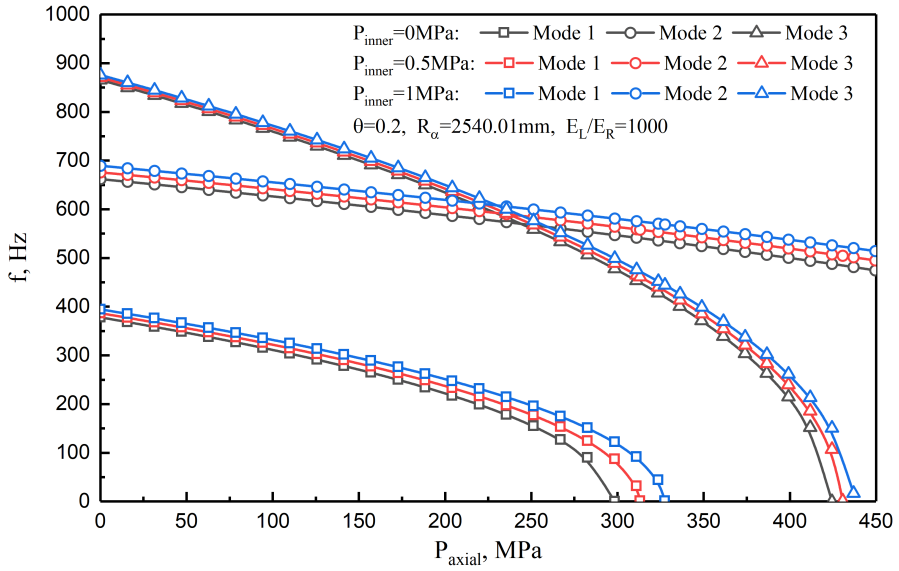

Fig. 5.80 Natural frequencies variation of the first 3 modes as a function of the increasing compressive loadings for different internal pressure values ($P_{inner} = 0$, 0.5, 1 MPa).

Finally, some MAC graphical representations to evaluate the similarity of mode shapes are presented. In detail, referring to the plots from Figs. 5.76 and 5.79, the corresponding MAC values are reported in Figs. 5.81 and 5.82. In detail, Fig. 5.81(a) illustrates that

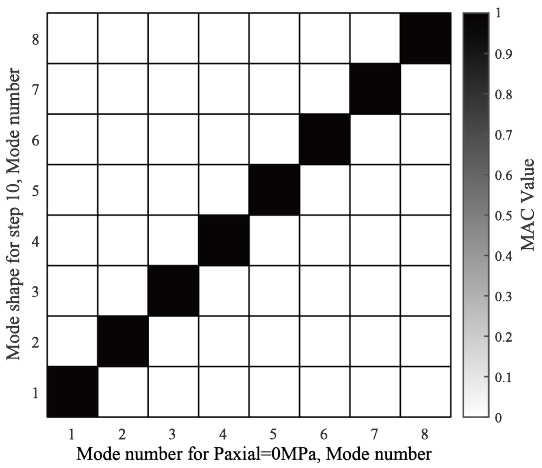

(a) Step 1 vs Step 10

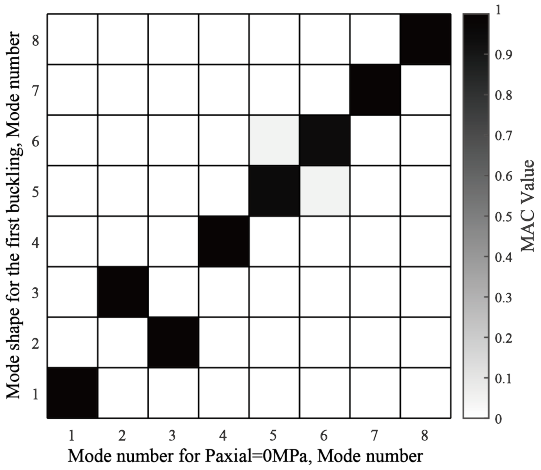

(b) Step 1 vs first buckling

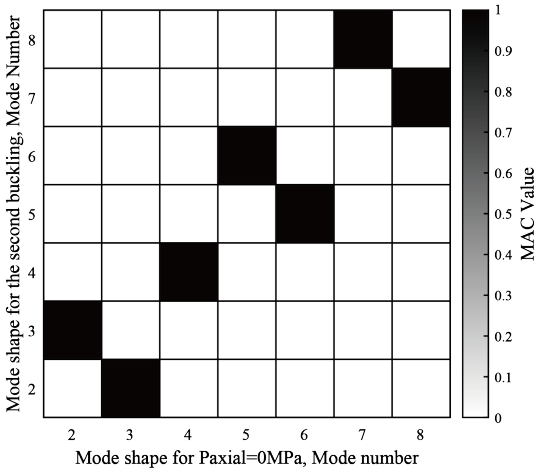

(c) Step 1 vs second buckling

Fig. 5.81 MAC representations for $P_{inner} = 0$ MPa, $E_L/E_R = 1000$, $\theta = 0.2$, $R_\alpha = 2540.01$ mm.

the mode shapes for step 1 ($P_{axial} = 0$ MPa) are identical to the mode shapes for step 10. Figure 5.81(b) shows the mode shape crossing between mode 2 and mode 3, whereas Fig. 5.81(c) exhibits the mode shape crossing between mode 2 and 3, mode 5 and 6, and mode 7 and 8. Figure 5.82(a) illustrates the MAC representation comparing mode shapes at step 1 vs step 19. Figure 5.82(c) displays the veering phenomenon between mode 5 and 6 from step 17 to step 22. Finally, Fig. 5.82(b) provides the MAC representation after veering.

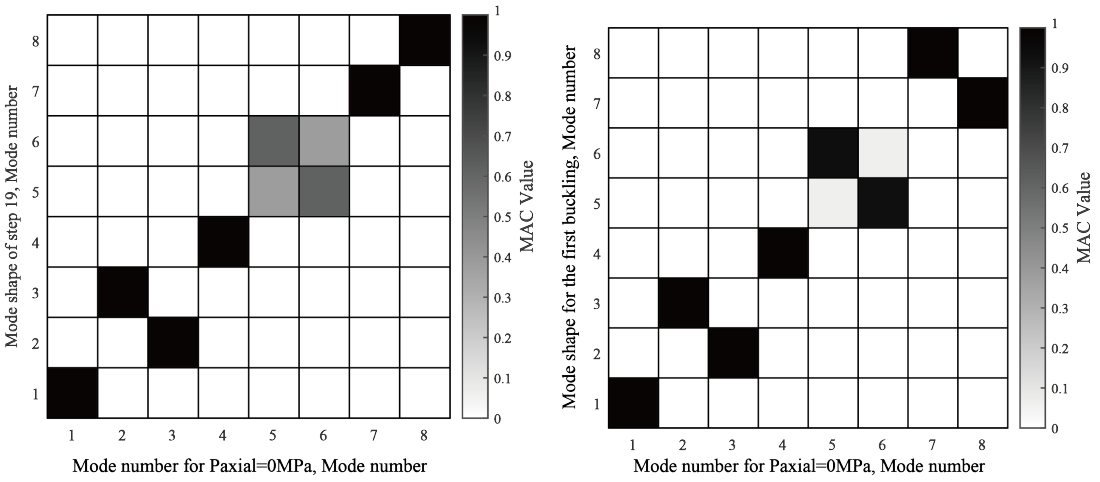

(a) Step 1 vs Step 19

(b) Step 1 vs first buckling

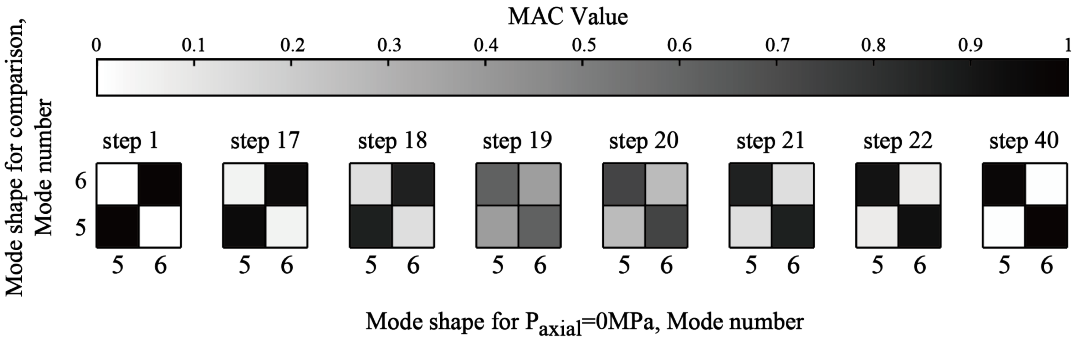

(c) Veering between mode 5 and 6

Fig. 5.82 MAC representations for $P_{inner} = 1$ MPa, $E_L/E_R = 1000$, $\theta = 0.2$, $R_\alpha = 2540.01$ mm.

5.2.9 Isotropic beam subjected to thermal loadings

The following numerical assessment consists of an isotropic square cross-section beam structure subjected to thermal loadings. Two different configurations, L/h = 10 and L/h = 100, are considered. In detail, the beam, illustrated in Fig. 5.83, has L equal to 1 m, a = 0.1 m / 0.01 m and h = 0.1 m / 0.01 m. The structure was made of aluminium with Young's modulus, Poisson's ratio, density and linear thermal expansion coefficient equal to $E = 73$ GPa, $\nu = 0.34$, $\rho = 2700$ kg/m^3 and $\alpha = 25{\times}10^{-6}$ $^\circ C^{-1}$, respectively.

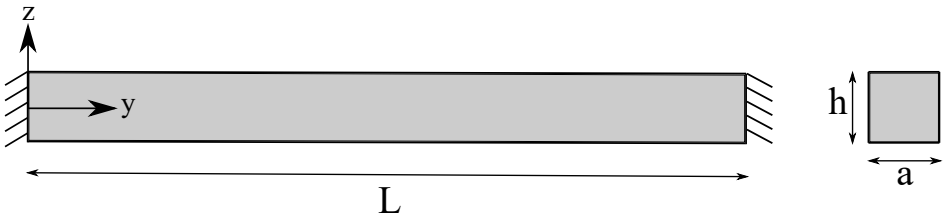

Fig. 5.83 Geometry and boundary condition of the clamped-clamped beam structure subjected to thermal loadings.

After convergence analyses, not displayed here for the sake of brevity, the mathematical model consists of four L9 on the cross-section $(x - z)$ and ten B4 beam finite elements along the y-direction. Therefore the number of DOFs is 2325. The accuracy of the approximation chosen, according to the CUF theory, was verified by making a comparison with the results of the modal analysis obtained through the commercial FE software Abaqus, see Table 5.6.

Model	I flexural mode	II flexural mode	I torsional mode
CUF LE9 [Hz]	508.85	1303.07	1476.05
Abaqus Hex20 [Hz]	509.01	1303.90	1471.52

Table 5.6 Comparison between the CUF methodology and Abaqus solution. Isotropic beam (L/h = 10) subjected to thermal loadings.

The first three free vibration mode shapes of both thick and thin isotropic beam structures are provided in Fig. 5.84.

Generally speaking, the application of a thermal load to a structure in particular constraint conditions involves the rise of a state of stress generated by the expansion of the structure. Especially considering the boundary conditions of the present beam with both edges clamped, the application of a thermal load, due to a uniform variation of the temperature on the whole model, leads to a state of compression stress that can lead to buckling of the structure.

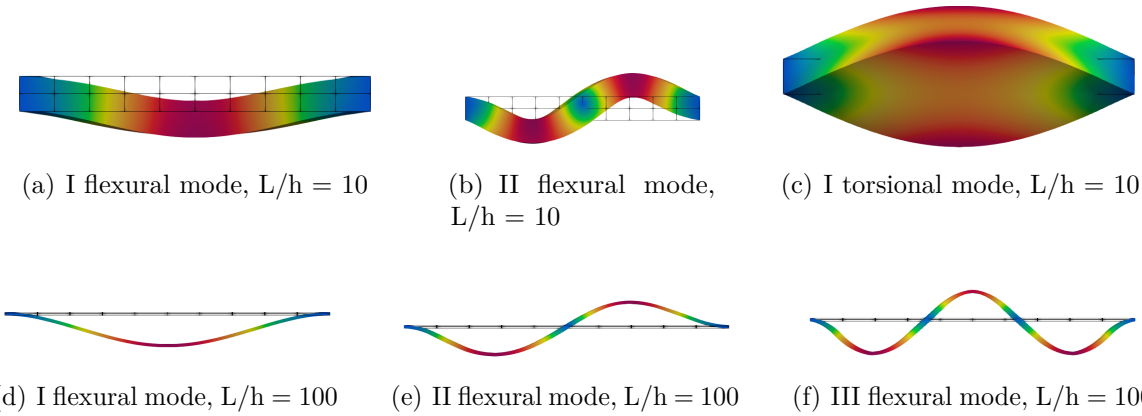

(a) I flexural mode, L/h = 10

(b) II flexural mode, L/h = 10

(c) I torsional mode, L/h = 10

(d) I flexural mode, L/h = 100

(e) II flexural mode, L/h = 100

(f) III flexural mode, L/h = 100

Fig. 5.84 Mode shapes of the first three free vibrations for clamped-clamped isotropic beams subjected to thermal loadings.

Figure 5.85 plots the comparison between the variation of natural frequencies versus increasing thermal loadings computed through the present linearized methodology and Abaqus. The results obtained show a good correlation with the Abaqus ones, allowing one to predict the buckling load and describe the variation of natural frequencies with high accuracy. Particularly, graphs suggest that instability phenomena occur for a thermal load corresponding to 1139.03 $°C$ for the case of the thick beam and 13.04 $°C$ for the slender one. Regarding the thick structure, see Fig. 5.85a, given the very high ΔT_{cr} value obtained for the beam in an isotropic material, similar to an aluminium alloy, in this case, the instability configuration will never be reached. However, it is possible to have a considerable, albeit secondary, effect when considering a more complex load environment where the thermal load is only one of the contributors.

5.2.10 Laminated composite beam subjected to thermal loadings

A laminated composite beam structure subjected to thermal loadings is considered as a further example. The same geometrical data are used as in the previous example. The lamination sequence considered is [0°/90°/0°]. The material properties of this laminated structure involves E_1 = 144.8 GPa, $E_2 = E_3$ = 9.65 GPa, ν_{12} = 0.3, $G_{12} = G_{13}$ = 4.14 GPa, G_{23} = 3.45 GPa, ρ = 1450 kg/m^3, α_{11} = -2.6279×10^{-7} $°C^{-1}$ and α_{12} = 30.535×10^{-6} $°C^{-1}$. The convergent model for this beam structure is reached by employing at least ten B4 finite elements along the beam-axis and two Q9 for each layer.

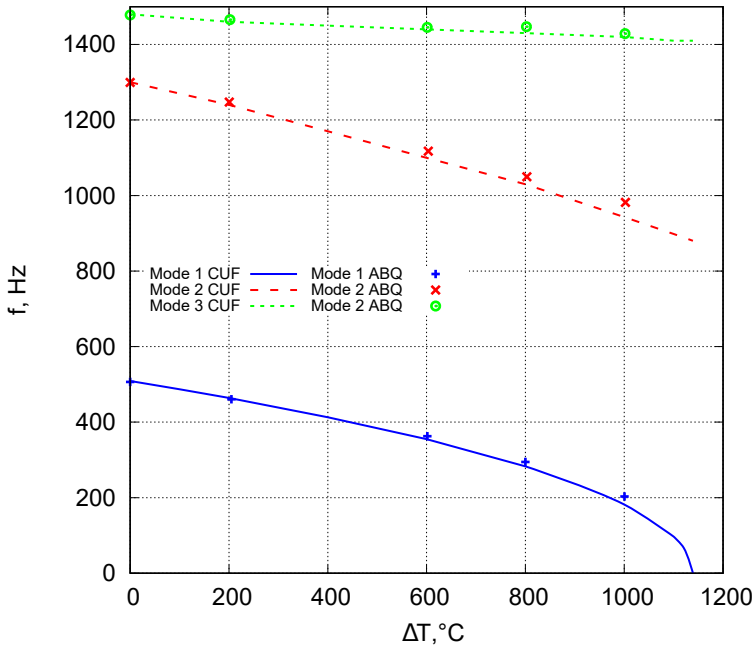

(a) L/h = 10

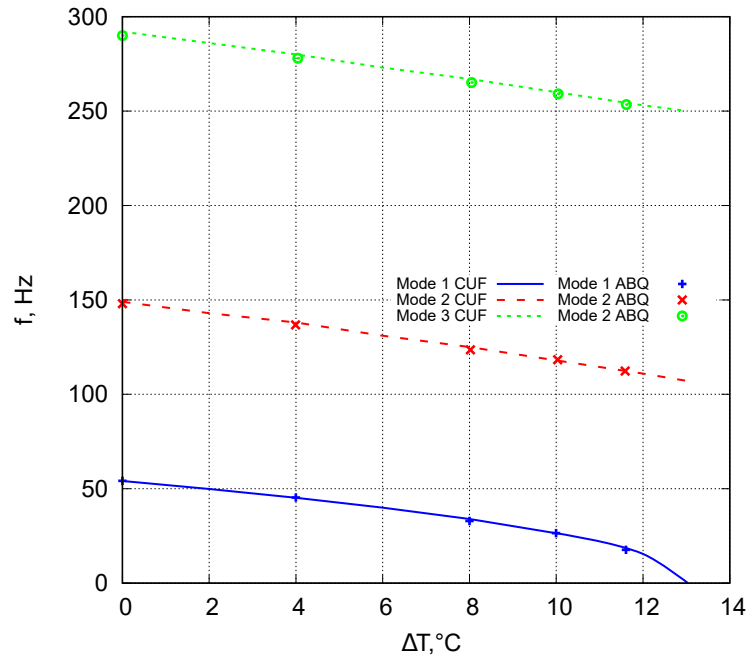

(b) L/h = 100

Fig. 5.85 Natural frequency variation versus thermal loadings for the isotropic beam.

Table 5.7 shows the comparison between the present formulation and Abaqus solution for the first six free natural frequencies. Furthermore, the mode shapes of both thick and

	CUF LE9 [Hz]	Abaqus Hex20 [Hz]
I flexural mode xy-plane	571.35	571.83
I flexural mode yz-plane	605.34	605.16
I torsional mode	773.82	773.20
II flexural mode xy-plane	1234.41	1235.90
II flexural mode yz-plane	1270.84	1273.80
II torsional mode	1551.99	1552.10

Table 5.7 Comparison between the present methodology and the Abaqus solution. Laminated composite [0°/90°/0°] beam. L/h = 10 subjected to thermal loadings.

thin laminated composite beam structures are depicted in Fig. 5.86.

Also, in this case, the instability behaviour of the composite beam under thermal loadings given by the uniform variation of the temperature ΔT was confirmed by the frequency trend of the beam modes with respect to the thermal load, see Fig 5.87. The current results were compared with those obtained with Abaqus. The comparisons revealed a perfect agreement between the two approaches within the considered thermal load interval.

5.2.11 Isotropic plate subjected to thermal loadings

An isotropic square plate structure subjected to thermal loadings is investigated in the following analysis case. Figure 5.88 illustrates the structure geometry, with a = 1 m, h = 0.01 m, and the boundary conditions used. The material data are the following: E = 73 GPa, ν = 0.34, ρ = 270 kg/m^3 and $\alpha = 25{\times}10^{-6}\ {}^{\circ}C^{-1}$. The mathematical model consisted of 10×10Q9 finite elements over the xy-plane, while the kinematic theory adopted along the thickness direction is only one LD2. Therefore, the number of degrees of freedom is 3969.

The values of the first four free vibration modes obtained using the CUF and Abaqus are tabulated in Table 5.8, whereas the mode shapes are depicted in Fig. 5.89.

Figure 5.90 shows the natural frequencies variation versus increasing thermal loadings via the present linearized approach, including the comparison with the Abaqus solution. The graph shows that the first instability mode of the isotropic plate with all edges clamped, corresponding to a uniform temperature variation $\Delta T_{cr} = 13.16\ {}^{\circ}C$, coincides with the vibrational mode (1,1).

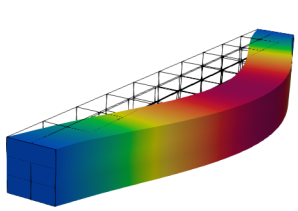

(a) I flexural xy, L/h = 10

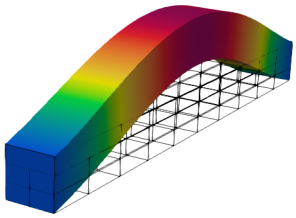

(b) I flexural yz, L/h = 10

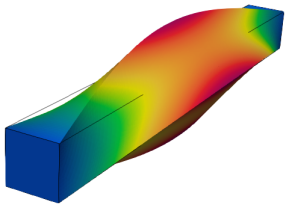

(c) I torsional, L/h = 10

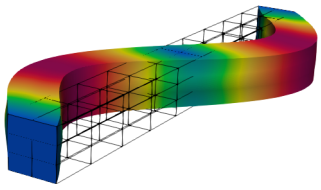

(d) I flexural xy, L/h = 10

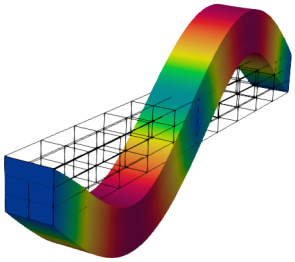

(e) I flexural yz, L/h = 10

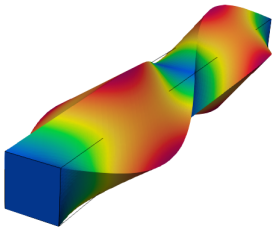

(f) II torsional, L/h = 10

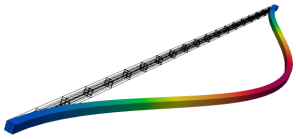

(g) I flexural xy, L/h = 100

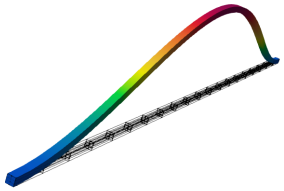

(h) I flexural yz, L/h = 100

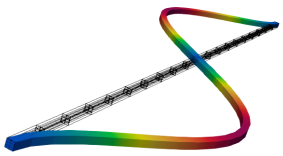

(i) II flexural xy, L/h = 100

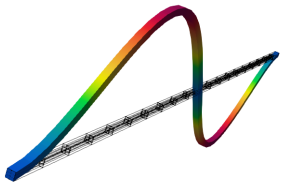

(j) II flexural yz, L/h = 100

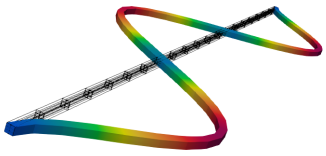

(k) III flexural xy, L/h = 100

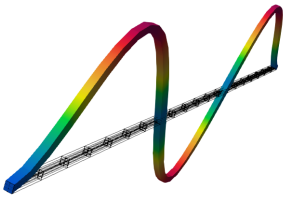

(l) III flexural yz, L/h = 100

Fig. 5.86 Characteristics first three free vibration mode shapes for clamped-clamped laminated composite [0°/90°/0°] thick and thin beams subjected to thermal loadings.

Model	Mode (1,1)	Mode (2,1)/(1,2)	Mode (2,2)
CUF [Hz]	93.89	194.90	287.01
Abaqus S8R [Hz]	91.40	186.47	275.77

Table 5.8 Comparison between the present methodology and the Abaqus solution. Isotropic plate (a/h = 100) subjected to thermal loadings.

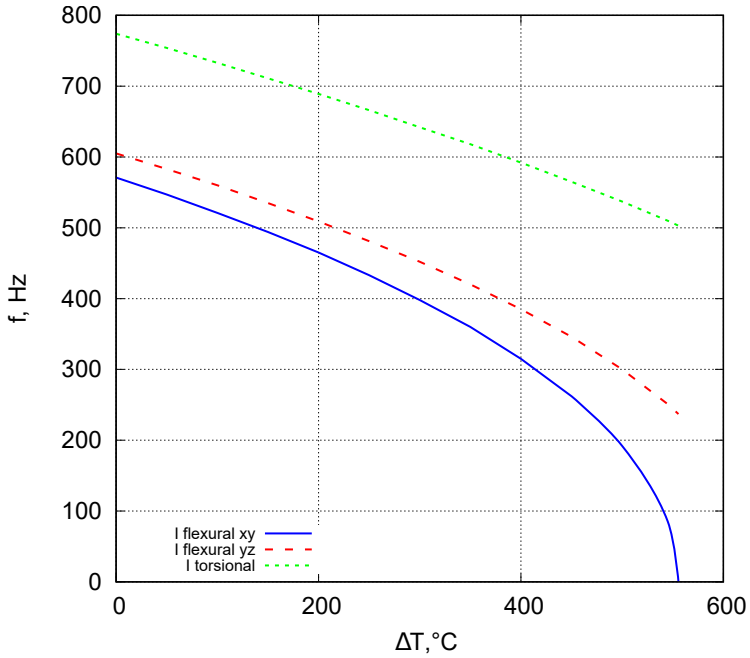

(a) L/h = 10

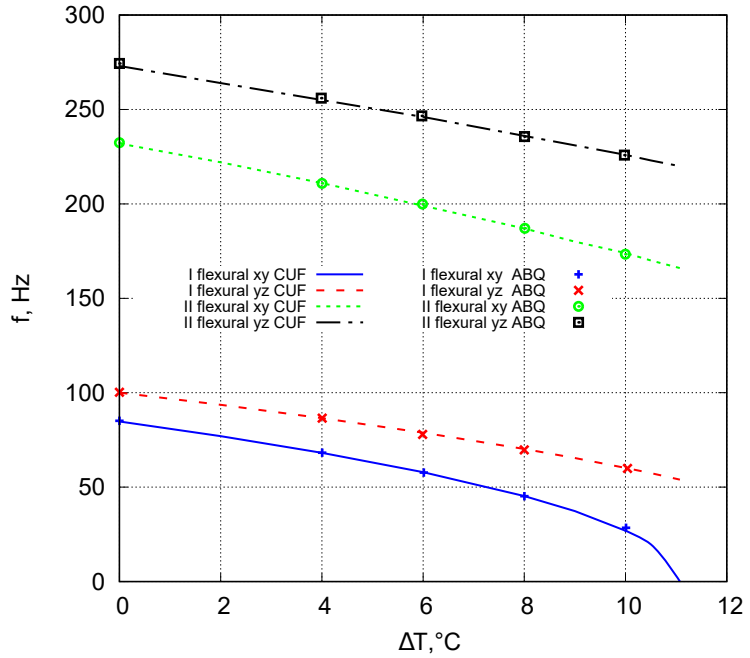

(b) L/h = 100

Fig. 5.87 Natural frequency variation versus thermal loadings for the laminated composite [0°/90°/0°] beam subjected to thermal loadings.

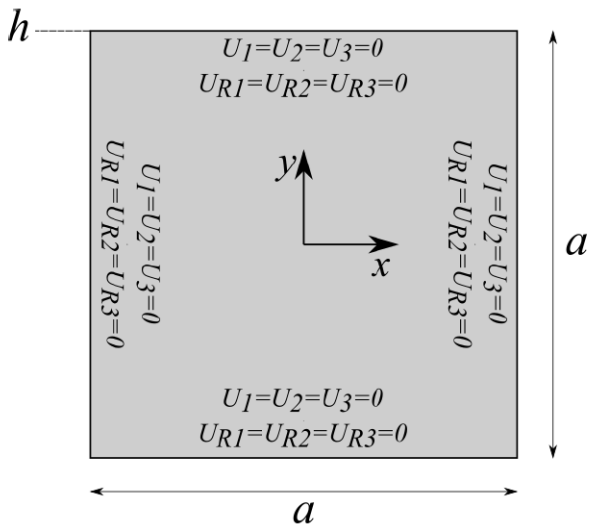

Fig. 5.88 Geometry and boundary condition of the clamped isotropic plate structure (a/h = 100) subjected to thermal loadings.

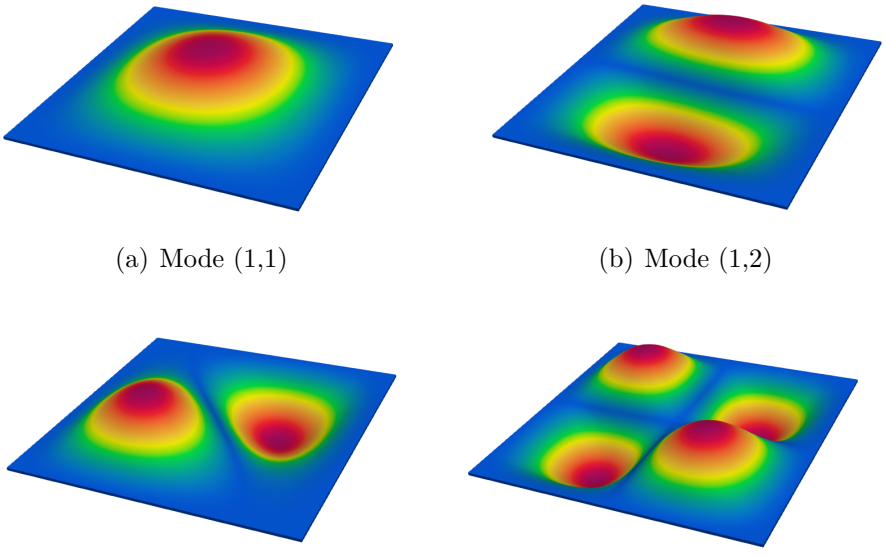

(a) Mode (1,1)

(b) Mode (1,2)

(c) Mode (2,1)

(d) Mode (2,2)

Fig. 5.89 Characteristics first four free vibration mode shapes for the clamped isotropic plate (a/h = 100) subjected to thermal loadings.

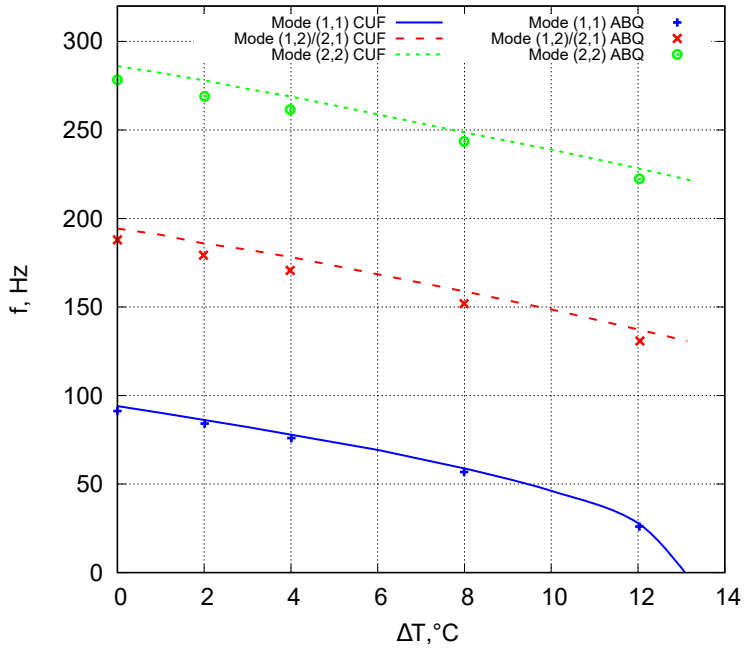

Fig. 5.90 Natural frequency variation versus thermal loadings for the isotropic plate (a/h = 100).

5.2.12 Laminated composite plate subjected to thermal loadings

As a final example, a laminated composite plate structure under thermal loadings is analyzed. This plate model has the same geometric data as the previous case. The material data of the plate are the following: $E_1 = 144.8$ GPa, $E_2 = E_3 = 9.65$ GPa, $\nu_{12} = 0.3$, $G_{12} = G_{13} = 4.14$ GPa, $G_{23} = 3.45$ GPa, $\rho = 1450$ kg/m^3, α_{11} = -2.6279×10^{-7} °C^{-1} and $\alpha_{12} = 30.535\times10^{-6}$ °C^{-1}. The structure is modelled employing 10×10Q9 for the surface mesh approximation, whereas only 1LD3 is used in each layer in the z-direction.

First, the dynamic behaviour of the composite plate considering a/h = 100 and three-layer with [0°/90°/0°] staking sequence is investigated. Then, a parametric study based on the variation of the lamination sequence and thickness of the structure is performed.

Table 5.9 and Fig. 5.91 provides the natural frequencies and mode shapes of the first five vibration modes, respectively.

Figure 5.92 shows the comparison between the variation of natural frequencies as a function of the increasing thermal loadings computed by using the present linearized approach and the Abaqus solution. It can be observed that the frequency of the second vibration mode (2,1) tends to zero at the buckling load value equal to 10.69 °C. Generally

Model	Mode (1,1)	Mode (2,1)	Mode (3,1)	Mode (1,2)	Mode (2,2)
CUF [Hz]	108.67	144.30	222.98	283.06	304.53
Abaqus S8R [Hz]	107.76	141.37	212.54	278.78	299.43

Table 5.9 Comparison between the CUF methodology and Abaqus solution. Composite [0°/90°/0°] plate (a/h = 100) under thermal loadings.

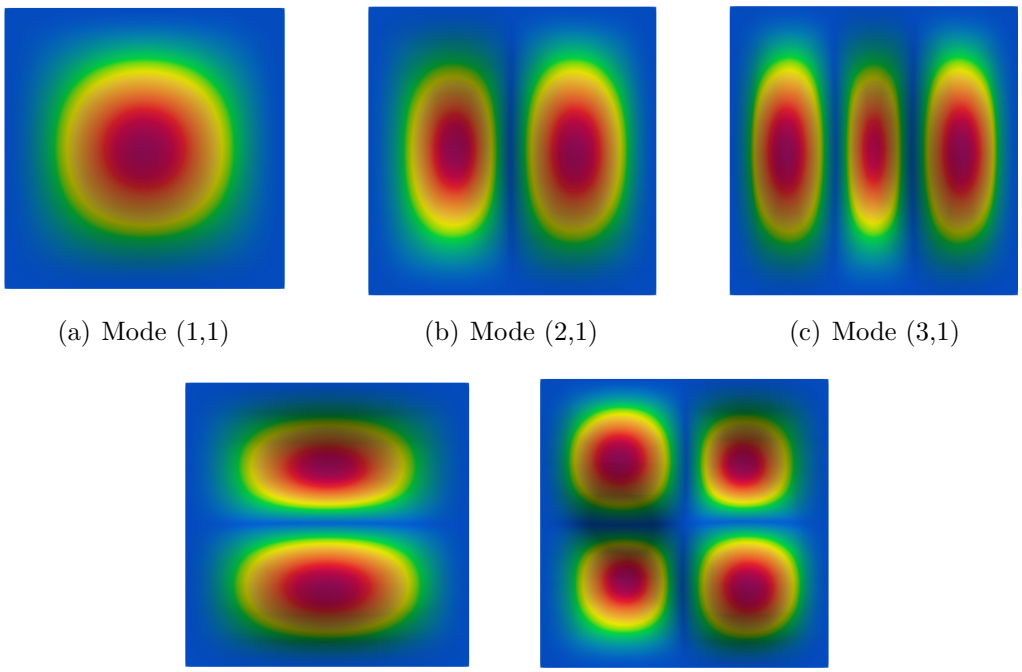

(a) Mode (1,1) (b) Mode (2,1) (c) Mode (3,1)

(d) Mode (1,2) (e) Mode (2,2)

Fig. 5.91 Mode shapes of the first five free vibration for the composite [0°/90°/0°] plate (a/h = 100) under thermal loadings.

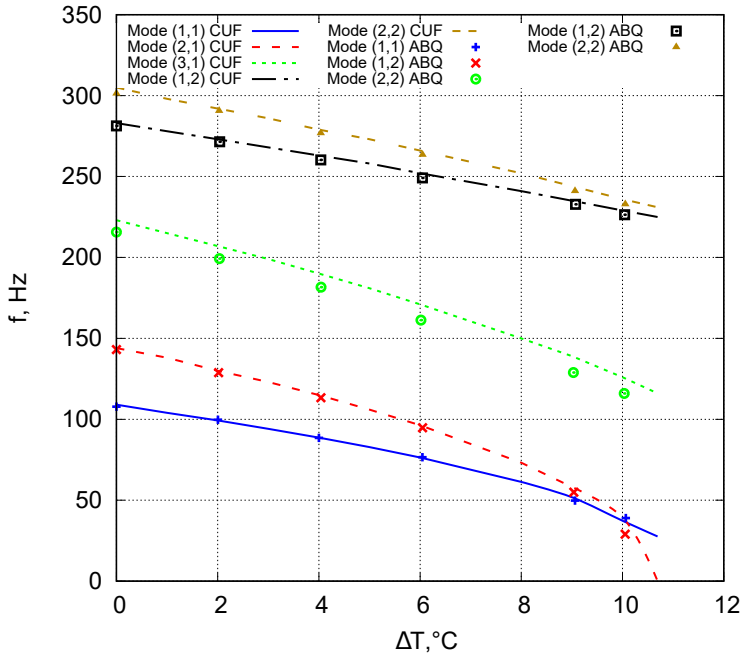

Fig. 5.92 Natural frequency variation versus thermal loadings for the composite $[0°/90°/0°]$ plate (a/h = 100).

speaking, the directionality of the fibers inside the laminate layers determines a variation in the dynamic behaviour of thin plates, affecting the buckling. This buckling phenomenon is induced by the state of tension that is generated by the application of thermal loads. For clarity, from the graphs of Fig. 5.93, it can be deduced that the application of a thermal load due to a uniform variation of the temperature ΔT on the entire laminated structure leads to the generation of compressive stresses. In particular, the stresses σ_{xx} are more intense in the central layer of the laminate, while the stresses σ_{yy} are more intense in the external layers. The structure is consequently subjected to a state of biaxial compression tension. At the critical value of temperature variation ΔT_{cr}, the compressive stresses are able to induce the phenomenon of instability.

Table 5.10 displays the buckling load values of the composite plates considering different lamination sequences. For the sake of clarity, numerical results come from simple linearized buckling analyses, where the $\boldsymbol{K}_T$ is approximated as the sum of the linear matrix and the geometric stiffness resulting from the linear stress state. These thermal buckling values are confirmed by the natural frequencies trend depicted in Fig. 5.94. It is significant to highlight how the choice of lamination affects the buckling behaviour of the structure. In fact, choosing a $[0°/90°/0°]$ lamination causes the variation of the mode shape of the first buckling mode of the plate, passing from a one half-wave, as for the laminations $[0°/45°/-45°]_s$ and $[45°/-45°]_s$, to two ones.

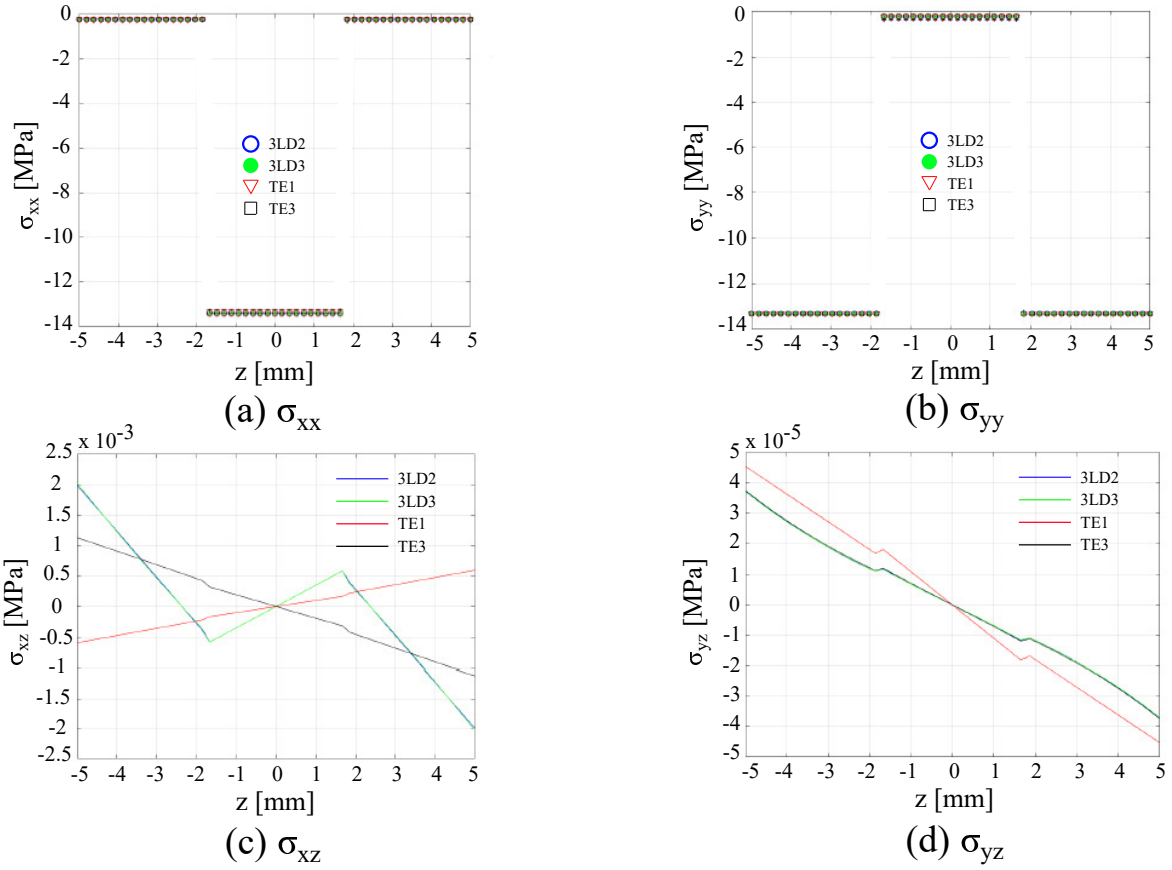

Fig. 5.93 Through-the-thickness stresses distribution for the composite [0°/90°/0°] plate (a/h = 100) under $\Delta T = 3°C$ at x = -0.25 m and $y = 0$ m considering different kinematic expansion.

Lamination	Buckling mode shape	CUF [°C]	Abaqus [°C]
[0°/90°/0°]	Mode (2,1)	10.69	10.42
$[0°/45°/-45°]_s$	Mode (1,1)	11.42	11.30
$[45°/-45°]_s$	Mode (1,1)	9.02	8.91

Table 5.10 The first critical buckling load considering different lamination sequences. Composite plate (a/h = 100) under thermal loadings.

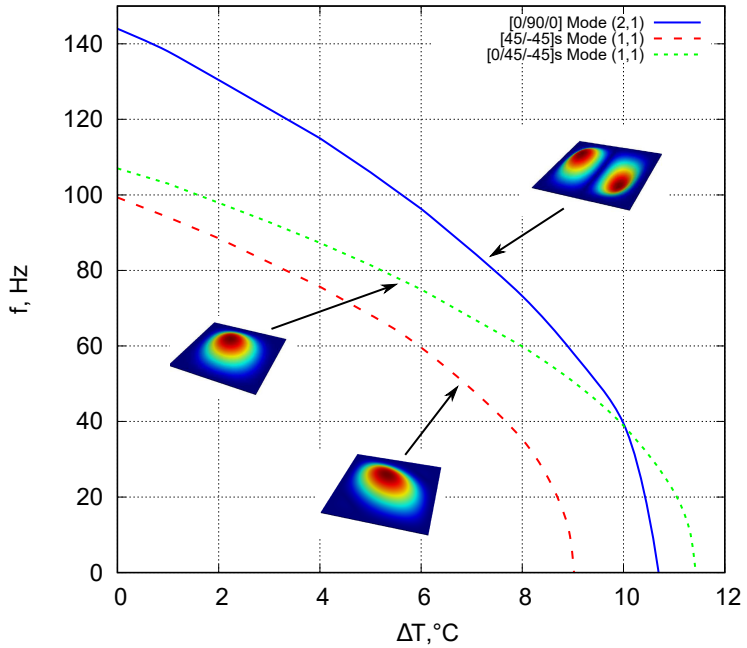

Fig. 5.94 Effect of lamination on the natural frequency variation versus increasing thermal loadings. Laminated composite plate (a/h = 100).

In addition, the thickness effect on the frequencies and buckling loads is presented in Fig. 5.95 and Table 5.11. The results suggest that as the thickness of the laminated

a/h	Buckling mode shape	CUF [$°C$]	Abaqus [$°C$]
10	Mode (2,1)	10.69	10.42
20	Mode (2,1)	40.80	40.221
50	Mode (2,1)	206.01	206.96
100	Mode (1,1)	502.46	504.60

Table 5.11 The first critical buckling load considering different thickness values of the laminated composite [0°/90°/0°] plate subjected to thermal loadings.

composite plate increases, there is a noticeable rising in natural frequencies and buckling loads due to increasing stiffness of the structure.

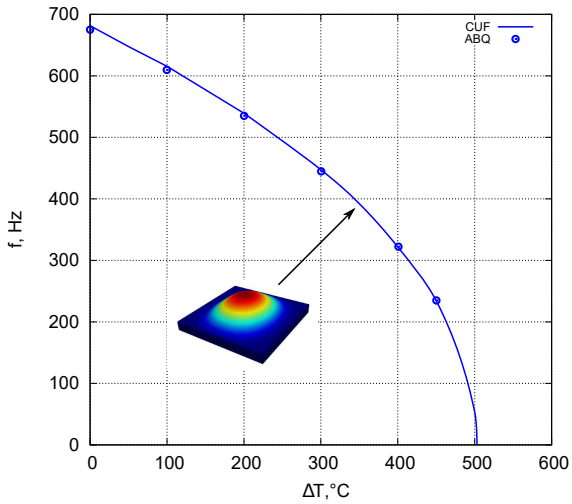

(a) a/h = 10

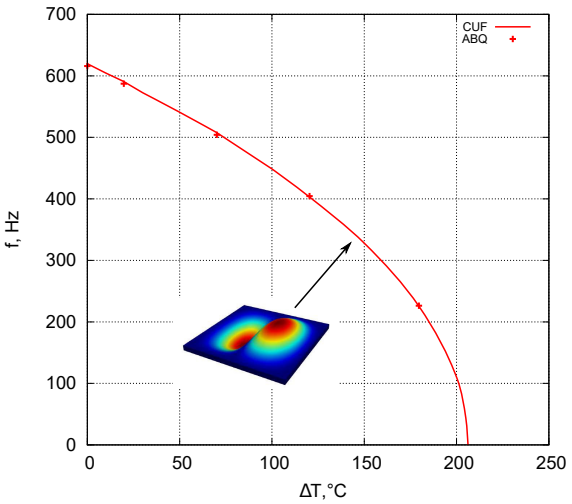

(b) a/h = 20

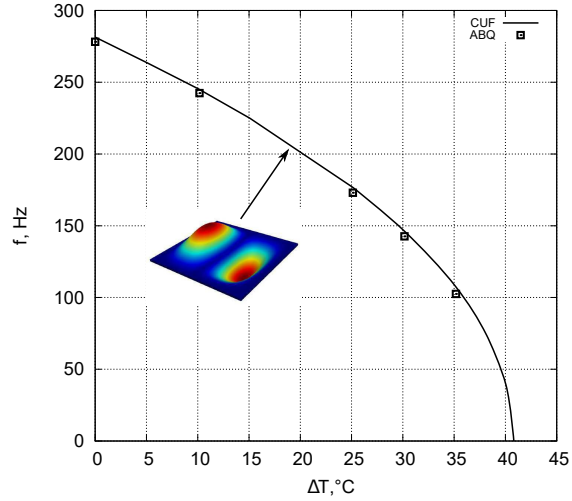

(c) a/h = 50

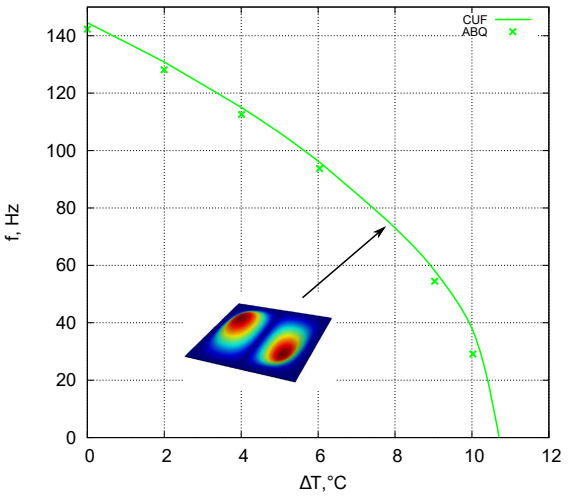

(d) a/h = 100

Fig. 5.95 Effect of thickness on the natural frequency variation versus increasing thermal loadings. Laminated composite [0°/90°/0°] plate.

Chapter 6

Conclusions

6.1 Outline

This thesis aims to present an efficient tool for nonlinear vibration analyses of isotropic and composite beam, plate and shell structures. Exploiting the potentialities of the Carrera Unified Formulation (CUF) as a generator of refined one-dimensional (1D) and two-dimensional (2D) models, large-deflection, buckling, post-buckling, vibration, time response and multibody analyses were carried out. CUF allows to easily implement low- to higher-order theories in a compact and automatic way. Thanks to its intrinsic scalable nature, by adopting a total Lagrangian approach, the predictions from three-dimensional (3D) full Green-Lagrange nonlinear strain components to simplified nonlinear von Kármán strains are automatically obtained. In fact, in the CUF framework, the nonlinear governing equations and the related finite element (FE) arrays of any model are formulated through *Fundamental Nuclei* (*FNs*), whose structure is independent of the theory approximation order and the strain approximation assumed. Both Lagrange (LE) and Taylor (TE) functions have been employed and compared.

First, beam, plate and shell models were presented and employed to carry out geometrically nonlinear analyses of isotropic and composite structures. The models are validated with those coming from literature and research activities are conducted to analyze the large-deflections and post-buckling behaviours of complicated structures (in terms of stacking sequences and cross-section geometry). Particular attention was paid to providing an efficient tool able to accurately compute the 3D stresses distribution in structures subjected to different loads and boundary conditions in highly nonlinear regimes. In addition, the capabilities of variable-kinematic finite beam elements for the dynamic analyses of 3D structures undergoing large displacements and rotations are explored. Regardless of which structural model was selected, the dynamic equilibrium of

the structure was obtained by incrementing the generalized coordinate vector and the associated temporal derivatives by adopting an iterative Newton-Raphson procedure and the HHT-α method. Results suggested that higher-order and full nonlinear models are mandatory to obtain an efficient method able to perform accurate analyses.

Then, particular interest has been focused on buckling prediction using vibration data, which has played an important part in the entire research activities described in the present thesis work. Thus, analytical solutions are developed for beam/plate/shell structures using the Navier method and classical and first-order shear deformation theories, including the nonlinear von Kármán model. They are presented for the buckling evaluation using the dynamic criterion. In particular, simply-supported boundary conditions are considered. When closed-form solution can be derived, they are preferred to the numerical ones. However, when exact closed-form solution cannot be developed, numerical solution based on the finite element method (FEM) are the best alternative. In this context, a novel virtual Vibration Correlation Technique (VCT) approach capable of predicting the buckling load, characterizing the natural frequencies' variation, and having an efficient means to verify the experimental VCT results was provided. This method becomes a powerful method when it is necessary to investigate cases that are difficult to analyze experimentally, such as structures subjected to thermal loads or shear loads and with complicated boundary conditions, among others.

6.1.1 Main contributions

The main novelties and important results obtained during this period of the doctoral research can be summarized as follows:

- The proposed 1D and 2D models are able to describe accurately nonlinear equilibrium states of isotropic and composite beams, plates and shells;
- The Equivalent Single Layer (ESL), as well as the Layerwise (LW) approach, is able to accurately derive nonlinear equilibrium curves of laminated composite structures in the case of moderate and large displacements. Results are in agreement with those from the literature or obtained using commercial software;
- The proposed CUF-based LW models can predict interlaminar stress distributions in both linear and nonlinear equilibrium states with unprecedented accuracy. Accurate stress analyses in large-deflections and post-buckling fields are extremely useful for failure considerations. In addition, results presented represent benchmark cases for future studies;

- Classical theories, such as the first-order approximation, can bring to wrong and, eventually, unconservative stress distributions, especially in nonlinear fields. On the other hand, higher-order approximations, e.g., TE3 or TE4, can give good results in some circumstances. LW is mandatory for stress analysis and to perform accurate evaluation, for example, in nonlinear static and dynamic analyses with large deformation;

- The present approach, based on the CUF, represent an efficient tool for comparing various geometrically nonlinear strain measures and kinematic approximation orders in an automatic way. Simplifications of the 3D full Green-Lagrange nonlinear strains, such as the von Kármán theory, can provide good results for small/moderate displacements in nonlinear regimes, while in the regime of large displacements/rotations these simplified models present unacceptable results;

- Increasing the number of layers of composite plates results in the higher buckling strength and load-carrying capacity of the composite structures. For the angle-ply laminate subjected to the combined loadings (in-plane shear and bi-axial compression), the direction of the applied shear plays a crucial role in post-buckling behaviours of composite plates, and the angle-ply plates with positive shear loading show higher rigidity and load-carrying capacity. The buckling strength and the load-carrying capacity of composite plates with the clamped conditions are higher compared to other investigated boundary conditions, and the presence of a free edge reduces the buckling strength significantly;

- The linear buckling analysis cannot be adopted to compute the buckling load of structures. However, the buckling loads predicted by linear buckling analyses for symmetric composite structures are almost the same as those based on CUF Full NL plate model;

- An innovative approach to study the vibrations of structures subjected to mechanical or thermal loadings was developed;

- Natural frequencies and mode shapes may be seriously affected by pre-stress states. This is even more evident in the case of large displacement equilibrium states. As expected, compressive loadings may cause a non-monotonic variation of the natural frequencies. Because this variation differs from mode to mode, aberrations like veering and crossing are generally observed;

- Anisotropy can be considered as a means to limit nonlinear frequency and mode change. In this context, accurate structural theories such as those proposed in this work are mandatory;
- It was shown that eigenfrequencies and eigenmodes can suffer abrupt aberrations in a deep nonlinear regime;
- Mode aberration is evident compared to the modes computed employing the full nonlinear approach with those obtained in the trivial state. Furthermore, for problems in which bifurcations do not exist or whenever the pre-buckling state is unstable, full geometrical nonlinear analyses should be preferred to trivial linearized solutions;
- The presented nonlinear methodology, based on the CUF, represent an efficient tool for performing nonlinear dynamic investigations and comparing various kinematic approximations and geometrically nonlinear strain measures in an automatic way;
- The CW models are used because of the accurate evaluation of the solution. Both global and local modes are correctly obtained with a significant reduction of the computational costs;
- As far as compact beam-like structures were concerned, the low-order CUF 1D elements provided similar results to classical beam formulations with comparable computational efforts. Instead, when the dynamic response of highly-deformable structures was considered, the possibility of selecting the kinematic assumptions represented a valuable feature for detecting the cross-section deformations and local instabilities. In detail, LE and TE models result in good agreement when the dynamic response of simple compact cross-sections is evaluated, whereas significant differences are present if open channel-sections are considered. For the latter, the use of Lagrange expansion functions is necessary;
- Simplifications of the 3D full Green-Lagrange nonlinear strain components, such as the von Kármán or neglecting some nonlinear term, provide unacceptable dynamic results if very large amplitude are considered;
- Finally, some simple multibody examples are shown to present the potential of this CUF-based approach, where the main advantage is to consider flexible components simply and with high accuracy. The proposed CUF-based multibody tool provided reasonable confidence for future applications in this topic.

6.1.2 Future activities

Many and different perspective developments of the present thesis work seem interesting. Within this research, the CUF has demonstrate excellent performance in static and dynamic analyses of isotropic and composite beams, plates and shells, thus paving the way for future research that will include:

- introduction of damping effects;
- extension to physical nonlinearities;
- extension to rotordynamics;
- extension to acoustics applications;
- extension to fluid-structure problems;
- development of a more efficient multibody tool.

In detail, the damping and physical nonlinearities can be easily incorporated into the aforementioned problems and investigated to investigate their important influence. The methodology depicts the correct free and forced vibration behaviour of complex structures within any frequency range of interest. This aspect can be extremely effective when extended to rotordynamic response analysis of metallic and composite structures because accurate solutions can only be obtained by capturing all necessary high-frequency wave modes. The formulation of rotordynamics has already been extensively studied in the CUF domain for linear domains and beam structures. The next task is to extend this formulation to the nonlinear one, considering plate and shell models. Furthermore, given the effectiveness of CUF models in treating thin-walled structures, attention can also be focused on acoustic applications, particularly aerospace construction. Then, the introduction of aerodynamic theories coupled with CUF dynamic formulations will allow studying typical aeroelastic problems, investigating the effect of the fluid-structure interaction.

References

[1] Z.P. Bazant and L. Cedolin. *Stability of structures: elastic, inelastic, fracture and damage theories*. World Scientific, Singapore, 2010.

[2] J. Singer, J. Arboz, and T. Weller. *Buckling Experiments: Experimental Methods in Buckling of Thin Walled Structures. Volume 1: Basic Concepts, Columns, Beam and Plates*, volume 21. Book Reviews, 1999.

[3] J. Singer, J. Arbocz, and T. Weller. *Buckling experiments: experimental methods in buckling of thin-walled structures, Volume 2: Shells, built-up structures, composites and additional topics*, volume 2. John Wiley & Sons, 2002.

[4] M.L. Gambhir. *Stability analysis and design of structures*. Springer Science & Business Media, 2004.

[5] W.T. Koiter. On foundations of linear theory of thin elastic shells. *Proceedings of the Koninklijke Nederlandse Akademie van Wetenschappen Series B-Physical Sciences*, 73(3):169–195, 1970.

[6] L.B. Rall and D. Rall. *Computational solution of nonlinear operator equations*. Wiley, 1969.

[7] D.O. Brush, B.O. Almroth, and J.W. Hutchinson. Buckling of bars, plates, and shells. *Journal of Applied Mechanics*, 42(4):991, 1975.

[8] L. Euler. Methodus inveniendi lineas curvas maximi minimive proprietate gaudentes (appendix, de curvis elasticis). *Lausanne und Genf*, 1744(1774):6, 1774.

[9] T. Young. *A course of lectures on natural philosophy and the mechanical arts: in two volumes*, volume 2. Johnson, 1807.

[10] G. Kirchhoff. Ueber das gleichgewicht und die bewegung eines unendlich dünnen elastischen stabes. 1859.

[11] F. Engesser. Die Knickfestigkeit Gerader Stäbe. Z. Architekten und Ing. *Vereins zu Hannover*, 35:455–455, 1889.

[12] E. Carrera. The effects of shear deformation and curvature on buckling and vibrations of cross-ply laminated composite shells. *Journal of Sound and Vibration*, 150(3):405–433, 1991.

[13] E. Carrera and M. Villani. Effects of boundary conditions on postbuckling of compressed, symmetrically laminated thick plates. *AIAA Journal*, 33(8):1543–1546, 1995.

[14] S.M. Ibrahim, E. Carrera, M. Petrolo, and E. Zappino. Buckling of thin-walled beams by a refined theory. *Journal of Zhejiang University Science A*, 13(10):747–759, 2012.

[15] E. Carrera, A. Pagani, and J.R. Banerjee. Linearized buckling analysis of isotropic and composite beam-columns by Carrera Unified Formulation and dynamic stiffness method. *Mechanics of Advanced Materials and Structures*, 23(9):1092–1103, 2016.

[16] E. Carrera, R. Azzara, E. Daneshkhah, A. Pagani, and B. Wu. Buckling and post-buckling of anisotropic flat panels subjected to axial and shear in-plane loadings accounting for classical and refined structural and nonlinear theories. *International Journal of Non-Linear Mechanics*, 133:103716, 2021.

[17] R.S. Barsoum. Finite element method applied to the problem of stability of a non-conservative system. *International Journal for Numerical Methods in Engineering*, 3(1):63–87, 1971.

[18] M.M Attard and I.J. Somervaille. Stability of thin-walled open beams under nonconservative loads. *Journal of Structural Mechanics*, 15(3):395–412, 1987.

[19] M.H. Richardson and K.A. Ramsey. Integration of dynamic testing into the product design cycle. *Sound and Vibration*, 15(11):14–27, 1981.

[20] K.G. McConnell and P.S. Varoto. *Vibration testing: theory and practice*. John Wiley & Sons, 1995.

[21] R.V. Southwell. On the general theory of elastic stability. *Philosophical Transactions of the Royal Society of London. Series A, Containing Papers of a Mathematical or Physical Character*, 213(497-508):187–244, 1914.

[22] GD Galletly. A simple extension of southwell's method for determining the elastic general instability pressure of ring-stiffened cylinders subject to external hydrostatic pressure. *SESA Procedings*, 2010.

[23] A. Sommerfeld. Eine einfache vorrichtung zur veranschaulichung des knickungsvorganges. *Zeitschrift des Verein Deutscher Ingenieure (ZVDI)*, 49:1320–1323, 1905.

[24] T.H. Chu. *Determination of buckling loads by frequency measurements*. PhD thesis, California Institute of Technology, 1949.

[25] H. Lurie. *Lateral vibrations as related to structural stability*. PhD thesis, California Institute of Technology, 1950.

[26] J.H. Meier. The determination of the critical load of a column or stiffened panel in compression by the vibration method. In *Proceeding of the Society for Experimental Stress Analysis*, volume 11, 1953.

[27] W. Flügge. Die stabilität der kreiszylinderschale. *Ingenieur-Archiv 3.5*, pages 463–506, 1932.

[28] L.H. Donnell. *A new theory for the buckling of thin cylinders under axial compression and bending*. Guggenheim Aeronautical Laboratory, 1934.

[29] B. Budiansky. Dynamic buckling of elastic structures: criteria and estimates. In *Dynamic Stability of Structures*, pages 83–106. Elsevier, 1967.

[30] C.C. Chamis. Dynamic buckling and postbuckling of a composite shell. *International Journal of Structural Stability and Dynamics*, 10(04):791–805, 2010.

[31] V. Chitra and R.S. Priyadarsini. Dynamic buckling of composite cylindrical shells subjected to axial impulse. *Contributory Papers*, page 159, 2013.

[32] C. Bisagni. Dynamic buckling of fiber composite shells under impulsive axial compression. *Thin-walled Structures*, 43(3):499–514, 2005.

[33] T. Kubiak. *Static and dynamic buckling of thin-walled plate structures*. Springer, 2013.

[34] K.J. Bathe. *Finite element procedure*. Prentice Hall, Upper Saddle River, New Jersey, USA, 1996.

[35] J.T. Oden. *Finite elements of nonlinear continua*. Courier Corporation, 2006.

[36] O.C. Zienkiewicz and P.B. Morice. *The finite element method in engineering science*, volume 1977. MCgraw-Hill London, 1971.

[37] H.C. Martin. Large deflection and stability analysis by the direct stiffness method. Technical report, Pasadena, USA, 1965.

[38] D.W. Murray. *Large deflection analysis of plates*. SESM Report, University of California, 1967.

[39] R.W. Clough and E.L. Wilson. Dynamic finite element analysis of arbitrary thin shells. *Computers & Structures*, 1(1-2):33–56, 1971.

[40] E. Carrera, M. Cinefra, M. Petrolo, and E. Zappino. *Finite Element Analysis of Structures through Unified Formulation*. John Wiley & Sons, Chichester, West Sussex, UK, 2014.

[41] E. Carrera. Theories and finite elements for multilayered, anisotropic, composite plates and shells. *Archives of Computational Methods in Engineering*, 9(2):87–140, 2002.

[42] E. Carrera. Theories and finite elements for multilayered plates and shells: a unified compact formulation with numerical assessment and benchmarking. *Archives of Computational Methods in Engineering*, 10(3):215–296, 2003.

[43] E. Carrera, G. Giunta, and M. Petrolo. *Beam Structures: Classical and Advanced Theories*. John Wiley & Sons, 2011.

[44] M.H. Nagaraj, I. Kaleel, E. Carrera, and M. Petrolo. Elastoplastic micromechanical analysis of fiber-reinforced composites with defects. *Aerotecnica Missili & Spazio*, 101(1):53–59, 2022.

[45] A. Pagani, M. Enea, and E. Carrera. Quasi-static fracture analysis by coupled three-dimensional peridynamics and high order one-dimensional finite elements based on local elasticity. *International Journal for Numerical Methods in Engineering*, 123(4):1098–1113, 2022.

[46] A. Pagani and A.R. Sanchez-Majano. Influence of fiber misalignments on buckling performance of variable stiffness composites using layerwise models and random fields. *Mechanics of Advanced Materials and Structures*, 29(3):384–399, 2022.

[47] A.R. Sánchez-Majano, R. Azzara, A. Pagani, and E. Carrera. Accurate stress analysis of variable angle tow shells by high-order equivalent-single-layer and layer-wise finite element models. *Materials*, 14(21):6486, 2021.

[48] I. Kaleel, M. Petrolo, A.M. Waas, and E. Carrera. Micromechanical progressive failure analysis of fiber-reinforced composite using refined beam models. *Journal of Applied Mechanics*, 85(2), 2018.

[49] A. Pagani, R. Azzara, B. Wu, and E. Carrera. Effect of different geometrically nonlinear strain measures on the static nonlinear response of isotropic and composite shells with constant curvature. *International Journal of Mechanical Sciences*, 209:106713, 2021.

[50] A.G. de Miguel, A. Pagani, and E. Carrera. Structural health monitoring: Numerical simulation of Lamb waves via higher-order models. In *Advances in Predictive Models and Methodologies for Numerically Efficient Linear and Nonlinear Analysis of Composites*, pages 125–140. Springer, 2019.

[51] R. Azzara, E. Carrera, and A. Pagani. Nonlinear and linearized vibration analysis of plates and shells subjected to compressive loading. *International Journal of Non-Linear Mechanics*, 141:103936, 2022.

[52] R. Azzara, E. Carrera, M. Filippi, and A. Pagani. Time response stress analysis of solid and reinforced thin-walled structures by component-wise models. *International Journal of Structural Stability and Dynamics*, 20(14):2043010, 2020.

[53] H. Ziegler. *Principles of structural stability*, volume 35. Birkhäuser, 2013.

[54] C.E. Massonnet. Voilement des plaques planes sollicitées dans leur plan. *Final Report of the 3rd Congress of the International Association for Bridge and Structural Engineering (Brussels, BE, 1948)*, 1948.

[55] L.N. Virgin. *Vibration of axially-loaded structures*. Cambridge University Press, Cambridge, UK., 2007.

[56] F. Franzoni, S.F.M. de Almeida, and C.A.E. Ferreira. Numerical and experimental dynamic analyses of a postbuckled box beam. *AIAA Journal*, 54(6):1987–2003, 2016.

[57] H. Abramovich. *Stability and vibrations of thin-walled composite structures*. Woodhead Publishing, 2017.

[58] C.E. Massonnet. *Les relations entre les modes normaux de vibration et la stabilité des systèmes élastiques*. Goemaere, Brussels, 1940.

[59] R.V. Southwell. On the analysis of experimental observations in problems of elastic stability. *Proceedings of the Royal Society of London. Series A, Containing Papers of a Mathematical and Physical Character*, 135(828):601–616, 1932.

[60] L.H. Donnell. On the application of Southwell's method for the analysis of buckling tests. *Stephan Timoshenko 60th Anniversary Volume*, pages 27–38, 1938.

[61] H.R. Fisher. An extension of Southwell's method of analysing experimental observations in problems of elastic stability. *Proceedings of the Royal Society of London. Series A, Containing Papers of a Mathematical and Physical Character*, 144(853):609–630, 1934.

[62] W.H. Horton, F.L. Cundari, and R.W. Johnson. The analysis of experimental data obtained from stability studies on elastic column and plate structures. In *Israel Journal of Technology*, volume 5, page 104, 1967.

[63] T.J. Stratford, C.J. Burgoyne, H.P.J. Taylor, and R.V. Southwell. Stability design of long precast concrete beams. *Proceedings of the Institution of Civil Engineers-Structures and Buildings*, 134(2):155–168, 1999.

[64] T.J. Stratford, C.J. Burgoyne, and R.V. Southwell. Lateral stability of long precast concrete beams. *Proceedings of the Institution of Civil Engineers-Structures and Buildings*, 134(2):169–180, 1999.

[65] W.P. Vann and J. Sehested. Experimental techniques for plate buckling. *International Specialty Conference on Cold-Formed Steel Structures*, 2, 1973.

[66] H. Lurie. Effective end restraint of columns by frequency measurements. *Journal of the Aeronautical Sciences*, 18(8):566–567, 1951.

[67] R.H. Plaut and L.N. Virgin. Use of frequency data to predict buckling. *Journal of Engineering Mechanics*, 116(10):2330–2335, 1990.

[68] L.N. Virgin and R.H. Plaut. Axial load effects on the frequency response of a clamped beam. In *Proceeding of XXI IMAC Conference and Exposition on Structural Dynamics*, 2003.

[69] T.A. Alexander. The relationship between the buckling load factor and the fundamental frequency of a structure. In *Structures Congress 2005: Metropolis and Beyond*, pages 1–17, 2005.

[70] E.E. Johnson and B.F. Goldhammer. A determination of the critical load of a column or stiffened panel in compression by the vibration method. *In: Proceedings of the Society for Experimental Stress Analysis*, 11:233–234, 1953.

[71] P. Mandal. Prediction of buckling load from vibration measurements. In *New Approaches to Structural Mechanics, Shells and Biological Structures*, pages 175–188. Springer, 2002.

[72] M. Chaves-Vargas, A. Dafnis, H.G. Reimerdes, and K.U. Schröder. Modal parameter identification of a compression-loaded CFRP stiffened plate and correlation with its buckling behaviour. *Progress in Aerospace Sciences*, 78:39–49, 2015.

[73] D. Kennedy and K.I. Lo. Critical buckling predictions for plates and stiffened panels from natural frequency measurements. In *Journal of Physics: Conference Series*, volume 1106, page 012018. IOP Publishing, 2018.

[74] S. Okubo and J.S. Whittier. A note on buckling and vibrations of an externally pressurized shallow spherical shell. *Journal of Applied Mechanics*, 34(4):1032–1034, 1967.

[75] Y. Segal. Prediction of buckling load and loading conditions of stiffened shells from vibration tests. *M.Sc. Thesis. Haifa, Israel nstitute ol Technology, Haifa*, 1980.

[76] M.A. Souza, W.C. Fok, and A.C. Walker. Review of experimental techniques for thin-walled structures liable to buckling. *Experimental Techniques*, 7(9):21–25, 1983.

[77] M.A. Souza and L.M.B. Assaid. A new technique for the prediction of buckling loads from nondestructive vibration tests. *Experimental Mechanics*, 31(2):93–97, 1991.

[78] H. Abramovich, D. Govich, and A. Grunwald. Buckling prediction of panels using the vibration correlation technique. *Progress in Aerospace Sciences*, 78:62–73, 2015.

[79] E. Jansen, H. Abramovich, and R. Rolfes. The direct prediction of buckling loads of shells under axial compression using VCT-towards an upgraded approach. In *29th congress on the International Council of the Aeronutical Science*, pages 1–9, 2014.

[80] M.A. Arbelo, S.F.M. De Almeida, M.V. Donadon, S.R. Rett, R. Degenhardt, S.G.P. Castro, K. Kalnins, and O. Ozoliņš. Vibration correlation technique for the estimation of real boundary conditions and buckling load of unstiffened plates and cylindrical shells. *Thin-Walled Structures*, 79:119–128, 2014.

[81] M.A. Arbelo, K. Kalnins, O. Ozolins, E. Skukis, S.G.P. Castro, and R. Degenhardt. Experimental and numerical estimation of buckling load on unstiffened cylindrical shells using a vibration correlation technique. *Thin-Walled Structures*, 94:273–279, 2015.

[82] P. Singhatanadgid and P. Sukajit. Determination of buckling load of rectangular plates using measured vibration data. In *ICEM 2008: International Conference on Experimental Mechanics 2008*, volume 7375, pages 929–935. SPIE, 2009.

[83] E. Skukis, O. Ozolins, J. Andersons, K. Kalnins, and M.A. Arbelo. Applicability of the vibration correlation technique for estimation of the buckling load in axial compression of cylindrical isotropic shells with and without circular cutouts. *Shock and Vibration*, 2017, 2017.

[84] F. Franzoni, F. Odermann, E. Lanbans, C. Bisagni, M.A. Arbelo, and R. Degenhardt. Experimental validation of the vibration correlation technique robustness to predict buckling of unstiffened composite cylindrical shells. *Composite Structures*, 224:111107, 2019.

[85] F. Franzoni, J. Degenhardt, R.and Albus, and M.A. Arbelo. Vibration correlation technique for predicting the buckling load of imperfection-sensitive isotropic cylindrical shells: An analytical and numerical verification. *Thin-Walled Structures*, 140:236–247, 2019.

[86] E. Labans, H. Abramovich, and C. Bisagni. An experimental vibration-buckling investigation on classical and variable angle tow composite shells under axial compression. *Journal of Sound and Vibration*, 449:315–329, 2019.

[87] F. Franzoni. *Predicting buckling from vibration: an analytical, numerical, and experimental verification for cylindrical shells*. PhD thesis, Universität Bremen, 2020.

[88] L. Euler. *De curvis elasticis*. Lausanne and Geneva: Bousquet, 1744.

[89] A. de Saint-Venant. Mèmoire sur la torsion des prismes. *Acadèmie des Sciences de l'Institut Impèrial de Frances*, 14:233–560, 1856.

[90] S.P. Timoshenko. On the corrections for shear of the differential equation for transverse vibrations of prismatic bars. *Philosophical Magazine*, 41:744–746, 1922.

[91] D.T. Mucichescu. Bounds for stiffness of prismatic beams. *Journal of Structural Engineering*, 110(6):1410–1414, 1984.

[92] V.V. Novozhilov. *Theory of elasticity*. Pergamon, Elmsford, 1961.

[93] F. Gruttmann and W. Wagner. Shear correction factors in Timoshenko's beam theory for arbitrary shaped cross-sections. *Computational Mechanics*, 27:199–207, 2001.

[94] G.R. Cowper. The shear coefficient in Timoshenko's beam theory. *Journal of Applied Mechanics*, 33(2):335–340, 1966.

[95] W. Carnegie and J. Thomas. The effects of shear deformation and rotary inertia on the lateral frequencies of cantilever beams in bending. *Journal of Engineering for Industry*, 94(1):267–278, 1972.

[96] M. Levinson. A new rectangular beam theory. *Journal of Sound and Vibration*, 74(1):81–87, 1981.

[97] S. Benscoter. A theory of torsion bending for multicell beams. *Journal of Applied Mechanics*, 21(1):25–34, 1954.

[98] P. Ladevèze. *Nonlinear computational structural mechanics*. Springer Verlag, New York, 1998.

[99] P. Vidal, L. Gallimard, and O. Polit. Composite beam finite element based on the proper generalized decomposition. *Computers & Structures*, 102:76–86, 2012.

[100] V.V. Volovoi, D.H. Hodges, V.L. Berdichevsky, and V.G. Sutyrin. Asymptotic theory for static behavior of elastic anisotropic I-beams. *International Journal of Solids and Structures*, 36:1017–1043, 1999.

[101] R. Schardt. Generalized beam theory - An adequate method for coupled stability problems. *Thin-Walled Structures*, 19:161–180, 1994.

[102] E. Carrera and G. Giunta. Refined beam theories based on a unified formulation. *International Journal of Applied Mechanics*, 2(1):117–143, 2010.

[103] K. Washizu. *Variational Methods in Elasticity and Plasticity*. Pergamon, Oxford, 1968.

[104] R. K. Kapania and S. Raciti. Recent advances in analysis of laminated beams and plates. Part I: Shear effects and buckling. *AIAA Journal*, 27(7):923–935, 1989.

[105] R. K. Kapania and S. Raciti. Recent advances in analysis of laminated beams and plates. Part II: Vibrations and wave propagation. *AIAA Journal*, 27(7):935–946, 1989.

[106] E. Carrera, A. Pagani, M. Petrolo, and E. Zappino. Recent developments on refined theories for beams with applications. *Mechanical Engineering Reviews*, 2(2):1–30, 2015.

[107] A.V. Srinivasan. Non-linear vibrations of beams and plates. *International Journal of Non-Linear Mechanics*, 1(3):179–191, 1966.

[108] L. Azrar, R. Benamar, and R.G. White. Semi-analytical approach to the non-linear dynamic response problem of S–S and C–C beams at large vibration amplitudes part I: General theory and application to the single mode approach to free and forced vibration analysis. *Journal of Sound and Vibration*, 224(2):183–207, 1999.

[109] L. Azrar, R. Benamar, and R.G. White. A semi-analytical approach to the non-linear dynamic response problem of beams at large vibration amplitudes, part II: Multimode approach to the steady state forced periodic response. *Journal of Sound and Vibration*, 255(1):1–41, 2002.

[110] H. Abramovich. Natural frequencies of Timoshenko beams under compressive axial loads. *Journal of Sound Vibration*, 157(1):183–189, 1992.

[111] G. Piana, E. Lofrano, A. Manuello, and G. Ruta. Natural frequencies and buckling of compressed non-symmetric thin-walled beams. *Thin-Walled Structures*, 111:189–196, 2017.

[112] A. Elkaimbillah, B. Braikat, F. Mohri, and N. Damil. A one-dimensional model for computing forced nonlinear vibration of thin-walled composite beams with open variable cross-sections. *Thin-Walled Structures*, 159:107211, 2021.

[113] L.N. Virgin and R.H. Plaut. Effect of axial load on forced vibrations of beams. *Journal of Sound and Vibration*, 168(3):395–405, 1993.

[114] P. Cabral, E. Carrera, H.E.A.A. dos Santos, P.H.G. Galeb, A. Pagani, D. Peeters, and A.P. Prado. Experimental and numerical vibration correlation of pre-stressed laminated reinforced panel. *Mechanics of Advanced Materials and Structures*, pages 1–13, 2020.

[115] J.R. Banerjee. Free vibration of axially loaded composite Timoshenko beams using the dynamic stiffness matrix method. *Computers & Structures*, 69(2):197–208, 1998.

[116] T.P. Vo and J. Lee. Free vibration of thin-walled composite box beams. *Composite Structures*, 84(1):11–20, 2008.

[117] T.P. Vo and J. Lee. Flexural–torsional buckling of thin-walled composite box beams. *Thin-walled Structures*, 45(9):790–798, 2007.

[118] T.P. Vo and J. Lee. Interaction curves for vibration and buckling of thin-walled composite box beams under axial loads and end moments. *Applied Mathematical Modelling*, 34(10):3142–3157, 2010.

[119] A. Pagani, R. Augello, and E. Carrera. Virtual vibration correlation technique (VCT) for nonlinear analysis of metallic and composite structures. In *ASME International Mechanical Engineering Congress and Exposition*, volume 52002. American Society of Mechanical Engineers, 2018.

[120] R. Augello, E. Daneshkhah, X. Xu, and E. Carrera. Efficient CUF-based method for the vibrations of thin-walled open cross-section beams under compression. *Journal of Sound and Vibration*, 510:116232, 2021.

[121] H. Yang, E. Daneshkhah, R. Augello, X. Xu, and E. Carrera. Numerical vibration correlation technique for thin-walled composite beams under compression based on accurate refined finite element. *Composite Structures*, 280:114861, 2022.

[122] J. Gutiérrez Álvarez and C. Bisagni. A study on thermal buckling and mode jumping of metallic and composite plates. *Aerospace*, 8(2):56, 2021.

[123] K. Murphy and D. Ferreira. Thermal buckling of rectangular plates. *International Journal of Solids and Structures*, 38(22-23):3979–3994, 2001.

[124] V. Bhagat and P. Jeyaraj. Experimental investigation on buckling strength of cylindrical panel: Effect of non-uniform temperature field. *International Journal of Non-Linear Mechanics*, 99:247–257, 2018.

[125] P. Jeyaraj. Buckling and free vibration behavior of an isotropic plate under nonuniform thermal load. *International Journal of Structural Stability and Dynamics*, 13(3):1250071, 2013.

[126] J.G. Álvarez and C. Bisagni. Investigation on buckling and mode jumping of composite plates under thermomechanical loads. *International Journal of Non-Linear Mechanics*, 138:103837, 2022.

[127] G. Kirchhoff. Über das gleichgewicht und die bewegung einer elastischen scheibe. *Journal Für die Reine und Angewandte Mathematik (Crelles Journal)*, 1850(40):51–88, 1850.

[128] E. Reissner. The effect of transverse shear deformation on the bending of elastic plates. *Journal of Applied Mechanics*, 12(2):69–77, 1945.

[129] R.D. Mindlin. Influence of rotatory inertia and shear flexural motions of isotropic elastic plates. *J. appl. Mech.*, 18:1031–1036, 1951.

[130] Y. Stavsky and R. Loewy. On vibrations of heterogeneous orthotropic cylindrical shells. *Journal of Sound and Vibration*, 15(2):235–256, 1971.

[131] J.M. Whitney. The effect of transverse shear deformation on the bending of laminated plates. *Journal of Composite Materials*, 3(3):534–547, 1969.

[132] E. Carrera. A class of two dimensional theories for multilayered plates analysis. *Atti Accademia delle Scienze di Torino, Memorie Scienze Fisiche*, 19-20:49–87, 1995.

[133] E. Carrera. CZ requirements-models for the two dimensional analysis of multilayered structures. *Composite Structures*, 37(3-4):373–383, 1997.

[134] A.K. Noor and P.L. Rarig. Three-dimensional solutions of laminated cylinders. *Computer Methods in Applied Mechanics and Engineering*, 3(3):319–334, 1974.

[135] T.K. Varadan and K. Bhaskar. Bending of laminated orthotropic cylindrical shells — An elasticity approach. *Composite Structures*, 17(2):141–156, 1991.

[136] F.B. Hildebrand, E. Reissner, and G.B. Thomas. Notes on the foundations of the theory of small displacements of orthotropic shells. Technical report, 1949.

[137] L. Librescu. *Elastostatics and kinetics of anisotropic and heterogeneous shell-type structures*, volume 2. Springer Science & Business Media, 1975.

[138] K.H. Lo, R.M. Christensen, and E.M. Wu. A high-order theory of plate deformation — Part 1: Homogeneous plates. *AME J. Appl. Mech.*, 44(4):663–668, 1977.

[139] K.H. Lo, R.M. Christensen, and E.M. Wu. A high-order theory of plate deformation — Part 2: Laminates plates. *AME J. Appl. Mech.*, 44(4):669–676, 1977.

[140] N.S. Putcha and J.N. Reddy. Stability and natural vibration analysis of laminated plates by using a mixed element based on a refined plate theory. *Journal of Sound and Vibration*, 104(2):285–300, 1986.

[141] E. Carrera. Evaluation of layerwise mixed theories for laminated plates analysis. *AIAA Journal*, 36(5):830–839, 1998.

[142] E. Carrera. An assessment of mixed and classical theories on global and local response of multilayered orthotropic plates. *Composite Structures*, 50(2):183–198, 2000.

[143] E. Carrera. Developments, ideas and evaluation based upon Reissner's mixed variational theorem in the modeling of multilayered plates and shells. *Applied Mechanics Review*, 54:301–329, 2001.

[144] E. Carrera and A. Ciuffreda. A unified formulation to asses theories of multilayered plates for various bending problems. *Composite Structures*, 69:271–293, 2005.

[145] E. Carrera and M. Petrolo. Guidelines and recommendations to construct theories for metallic and composite plates. *AIAA Journal*, 48(12):2852–2866, 2010. doi: 10.2514/1.J050316.

[146] J. Marcinkowski. Postbuckling behaviour of rectangular plates in axial compression. *Archives of Civil Engineering*, 45(2):275–288, 1999.

[147] T. von Kármán. Encyklopadie der mathematischen wissenschaften. *Vol. IV*, 349:422, 1910.

[148] H.N. Chu and G. Herrmann. Influence of large amplitudes on free flexural vibrations of rectangular elastic plates. 1956.

[149] J.N. Reddy. A general non-linear third-order theory of plates with moderate thickness. *International Journal of Non-Linear Mechanics*, 25(6):677–686, 1990.

[150] M. Stein. *Loads and deformations of buckled rectangular plates*. National Aeronautics and Space Administration, 1960.

[151] D. Schaeffer and M. Golubitsky. Boundary conditions and mode jumping in the buckling of a rectangular plate. *Communications in Mathematical Physics*, 69(3):209–236, 1979.

[152] R. Maaskant and J. Roorda. Mode jumping in biaxially compressed plates. *International Journal of Solids and Structures*, 29(10):1209–1219, 1992.

[153] M. Uemura and O. Byon. Secondary buckling of a flat plate under uniaxial compression, Part 1: Theoretical analysis of simply supported flat plate. *International Journal of Non-Linear Mechanics*, 12(6):355–370, 1977.

[154] H. Troger and A. Steindl. *Nonlinear stability and bifurcation theory: an introduction for engineers and applied scientists*. Springer Science & Business Media, 2012.

[155] P.R. Everall and G.W. Hunt. Mode jumping in the buckling of struts and plates: A comparative study. *International Journal of Non-Linear Mechanics*, 35(6):1067–1079, 2000.

[156] G.W. Hunt and P.R. Everall. Arnold tongues and mode-jumping in the supercritical post-buckling of an archetypal elastic structure. *Proceedings of the Royal Society of London. Series A: Mathematical, Physical and Engineering Sciences*, 455(1981):125–140, 1999.

[157] L.M.H. Navier. Extrait des recherches sur la flexion des plans elastiques. *Bull. Sci. Soc. Philomat.*, pages 95–102, 1823.

[158] S.D. Poisson. Mémoire sur l'équilibre et le mouvement des corps élastiques. *Mm. Acad. Sci. Instr. Fr.*, 8:357–570, 1829.

[159] G. Gerard. *Handbook of Structural Stability: Buckling of curved plates and shells.* National Aeronautics and Space Administration, 1959.

[160] E.H. Baker, L. Kovalevsky, and F.L. Rish. *Structural analysis of shells.* Krieger Publishing Company, 1981.

[161] A.W. Leissa. Vibration of plates. *NASA SP-160. Washington, DC: US Government Printing Office*, 1969.

[162] C.Y. Chia. *Nonlinear analysis of plates.* McGraw-Hill International Book Company, 1980.

[163] C.Y. Chia. Geometrically nonlinear behavior of composite plates: A review. *Applied Mechanics Reviews*, 41(12):439–451, 1988.

[164] A.K. Noor, C.M. Andersen, and J.M. Peters. Reduced basis technique for nonlinear vibration analysis of composite panels. *Computer Methods in Spplied Mechanics and Engineering*, 103(1-2):175–186, 1993.

[165] B. Harras, R. Benamar, and R.G. White. Geometrically non-linear free vibration of fully clamped symmetrically laminated rectangular composite plates. *Journal of Sound and Vibration*, 251(4):579–619, 2002.

[166] M. Amabili. Nonlinear vibrations of rectangular plates with different boundary conditions: Theory and experiments. *Computers & Structures*, 82(31-32):2587–2605, 2004.

[167] M. Amabili. Theory and experiments for large-amplitude vibrations of rectangular plates with geometric imperfections. *Journal of Sound and Vibration*, 291(3-5):539–565, 2006.

[168] D. Shahgholian-Ghahfarokhi, M. Aghaei-Ruzbahani, and G. Rahimi. Vibration correlation technique for the buckling load prediction of composite sandwich plates with iso-grid cores. *Thin-Walled Structures*, 142:392–404, 2019.

[169] V.V. Novozhilov. *Thin shell theory.* Noordhoff Ltd., Groningen, The Netherlands, 1964.

[170] C.R. Calladine. *Theory of shell structures.* Cambridge University Press, 1989.

[171] F.I. Niordson. *Shell theory*, volume 29. North-Holland Series in Applied Mathematics and Mechanics, 1985.

[172] A.E.H. Love. Mathematical Theory of Elasticity. *Cambridge University Press*, 2013.

[173] G. Kirchhoff. Uber da gleichgewicht und die bewegung einer elastischen scheibe. *Journal Für Die Reine und Angewandte Mathematik*, 40:51–88, 1850.

[174] E. Reissner. The effect of transverse shear deformation on the bending of elastic plates. *Journal of Applied Mechanics*, 12:69–76, 1945.

[175] A.L. Cauchy. Sur l'equilibre et le mouvement d'une plaque solide. *Exerc. Math.*, 3:328–355, 1828.

[176] J.N. Reddy and C.F. Liu. A higher-order shear deformation theory of laminated elastic shells. *International Journal of Engineering Science*, 23(3):319–330, 1985.

[177] D.S. Mashat, E. Carrera, A.M. Zenkour, S.A. Al Khateeb, and A. Lamberti. Evaluation of refined theories for multilayered shells via Axiomatic/Asymptotic method. *Journal of Mechanical Science and Technology*, 28(11):4663–4672, 2014.

[178] G. Li, E. Carrera, M. Cinefra, A.G. de Miguel, A. Pagani, and E. Zappino. An adaptable refinement approach for shell finite element models based on node-dependent kinematics. *Composite Structures*, 210:1–19, 2019.

[179] M. Cinefra and S. Valvano. A variable kinematic doubly-curved MITC9 shell element for the analysis of laminated composites. *Mechanics of Advanced Materials and Structures, In Press*, 23(11):1312–1325, 2016.

[180] K.J. Bathe and D. Chapelle. *Finite Element Analysis of Shells – Fundamentals*. Springer-Verlag Telos, 2003.

[181] V.V. Novozhilov. *Foundations of the nonlinear theory of elasticity*. Courier Corporation, 1999.

[182] P.M. Naghdi and R.P. Nordgren. On the nonlinear theory of elastic shells under the Kirchhoff hypothesis. *Quarterly of Applied Mathematics*, 21(1):49–59, 1963.

[183] A. Libai and J. Simmonds. Nonlinear elastic shell theory. In *Advances in Applied Mechanics*, volume 23, pages 271–371. Elsevier, 1983.

[184] S.T. Dennis and A.N. Palazotto. Large displacement and rotational formulation for laminated shells including parabolic transverse shear. *International Journal of Non-Linear Mechanics*, 25(1):67–85, 1990.

[185] Y. Matsuzaki. A theoretical and experimental study of the nonlinear flexural vibration of thin circular cylindrical shells with clamped ends. *Trans. Jpn. Soc. Aero. Space Sci.*, 12(21):55, 1969.

[186] M. Amabili. Nonlinear vibrations of circular cylindrical shells with different boundary conditions. *AIAA Journal*, 41(6):1119–1130, 2003.

[187] W. Haynie and M. Hilburger. Comparison of methods to predict lower bound buckling loads of cylinders under axial compression. In *51st AIAA/ASME/ASCE/AHS/ASC Structures, Structural Dynamics, and Materials Conference*, page 2532, Orlando, Florida, 12-15 April 2010.

[188] W.H. Horton, E.M. Nassar, and M.K. Singhal. Determination of the critical loads of shells by nondestructive methods. *Experimental Mechanics*, 17(4):154–160, 1977.

[189] H. Fan. Critical buckling load prediction of axially compressed cylindrical shell based on non-destructive probing method. *Thin-Walled Structures*, 139:91–104, 2019.

[190] J.W. Hutchinson and J.M.T. Thompson. Nonlinear buckling interaction for spherical shells subject to pressure and probing forces. *Journal of Applied Mechanics*, 84(6), 2017.

[191] J.M.T. Thompson. Advances in shell buckling: theory and experiments. *International Journal of Bifurcation and Chaos*, 25(01):1530001, 2015.

[192] F. Alijani and M. Amabili. Non-linear vibrations of shells: A literature review from 2003 to 2013. *International Journal of Non-linear Mechanics*, 58:233–257, 2014.

[193] M. Amabili and M.P. Païdoussis. Review of studies on geometrically nonlinear vibrations and dynamics of circular cylindrical shells and panels, with and without fluid-structure interaction. *Appl. Mech. Rev.*, 56(4):349–381, 2003.

[194] G. Abaqus. Abaqus 6.11. *Dassault Systemes Simulia Corporation, Providence, RI, USA*, 2011.

[195] P.F. Pai. *Highly Flexible Structures: Modeling, Computation, and Experimentation*. 2007.

[196] A.L. Gol'Denveizer. *Theory of Elastic Thin Shells. Solid and Structural Mechanics*. Pergamon Press, 1961.

[197] S.W. Tsai. *Composites Design*. Think Composites, P.O. Box 581, Dayton, Ohio 45419, USA, 1988.

[198] J.N. Reddy. *Mechanics of Laminated Composite Plates and Shells: Theory and Analysis*. New York: CRC Press, 2004.

[199] Z. Gurdal and R. Olmedo. In-plane response of laminates with spatially varying fiber orientations-variable stiffness concept. *AIAA Journal*, 31(4):751–758, 1993.

[200] E. Viglietti, A.and Zappino and E. Carrera. Analysis of variable angle tow composites structures using variable kinematic models. *Composites Part B: Engineering*, 171:272–283, 2019.

[201] E. Carrera, G. Giunta, P. Nali, and M. Petrolo. Refined beam elements with arbitrary cross-section geometries. *Computers and Structures*, 88(5–6):283–293, 2010.

[202] E. Oñate. *Structural Analysis with the Finite Element Method. Linear Statics. Volume 1: Basics and Solids*. Springer Science & Business Media, 2009.

[203] E. Carrera, M. Maiarú, and M. Petrolo. Component-wise analysis of laminated anisotropic composites. *International Journal of Solids and Structures*, 49(13):1839–1851, 2012.

[204] E. Carrera, A. Pagani, and M. Petrolo. Classical, refined and component-wise theories for static analysis of reinforced-shell wing structures. *AIAA Journal*, 51(5):1255–1268, 2013.

[205] E. Carrera, A. Pagani, and M. Petrolo. Component-wise method applied to vibration of wing structures. *Journal of Applied Mechanics*, 80(4):041012, 2013.

[206] A. Pagani and E. Carrera. Large-deflection and post-buckling analyses of laminated composite beams by Carrera Unified Formulation. *Composite Structures*, 170:40–52, 2017.

[207] E. Carrera. A study on arc-length-type methods and their operation failures illustrated by a simple model. *Computers & Structures*, 50(2):217–229, 1994.

[208] A. Pagani and E. Carrera. Unified formulation of geometrically nonlinear refined beam theories. *Mechanics of Advanced Materials and Structures*, 25(1):15–31, 2018.

[209] M. A. Crisfield. A fast incremental/iterative solution procedure that handles "snap-through". *Computers & Structures*, 13(1):55–62, 1981.

[210] J.L. Batoz and G. Dhatt. Incremental displacement algorithms for nonlinear problems. *International Journal for Numerical Methods in Engineering*, 14(8):1262–1267, 1979.

[211] G. Kerschen. *Modal analysis of nonlinear mechanical systems*, volume 555. Springer, 2014.

[212] A. W. Leissa. On a curve veering aberration. *Zeitschrift für angewandte Mathematik und Physik ZAMP*, 25(1):99–111, 1974.

[213] R.W.T. Doll and C.D. Mote Jr. On the dynamic analysis of curved and twisted cylinders transporting fluids. 1976.

[214] P.S. Nair and S. Durvasula. On quasi-degeneracies in plate vibration problems. *International Journal of Mechanical Sciences*, 15(12):975–986, 1973.

[215] C. Pierre. Mode localization and eigenvalue loci veering phenomena in disordered structures. *Journal of Sound and Vibration*, 126(3):485–502, 1988.

[216] S. Natsiavas. Mode localization and frequency veering in a non-conservative mechanical system with dissimilar components. *Journal of Sound and Vibration*, 165(1):137–147, 1993.

[217] A. Entezari, M. Filippi, and E. Carrera. Unified finite element approach for generalized coupled thermoelastic analysis of 3d beam-type structures, part 1: Equations and formulation. *Journal of Thermal Stresses*, 40(11):1386–1401, 2017.

[218] M.A. Dokainish and K. Subbaraj. A survey of direct time-integration methods in computational structural dynamics — I. Explicit methods. *Computers & Structures*, 32(6):1371–1386, 1989.

[219] K. Subbaraj and M.A. Dokainish. A survey of direct time-integration methods in computational structural dynamics — II. Implicit methods. *Computers & Structures*, 32(6):1387–1401, 1989.

[220] N.M. Newmark. A method of computation for structural dynamics. *Journal of the Engineering Mechanics Division*, 85(3):67–94, 1959.

[221] H.M. Hilber, T.J.R. Hughes, and Robert L. Taylor. Improved numerical dissipation for time integration algorithms in structural dynamics. *Earthquake Engineering & Structural Dynamics*, 5(3):283–292, 1977.

[222] J. Chung and G.M. Hulbert. A time integration algorithm for structural dynamics with improved numerical dissipation: The generalized-α method. *ASME Journal of Applied Mechanics*, 60(2):371–375, 1993.

[223] K.Y. Sze, X.H. Liu, and S.H. Lo. Popular benchmark problems for geometric nonlinear analysis of shells. *Finite Elements in Analysis and Design*, 40:1551–1569, 2004.

[224] B. Wu, A. Pagani, W.Q. Chen, and E. Carrera. Geometrically nonlinear refined shell theories by carrera unified formulation. *Mechanics of Advanced Materials and Structures*, pages 1–21, 2019.

[225] E. Carrera and A. Varello. Dynamic response of thin-walled structures by variable kinematic one-dimensional models. *Journal of Sound and Vibration*, 331(24):5268–5282, 2012.

[226] A. Pagani, M. Petrolo, G. Colonna, and E. Carrera. Dynamic response of aerospace structures by means of refined beam theories. *Aerospace Science and Technology*, 46:360–373, 2015.

[227] MSC Nastran. Dynamic analysis user's guide. *MSC Software*, 2010.

[228] J. Chen, D.J. Dawe, and S. Wang. Nonlinear transient analysis of rectangular composite laminated plates. *Composite Structures*, 49(2):129–139, 2000.

[229] W. Flügge. *Stresses in shells*. Springer Science & Business Media, 2013.

[230] A. Pagani, E. Carrera, and R. Augello. Evaluation of various geometrical nonlinearities in the response of beams and shells. *AIAA Journal*, 57(8):3524–3533, 2019.

[231] M. Cinefra, C. Chinosi, and L. Della Croce. MITC9 shell elements based on refined theories for the analysis of isotropic cylindrical structures. *Mechanics of Advanced Materials and Structures*, 20(2):91–100, 2013.

[232] J.E.M. Jubb, I.G. Phillips, and H. Becker. Interrelation of structural stability, stiffness, residual stress and natural frequency. *Journal of Sound and Vibration*, 39(1):121–134, 1975.

[233] S. Ilanko and S.M. Dickinson. The vibration and post-buckling of geometrically imperfect, simply supported, rectangular plates under uni-axial loading, Part I: Theoretical approach. *Journal of Sound and Vibration*, 118(2):313–336, 1987.

[234] S. Ilanko and S.M. Dickinson. The vibration and post-buckling of geometrically imperfect, simply supported, rectangular plates under uni-axial loading, Part II: Experimental investigations. *Journal of Sound and Vibration*, 118(2):317–351, 1987.

[235] R.J. Allemang. The Modal Assurance Criterion - twenty years of use and abuse. *Sound and Vibration*, 37(8):14–23, 2003.

[236] M. Pastor, M.and Binda and T. Harčarik. Modal Assurance Criterion. *Procedia Engineering*, 48:543–548, 2012.

[237] A.K. Noor and M.D. Mathers. Anisotropy and shear deformation in laminated composite plates. *AIAA Journal*, 14(2):282–285, 1976.

[238] A. Boujelben and A. Ibrahimbegovic. Finite-strain three-dimensional solids with rotational degrees of freedom: non-linear statics and dynamics. *Advanced Modeling and Simulation in Engineering Sciences*, 4(1):1–24, 2017.

[239] R. Courant. *Differential and Integral Calculus*. Interscience Pubblishers, 1937.

[240] G. Strang. *Calculus*. Welles-Cambridge Press, 1991.

[241] E. Carrera, A. Pagani, and M. Petrolo. Use of Lagrange multipliers to combine 1D variable kinematic finite elements. *Computers & Structures*, 129:194–206, 2013.

[242] M. Sharifnia. A higher-order nonlinear beam element for planar structures by using a new finite element approach. *Acta Mechanica*, 233(2):495–511, 2022.

Appendix A

Other important nonlinear problems

A.1 Large-deflections and post-buckling analysis

A.1.1 Cross-ply $[0°/90°]_s$ composite square plate

The first assessment deals with a composite square plate with the following stacking sequence $[0°/90°]_s$. The dimensions of this structure are width $a = b = 30.48$ cm and thickness $h = 7.62$ mm. The plate is subjected to a uniform transverse pressure. For this case, two different cases of boundary conditions are considered: (a) all edges are completely clamped, i.e., $u = v = w = 0$ at $x = 0, a$ and $y = 0, b$; (b) all edges are simply-supported, i.e., $u = v = w = 0$ at $x = 0, a,\ z = 0$ and $y = 0, b,\ z = 0$. The material data for this laminated plate are: $E_1 = 12.60$ GPa, $E_2 = E_3 = 12.62$ GPa, $G_{12} = G_{13} = 2.15$ GPa and $\nu_{12} = \nu_{13} = 0.2395$.

In this work, it is of fundamental importance to conduct convergence analyses, reported in Fig.A.1, to evaluate the effects of mesh approximation and kinematic expansion in order to obtain reliable results. So first, 4×4Q9, 8×8Q9, and 12×12Q9 finite plate elements with the fixed LD1 theory approximation order for each layer are considered. Then, the kinematic expansion order in the thickness direction is varied from LD1 to LD3. For clarity, the transverse displacements are evaluated at the middle of the composite plate. Furthermore, the values of transverse displacement for different models and loads, including the DOFs, are given in Table A.1. As observed from Fig. A.1 and Table A.1, the 12×12Q9+LD1 model is a reliable convergent model, which will be adopted to investigate the nonlinear equilibrium path of the present composite structure.

The nonlinear equilibrium curves for this composite structure by considering both clamped and simply-supported edge conditions are shown in Fig. A.2, which plots the normalized values of the displacement in the middle point of the plate as a function of

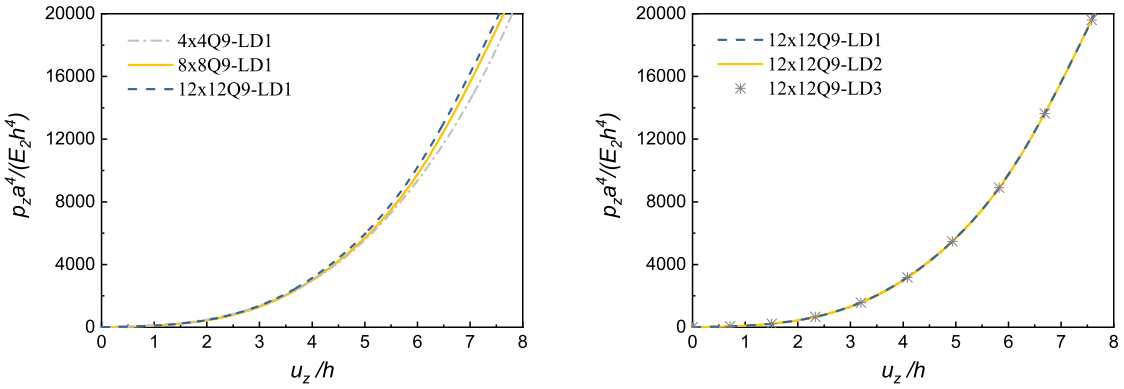

(a) (b)

Fig. A.1 Convergence analyses for the 4-layer $[0°/90°]_s$ clamped laminated composite plate structure subjected to transverse pressure. (a) Mesh approximation; (b) Kinematic expansion.

CUF models	DOFs	u_z/h	
		$p_z a^4/E_2 h^4 = 4000$	$p_z a^4/E_2 h^4 = 16000$
4 ×4Q9+LD1	1215	4.44	7.16
8 ×8Q9+LD1	4335	4.42	7.03
12×12Q9+LD1	9375	4.41	6.98

Table A.1 Transverse displacements a the center of the 4-layer $[0°/90°]_s$ clamped composite plate subjected to transverse pressure for different CUF models and load values.

the normalized values of the applied transverse pressure. Consequently, the equilibrium curves predicted by the CUF linear and Full nonlinear (Full NL) plate models match well with those of the available literature, in which a FSDT theory is used [198]. Furthermore, the difference between linear and nonlinear models is more significant as the transverse pressure value increases. In addition, the load-carrying capacity of the composite plate with the clamped edge conditions is higher than that of the composite plate with the simply-supported ones.

For the sake of completeness, the displacement values based on different CUF 2D models and solutions found in the available literature [198] at the fixed load of $\frac{P_z a^4}{E_2 h^4} = 100$ for the clamped edge conditions, and at the fixed load of $\frac{P_z a^4}{E_2 h^4} = 25$ for the simply-supported edge conditions are tabulated in Table A.2. According to this table, the results show how the CUF linear and nonlinear models agree well with the corresponding values of those of the literature [198].

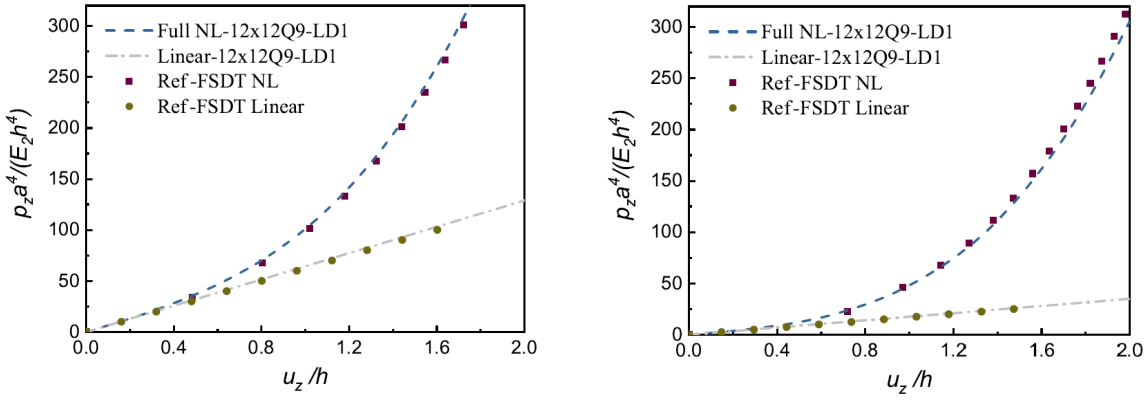

(a) Clamped edge conditions

(b) Simply-supported edge conditions

Fig. A.2 Nonlinear equilibrium curves of the 4-layer $[0°/90°]_s$ composite plate subjected to pressure for different constraints, including the comparison with reference solution [198].

A.1.2 Composite square plate with $[45°/\text{-}45°/0°/0°/45°/\text{-}45°/90°/90°]_s$ lamination

A fully clamped square composite plate with 16 layers is considered as the following example, see Fig. A.3. The lamination of the present structures is $[45°/-45°/0°/0°/45°/-45°/90°/90°]_s$. The geometric data are $a = b = 25.4$ cm and total thickness $h = 2.11$ mm. The structure exhibits large-deflection due to a uniform transverse pressure. The material

Models	Clamped	Simply-supported
	u_z [mm]	u_z [mm]
Full NL 12×12Q9+LD1	7.57	5.62
Ref [198] - FSDT NL	7.71	5.67
Linear 12×12Q9+LD1	11.81	10.86
Ref [198] - FSDT Linear	12.19	11.21

Table A.2 Comparison of the transverse displacements for various CUF models and reference solutions [198] for the 4-layer $[0/90]_s$ composite plate subjected to transverse pressure at the fixed $\frac{P_z a^4}{E_2 h^4} = 100$ for the clamped conditions case, and at the fixed $\frac{P_z a^4}{E_2 h^4} = 25$ for the simply-supported ones.

data of this laminated plate are: $E_1 = 131$ GPa, $E_2 = E_3 = 13.03$ GPa, $G_{12} = G_{13} = 6.41$ GPa, $G_{12} = 4.72$ GPa and $\nu_{12} = \nu_{13} = 0.38$.

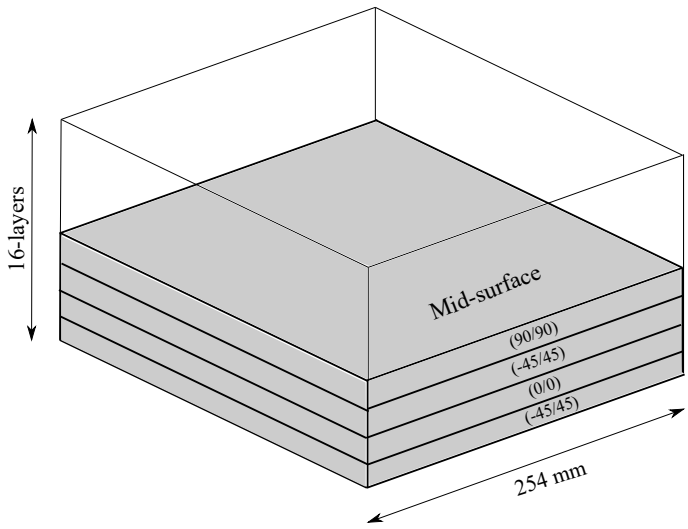

Fig. A.3 Schematic representation of the 16-layer $[45°/-45°/0°/0°/45°/-45°/90°/90°]_s$ composite plate structure.

Again, convergence analyses to determine the finite element discretization of the present composite model are performed, see Fig. A.4. In detail, Fig. A.4a provides the in-plane mesh approximation variation, in which from 16Q9 to 144Q9 FEs are used, whereas only one LD1 is adopted for each layer in the z-direction. Instead, analyses based on different through-the-thickness kinematic approximations are illustrated in Fig. A.4b. For completeness, the transverse displacement values for different CUF plate models and loads are reported in Table A.3, including the DOFs. As evident from Fig. A.4

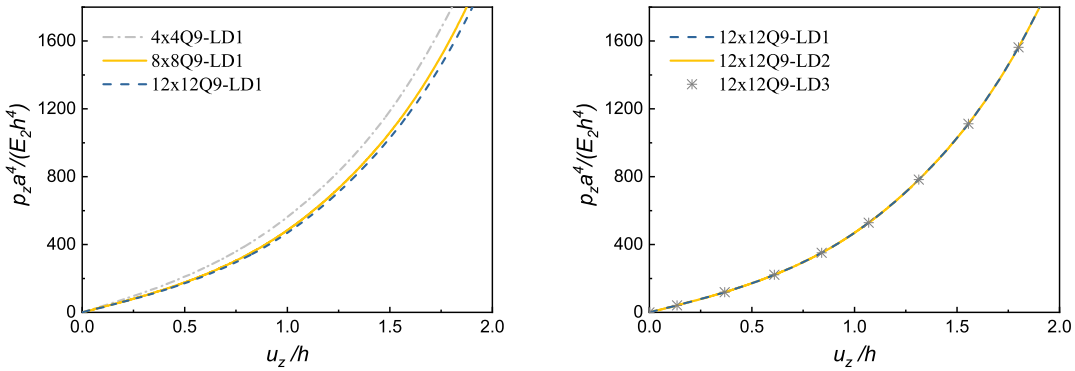

(a) (b)

Fig. A.4 Convergence analyses for the 16-layer $[45°/-45°/0°/0°/45°/-45°/90°/90°]_s$ laminated composite plate structure with clamped edge conditions subjected to transverse pressure. (a) Mesh approximation; (b) Kinematic expansion.

CUF models	DOFs	u_z/h	
		$p_z a^4/E_2 h^4 = 400$	$p_z a^4/E_2 h^4 = 1600$
4×4Q9+LD1	4131	0.81	1.71
8×8Q9+LD1	14739	0.89	1.80
12×12Q9+LD1	31875	0.90	1.82

Table A.3 Transverse displacements at the middle of the 16-layer $[45°/-45°/0°/0°/45°/-45°/90°/90°]_s$ composite plate with clamped conditions subjected to transverse pressure for various CUF plate models and load values.

and Table A.3, the convergence is achieved for the nonlinear static response when the 12×12Q9+LD1 model is employed.

Figure A.5 displays the nonlinear equilibrium path at the center of the laminated plate, including the comparison with reference solution [237].

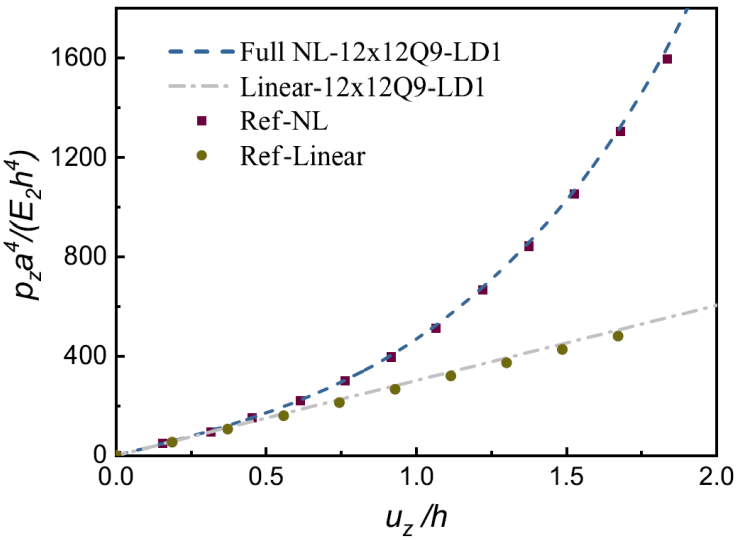

Fig. A.5 Nonlinear equilibrium curves of the 16-layer $[45°/-45°/0°/0°/45°/-45°/90°/90°]_s$ composite plate with clamped conditions subjected to transverse pressure, including the comparison with reference solution [237].

A.1.3 Cross-ply $[0°/90°]_2$ composite rectangular plate

Regarding the post-buckling evaluations, a rectangular composite plate with 4 layers $[0°/90°]_2$ is investigated as the first example. The geometrical data of the considered structure has: the length of $a = 20$ cm, the width of $b = 5$ cm, and the thickness of $h = 2$ mm. The plate is subjected to in-plane compressive line loads in the x-axis direction, N_x (force per unit width), see Fig. A.7. Simply-supported boundary conditions are adopted, in which the edges along width $x = 0, a$ satisfy $v = w = 0$ (see S1 in Fig. A.7), while edges along the length $y = 0, b$ satisfy $w = 0$ at $z = 0$ (see S2 in Fig. A.7). In addition, a further constraint is consider that satisfying $u = v = 0$ in the central point of the plate to avoid the rigid-body motion of the structure. The material properties for this composite plate are: $E_1 = 220$ GPa, $E_2 = E_3 = 5.5$ GPa, $G_{12} = G_{13} = 3.3$ GPa, $G_{12} = 2.75$ GPa and $\nu_{12} = \nu_{13} = 0.25$.

For this analysis, convergence analyses on the model approximation are shown in Fig. A.6, in which the normalized values of the displacement at the center of the plate

as a function of the normalized values of the applied compressive line load are plotted. First, 10×2Q9, 20×5Q9, and 40×10Q9 finite plate elements are considered, setting the LD1 kinematic expansion for each layer in the z-direction. Then, the expansion order along the thickness direction is varied from LD1 to LD3, whereas the in-plane mesh approximation is fixed at 20×5Q9. For completeness, the transverse displacements for different CUF plate models and loads are tabulated in Table A.4. Thus, as evident from Fig. A.6 and Table A.4, the convergence for the nonlinear response curves is obtained by adopting the 20×5Q9+LD1 plate model.

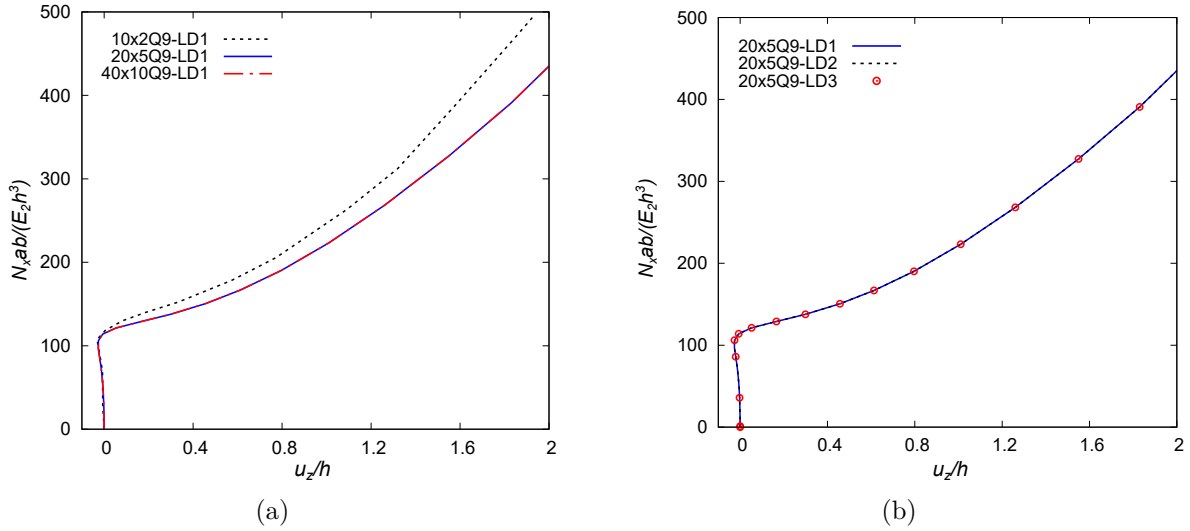

(a) (b)

Fig. A.6 Convergence analysis for the cross-ply $[0°/90°]_2$ rectangular composite plate structure with simply-supported conditions subjected to compressive line loads. (a) Mesh approximation; (b) Kinematic expansion.

CUF models	DOFs	u_z/h	
		$N_x ba/E_2 h^3 = 200$	$N_x ba/E_2 h^3 = 400$
10 × 2Q9+LD1	1575	0.731	1.618
20 × 5Q9+LD1	6765	0.859	1.865
40 × 10Q9+LD1	25515	0.859	1.865

Table A.4 Transverse displacements at the center of the cross-ply $[0°/90°]_2$ simply-supported rectangular composite plate structure subjected to compressive line loads for various CUF models and loads.

Figure A.7 depicts the nonlinear equilibrium path of the cross-ply $[0°/90°]_2$ rectangular composite plate structure achieved by using the CUF 2D Full NL model, ABQ 2D shell

model and ABQ 3D solid model. As illustrated in Fig. A.7, the equilibrium curves obtained by the CUF 2D Full NL model agree well with the ABQ 3D solid model. On the contrary, the ABQ 2D shell model predicts reliable results only in the range of small/moderate displacements, whereas the difference become more remarkable when large displacements are analyzed. For clarity, in the nonlinear analysis using the ABQ 3D solid model, a fine mesh employing C3D20R elements is employed to overcome the mesh instability problem due to the hourglassing. Figure A.8 shows the deformed configurations

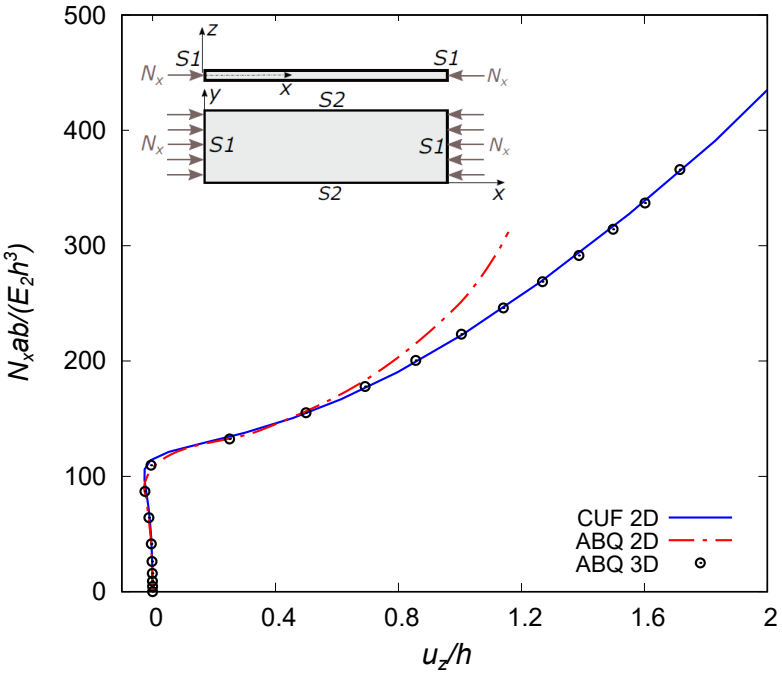

Fig. A.7 Nonlinear equilibrium path for a cross-ply $[0°/90°]_2$ rectangular composite plate structure with simply-supported conditions subjected to compressive line loads. Comparison between the CUF 2D Full NL model (20×5Q9+LD1), ABQ 2D NL model (60×15 S8R) and ABQ 3D NL model (60×15×4 C3D20R).

and the displacement contours based on the CUF 2D Full NL model (20×5Q9+LD1), ABQ 2D shell model (60×15 S8R) and ABQ 3D solid model(60×15×4 C3D20R) at the fixed load of $\frac{N_x ba}{E_2 h^3} = 300$ for the considered rectangular composite structure. It is clear from this figure that the buckled pattern and the displacement values of different regions predicted by the CUF 2D model have a good consistency with those based on the ABQ models. Finally, Table A.5 provides the displacements values at the fixed load of $\frac{N_x ba}{E_2 h^3} = 300$ and the linear buckling loads predicted by the three models for the considered rectangular composite plate structure.

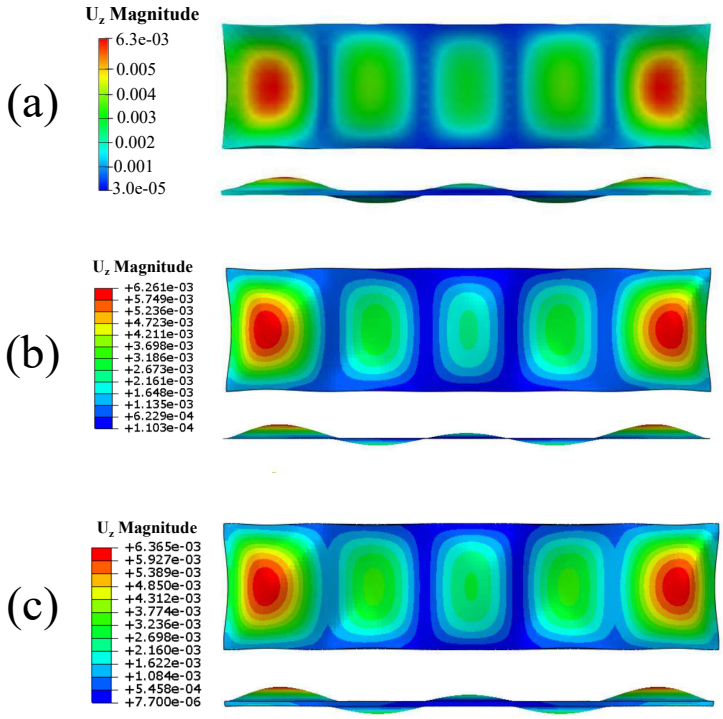

Fig. A.8 Transverse displacement contours at the fixed load of $\frac{N_x ba}{E_2 h^3} = 300$ for the cross-ply $[0°/90°]_2$ rectangular composite plate with simply-supported conditions subjected to compressive line loads based on (a) CUF 2D Full NL 20×5Q9+LD1 model, (b) ABQ 2D NL 60×15 S8R model and (c) ABQ 3D NL 60×15×4 C3D20R model.

Models	u_z [mm]	Linear Buckling Load [N/m]
CUF 2D Full NL 20×5Q9+LD1	1.422	503360
ABQ 2D NL 60×15 S8R	1.134	497658
ABQ 3D NL 60×15×4 C3D20R	1.428	498976

Table A.5 Comparison of displacements at the fixed $\frac{N_x ba}{E_2 h^3} = 300$ and the normalized linear buckling loads for a cross-ply $[0°/90°]_2$ rectangular composite plate structure with simply-supported conditions subjected to compressive line load.

A.1.4 Angle-ply $[45°/\text{-}45°]_s$ composite square plate

The next case concerns an angle-ply $[45°/-45°]_s$ composite square plate with simply-supported constraints subjected to combined loadings. The dimension of this plate are: width $a = b = 0.25$ m and the thickness is $h = 2.5$ mm. Various loading cases are considered for the composite plate, such as the combination of uniformly distributed in-plane compressive bi-axial line loads of N_x and N_y ($N_x = N_y$ in the current example), the in-plane shear load of $N_{xy} = N_x$, and the uniform transverse pressure of $P_z = 0.1N_x$, see Fig. A.9. The material properties are the following: $E_1 = 206.9$ GPa, $E_2 = E_3 = 5.2$ GPa, $G_{12} = G_{13} = 2.6$ GPa, and $\nu_{12} = \nu_{13} = 0.25$.

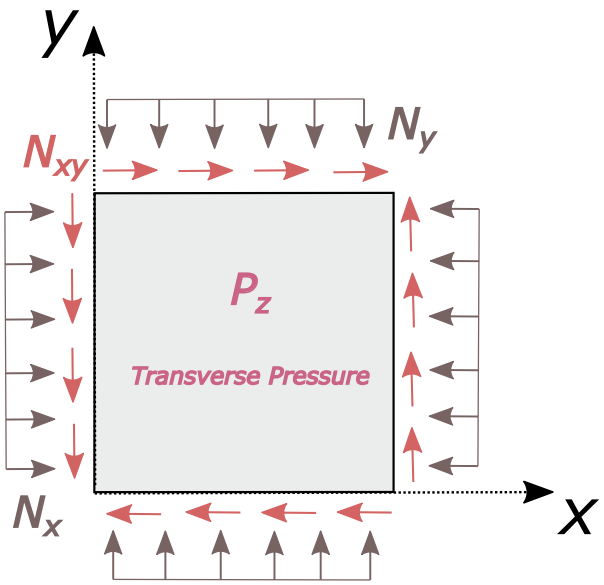

Fig. A.9 Combined loadings of the laminated plate structure: positive in-plane shear, in-plane compression, and uniform transverse pressure.

For this case study, convergence analyses are performed in order to obtain a convergent model approximation. In detail, the nonlinear equilibrium curves are provided in Fig. A.10, in which the normalized values of the displacement in the central point of the plate as a function of the loading factor (λ) values are plotted. As a consequence, the convergence is reached at least by adopting the 15×15Q9+LD1 plate model.

The nonlinear equilibrium trends for this angle-ply composite plate subjected to different combined loadings are illustrated in Fig. A.11. The horizontal lines in this figure represents the corresponding linear buckling loads predicted by the CUF method. It is noted from Fig. A.11 that for this symmetric composite structure, the buckling loads computed by the linear buckling analysis are almost the same as those based on CUF Full NL plate model, even if there exists uniform transverse pressure applied to the

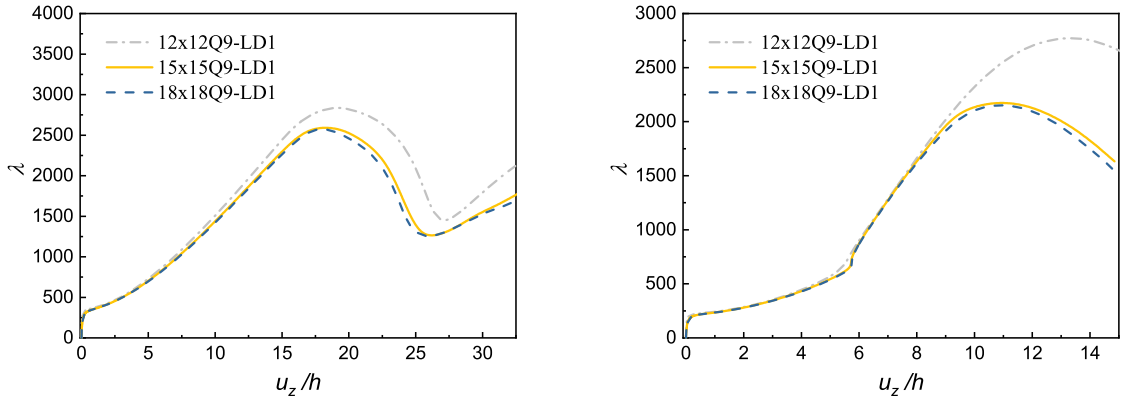

Fig. A.10 Convergence analyses for the angle-ply $[45°/-45°]_s$ composite plate structure with simply-supported conditions subjected to combined loadings. (a) Positive shear; (b) Negative shear.

plate. Thus, the linear buckling analysis can be exploited to first predict the buckling load of the symmetric composite structure. Furthermore, the linear buckling load of the angle-ply plate with positive shear is higher than other loading cases, which proves that the angle-ply plate with positive shear loading has higher rigidity and load-carrying capacity. Finally, it is observed that since the transverse pressure is relatively small compared to in-plane loads, the equilibrium curves with transverse pressure gradually approach those without transverse pressure as the load is continuously increased.

For the sake of completeness, Fig. A.12 shows the trend of transverse displacements with respect to the increasing loading after the bifurcation point. The results suggest that the direction of the applied shear loading plays a crucial role in post-buckling behaviours of angle-ply composite plates. Especially, the angle-ply plate with positive shear loading exhibits higher rigidity and load-carrying capacity than the one with negative shear loading, as observed previously.

A.1.5 Composite pinched cylindrical shell

A composite cylindrical shell under a pinching force is investigated as the next case. The vertical displacement and the rotation around the β-axis are constrained along its longitudinal edges in addition to the clamped present at $\beta = 0$. Two different stacking sequences are considered: $[90°, 0°, 90°]$ and $[45°, 0°, -45°]$. The geometrical data of the considered model are: L = 3.048 m, R_α = 1.016 m, and h =0.03 m, while the material properties are: $E_L = 2068.5\times10^4$ N/m^2, $E_T = 517.125\times10^4$ N/m^2, $G_{LT} = 795.6\times10^4$

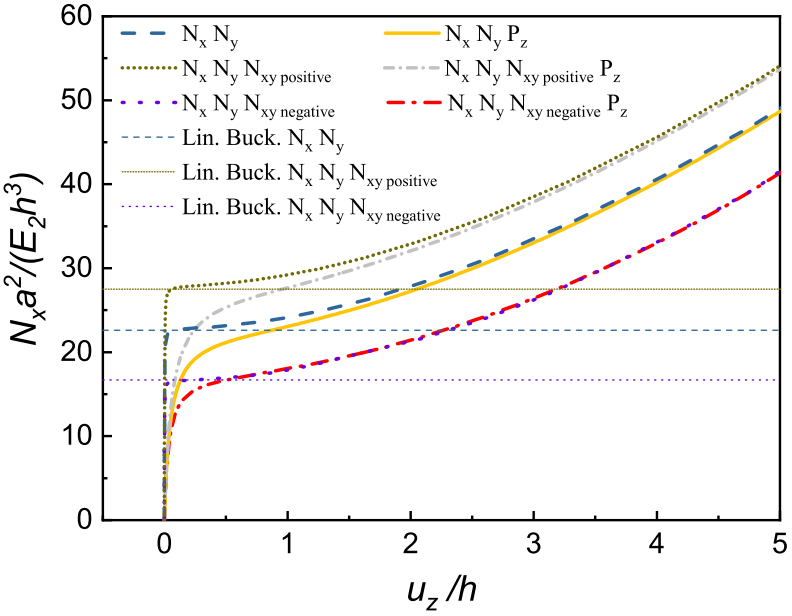

Fig. A.11 Nonlinear equilibrium curves for the angle-ply $[45°/-45°]_s$ composite plate with simply-supported conditions subjected to different combined loadings.

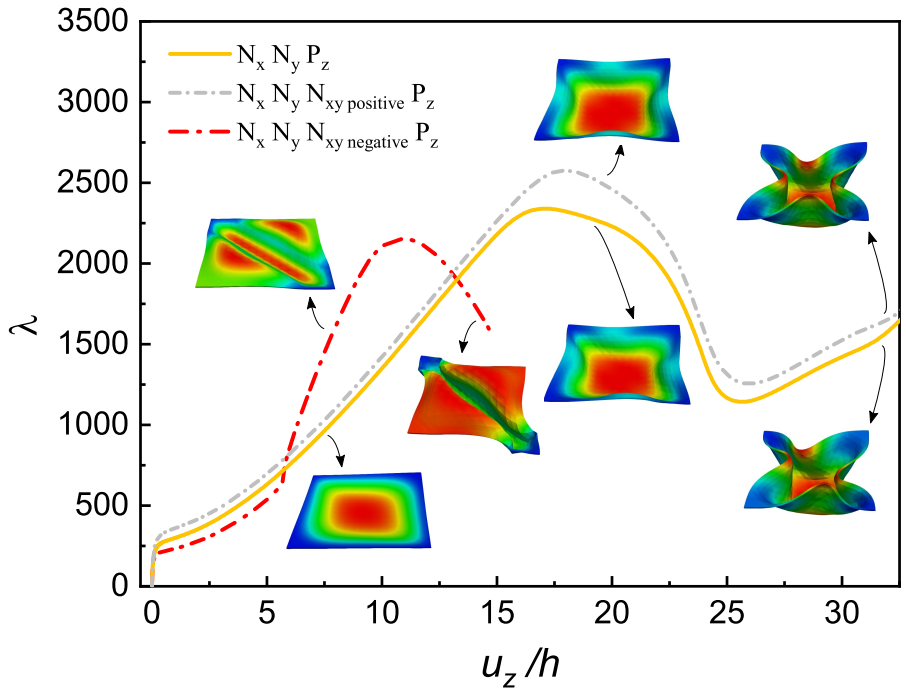

Fig. A.12 Post-buckling behaviours of the angle-ply $[45°/-45°]_s$ composite plate structure with simply-supported conditions subjected to different combined loadings.

N/m^2 and ν_{LT} =ν_{TT} = 0.3. For clarity, the subscripts L and T denote the longitudinal and transverse (fiber) direction. The nonlinear equilibrium curve of this structure was presented by Sze *et al.* [223] and Wu *et al.* [224], while stress benchmarks have not yet been provided through-the-thickness. In this work, stress solutions for the pinched composite cylindrical shell is shown as an addition to the literature.

First, convergence studies on the in-plane finite element mesh is carried out to perform accurate investigations. Figure A.13 plots the transverse displacements at the loading point for various 2D models, and from 256Q9 to 1024Q9 FEs are used for the in-plane mesh approximation, while 1LD2 is employed in each layer in the z-direction. For validation reasons, the comparison with reference and Abaqus solutions is also provided. Moreover, Table A.6 shows the transverse displacement values for different models and

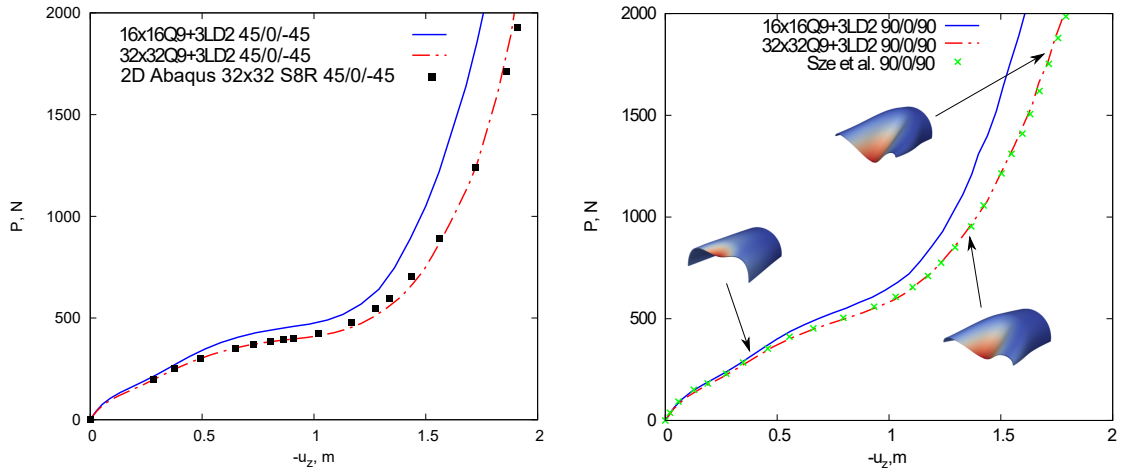

Fig. A.13 Nonlinear response curves for the composite pinched cylindrical shell at the loading point, including convergence analyses on the surface mesh approximation. Stacking sequence: (a) $[45°, 0°, -45°]$, (b) $[90°, 0°, 90°]$.

loads, including the DOFs. As a result, the 32×32Q9 mesh is a reliable approximation for the in-plane description. Then, to perform an accurate stress prediction, various LE and TE expansion functions in the thickness direction are compared. Figure A.14 illustrates the 3D stress distributions, including the circumferential normal stress $\sigma_{\alpha\alpha}$ and the transverse shear stress $\sigma_{\beta z}$ components, for different through-the-thickness kinematic approximations. The corresponding stress values are given in Table A.7 for various shell theories and loads. Clearly, the LW model kinematics should be exploited to accurately predict the stress values, using at least the 3LD3 theory. The results suggest that the ESL model is sufficient to calculate the circumferential normal stress, while it is inadequate to accurately compute the transverse shear stress component. Furthermore, about the

Model	DOFs	-u_z [m]			
		$[45°, 0°, -45°]$		$[90°, 0°, 90°]$	
		500 N	1000 N	500 N	1000 N
16x16Q9+3LD2	22869	1.086	1.481	0.684	1.273
32x32Q9+3LD2	88725	1.267	1.632	0.807	1.394
Sze *et al.* [223]	-	-	-	0.798	1.393

Table A.6 Transverse displacement values of the composite pinched cylindrical shell for two in-plane mesh approximations and loads at $\alpha = 1.596$ m, $\beta = 3.048$ m and $z = 0.015$ m.

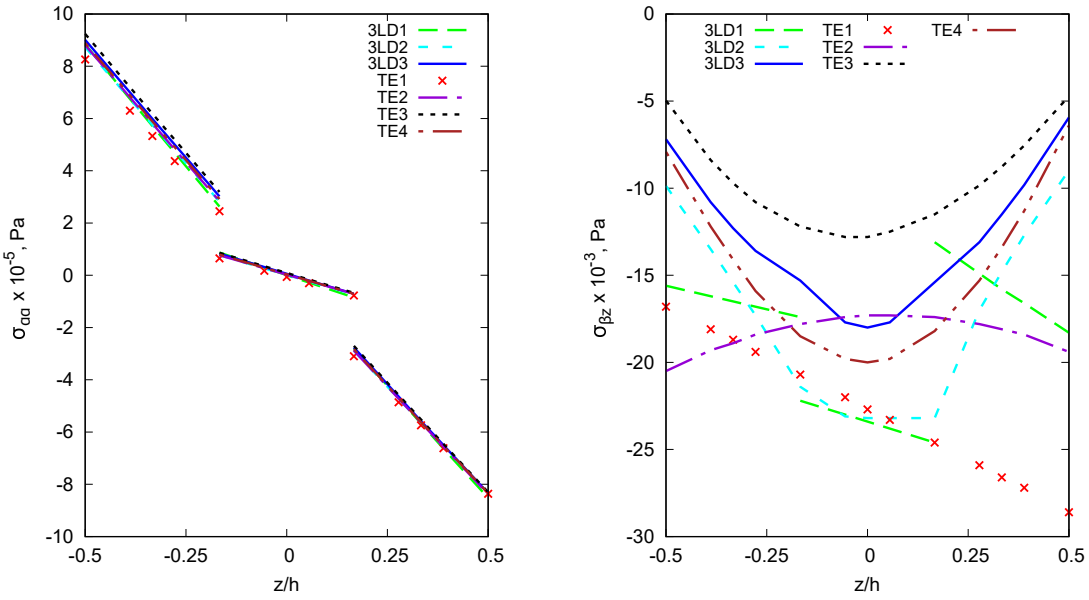

(a) $\sigma_{\alpha\alpha}$ (b) $\sigma_{\beta z}$

Fig. A.14 Convergence analyses of the composite pinched cylindrical shell under P = 1000 N for stresses evaluation at $\alpha = 1.596$ m and $\beta = 1.524$ m, including the comparison between Lagrange and Taylor expansion functions. Lamination sequence $[90°, 0°, 90°]$.

Theory	DOFs	$[90°, 0°, -90°]$			
		$\sigma_{\alpha\alpha}$ [Pa×10^5]		$\sigma_{\beta z}$ [Pa×10^3]	
		500 N	1000 N	500 N	1000 N
TE1	25350	-1.280	-8.356	-1.151	-22.658
TE2	38025	-1.291	-8.375	-1.110	-17.291
TE3	50700	-1.272	-8.298	-1.573	-12.760
TE4	63375	-1.282	-8.344	-1.657	-19.973
3LD1	50700	-1.309	-8.519	-1.622	-23.399
3LD2	88725	-1.289	-8.350	-1.600	-23.185
3LD3	126750	-1.289	-8.350	-1.776	-18.001

Table A.7 Circumferential normal stress and transverse shear stresses of the composite pinched cylindrical shell for various theories and loads at $\alpha = 1.596$ m and $\beta = 1.524$ m and $z = 0.015$ m $\sigma_{\alpha\alpha}$ and $z = 0$ m for $\sigma_{\beta z}$.

transverse shear distribution, TE3 and TE4 show a similar distribution compared to the most accurate LD3. This aspect underlines the needs to take into account the cubic terms of the thickness expansion for an accurate evaluation of the through-the-thickness stress component. Figures A.15 and A.16 show the circumferential normal and transverse shear stresses in the thickness direction for different loads and for the two laminations using both ESL and LW approaches to highlight the different capabilities. The linear interpolation (*FSDT-like*) provided by the ESL model is, clearly, not enough to catch the transverse shear stress distribution of the laminated pinched cylindrical shell, as illustrated in Figs. A.15d and A.16d.

A.2 Nonlinear transient response analysis

Several beam and plate structures with different initial configurations, loadings and boundary conditions are investigated in this section to prove the accuracy and capability of the presented nonlinear dynamic methodology. Results are compared to commercial FEM software solutions and with results found in the available literature. Dynamic analyses are performed over different time intervals using the Newmark and HHT-α methods. As is well known, the computational analysis cost is related directly to the size of the time step, which has to be adopted for accuracy and stability. For this reason, convergence analyses of the mesh approximation and time step size are performed for each case study. Note that for all the considered examples, damping is neglected and higher-order beam/plate models are adopted. Particular emphasis is related to

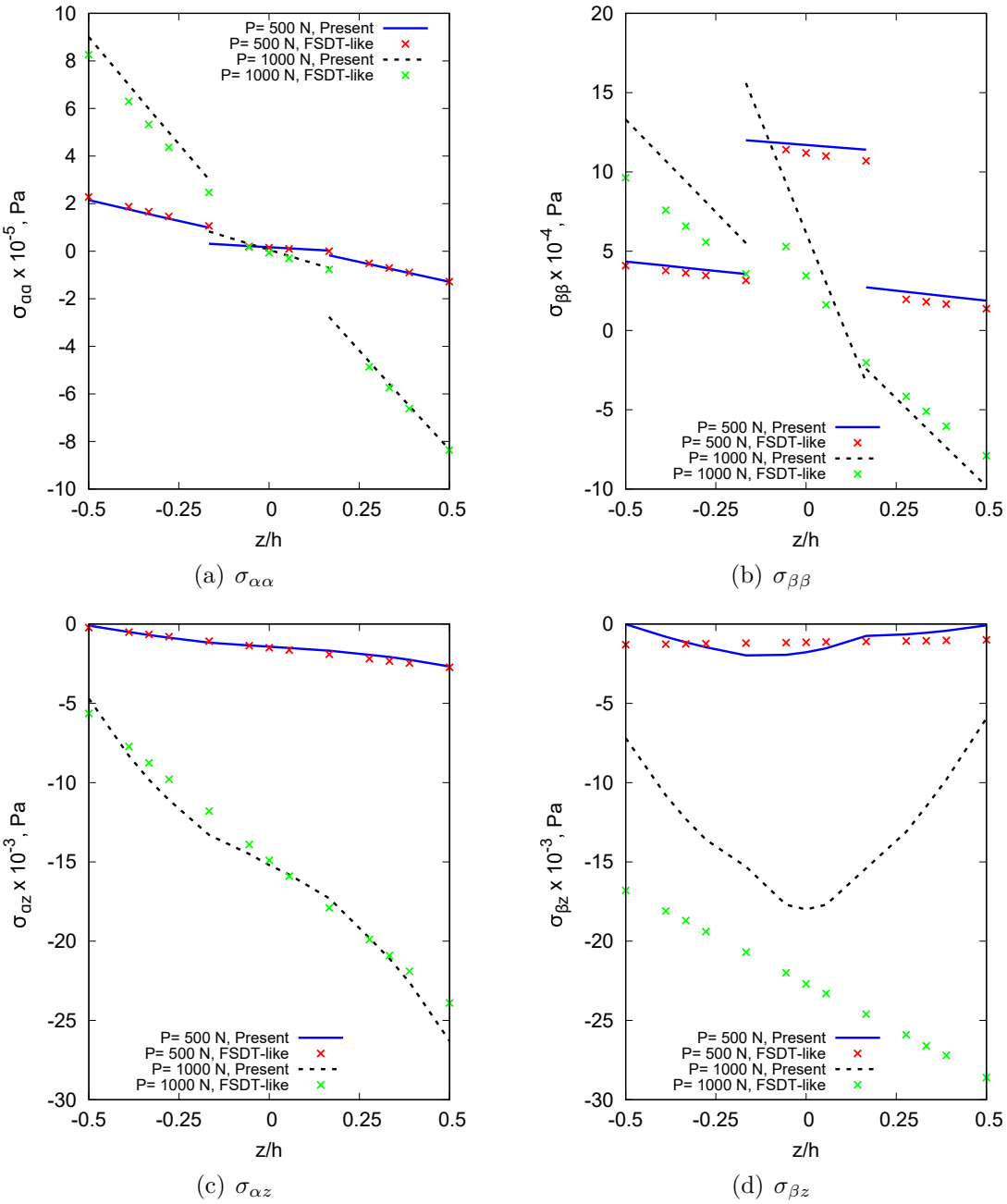

(a) $\sigma_{\alpha\alpha}$ (b) $\sigma_{\beta\beta}$

(c) $\sigma_{\alpha z}$ (d) $\sigma_{\beta z}$

Fig. A.15 Through-the-thickness stress distribution for two load values at $\alpha = 1.596$ m and $\beta = 1.524$ m. Composite pinched cylindrical shell. Lamination sequence $[90°, 0°, 90°]$.

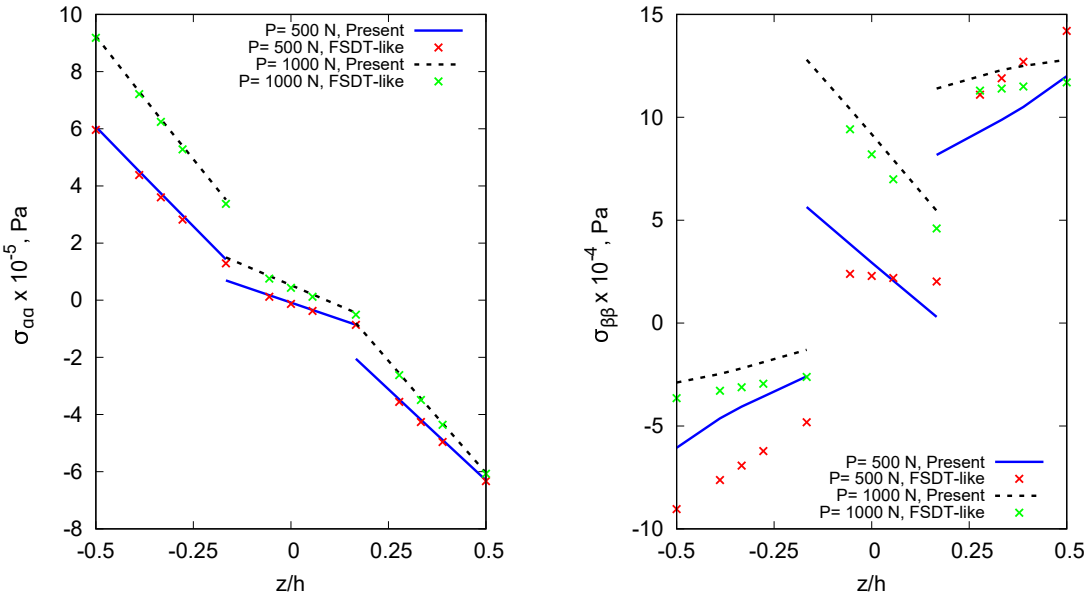

(a) $\sigma_{\alpha\alpha}$

(b) $\sigma_{\beta\beta}$

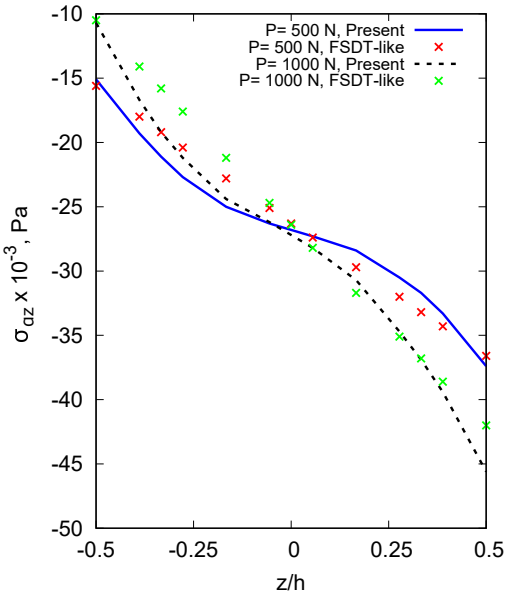

(c) $\sigma_{\alpha z}$

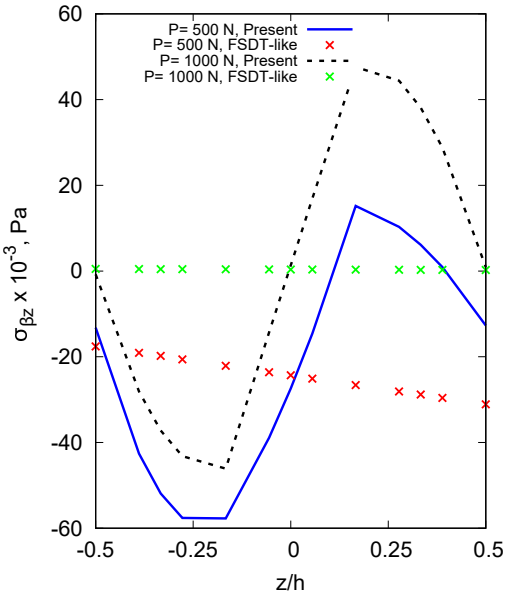

(d) $\sigma_{\beta z}$

Fig. A.16 Through-the-thickness stress distribution for two load values at $\alpha = 1.596$ m and $\beta = 1.524$ m. Composite pinched cylindrical shell. Lamination sequence $[45°, 0°, -45°]$.

the importance of choosing the appropriate kinematic theory to accurately describe the dynamic behaviours of the considered structure. Finally, some preliminary simple multibody problems are presented to show the capability of the proposed CUF-based multibody tool.

A.2.1 Cantilever square cross-section beams

Two cantilever beams subjected to transverse loadings are considered as the first nonlinear dynamic simulation. Dimensions, material data, boundary and loading conditions are illustrated in Fig. A.17. The length-to-thickness ratios (L/h) were 100 and 10 for *Case I* and *Case II*, respectively. The modellation of the structure consists of 10 B4 finite beam elements along the y-axis for both cases.

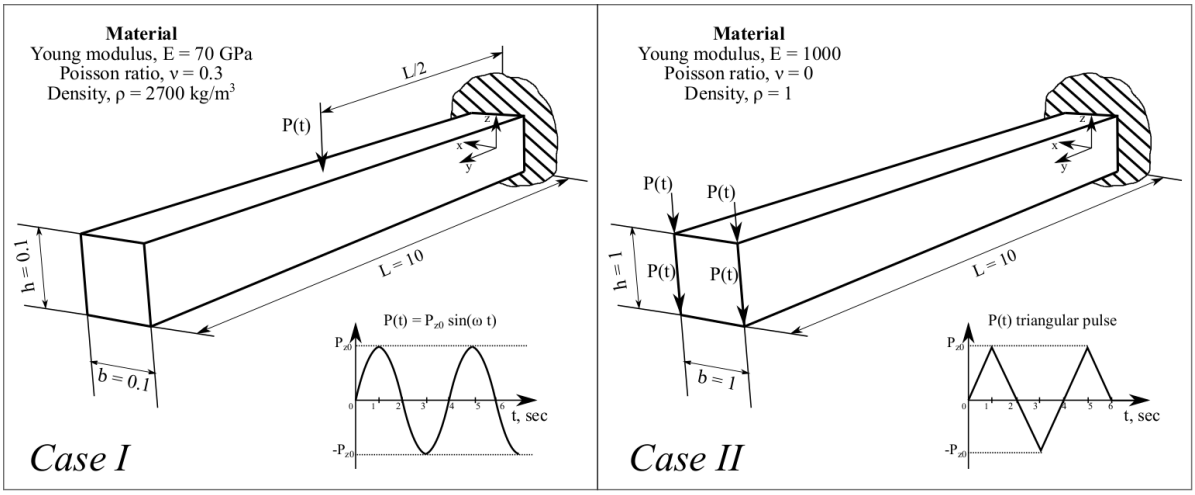

Fig. A.17 Geometry and loading conditions of cantilever beams.

The transverse displacements over the time at the mid-span of the beam computed by using the TE1 and 1L9 are plotted in Fig. A.18. Furthermore, two reference solutions evaluated with the commercial software Nastran are provided for validation purposes. The 1D and 3D Nastran reference models consist of 30 finite beam elements and 4×30×4 8-node brick elements, respectively. The time-step and the control parameter employed in the following analyses are chosen equal to Δt = 0.004 s and α = -0.05. A significant agreement between the CUF 1D solutions and the 3D reference solution is obtained. Instead, after roughly 5 seconds, we may note a moderate lag in the 1D reference curve and slight discrepancies in peak amplitude. It should be underlined that the 1D reference solution is convergent, although the corresponding number of DOF is the lowest. However, the TE1 and the 1L9 theories determine reductions of approximately 80% and 28% in the unknown number compared to the 3D model.

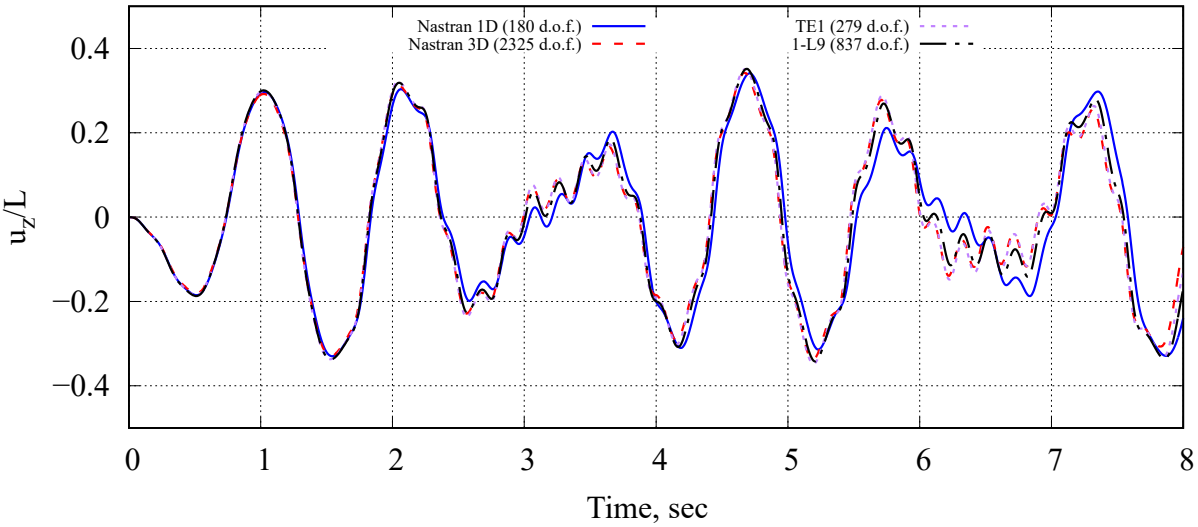

Fig. A.18 Transverse displacement over the time at point (0, L/2, 0) for different models. *Case I* considering P_{z_0}= -25000 N and $\omega = 7$ rad/s.

For *Case II*, the dynamic response at the beam's tip with $\Delta t = 0.05$ seconds and α = -0.05 is evaluated by using linear (TE1 and 1L4), quadratic (TE2 and 1L9), and cubic (TE3) kinematic theories. The related curves are depicted in Fig. A.19, including the results found in the literature [238] and a 3D FE solution. Contrary to what was observed for the previous configuration, the approaches led to different solutions due to the reduced slenderness ratio of the structure. First, consistent transient responses in the first 50 seconds are predicted using linear and quadratic models, whereas the TE3 solution differs in the peaks' number and amplitude. Then, as time increases, the dynamic responses related to low-order expansions (TE1 and 1L4) agree with the Nastran solution obtained with 2×30×2 8-node hexahedral elements, whilst the higher-order theories have provided larger deflections. Furthermore, we observed a difference in the oscillation period predicted by the TE3 expansion and those related to the other approaches in the first 100 seconds and a substantial agreement in the remaining interval. Finally, results proposed by Boujelben and Ibrahimbegovic in Ref. [238], obtained with an advanced solid FE formulation, slightly underestimated the amplitude oscillations. This discrepancy may be attributed to the coarse mesh and the different time interval used for the analysis.

A.2.2 Thin and thick beam structures

Nonlinear transient analyses of both thin and thick beam structures subjected to a step loading are investigated in this example. In particular, two different load values are considered, showing the importance of performing nonlinear dynamic analyses to obtain

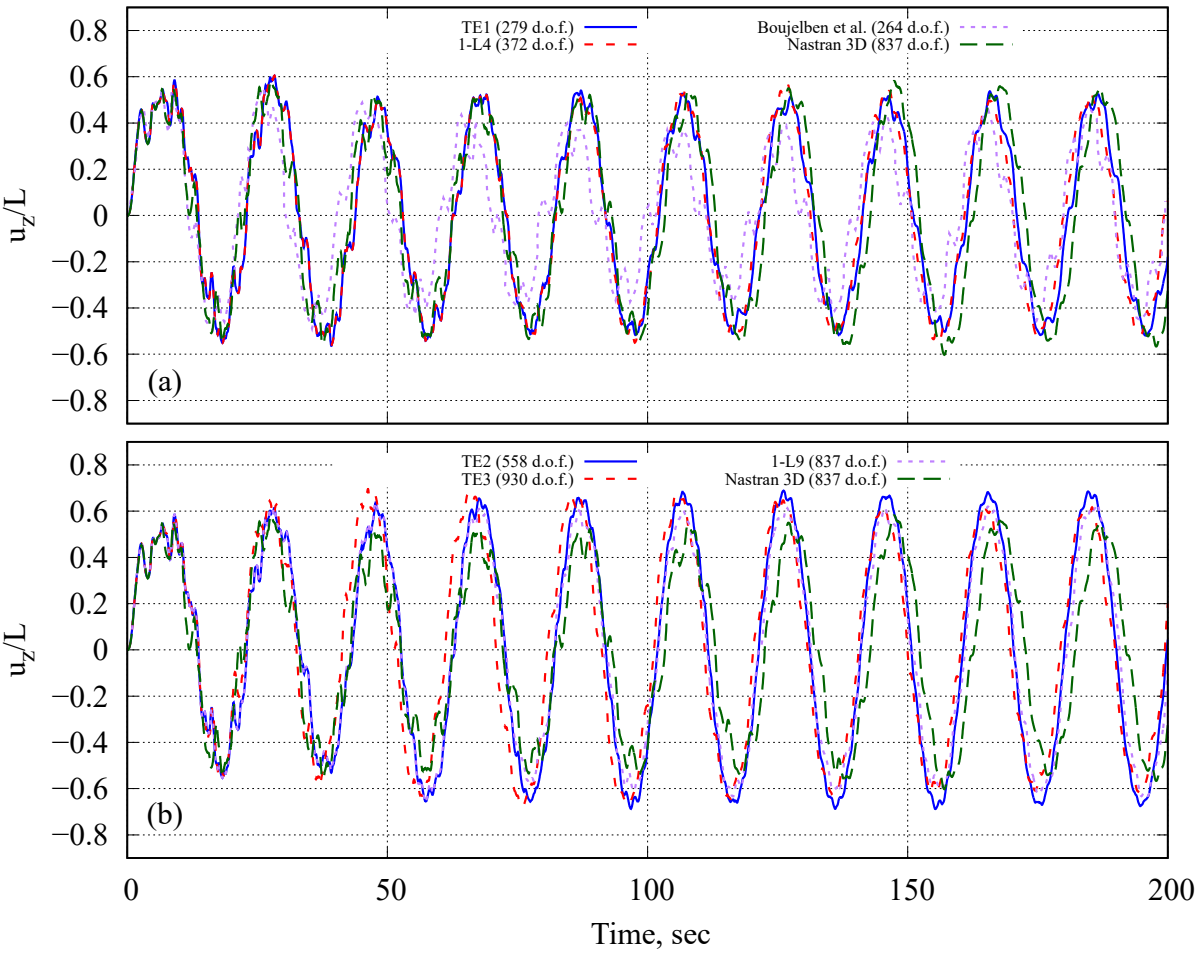

Fig. A.19 Transverse displacement as a function of the time at point (0, L, 0) for different FE models. *Case II* of Fig. A.17 with $P_{z_0} = 2$ N.

accurate investigations. In detail, step loads of F = -70000000 N for the thick beam and F = -300000/-700000 N for the thin structure are applied to achieve maximum deflections at the tip, considering the linear dynamic response of approximately 35% and 80%, respectively. Dimensions of considered square cross-section beams are $a = 0.001$ m and the length-to-height ratio L/a is equal to 1 m (thin) and 0.1 m (thick).

Figure A.20 plots equilibrium curves of beam structures. To perform accurate

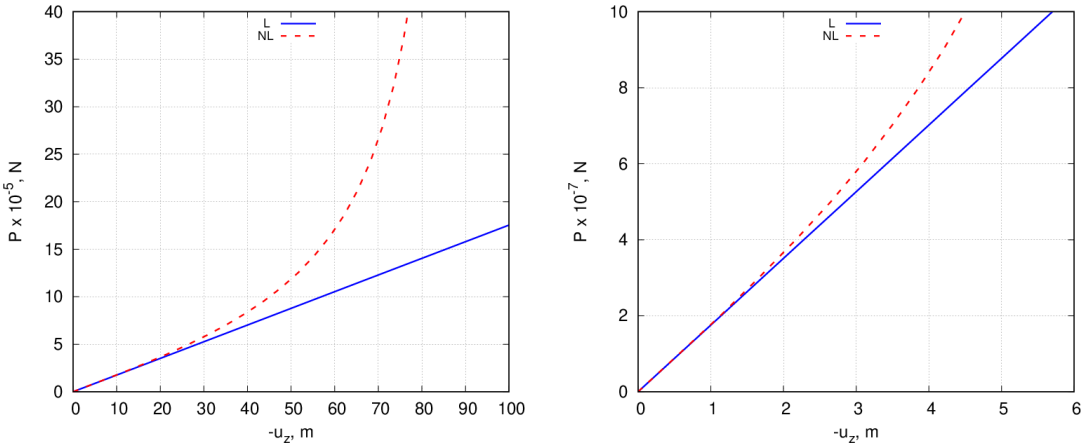

(a) Thin (b) Thick

Fig. A.20 Static equilibrium curve of the thin and thick structures subjected a transverse load.

nonlinear dynamic responses, both convergence studies on the opportune time step in the Newmark algorithm and mesh discretization along the y-direction are carried out. Regarding the time step, Fig. A.21 provides the convergences for the thin beam structure. As a consequence, 400 steps ($\Delta t = 0.1$ sec) are enough to obtain an accurate dynamic response considering a step load of F = -300000 N, whereas 4000 steps ($\Delta t = 0.01$ sec) are necessary if the applied step load is F = -700000 N. Similarly, for the thick beam case, the convergence analysis suggest that at least 400 steps allow obtaining the accurate nonlinear dynamic response. For brevity, these convergence analyses are not reported here. Figures A.22 and A.23 prove that discretizing using 10 B4 finite elements in the y-axis and 1L9 on the cross-section allows reaching convergent models.

Finally, the linear and nonlinear dynamic responses at the tip of the beam structures are illustrated in Figs. A.24 and A.25 for the thin and thick beams, respectively. These graphs show significant differences between linear and nonlinear responses. In particular, considering very large deformations (Figs. A.24b and A.25), the nonlinear approach exhibit evident reductions in the amplitude and phase shift in the response with respect to the linear approach.

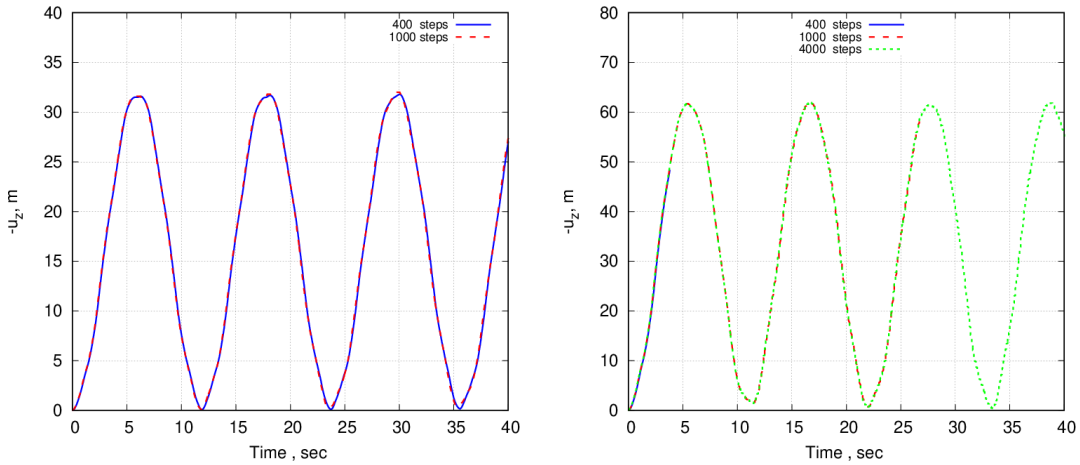

(a) F = -300000 N (b) F = -700000 N

Fig. A.21 Convergence analyses on the time step value. Thin beam.

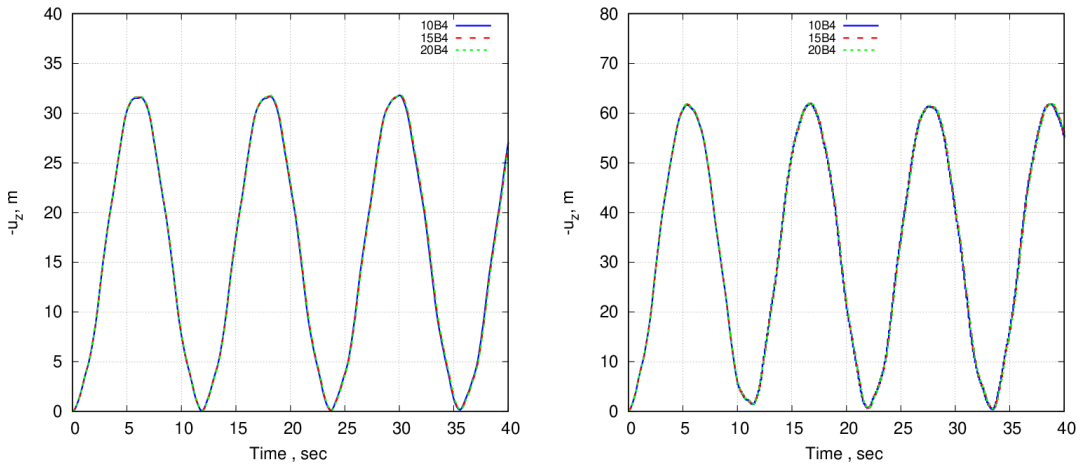

(a) F = -300000 N (b) F = -700000 N

Fig. A.22 Convergence analyses on the finite element approximations. Thin beam.

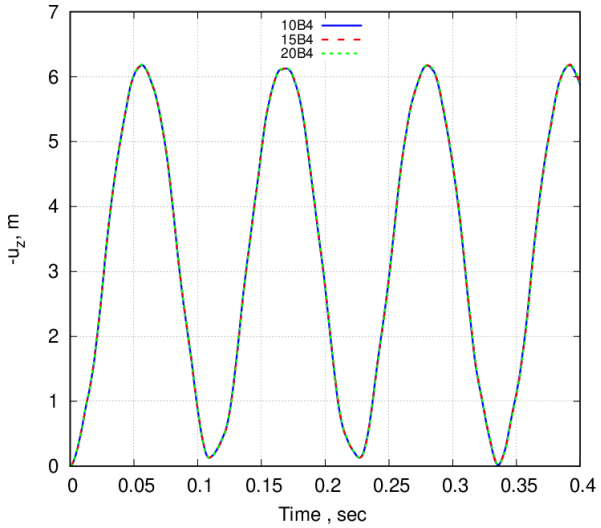

Fig. A.23 Convergence analyses on the finite element approximations. Thick beam. F = -70000000 N.

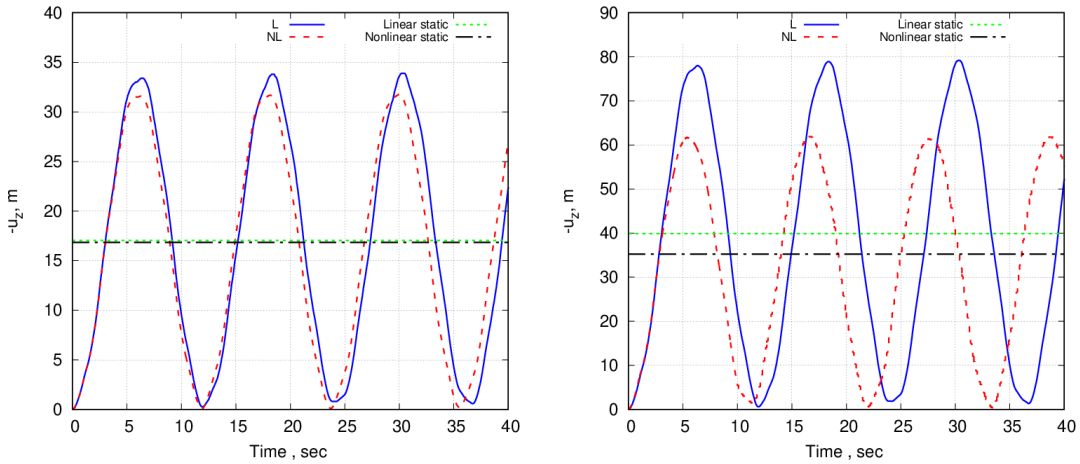

(a) F = -300000 N (b) F = -700000 N

Fig. A.24 Comparison between the linear and nonlinear dynamic analysis. Thin structure.

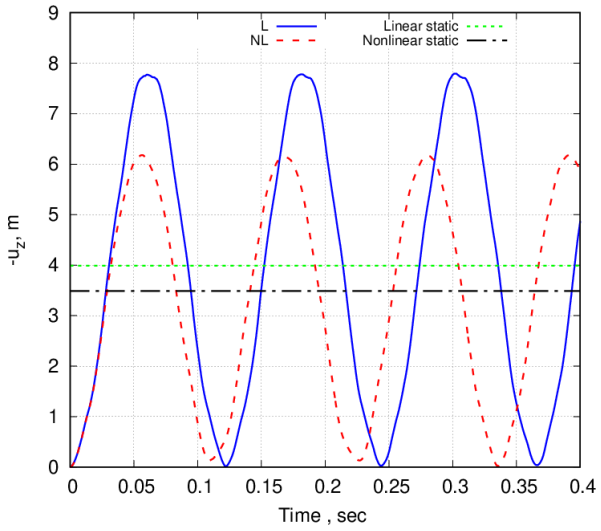

Fig. A.25 Comparison between the linear and nonlinear dynamic analysis. Thick structure. F = -70000000 N.

A.2.3 Cantilever thin-walled rectangular beam

The next case concerns a cantilever thin-walled rectangular beam structure subjected to a step loading ($P_{z0} = 50$ kN) distributed on the top surface, see Fig. A.26. Results are obtained by using both the TE2 and 10L9 kinematic theories. In addition, the beam is modelled using 15 B4 along the span for all analyses. Figure A.27 shows the linear and nonlinear dynamic responses calculated with the two kinematic models at the tip of the beam structure.

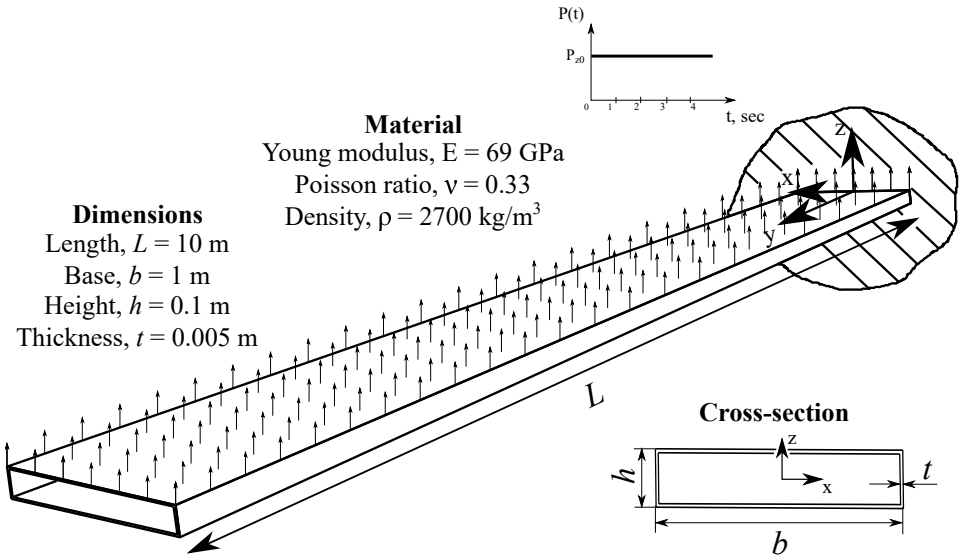

Fig. A.26 Geometry and material data of the cantilever thin-walled beam structure.

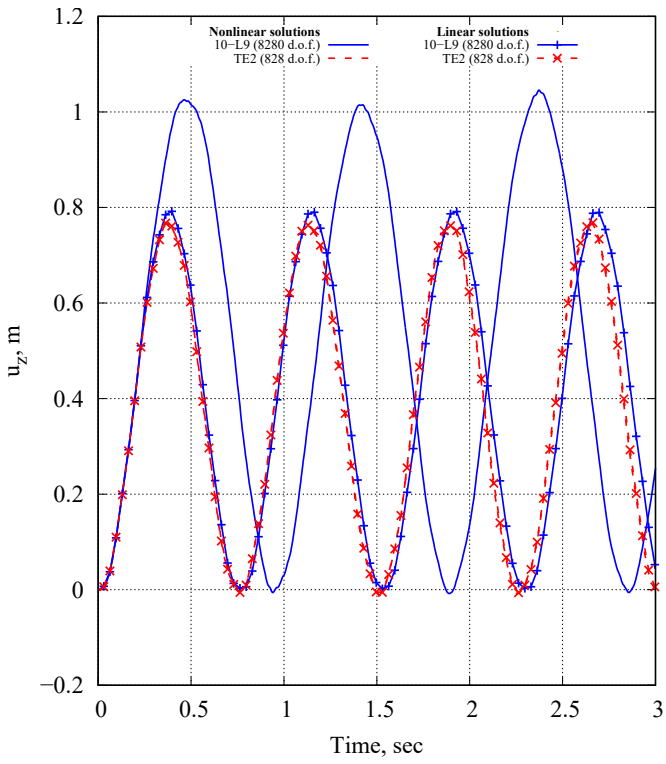

Fig. A.27 Linear and nonlinear dynamic analyses of the thin-walled structure at (0, L, $h/2$) using Δt = 0.0034, α = -0.05.

It can be noted that the 10L9 nonlinear solution significantly differs from the other results in both oscillation amplitude and period. These discrepancies were due to local instabilities occurring at the clamped root that determined a reduction of the structural stiffness. Such a softening effect can be described if the kinematic model enables cross-sectional deformations to be derived accurately. Figure A.28 depicts the linear and nonlinear equilibrium trends at different locations along the span of the beam structure. According to the 10L9 model, the top panel near the fixed end suddenly buckles when the load is approximately 15 kN. On the other hand, the nonlinear solution obtained with TE2 model strongly agreed with the linear predictions; indeed, no stiffness variation has been revealed in the analyzed load range. Figure A.29 displays the deformed configurations

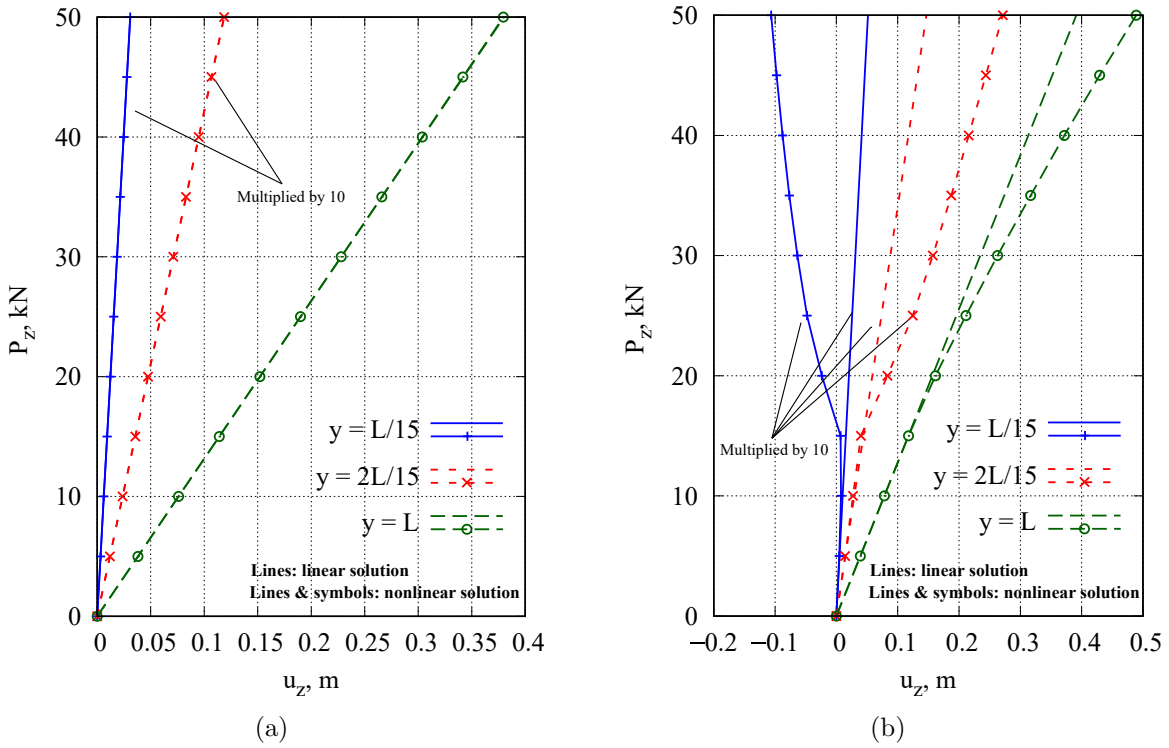

Fig. A.28 Linear and nonlinear equilibrium trends evaluated in three locations at the thin-walled beam span $(0, y, h/2)$. Comparison between (a) TE2 and (b) 10L9 models.

and the axial stress distributions at $t = 0.34$ sec and $L = 1.34$ m employing both the nonlinear and linear approaches. The nonlinear solution exhibits that the bottom edge significantly deforms, and the top surface is subjected to a compressive-tensile stress state, contrary to what predicted by the linear result.

Eventually, the same structure subjected to sinusoidal loading is investigated. In particular, a time-dependent sinusoidal load with amplitude P_{z_0} = -10000 N and angular

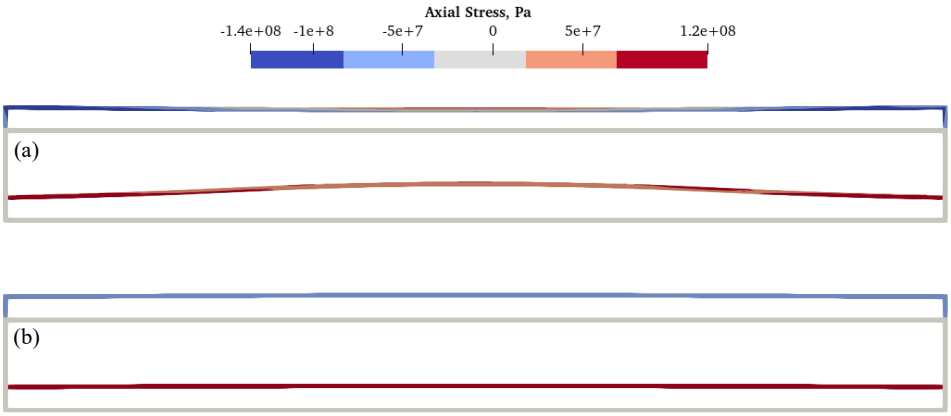

Fig. A.29 The distribution of the axial stress at $t = 0.34$ sec and $L = 1.34$ m. (a) Nonlinear and (b) linear solutions distributions using the 10L9 model.

frequency $\omega = 7$ rad/s or 30 rad/s is considered. In the first investigation, the load is applied at point 1, as shown in Fig. A.30 at $y = L/4$ and then at $y = L$. Figure A.31

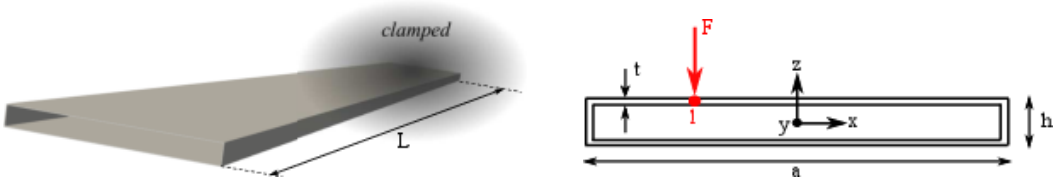

(a) 3D model (b) Cross-section

Fig. A.30 Thin-walled rectangular beam model subjected to sinusoidal loadings.

provides the transverse displacements versus time at the loading point of the structure under sinusoidal loadings at $y = L/4$, considering $\omega = 30$ rad/s. The same case with the load applied at $y = L$ is reported in Fig. A.32. For completeness, the time response adopting an angular frequency $\omega = 7$ rad/s (near the first natural frequency of the initial configuration) and the load applied at $y = L$ is given in Fig. A.33. Finally, Fig. A.34 depicts deformed configurations of the thin-walled rectangular structure at $t = 2.5$ sec.

A.2.4 Isotropic plate

The thin isotropic plate analyzed here has the following dimensions: a = b = 250 mm and h = 5 mm, while the material properties are set as $E = 70$ GPa, $\nu = 0.33$ and $\rho = 2780$ kg/m^2. The structure is subjected to a uniform step loading of relatively high intensity of 1 N/mm^2 over the whole surface at any instant of time. 100 steps are used for determining the dynamic response.

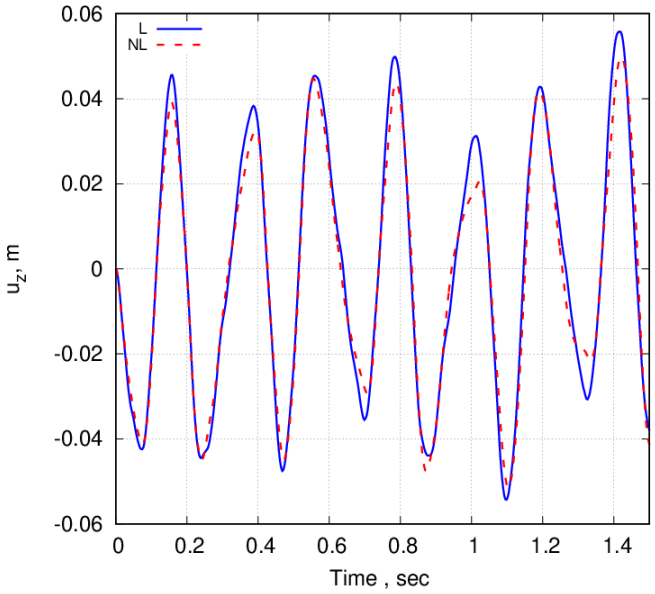

Fig. A.31 Transverse displacements versus time at the load point of the thin-walled rectangular structure subjected to sinusoidal loadings at $y = L/4$. P_{z_0} = -10000 and ω = 30 rad/s.

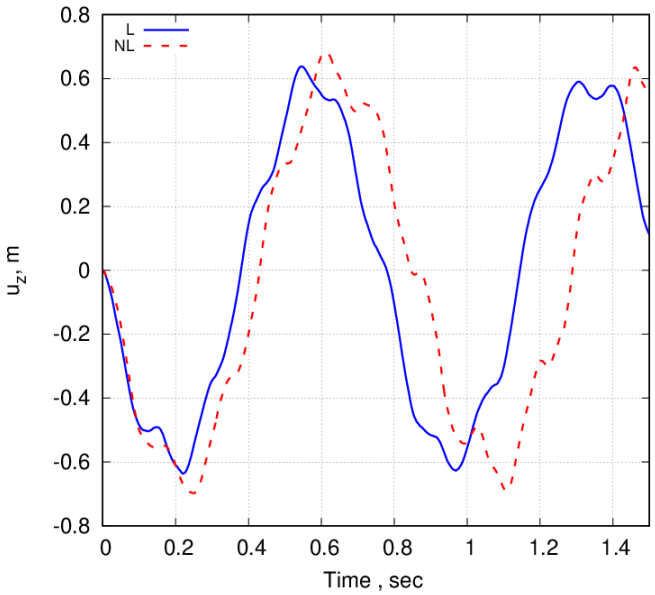

Fig. A.32 Transverse displacements versus time at the load point of the thin-walled rectangular structure subjected to sinusoidal loadings at $y = L$. P_{z_0} = -10000 and ω = 30 rad/s.

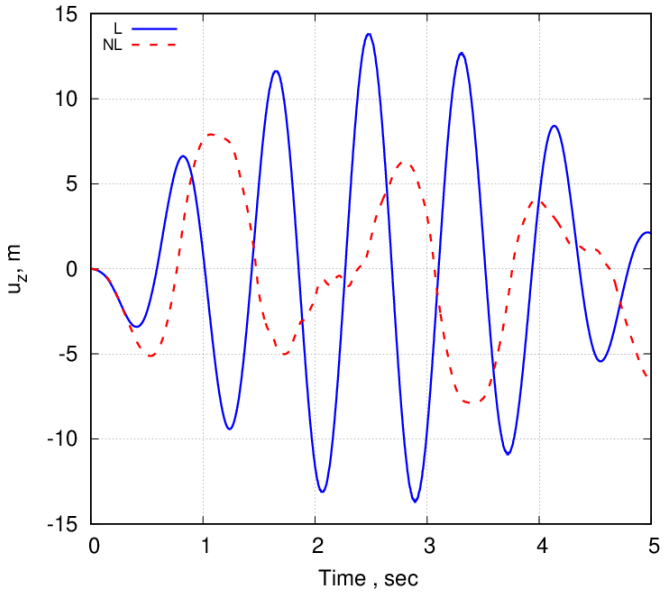

Fig. A.33 Transverse displacements versus time at the load point of the thin-walled rectangular structure subjected to sinusoidal loadings at $y = L$. P_{z_0} = -10000 and $\omega = 7$ rad/s.

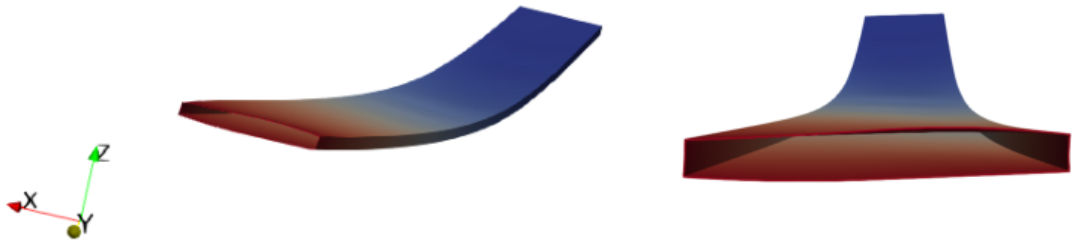

Fig. A.34 Deformed configurations of the thin-walled rectangular structure subjected to sinusoidal loadings at $t = 2.5$ sec.

The response of the isotropic plate to the high-loading is shown in Fig. A.35 for clamped-clamped boundary conditions and in Fig. A.36 for simply-supported ones, respectively. Convergence studies on the in-plane finite element mesh approximations and along the z-direction and the comparison with the Abaqus solution is also depicted in these figures. Figure A.37 illustrates the stress distribution over the time, including

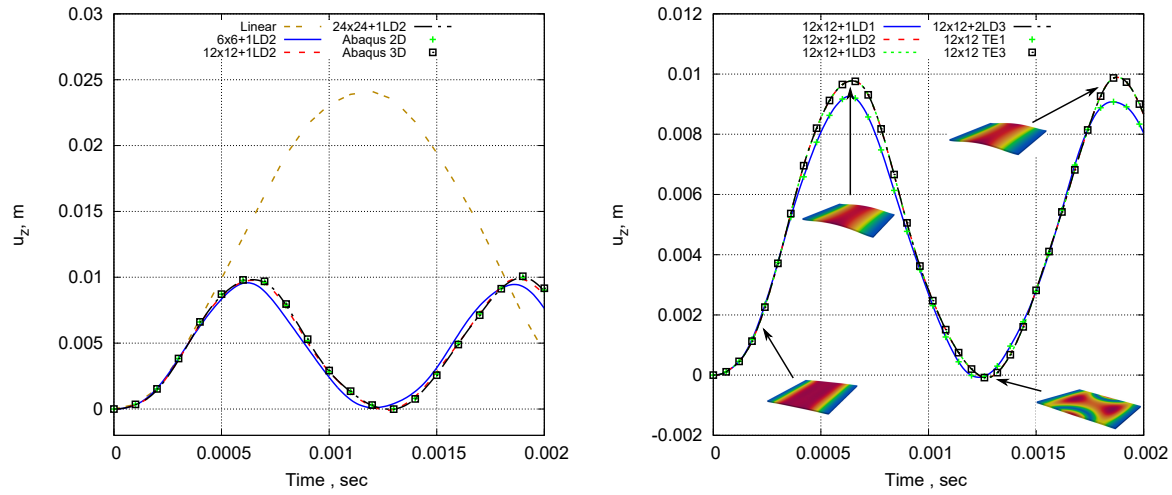

(a) Mesh approximation

(b) Kinematic expansion

Fig. A.35 Dynamic response of the clamped-clamped isotropic plate. a/h = 50.

a comparison between different plate theories and Abaqus solutions. The axial stress distributions in the thickness direction at a quarter of the plate (x = a/4, y = b/4) are plotted in Fig. A.38. It can be noted that results obtained using the proposed nonlinear methodology and Abaqus solutions agree very closely for deflection and stressses. Furthermore, it can also be noted that linear predictions overestimate the response with respect to the correct nonlinear solution at this load level.

A.2.5 Cantilever rectangular beam with different initial deformations

In the following example, the nonlinear transient responses of beam structures with different initial configurations are evaluated in order to show the effect of nonlinearities in small- to very large-deformation dynamic analyses.

The first analysis case deals with an isotropic cantilever beam with a compact rectangular cross-section. The geometry and different initial configurations considered are depicted in Fig. A.39, where L = 1 m, a = 0.01 m and h = 0.014 m. The material

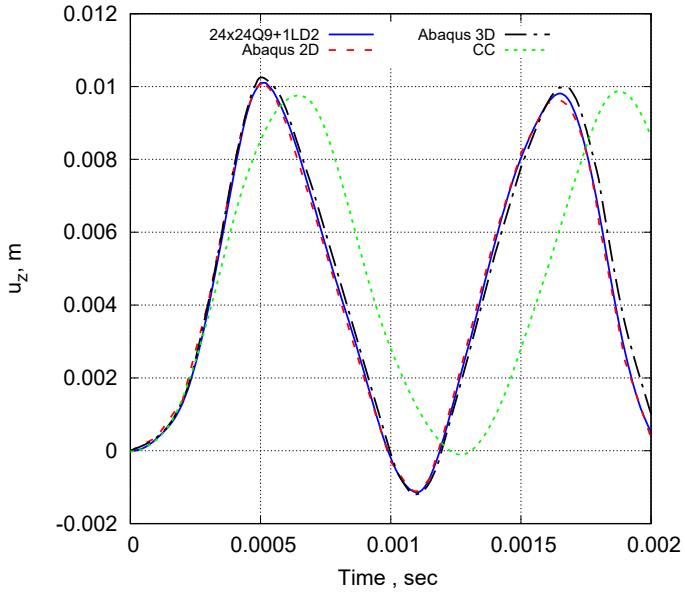

Fig. A.36 Dynamic response of the simply-supported isotropic plate. a/h = 50.

data are $E = 70$ GPa, $\nu = 0.3$ and $\rho = 2700$ kg/m^3. The convergent structural model is discretized through 10 B4 finite elements along the y-axis and 1L9 on the cross-section.

Figure A.40 displays the linear and nonlinear static equilibrium curves of the rectangular cross-section beam using different kinematic theories and nonlinear measures. The displacement is evaluated at point P. For the sake of clarity, only the most significant nonlinear models were reported in the graph. For completeness, the solution computed through the commercial code Abaqus is also provided for comparison and validation reasons. In essence, the Abaqus 1D beam model (20 B32) and Abaqus 3D solid model (54×54×2 C3D20R) are adopted. The classical nonlinear von Kármán strain models are employed and, clearly, they lead to inaccurate results for moderate-large deformations. In addition, the results show as some nonlinear models, for example, Model 13 and Model 21, provide the same solutions as the LE Full, whereas Model 2 and Model 11 lead to different results.

In this section, we perform nonlinear dynamic analyses to study the dynamical behaviour of structures considering several initial configurations by using the proposed nonlinear methodology. In detail, different configurations, from 10% to 90% of deflection, of the rectangular beam structure were analyzed to investigate the dynamic response. In more detail, the nonlinear dynamic analyses are carried out by adopting the HHT-α integration scheme with α = -0.1 and a time step of Δt = 0.01 sec.

The time (t) response of the system for different initial deflections is plotted in Fig. A.41. It is noted that by reaching the deflection percentage of 80%, the structure has lost

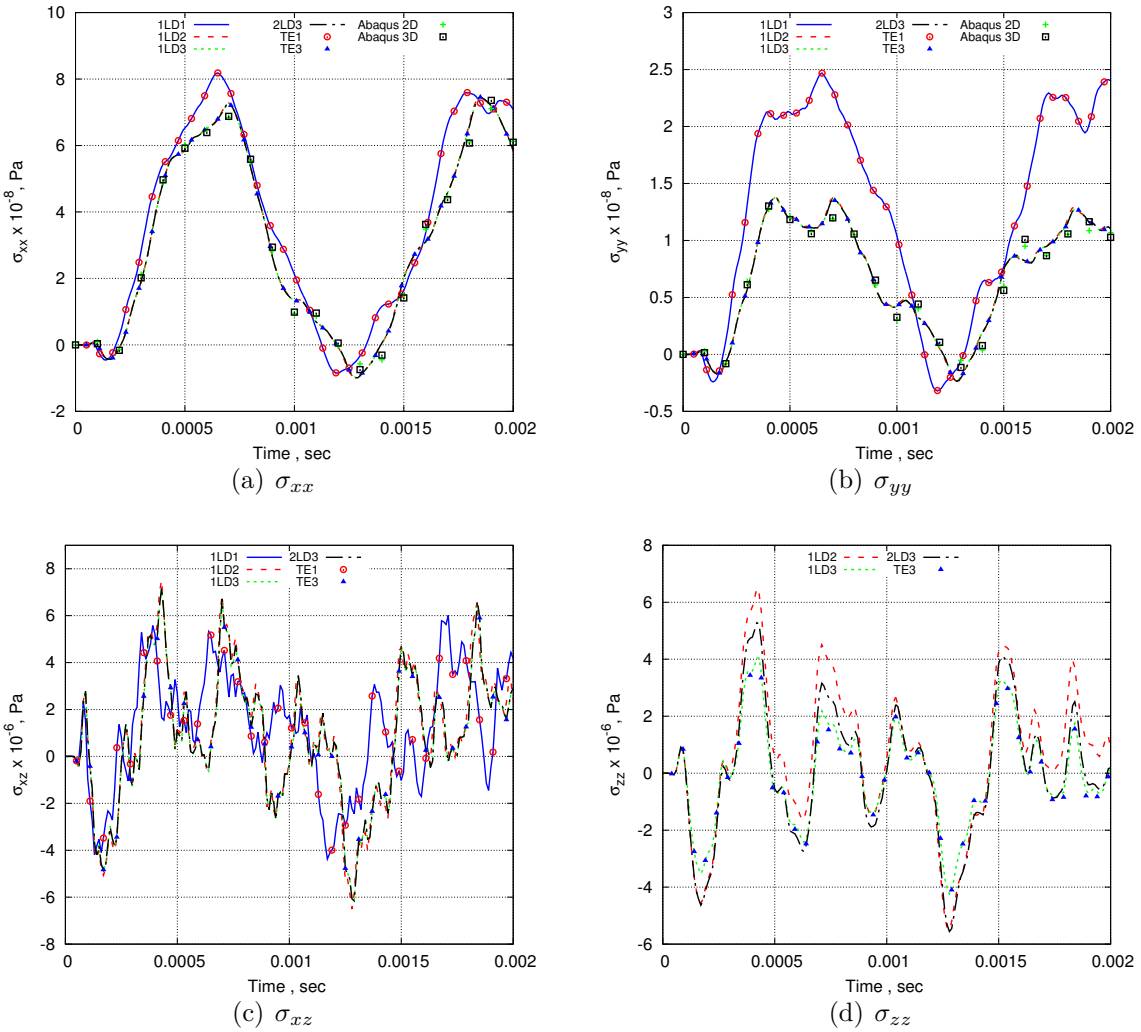

(a) σ_{xx} (b) σ_{yy}

(c) σ_{xz} (d) σ_{zz}

Fig. A.37 Nonlinear stress distribution versus time. Clamped-clamped isotropic plate. a/h = 50.

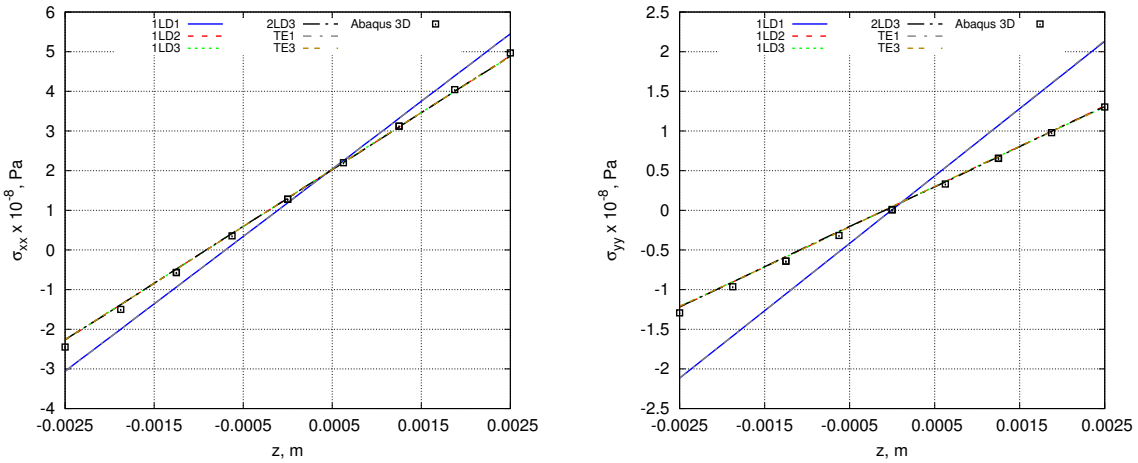

(a) σ_{xx} (b) σ_{yy}

Fig. A.38 Through-the-thickness nonlinear stress distribution at $t = 4{\times}10^{-4}$ sec for the clamped-clamped isotropic plate. a/h = 50.

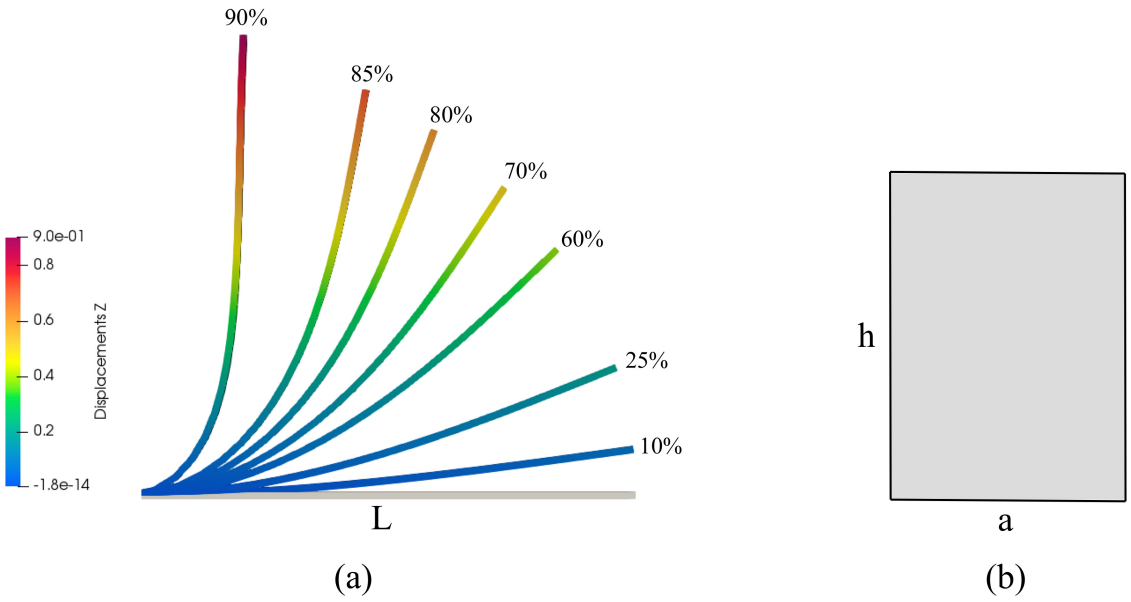

Fig. A.39 (a) Different initial conditions; (b) Rectangular cross-section of the beam structure.

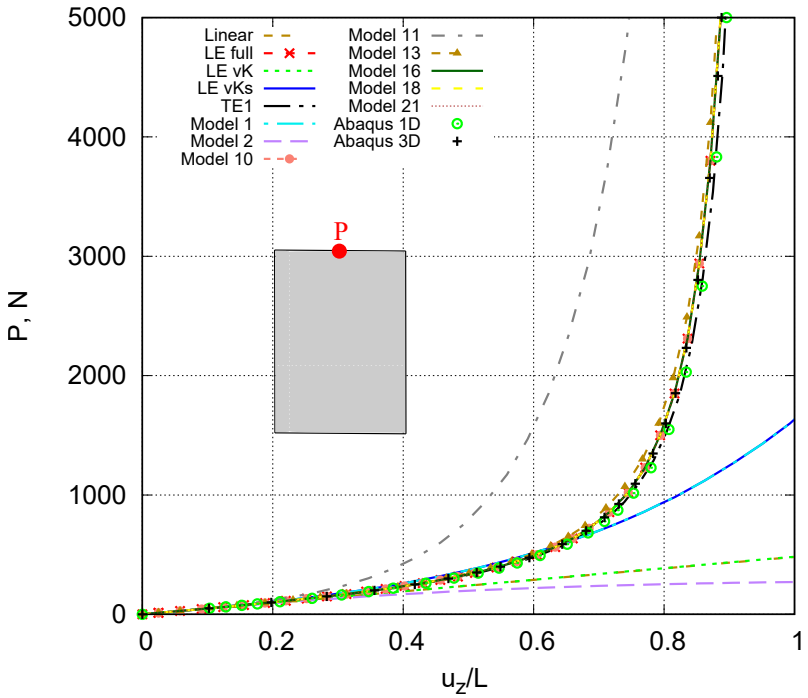

Fig. A.40 Equilibrium curves considering different kinematic theories and nonlinear strain models. Rectangular cross-section beam.

its stable periodic motion. As illustrated in Fig. A.41g, the system starts to exhibit a nonlinear chaotic response at $t = 1.27$ sec. Finally, the chaotic aspect can be also observed through the Poincaré maps, see Fig. A.42. One can notice the random structure of the Poincaré section. For the sake of completeness and validation reasons, a comparison between the present study and the Abaqus 3D solution is reported for a particular initial deflection (82%), see Fig. A.43, in which it is also possible to observe this non-periodic motion. In detail, the chaotic phenomenon starts from $t = 1.18$ sec.

Figure A.44 shows the transverse displacement time responses and phase space portraits at 90% of deflection for the rectangular cross-section beam by comparing the solution obtained adopting the Lagrange and Taylor kinematic theory. Results suggest that a TE1 is able to describe the establishment of chaotic motion for a compact rectangular cross-section beam structure.

The effect of different geometrically nonlinear strain measures on the dynamic nonlinear response of the cantilever rectangular cross-section beam is provided in the following figure, see Fig. A.45. In detail, the dynamic response, considering the configuration with 80% of deflection, obtained using the vK, vKs, Model 2, Model 13, Model 20 and LE full models are compared. It is evident that the LE full model is necessary to perform

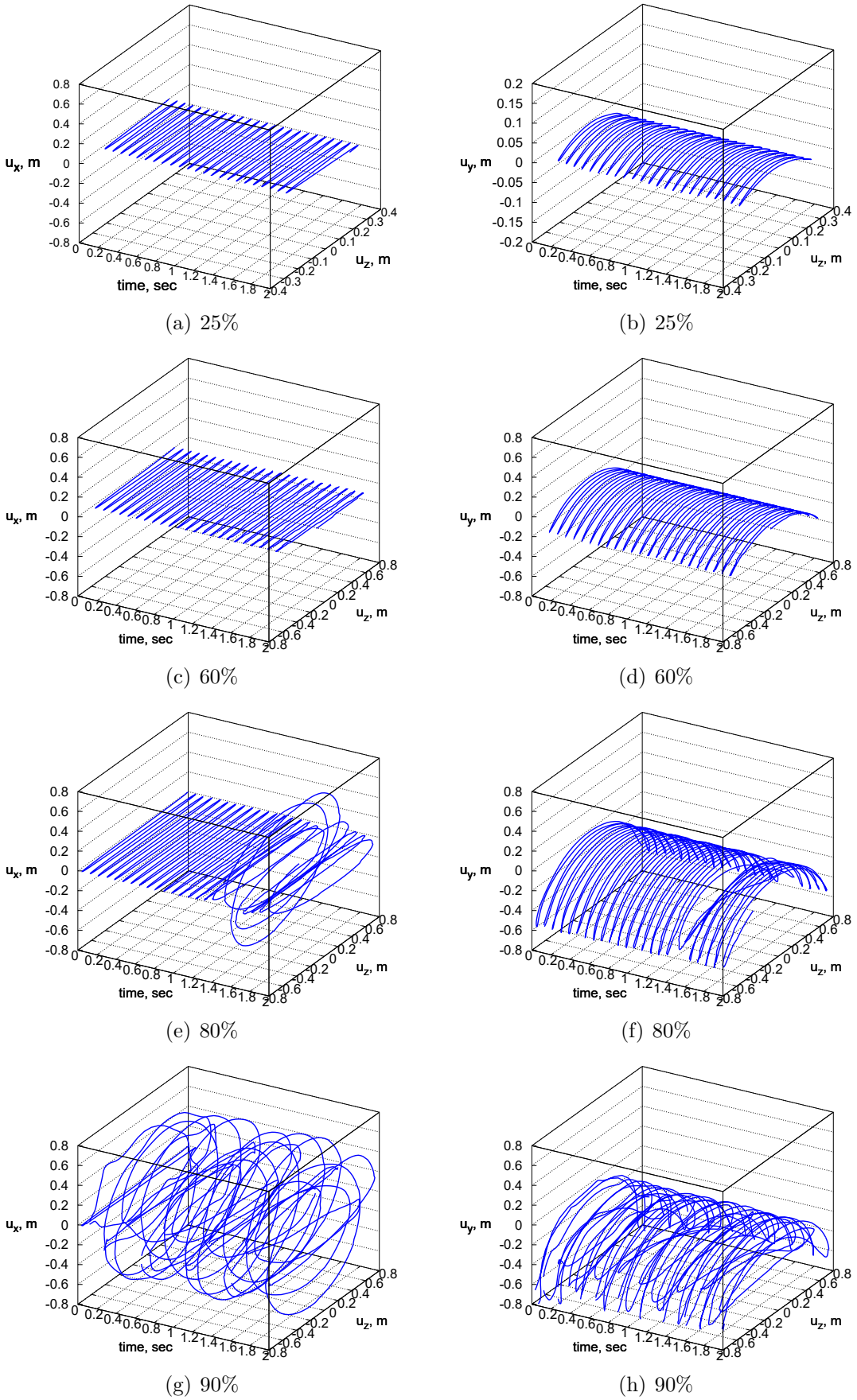

(a) 25% (b) 25%

(c) 60% (d) 60%

(e) 80% (f) 80%

(g) 90% (h) 90%

Fig. A.41 3D plots for different deflections. LE full model. Rectangular cross-section beam structure.

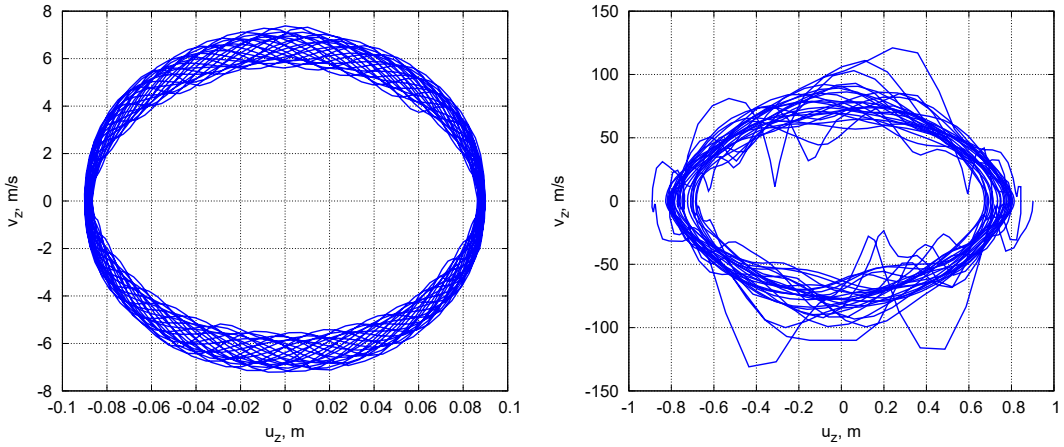

(a) 10% (b) 90%

Fig. A.42 Poincarè sections. Rectangular cross-section beam.

reliable investigations and to accurately describe real behaviours of the structure for medium-large amplitudes, in which it is essential to consider all nonlinear effects.

This important change of motion is related to the phenomena of mode change that occurs when large initial amplitudes are considered. Therefore, it is crucial to also investigate the natural frequencies and mode shapes of the structure for the different case studies. These effects are provided here through the MAC values. In particular, the MAC is employed to highlight the differences between the modes for different initial configurations of the structure. The most significant MAC graphical representations are displayed in Fig. A.46. Different configurations of the structure are considered in comparison with the case of 0% of initial deflection. The figures compare the first 30 modes for increasing deflection of the initial configuration. As shown by these graphical representations, natural modes for the case with a low deflection in the initial configuration (Fig. A.46a) are identical to those related to the 0% deflection case; i.e., all the MAC values in the diagonal are equal to 1. On the other hand, in Fig. A.46c, the state is entirely nonlinear; in fact, there are several interactions between the modes.

A.3 Multibody analysis

Dynamic analysis of multibody systems has become a subject of many investigations. The current interest in the subject has been motivated by requests for analysis and study of large-scale systems consisting of interconnected rigid and flexible bodies, each of which can undergo large translations and angular rotations. The demand for accurate

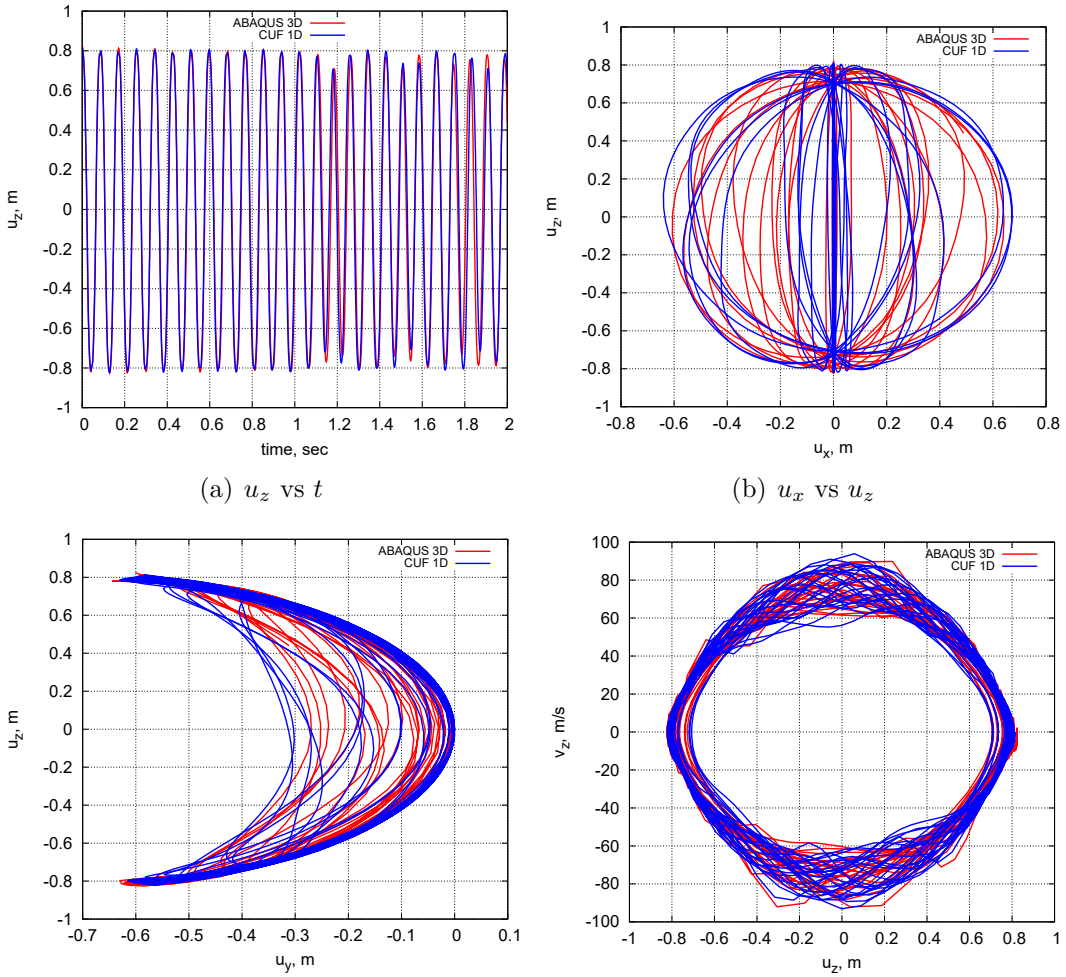

(a) u_z vs t

(b) u_x vs u_z

(c) u_y vs u_z

(d) u_z vs v_z

Fig. A.43 Comparison between the present study and ABAQUS 3D solution. Initial condition at 82% deflection. Rectangular cross-section beam.

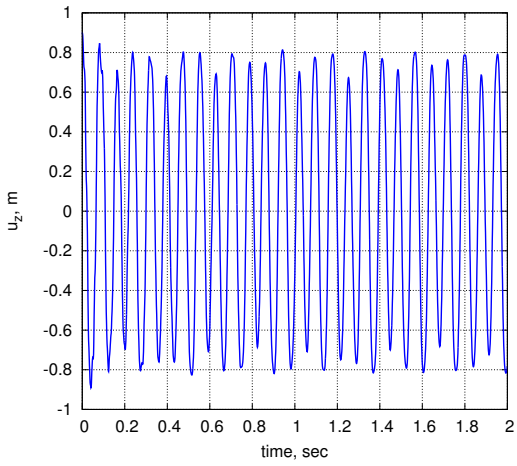

(a) u_z vs t, LE full

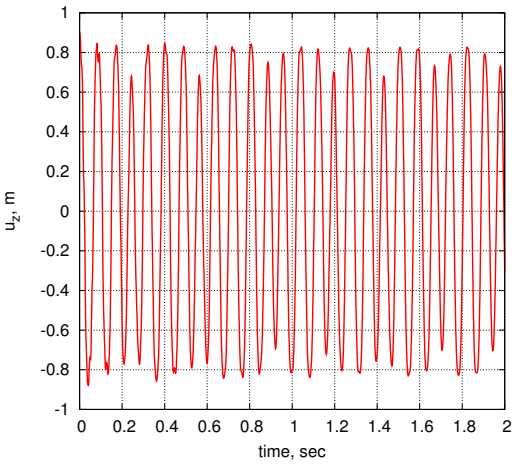

(b) u_z vs t, TE1

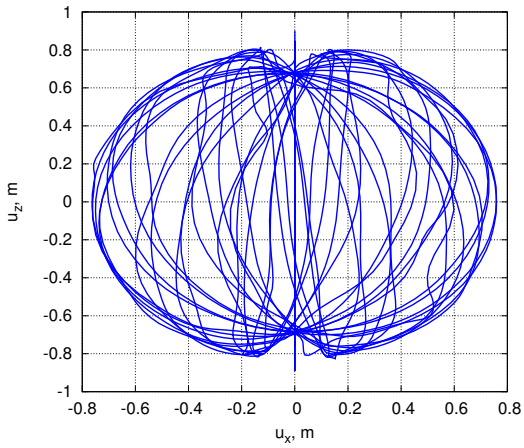

(c) u_x vs u_z, LE full

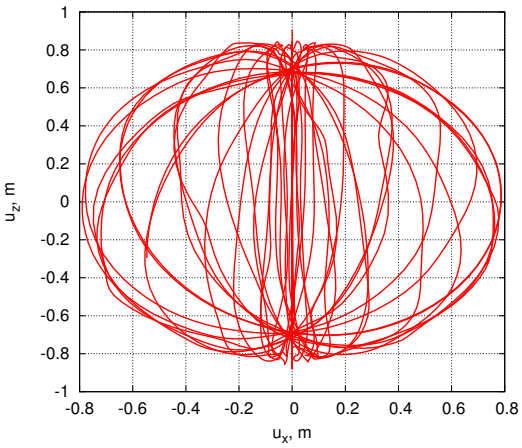

(d) u_x vs u_z, TE1

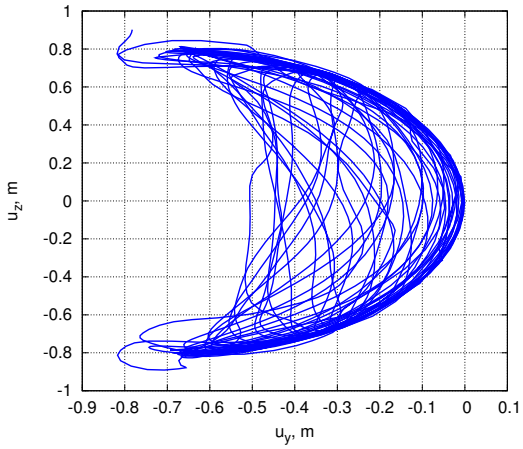

(e) u_y vs u_z, LE full

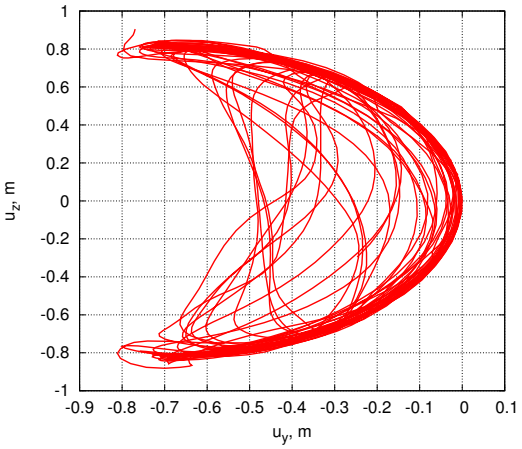

(f) u_y vs u_z, TE1

Fig. A.44 90% LE full vs TE1. Rectangular cross-section beam structure.

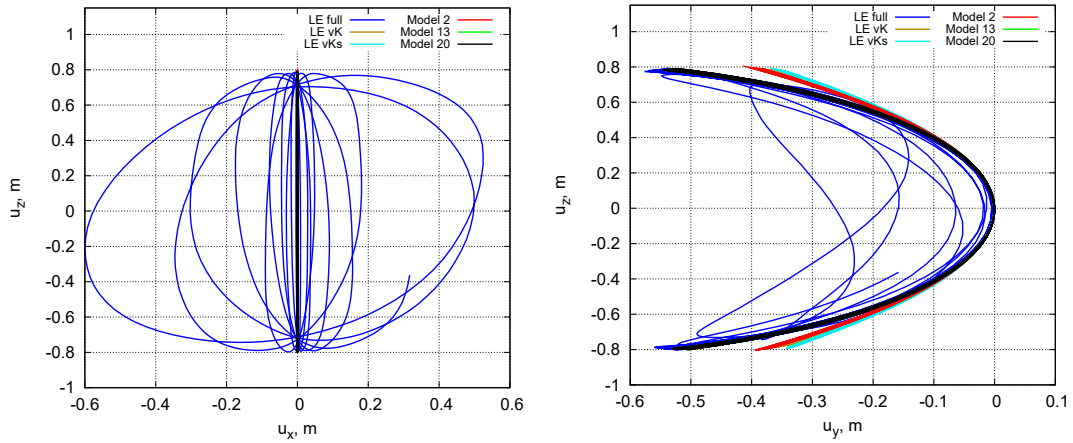

(a) u_x vs u_z (b) u_y vs u_z

Fig. A.45 Comparison between different geometrically nonlinear strain models. Initial condition at 80% deflection. Rectangular cross-section beam.

mathematical models incorporating significant effects necessitated consideration of the flexibility of the system components. The research area on multibody dynamics of greatest interest is the incorporation of flexibility effects into the governing dynamics equations. This interest is stimulated by the numerous applications with large systems, in particular, space and vehicle systems. Interest is also stimulated by unresolved questions about optimal modelling and approximation procedures.

In this context, the ultimate goal of this research activity is to lay the foundations for the creation of a tool capable of performing multibody analyses with both modelling and accuracy advantages. In detail, the presented approach is based on the use of Lagrange multipliers (LM) for joint modelling, which is a central aspect in the development of appropriate computational methodology for multibody dynamics and employs the HHT-α algorithm to find the solution of nonlinear systems algebraic equations.

A.3.1 Lagrange multipliers

The Lagrange multiplier method gives the stationary conditions of a constrained function. The computation of the stationary conditions of a functional with n variables and k constraints is reduced to a stationary points problem of an unconstrained functional of $n + k$ variables. The use of the Lagrange multipliers [239–241] to the proposed CUF-based multibody method is presented in this section.

The Lagrange multipliers method is generally employed in FEM when multiple-points constraints have to be imposed. In detail, Lagrange multipliers were used for the imposi-

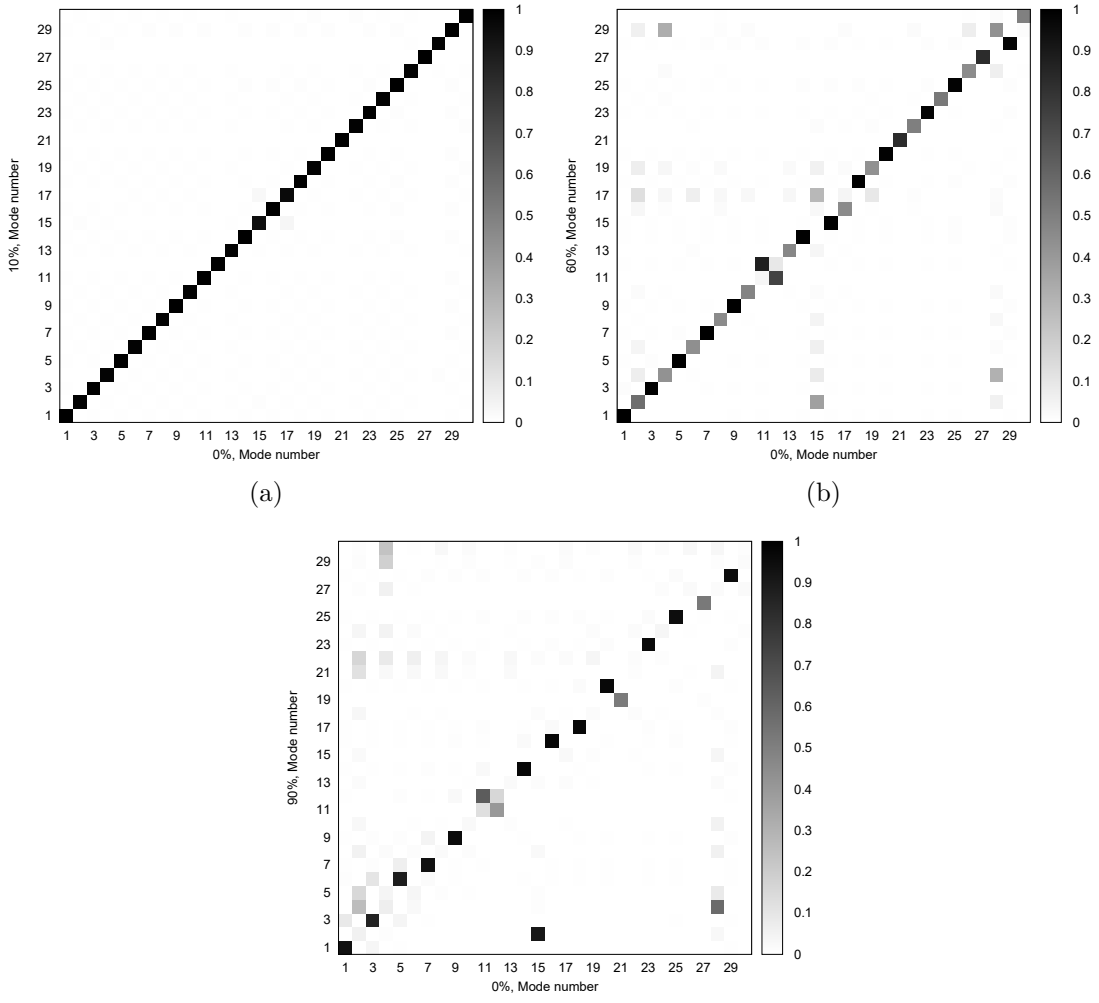

(a) (b)

(c)

Fig. A.46 MAC values between the modes of different initial configurations for the rectangular cross-section beam structure.

tions of localized constraints and displacements on high-order beam models. Nevertheless, the most important characteristics of this multipliers method is the imposition of generic relations between the displacements of two (or more) arbitrary points. In the CUF framework, we have:

$$\boldsymbol{u}^1(x_k, y_k, z_k) - \boldsymbol{u}^2(x_k, y_k, z_k) = 0 \tag{A.1}$$

in which $\boldsymbol{u}^1(x_k, y_k, z_k)$ represents the displacement of a point on the interface cross-section of the first body, while $\boldsymbol{u}^2(x_k, y_k, z_k)$ denotes the displacement of the same point on the interface cross-section of the second body. So, we have:

$$\Pi = \lambda^{\mathrm{T}} \left(\boldsymbol{u}^1(x_k, y_k, z_k) - \boldsymbol{u}^2(x_k, y_k, z_k) \right) \tag{A.2}$$

in which k indicates a point on the interface cross-section and λ stands for the vector containing the Lagrange multipliers. Eq. A.2 may be expressed in terms of CUF:

$$\Pi = \lambda^{\mathrm{T}} \boldsymbol{B} \boldsymbol{q} \tag{A.3}$$

in which the FN of the matrix $\boldsymbol{B}$ is:

$$\boldsymbol{B}^{\tau i} = \left(F_\tau^1(x_k, z_k) N_i^1(y_k) - F_\tau^2(x_k, z_k) N_i^2(y_k) \right) \boldsymbol{I} \tag{A.4}$$

in which $\boldsymbol{I}$ represent the identity matrix.

The solution of the problem is derived by finding $\boldsymbol{q}$ and λ from the following linear system in matrix form:

$$\begin{bmatrix} \boldsymbol{K} & \boldsymbol{B}^{\mathrm{T}} \\ \boldsymbol{B} & 0 \end{bmatrix} \begin{bmatrix} \boldsymbol{q} \\ \lambda \end{bmatrix} = \begin{bmatrix} \boldsymbol{F} \\ 0 \end{bmatrix} \tag{A.5}$$

A.3.2 Numerical examples

These preliminary examples investigate the popular multibody problem of a simple pendulum, double-pendulum and slider-crank to show the accuracy and capability of the presented tool. Numerical results are compared to analytical solutions and with solutions obtained using the commercial software MSC Adams.

Flexible pendulum

Two deformable pendulums subjected to the gravity force ($\mathrm{P}_z = \int_V \mathrm{dP}_z \, \mathrm{d}V$) are examined as the first numerical multibody assessment to validate the presented numerical approach.

Figure A.47 shows the dimensions and mechanical data of the models, called "Pendulum I" and "Pendulum II". The structures, modelled using 10 B4 beam elements, may elastically deform and rigidly rotate since they were hinged at one end. The time-step $\Delta t = 0.001$ sec and the control parameter value α = -0.05 are used for all of the following analyses.

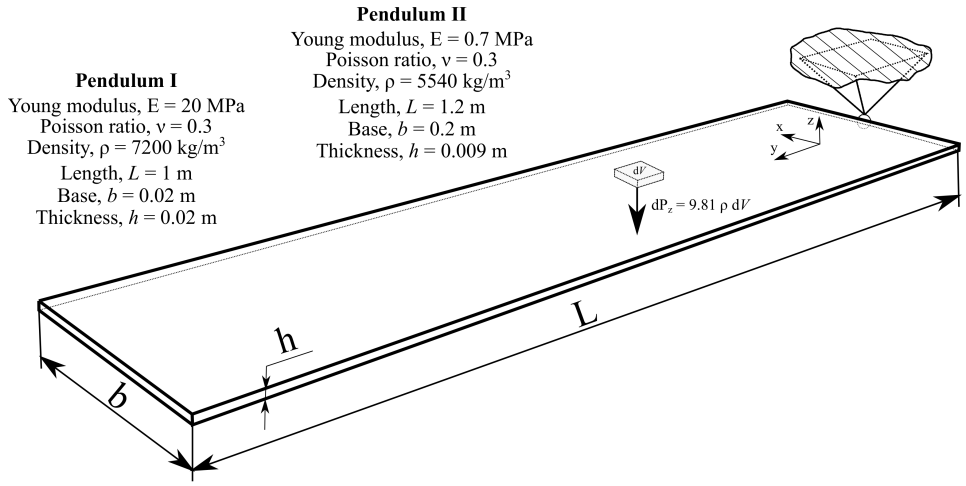

Fig. A.47 Geometry and loading conditions of deformable pendulums under gravity loadings.

The positions of the central point at the free-ends is depicted in Fig. A.48. Regarding the Pendulum I, the various CUF 1D models show the same results, accurately reproducing the reference solution obtained employing a Euler-Bernoulli model [242]. On the contrary, it is possible to note discrepancies between the models for the second configuration due to its higher flexibility. As the order of the theory increases, the cross-section deformations related to the inertial effects are detected. These deformation mechanisms significantly affect the dynamic analyses over the time, as provided in Fig. A.49.

Double-pendulum

With the aim of highlighting the functionality of the present formulation for a problem with joints between two bodies, a double-pendulum in free falling under the effect of gravity (g = 9.81 m/s^2) is studied. The double pendulum is the simplest example of a time-independent system that exhibits chaotic behaviour. The classical double-pendulum system is a planar structure that consists of two revolute joints and two bodies free to rotate in a plane. The double-pendulum exhibits a rich behaviour and provides a significant demonstration of nonlinear dynamics and chaos. Its behaviour varies from regular motion at low energies, to chaos at intermediate energies, and back to regular motion at high energies.

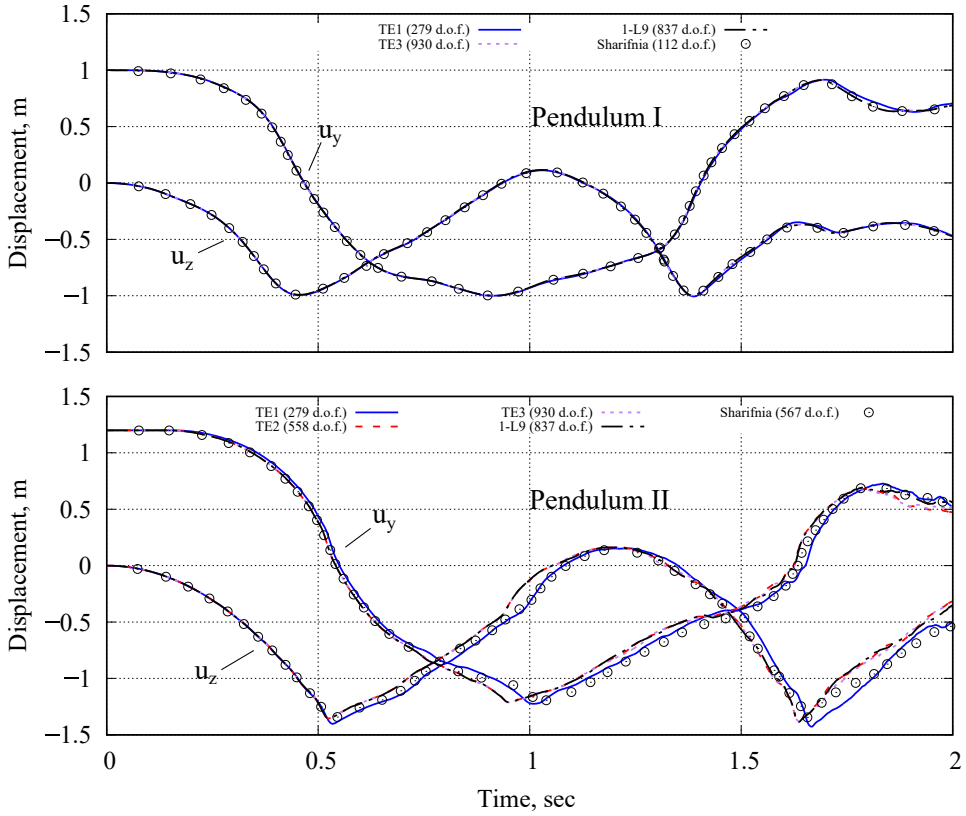

Fig. A.48 Transverse displacements at $(0,L,0)$ evaluated for different beam models.

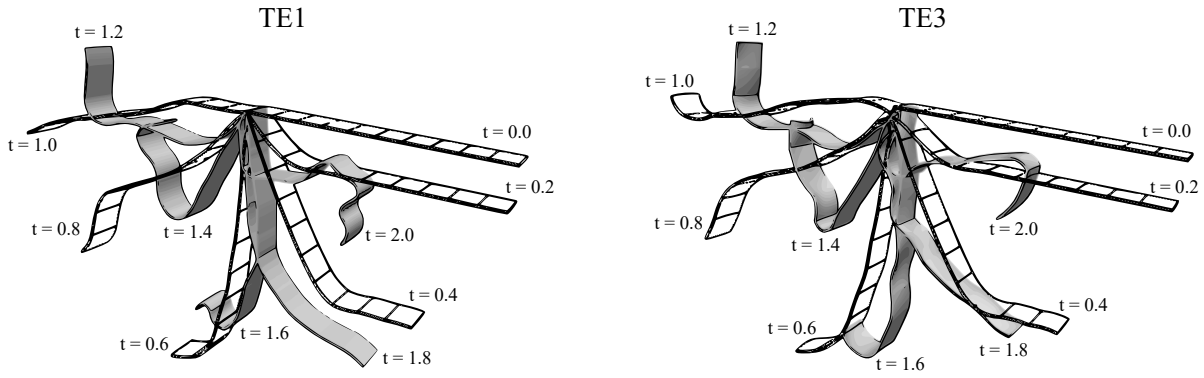

Fig. A.49 Motion of Pendulum II evaluated for two kinematic beam models.

The geometric and material data of the considered system are illustrated in Fig. A.50. The structures is modelled by adopting 5 B4 finite elements along the y-axis and 1L9 on the cross-section for each body. In the initial configuration, the double-pendulum is

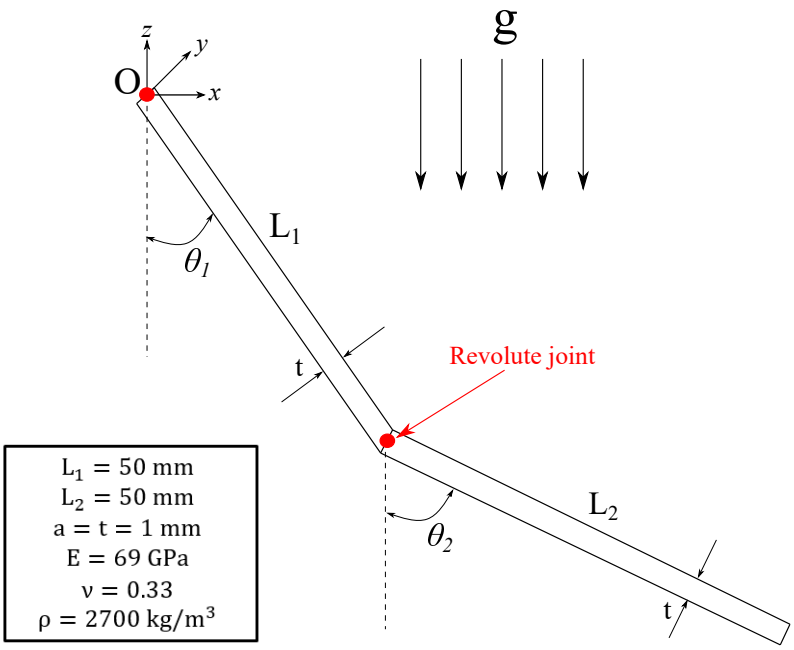

Fig. A.50 Double-pendulum system.

horizontal and has zero initial velocity. For all simulations, the used time-step was Δt = 0.01 seconds, while the value of the control parameter α remained unchanged with respect to the previous analyses (α = -0.05).

The transverse deflection of the endpoint of the system is provided in Fig. A.51, including the comparison with the MSC Adams solution. Instead, Fig. A.52 shows the phase space portraits of the motion of the double-pendulum system. From the results presented in these figures, it is clear that the system starts to exhibit a nonlinear chaotic response.

Slider-crank mechanism

The dynamic analysis of a classical slider-crank mechanism is investigated as the final example. The mechanism consists of a driving beam which only exhibits rotation and a driven beam which is connected to the driving beam at one end and the other end is restricted to horizontal motion. The driving beam has the following dimensions: L_1 = 30 mm, a = 1 mm, t = 1 mm and of the driven beam L_2 = 70 mm, a = 1 mm, t = 1 mm, whereas the material properties for both beams are: E = 71.705E11 Pa, ν = 0.33

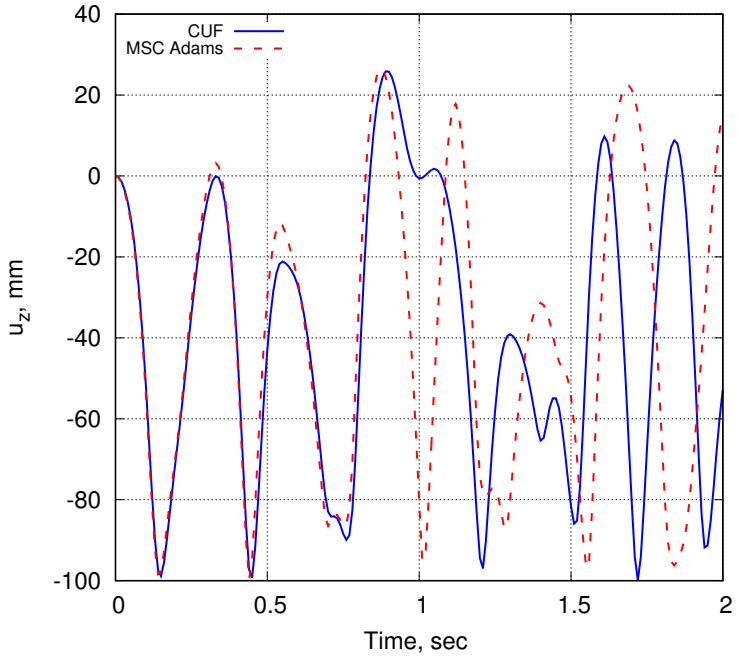

Fig. A.51 Transverse deflection at the endpoint of the double-pendulum.

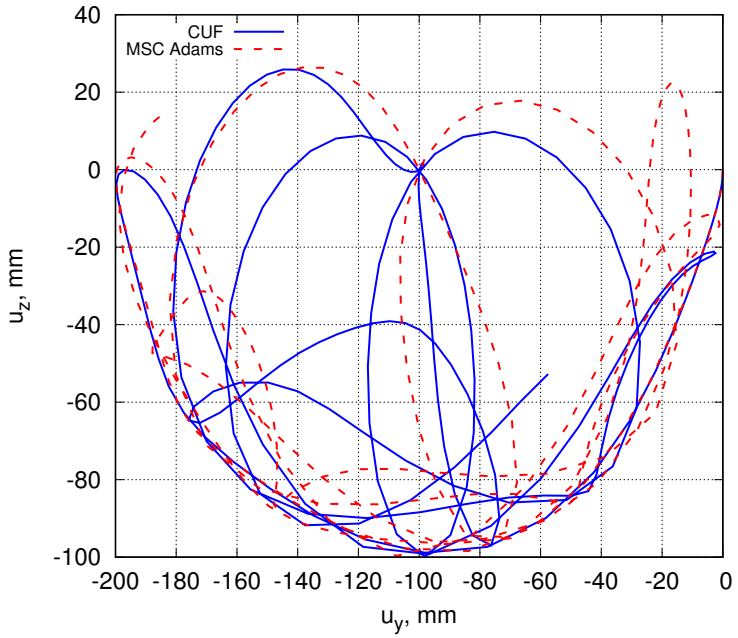

Fig. A.52 u_z vs u_y. Double-pendulum.

and $\rho = 2740$ kg/m^3. The structures is modelled by using a total of 1008 DOFs. The mechanism is driven by the force F, as illustrated in Fig. A.53, prescribed by an input motion given by:

$$\begin{cases} F_y = Fsin(\theta) \\ \\ F_z = Fcos(\theta) \end{cases} \tag{A.6}$$

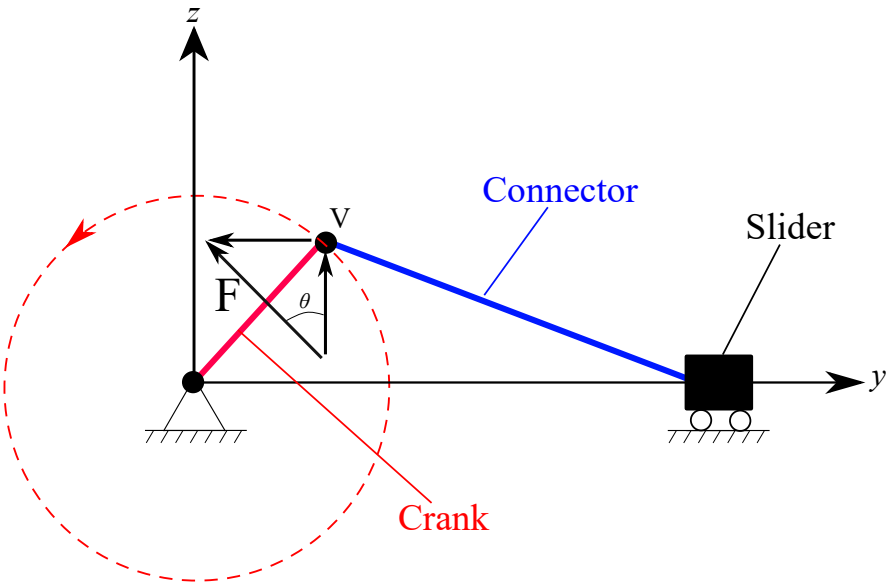

Fig. A.53 Representation of the geometry and loading conditions of the slider-crank mechanism.

Interest is focused on the vertical component of the displacement, velocity and acceleration of the point V. Figs. A.54-A.56 illustrate the position, velocity and acceleration diagrams at the endpoint of the crank, respectively, including the comparison with the MSC Adams solution. Results obtained using the proposed nonlinear multibody approach show an excellent correlation with the MSC Adams ones, providing reasonable confidence for future applications in this topic.

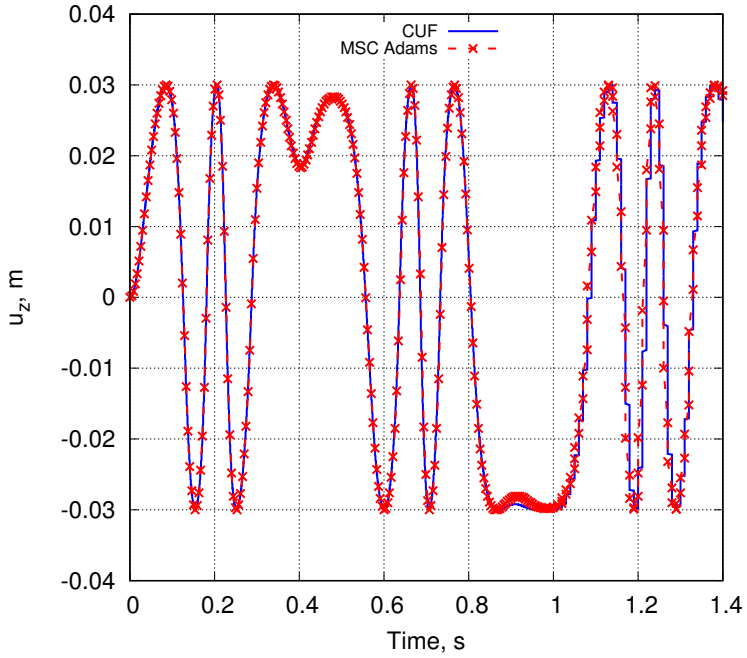

Fig. A.54 u_z vs time. Slider-crank mechanism.

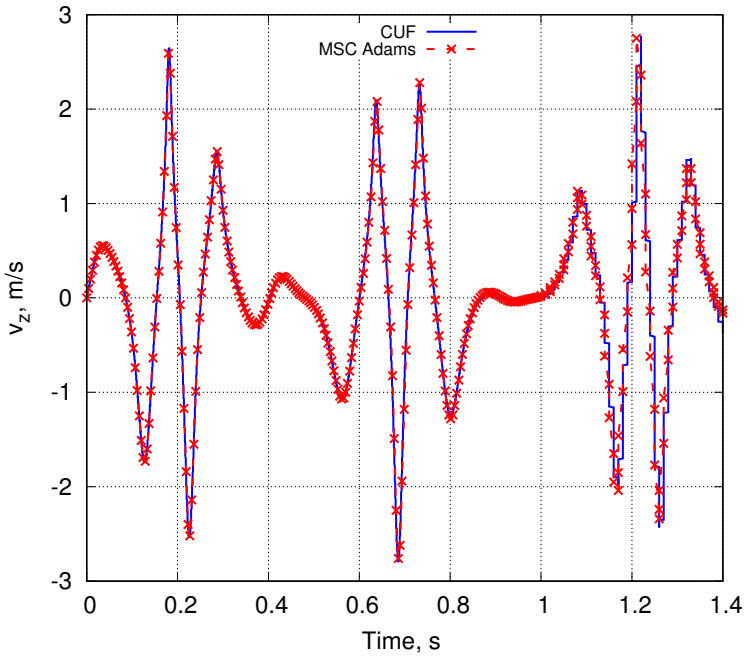

Fig. A.55 v_z vs time. Slider-crank mechanism.

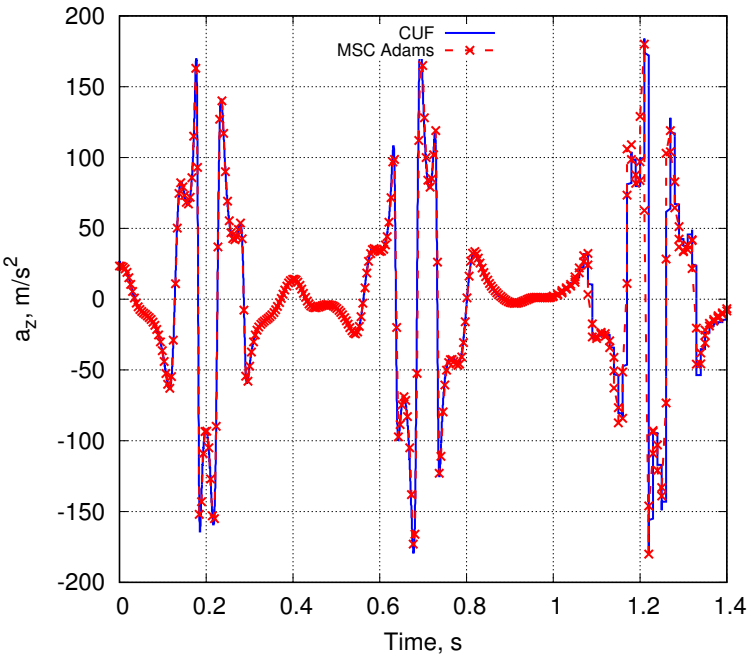

Fig. A.56 a_z vs time. Slider-crank mechanism.

Appendix B

List of publications

B.1 Journal Articles

- Pagani, A., **Azzara**, **R.**, Augello, R., Carrera, E., "Multibody simulation and descent control of a space lander", (2020), *ADVANCES IN AIRCRAFT AND SPACECRAFT SCIENCE*, Vol. 7, pp. 91-113, DOI: 10.12989/aas.2020.7.2.091.

- Pagani, A., **Azzara**, **R.**, Augello, R., Carrera, E., Wu, B., "Accurate through-the-thickness stress distributions in thin-walled metallic structures subjected to large displacements and large rotations", (2020), *VIETNAM JOURNAL OF MECHANICS*, Vol. 42, pp. 239-254, DOI: 10.15625/0866-7136/15042.

- Carrera, E., Pagani, A., **Azzara**, **R.**, Augello, R., "Vibration of metallic and composite shells in geometrical nonlinear equilibrium states", (2020), *THIN-WALLED STRUCTURES*, Vol. 157, DOI: 10.1016/j.tws.2020.107131.

- **Azzara**, **R.**, Carrera, E., Pagani, A., Filippi, M. "Time Response Stress Analysis of Solid and Reinforced Thin-Walled Structures by Component-Wise Models", (2020), *INTERNATIONAL JOURNAL OF STRUCTURAL STABILITY & DYNAMICS*, Vol. 20, DOI: 10.1142/S0219455420430105.

- Pagani, A., **Azzara**, **R.**, Carrera, E., Zappino, E., "Static and dynamic testing of a full-composite VLA by using digital image correlation and output only ground vibration testing", (2021), *AEROSPACE SCIENCE AND TECHNOLOGY*, Vol. 112, DOI: 10.1016/j.ast.2021.106632.

- Pagani, A., **Azzara**, **R.**, Wu, B., Carrera, E., "Effect of different geometrically nonlinear strain measures on the static nonlinear response of isotropic and com-

posite shells with constant curvature", (2021), *INTERNATIONAL JOURNAL OF MECHANICAL SCIENCES*, Vol. 209, DOI: 10.1016/j.ijmecsci.2021.106713.

- Pagani, A., **Azzara**, **R.**, Augello, R., Carrera, E., "Stress States in Highly Flexible Thin-Walled Composite Structures by Unified Shell Model", (2021), *AIAA JOURNAL*, Vol. 59, pp. 4243-4256, DOI: 10.2514/1.J060024.

- Carrera, E., **Azzara**, **R.**, Daneshkhah, E., Pagani, A., Wu, B., "Buckling and post-buckling of anisotropic flat panels subjected to axial and shear in-plane loadings accounting for classical and refined structural and nonlinear theories", (2021) *INTERNATIONAL JOURNAL OF NON-LINEAR MECHANICS*, Elsevier Ltd, pp. 13, Vol. 133, ISSN: 0020-7462, DOI: 10.1016/j.ijnonlinmec.2021.103716.

- Sanchez-Majano, R.A., **Azzara**, **R.**, Pagani, A., Carrera, E., "Accurate stress analysis of variable angle tow shells by high-order equivalent-single-layer and layer-wise finite element models", (2021), *MATERIALS*, Vol. 14, DOI: 10.3390/ma14216486.

- **Azzara**, **R.**, Carrera, E., Pagani, A., "Nonlinear and linearized vibration analysis of plates and shells subjected to compressive loading", (2022), *INTERNATIONAL JOURNAL OF NON-LINEAR MECHANICS*, DOI: 10.1016/j.ijnonlinmec.2022.103936.

- Pagani, A., **Azzara**, **R.**, Carrera, E., "Geometrically nonlinear analysis and vibration of in-plane-loaded variable angle tow composite plates and shells", (2022), *ACTA MECHANICA*, pp. 1-24, DOI: 10.1007/s00707-022-03226-2.

- Zhu, F., Augello, R., **Azzara**, **R.**, Pagani, A., Carrera, E., Chen, W., "Vibration and buckling analysis of curved panel subjected to combined internal pressure and axial compression", (2022), *AIAA JOURNAL*, DOI: 10.2514/1.J061999.

- **Azzara**, **R.**, Filippi, M., Pagani, A., "Variable-kinematic finite beam elements for geometrically nonlinear dynamic analyses", (2022), *MECHANICS OF ADVANCED MATERIALS AND STRUCTURES*, pp. 1-9, DOI: 10.1080/15376494.2022.2091185.

- **Azzara**, **R.**, Carrera, E., Filippi, M., Pagani, A., "Vibration analysis of thermally-loaded isotropic and composite beam and plate structures", (2022), *JOURNAL OF THERMAL STRESSES*, submitted.

B.2 Conference Proceedings

- Pagani, A., Carrera, E., Zappino, E., **Azzara**, **R.**, de Miguel, A.G., Lionetti, M.P., "Static and dynamic experimental analysis of a full composite VLA aircraft", In: *Proceedings of the XXV International Congress of Aeronautics and Astronautics, AIDAA XXV*, Rome, Italy, 9-12 September, 2019.

- Sanchez-Majano, A.R., **Azzara**, **R.**, Pagani, A., Carrera, E., "Stress analysis of variable angle tow shells by high-order unified elements", In: *Proceedings of the XXVI International Congress of the Italian Association of Aeronautics and Astronautics - AIDAA XXVI*, Virtual Congress, 31 August - 3 September, 2021.

- **Azzara**, **R.**, Pagani, A., Carrera, E., Sanchez-Majano, A.R., "A numerical nonlinear vibration-buckling investigation of variable stiffness composite plate and shell structures", In: *Proceedings of the XXVI International Congress of the Italian Association of Aeronautics and Astronautics - AIDAA XXVI*, Virtual Congress, 31 August - 3 September, 2021.

- **Azzara**, **R.**, Pagani, A., Carrera, E., "Nonlinear Vibration Correlation and Buckling Analysis of Flat Plates and Shells", In: *Proceedings of the ASME 2021 International Mechanical Engineering Congress and Exposition (IMECE2021)*, Virtual Congress, November 1-4, 2021.

- Zhu, F., Augello, R., **Azzara**, **R.**, Pagani, A., Carrera, E., Chen, W., "Vibration and buckling analysis of curved panel subjected to combined internal pressure and axial compression", *AIAA SCITECH 2022 Forum*, San Diego, CA & Virtual, 3-7 January, 2022.

- **Azzara**, **R.**, Filippi, R., Augello, R., Carrera, E., Pagani, A., "Nonlinear dynamic analyses of isotropic and composite structures using refined and unified one-dimensional finite elements", *International Conference on Nonlinear Solid Mechanics (ICoNSoM 2022)*, Alghero, Italy, 13-16 June, 2022.

- Carrera, E., Pagani, A., Augello, R., **Azzara**, **R.**, "Nonlinear vibration of composite beams, plates and shells subjected to compression and shear loadings by unified finite elements and comparison with VCT experiments", *25th International Conference on Composite Structures (ICCS25)*, Porto, Portugal, 19-22 July, 2022.

- **Azzara**, **R.**, Filippi, M., Pagani, A., Carrera, E., "Nonlinear vibration-buckling investigation of unstiffened and stiffened structures subjected to mechanical and

thermal loadings", *33rd Congress of the International Council of the Aeronautical Sciences (ICAS)*, Stockholm, Sweden, 4-9 September, 2022.

- Filippi, M., **Azzara**, **R.**, Carrera, E., "Variable kinematic shell finite elements for dynamic analyses of rotating structures", In: *Proceedings of the ASME 2022 International Mechanical Engineering Congress and Exposition (IMECE2022)*, Columbus, Ohio, USA, October 30 - November 3, 2022.

- **Azzara**, **R.**, Filippi, M., Carrera, E., "Nonlinear transient response of isotropic and composite structures with variable kinematic beam and plate finite elements", In: *Proceedings of the ASME 2022 International Mechanical Engineering Congress and Exposition (IMECE2022)*, Columbus, Ohio, USA, October 30 - November 3, 2022.